

CHARACTERIZATION OF ADSORPTION-DESORPTION PROPERTIES OF  
OXYGEN & WATER ON MIXED OXIDES

A THESIS SUBMITTED TO  
THE GRADUATE SCHOOL OF NATURAL AND APPLIED SCIENCES  
OF  
MIDDLE EAST TECHNICAL UNIVERSITY

BY

CİHAN ATEŞ

IN PARTIAL FULFILLMENT OF THE REQUIREMENTS  
FOR  
THE DEGREE OF MASTER OF SCIENCE  
IN  
CHEMICAL ENGINEERING

FEBRUARY 2015



Approval of thesis:

**CHARACTERIZATION OF ADSORPTION-DESORPTION PROPERTIES OF  
O<sub>2</sub>&H<sub>2</sub>O ON MIXED OXIDES**

submitted by **CIHAN ATEŞ** in partial fulfillment of the requirements for the degree of  
**Master of Science in Chemical Engineering Department, Middle East Technical  
University** by,

Prof. Dr. M. Gülbin Dural Ünver  
Director, Graduate School of **Natural & Applied Sciences**

Prof. Dr. Halil Kalıpçılar  
Head of Department, **Chemical Engineering**

Prof. Dr. Deniz Üner  
Supervisor, **Chemical Engineering Dept., METU**

**Examining Committee Members:**

Prof. Dr. Mahmut Parlaktuna  
Petroleum and Natural Gas Engineering Dept., METU

Prof. Dr. Deniz Üner  
Chemical Engineering Dept., METU

Asst. Prof. Dr. Harun Koku  
Chemical Engineering Dept., METU

Dr. İnci Ayrancı  
Chemical Engineering Dept., METU

Dr. Başar Çağlar  
Gate Elektronik, ANKARA

**Date:** 05.02.2015

**I hereby declare that all information in this document has been obtained and presented in accordance with academic rules and ethical conduct. I also declare that, as required by these rules and conduct, I have fully cited and referenced all material and results that are not original to this work.**

Name, Last name: Cihan Ateş

Signature:

## ABSTRACT

### CHARACTERIZATION OF ADSORPTION-DESORPTION PROPERTIES OF OXYGEN & WATER ON MIXED OXIDES

Ateş, Cihan

M.S., Department of Chemical Engineering

Supervisor: Prof. Dr. Deniz Üner

February 2015, 204 pages

The scope of this study includes the development of a methodology to determine a candidate material for two step thermochemical heat storage applications via fundamental principles of thermodynamics. The feasibility of utilizing stored thermochemical energy to produce CO from CO<sub>2</sub> and H<sub>2</sub> from H<sub>2</sub>O was demonstrated theoretically and experimentally. Metal oxide selection criteria were chosen as transport, kinetic and thermodynamic constraints. As a result Co<sub>3</sub>O<sub>4</sub> was considered worthy of further investigation. Thermal decomposition kinetics of Co<sub>3</sub>O<sub>4</sub> to CoO were measured experimentally. CO<sub>2</sub> and H<sub>2</sub>O were used as oxidants to reoxidize cobalt oxide reduced by thermal decomposition in repeated experiments. Co<sub>3</sub>O<sub>4</sub>/CoO redox couple has shown outstanding results for water splitting reaction compared to presented alternatives in the recent literature. Further studies on heat and mass transfer limitations in macroscopic scale were performed using COMSOL® Multiphysics platform. Finally, syngas production

using cobalt membrane reactors was probed theroretically. Modeling studies on membrane reactors indicated promising results for cobalt oxide.

**Keywords:** Syngas, thermodynamics, metal oxide, cobalt oxide, thermal decompostion, mathematical modeling, water splitting, carbon dioxide splitting.

## ÖZ

### KARIŞIK YAPILI METAL OKSİTLERDE OKSİJEN VE SU ADSORPSİYON- DESORPSİYON ÖZELLİKLERİNİN KARAKTERİZASYONU

Ateş, Cihan

Yüksek Lisans, Kimya Mühendisliği Bölümü

Tez Yöneticisi: Prof. Dr. Deniz Üner

Şubat 2015, 204 sayfa

Bu çalışmanın kapsamı termodinamiğin temel ilkeleri üzerinden iki adımlı termokimyasal ısı depolama uygulamaları için bir aday malzeme belirlemek üzere metodoloji geliştirilmesini içermektedir. Depolanmış termokimyasal enerjinin kullanılarak H<sub>2</sub>O'dan H<sub>2</sub> ve CO<sub>2</sub>'dan CO üretilmesinin uygulanabilirliği teorik ve deneysel olarak gösterilmiştir. Metal oksit seçim kriterleri taşınım, kinetik ve termodinamik sınırlamalar olarak seçilmiştir. Bunun sonucunda Co<sub>3</sub>O<sub>4</sub> ileri incelemeye değer kabul edilmiştir. Co<sub>3</sub>O<sub>4</sub>'ün CoO'e termal dekompozisyonun kinetiği deneysel olarak ölçülmüştür. Tekrarlanan deneylerde CO<sub>2</sub> ve H<sub>2</sub>O termal dekompozisyon ile indirgenmiş kobalt oksidi tekrar oksitlemek için oksidasyon maddesi olarak kullanılmıştır. Co<sub>3</sub>O<sub>4</sub>/CoO redoks çifti güncel literatürde sunulan alternatiflere kıyasla su ayrıştırma tepkimesi için çarpıcı sonuçlar göstermektedir. Makroskopik ölçekteki ısı ve kütle aktarım sınırlamaları hakkındaki daha

ileri çalıřmalar COMSOL® Multiphysics platformu kullanılarak yapılmıřtır. Son olarak, kobalt membran reaktör kullanılarak sentez gazı üretimi teorik olarak incelenmiřtir. Membran reaktörler üzerine modelleme çalıřmaları kobalt oksit için gelecek vaadeden sonuçlar göstermiřtir.

**Anahtar Kelimeler:** Sentez gazı, termodinamik, metal oksit, kobalt oksit, termal dekompozisyon, matematiksel modelleme, su ayrıřtırma, karbondioksit ayrıřtırma.

to Ceren  
&  
to life  
we will live  
to the fullest  
together

## ACKNOWLEDGMENTS

First and foremost, I would like to express my sincerest gratitude to my supervisor Prof. Dr. Deniz Üner for giving me the opportunity to be a part of her research group where I had the chance to explore my deep dreams and face the pitfalls on the intuitive path. Thank you for being a great thinker and a challenging mentor.

I want to thank all former members of CACTUS Research Group for their irreplaceable contribution for this beautiful environment. I wish to express my great appreciations to group members: Mustafa Yasin Aslan, Arzu Kanca, İbrahim Bayar, Hale Ay, Nevzat Can Aksu, Mert Mehmet Oymak, Deniz Kaya, Veysi Halvacı, Taymaz Tabari, Aziz Doğan İlgün and Ezgi Yavuzılmaz. I'd like to give special thanks to Atalay Çalışan for his excellent support and guidance. Without your knowledge and experience, all the problems I have faced might never be solved. Thanks for always being there for us. My sincere thanks are also to Necip Berker Üner for enthusiastic and inspiring discussions. Your criticism, suggestions and contributions were very valuable to me since my senior year. I am happy for being met with you all and having spent all that time together, who were beyond being colleagues: Güvenç Oğulgönen, Elif İrem Şenyurt, Özge Çimen, Merve Özkutlu, Berrak Erkmen and Burcu Şahin.

The technical staff of our department Süleyman Nazif Kuşhan, Ertuğrul Özdemir, Adil Demir, İsa Çağlar, Mihrican Açıkgöz, Gülten Orakçı and Turgut Aksakal were greatly appreciated for their help at different stages of my study.

The Scientific and Research Council of Turkey (TUBITAK) are kindly acknowledged for the financial support within the scope of the 1003 Project related to my graduate study.

I especially thank my mom, dad, and sister for their love and care. I would not have made it this far without them. Special thanks to my dear friend Zehra Atakan for all her advice and support. It has always been a relief to know you are beside me when times are rough.

The most restful and beautiful happening of the last few years is finding my better half whom is the best person out there for me. I heartily thank Ceren for her great support and unconditional love. These past several years have not been easy, both academically and personally. I truly thank you for seeing me through, especially when I was irritable and down.



## TABLE OF CONTENTS

ABSTRACT .....	v
ÖZ .....	vii
ACKNOWLEDGMENTS .....	x
TABLE OF CONTENTS .....	xiii
LIST OF TABLES.....	xvii
LIST OF FIGURES.....	xix
CHAPTERS	
1 INTRODUCTION .....	1
1.1 Syngas Production.....	3
1.1.1 Steam Reforming.....	6
1.1.2 Dry Reforming.....	8
1.1.3 Partial Oxidation.....	9
1.1.4 Autothermal Reforming.....	11
1.1.5 Alternative Technologies.....	12
2 OBJECTIVES OF THE STUDY.....	17
3 LITERATURE SURVEY.....	19
3.1 Thermochemical Heat Storage on Reducible Metal oxides .....	19
3.2 Syngas Production on Reducible Metal Oxides .....	23
3.3 Noncatalytic Gas–Solid Reactions .....	27
3.3.1 Tools for Noncatalytic Gas Solid Reaction Mechanisms .....	31
3.4 Cobalt Oxide: Phases, Characterization and Kinetics .....	33
3.4.1 Cobalt Oxide.....	33
3.4.2 Characterization, Thermal Analysis and Kinetics of Cobalt Oxides.....	34
4 METHODS AND MATERIALS .....	37

4.1	Thermodynamic Analysis .....	38
4.1.1	Selection of Metal Oxide Candidates.....	40
4.1.1.1	Theoretical Thermodynamic Efficiencies of Metal Oxides .....	41
4.2	Experimental Methods and Materials .....	43
4.2.1	Experimental Methods.....	43
4.2.1.1	Procurement of the Material.....	43
4.2.1.2	Material Characterization .....	43
4.2.1.3	BET Experiments .....	43
4.2.1.4	TGA Experiments.....	44
4.2.1.5	TPR and Water Splitting Experiments .....	44
4.2.1.6	Thermal Decomposition and CO <sub>2</sub> Splitting Experiments.....	46
4.3	Kinetic Analysis .....	48
4.4	Mass and Heat Transfer Limitations .....	51
4.4.1	Mass Transfer.....	51
4.4.1.1	Growth Model.....	51
4.4.2	Heat Transfer.....	55
4.4.2.1	Fundamental Calculations .....	56
4.4.2.2	Time Scales for the Heating/Cooling of Finite Geometries .....	56
4.4.3	Nonisothermal Effects: Simultaneous Heat and Mass Transfer within a Spherical Particle .....	57
5	RESULTS.....	59
5.1	Investigating the Feasibility of Redox Reactions through Thermodynamic Analysis.....	59
5.1.1	Understanding the State of Art in Syngas Production.....	59
5.1.1.1	Cobalt –Cobalt Oxide Phase Transformation.....	63
5.1.1.2	Partial Oxidation of Methane in the Presence of Cobalt .....	65
5.1.1.3	Steam Reforming of Methane in the Presence of Cobalt .....	68
5.1.1.4	Autothermal Thermal Reforming of Methane in the Presence of Cobalt.....	71

5.1.1.5	Concluding Remarks .....	79
5.1.2	Possibility of Syngas Production from CO <sub>2</sub> and H <sub>2</sub> O over Cobalt Oxide.....	81
5.2	Experimental Results.....	85
5.2.1	Material Characterization.....	85
5.2.2	Adsorption-Desorption of Oxygen on Cobalt Oxide.....	88
5.2.3	Thermal Decomposition of Cobalt Oxide.....	92
5.2.4	Production of Hydrogen over Reduced Cobalt Oxide.....	94
5.2.4.1	Reducibility of Spinel Cobalt Oxide.....	94
5.2.4.2	Water Splitting over Reduced Cobalt Oxide .....	95
5.2.5	Production of CO over Reduced Cobalt Oxide.....	96
5.2.5.1	Simulation of Heat Transfer Problem in the Reactors Used for CO Production .....	100
5.3	Kinetic Analysis .....	101
5.4	Mathematical Modeling of Thermal Decomposition of Cobalt Oxide .....	105
5.4.1	1-D Modeling: Transient Reduction of Cobalt Oxide in a Gradientless Reactor.....	105
5.4.2	3D Modeling: Transient Response of a Reactor with a Finite Geometry.....	112
5.5	Membrane Reactors: Heat and Mass Transfer Limitations.....	121
6	SUMMARY OF THE RESULTS AND FUTURE PROSPECTS .....	127
7	CONCLUSIONS .....	135
	REFERENCES.....	137
	APPENDICES	
A.	THERMODYNAMICS .....	149
A.1	Free Energy Change with Temperature for Various Oxides .....	153
A.2	Free Energy Minimization .....	154
A.2.1	Methodology Used .....	154
A.2.2	Lagrange Multipliers Method .....	154
A.2.3	Lagrange Multipliers for Free Energy Minimization .....	155
A.2.4	Other Constraints .....	155
A.2.5	Procedure .....	156
A.2.6	MATLAB Code .....	157

A.3 Thermal Efficiency Comparison .....	160
B. MASS AND HEAT TRANSFER CALCULATIONS .....	161
B.1 Diffusivity of Oxygen in Different Mediums .....	161
B.2 Metal-Oxygen Bond Energies .....	165
B.3 Fundamental Calculations in Heat Transfer .....	167
B.3.1 Number of molecules per $1\mu\text{m} \times 1\text{ cm}$ surface .....	167
B.3.2 Heat released/ $\text{m}^2$ .....	168
B.3.3 Increase in Temperature when 1 mol of $\text{Co}_3\text{O}_4$ is formed at 1000 K .....	168
B.3.4. Instantaneous Infinite Plane Source Emitting Half Space .....	169
B.3.5 Constant Surface Temperature and Heat Flux in a Semi-Infinite Plate .....	171
B.4 Heating/Cooling of a Finite Geometry .....	174
B.4.1 Cube of $\text{Co}_3\text{O}_4$ : Heating Problem .....	174
B.5 Numerical Solution of Simultaneous Mass and Heat Transfer within a Spherical Particle and Effectiveness Factor .....	179
B.5.1 Definition of Nonisothermal Effectiveness Factor .....	180
B.5.2 Solution of the ODE .....	181
B.5.3 Calculation of $\beta$ for Cobalt Oxide .....	184
B.6 Solution of the Growth Model .....	185
B.7 Simulation of Heat Transfer Problem in the Reactors Used for CO Production .....	188
B.7.1 Steel Reactor .....	188
B.7.2 Quartz Reactor .....	190
B.8 Physical Properties used in Reactor Modeling .....	192
C. EXPERIMENTAL DATA .....	193
C.1 Adsorption-Desorption of Oxygen on Cobalt Oxide .....	193
C.2 Production of Hydrogen over Reduced Cobalt Oxide .....	197
C.3 Kinetic Analysis .....	198
D. DERIVATION OF MATHEMATICAL MODELS .....	201
D.1 Isothermal Gradientless Reactor .....	201
D.2 Non-isothermal Gradientless Reactor .....	203

## LIST OF TABLES

### TABLES

Table 1:1 Classification of industrial gases based on their calorific values.....	3
Table 1:2 Syngas compositions for different industrial processes.....	5
Table 1:3 Cost and energy comparison for gaseous, liquid, and solid fuels.....	6
Table 1:4 Reactions in steam reforming.....	7
Table 1:5 Reactions in Methane Partial Oxidation.....	10
Table 3:1 Energy density based on heat storage medium.....	20
Table 3:2 Oxidation-reduction temperature ranges for various metal oxides.....	21
Table 3:3 Reactions of cyclic hydrogen production technologies.....	24
Table 3:4 Some examples for different types of redox cycles.....	25
Table 3:5 Hydrogen Production capacities for several metal oxide couples.....	27
Table 3:6 Noncatalytic gas solid reaction examples from industry.....	28
Table 3:7 Kinetic models for working function f.....	32
Table 3:8 Locations of $\text{Co}_3\text{O}_4$ and $\text{CoO}$ diffraction lines.....	34
Table 3:9 Characterization of cobalt oxide phases by FTIR and Raman Spectroscopy..	35
Table 3:10 Chemisorption of $\text{CO}$ , $\text{CO}_2$ , $\text{H}_2\text{O}$ and $\text{O}_2$ on Cobalt Surfaces.....	36
Table 4:1 Calcination Temperatures and Durations.....	44
Table 4:2 Diffusivities of oxygen and cobalt in cobalt oxide.....	55
Table 5:1 Chemical reactions in syngas production.....	61
Table 5:2 Irreversibly Adsorbed $\text{O}_2$ on $\text{Co}_3\text{O}_4$ samples after three adsorption-desorption cycles.....	90
Table 5:3 DTA peak temperatures at the heating rates of $5^\circ$ , $10^\circ$ and $15^\circ$ per minute for spinel cobalt oxide thermal decomposition.....	101
Table 5:4 Calculated Activation Energies from Kissinger Method via DTA couples...102	

Table 5:5 $\ln QdadT$ values for different heating rates (Q) at various $\alpha$ values.....	102
Table 5:6 Mesh size of the cubic reactor.....	114
Table 5:7 Hydrogen production via membrane reactor with changing thickness.....	122
Table 5:8 Comparison of membrane model results with the literature.....	123
Table A:1 Temperature averaged thermodynamic data for various oxides.....	149
Table A:2 Thermodynamic data at different temperatures used in thermodynamic analysis .....	152
Table A:3 Thermal efficiencies of various metal oxides .....	160
Table B:1 Diffusivities of oxygen in various metal-metal oxides .....	161
Table B:2 Metal-oxygen bond energies for various metal oxides .....	165
Table B:3 Effectiveness factors for several Thiele modulus values .....	183

## LIST OF FIGURES

### FIGURES

Figure 1:1 Syngas consumption in different industries in 2000.....	4
Figure 1:2 Methane conversion equilibrium for different steam to methane ratios.....	7
Figure 3:1 Schematic representation of various resistances in noncatalytic gas solid reactions.....	28
Figure 3:2 Shrinking Core Model.....	30
Figure 4:1 Free energy change with respect to temperature for selected formation reactions.....	40
Figure 4:2 Efficiency for the splitting reactions at various thermal reduction and re-oxidation temperatures (1000 – 1800 K) for water and CO <sub>2</sub> .....	42
Figure 4:3 Experimental setup for water splitting experiments.....	45
Figure 4:4 Setup for the CO <sub>2</sub> Splitting Experiments.....	47
Figure 4:5 Determination of shape index.....	49
Figure 4:6 Schematic representation of the growth model.....	52
Figure 5:1 Equilibrium composition for Co-O system.....	63
Figure 5:2 Equilibrium conversion and selectivity for partial oxidation of methane.....	65
Figure 5:3 Equilibrium conversion and selectivity for steam reforming of methane.....	68
Figure 5:4 Effect of oxygen addition to CO selectivity in autothermal thermal reforming of methane.....	71
Figure 5:5 Effect of oxygen addition to CO <sub>2</sub> selectivity in autothermal thermal reforming of methane.....	73
Figure 5:6 Effect of oxygen addition to H <sub>2</sub> selectivity in autothermal thermal reforming of methane.....	74

Figure 5:7 Effect of oxygen addition to methane conversion in autothermal thermal reforming of methane.....	76
Figure 5:8 Effect of oxygen addition to water conversion in autothermal thermal reforming of methane.....	77
Figure 5:9 Free energy comparison of syngas production reaction when oxygen is supplied from cobalt oxide.....	79
Figure 5:10 Schematic representation of a membrane reactor for syngas production....	80
Figure 5:11 Cobalt oxide phase transitions in oxygen environment at various temperatures and pressures.....	81
Figure 5:12 CO-CO <sub>2</sub> equilibrium for cobalt oxidation reactions for various pressures at 500, 1000 and 1200 K.....	82
Figure 5:13 H <sub>2</sub> O-H <sub>2</sub> equilibrium for cobalt oxidation reactions for various pressures at 500, 1000 and 1200 K.....	83
Figure 5:14 XRD patterns for Cobalt oxide samples.....	85
Figure 5:15 XRD patterns for sample CA-0913-1 before and after three months.....	87
Figure 5:16 Irreversible adsorption of oxygen on cobalt oxide.....	88
Figure 5:17 TGA curves for cobalt oxide in nitrogen atmosphere at different heating rates.....	92
Figure 5:18 Cobalt decomposition in inert and oxidative environment.....	93
Figure 5:19 Reduction of Co <sub>3</sub> O <sub>4</sub> to Co via H <sub>2</sub> in Ar flow (10°/min).....	94
Figure 5:20 Hydrogen production over reduced cobalt oxide with water splitting reaction.....	95
Figure 5:21 Hydrogen peak obtained for the third injection during the water splitting reaction.....	96
Figure 5:22 O <sub>2</sub> signal for Co <sub>3</sub> O <sub>4</sub> reduction for 1 g of sample CA-0913-0.....	97
Figure 5:23 O <sub>2</sub> signal for Co <sub>3</sub> O <sub>4</sub> reduction for 1 g of sample CA-0913-0 for second run.....	97
Figure 5:24 O <sub>2</sub> signal for Co <sub>3</sub> O <sub>4</sub> reduction for 15 g of sample CA-0913-0.....	98
Figure 5:25 CO production (left - o) and oxygen signal (right - x) for 15 g of sample CA0913-0.....	99

Figure 5:26 CO production for 15 g of sample CA0913-0 in the second consecutive run.....	99
Figure 5:27 Change of $\alpha$ with temperature for different heating rates.....	103
Figure 5:28 Derivation of $\ln A f \alpha$ values at mean alpha values.....	103
Figure 5:29 Derivation of order of reaction and pre-exponential factor.....	104
Figure 5:30 Dimensionless conversion of cobalt oxide reduction in isothermal batch reactor.....	106
Figure 5:31 Dimensionless conversion of cobalt oxide reduction in non-isothermal batch reactor.....	107
Figure 5:32 Change in temperature of the non-isothermal batch reactor during the reduction of cobalt oxide.....	108
Figure 5:33 Change in thermal decomposition time and average temperature for the non-isothermal batch reactor at various sizes.....	109
Figure 5:34 Dimensionless conversion of cobalt oxide reduction in adiabatic batch reactor at various initial temperatures.....	111
Figure 5:35 Schematic representation of the reactor used in 3D modeling.....	112
Figure 5:36 Concentration and temperature profiles for 3D reactor and comparison with a gradientless reactor with identical conditions.....	115
Figure 5:37 Resistances for partial oxidation (steam reforming) of methane via membrane reactor.....	121
Figure 5:38 Schematic representation of the model used for identifying heat transfer limitations in the membrane reactor.....	124
Figure 5:39 Temperature profile of the membrane during the steam reforming reaction.....	125
Figure A:1 Free energy change of various metal oxides .....	153
Figure B:1 Lattice structure of spinel cobalt oxide .....	167
Figure B:2 Transient temperature profile for infinite plane source emitting half space .	170
Figure B:3: Transient temperature profiles for constant surface temperature boundary condition .....	172
Figure B:4: Transient temperature profiles for constant surface flux boundary condition.....	173

Figure B:5 Diagonal transient temperature profile.....	175
Figure B:6 Temperature profiles at different time steps for 0.75 mm thin slab.....	177
Figure B:7 Transient temperature profiles as a function of slab thickness.....	178
Figure B:8 Nonisothermal effectiveness factor.....	183
Figure B:9 Increase in oxide layer thickness in time.....	186
Figure B:10 Reaction constant (1/s) and Diffusivity of Oxygen (cm <sup>2</sup> /s) as a function of temperature (K).....	187
Figure B:11 Da number as a function of temperature (K).....	188
Figure B:12 Temperature profile for the steel reactor.....	189
Figure B:13 Schematics of the quartz reactor.....	190
Figure B:14 Temperature of the midpoint in the quartz reactor as a function of time...	190
Figure B:15 Temperature profile of the midpoint cross section in the quartz reactor at steady state.....	191
Figure B:16 Temperature profile of the axial cross section in the quartz reactor at steady state.....	191
Figure C:1 Comparison of oxygen adsorption isotherms at room temperature for sample CA-0913-1 and CA-0913-1(2).....	193
Figure C:2 Area for the produced hydrogen for each cycle with water splitting reaction .....	197
Figure C:3 DTA curves obtained at the heating rates of 5° C, 10° C and 15° C for spinel cobalt oxide thermal decomposition .....	198

# CHAPTER 1

## INTRODUCTION

Catalysts participate in chemical reactions converting the reactants into desired products while remaining unchanged after each reaction cycle composed of many different steps. One of different types, heterogeneous catalysts, are quite critical and the key element in many industrial chemical processes. Out of many diversified areas, 90% of the processes depend on heterogeneous catalysis [1]. Explaining the behavior of heterogeneous catalysts is difficult since there are plenty of variations creating distinct surface chemistry phenomena. This variety creates the need for work requiring the expertise of chemists, physicists, material scientists and reaction engineers. Furthermore, developed recipes should be optimized for the necessity of the industry in terms of material composition and structure, methods of production and the possible ways the catalyst are to be used (like pellets having different physical properties). Disadvantages of heterogeneous catalysts can be listed as the lack of knowledge on the location of active center, difficulty in scaling-up the method of production and reproducibility of the recipe and the unavailability of the computational calculations on direct molecular simulations for high number of atoms making the estimations difficult. So, improvement on catalysis is usually considered to be an experimentally trial and error procedure [2].

Heterogeneous catalysts are industrially preferred mainly due to the fact that they can be easily separated from reaction medium and they have high surface areas, which enables a high number of active sites for a given reactor volume. In fact, a good catalyst has good

selectivity, stability, durability in the presence of catalyst poisons as well as its economic feasibility. It is also important that catalyst performance must be reproducible for a desired amount of time and it is desired to be environmentally tolerable. Given these, development of a catalyst requires a well-organized collaborated work. To illustrate the big picture, it is stated that there are more than 150 international cooperation developing around 100 types of catalysts mainly for petrochemical and chemical industries [3]. About 25% of the Gross National Product (GNP) of the developed countries like US, Japan comes from industrial catalysis and the market value of catalysis was appraised as US \$ 13 billion in 2004, globally [3]. Thousands of people are working in this area to develop better alternatives for existing processes and develop new catalytic processes to reduce undesired products and to use the reactants in a more efficient way to achieve more environmental methods requiring less energy and material input which also requires less capital investment.

Catalytic reactions are crucial for the development of existing chemical processes and for the invention of new routes for the need of society. Though, they must be considered together: any chemical system can only be designed by developing the process and the catalyst simultaneously. It has been told that “. . . designing catalysts to satisfy process needs is like writing prescriptions to cure illness” [4]. So, a catalytic study can be fitted into one of the following categories:

- Developing a new catalyst for a new process
- Developing an existing catalyst for its own process or for a similar process
- Developing recipes for scaling-up laboratory results to industrial scale production
- Clarification of a failure for a given catalyst-process couple

where the motivation of this study fits to the second category. One of the current objectives of the chemical industry is to develop solutions that enables to become sustainable, which includes modifying existing processes such that they will require less energy and reactants per product by achieving high selectivities leading to less and ideally no waste. Such desired combination of selectivity and profitability has been enabled for some ‘dream’ oxidation reactions after decades of studies like propane to acrylonitrile,

propene to propene oxide with hydrogen peroxide. Those reactions are labeled as dream oxidations since they provide more economic technologies and they are more environmentally friendly, one of which is the production of syngas directly from carbon dioxide and water.

Synthesizing CO and H<sub>2</sub> from carbon dioxide and water catalytically is the fundamental target of this study. Particularly, utilization of the stored thermal energy with the available solar thermal heat storage technologies via two step metal oxide redox reactions has been ruminated about to propose a solution to that need. Before going through the thermal heat storage applications and their usage for CO and H<sub>2</sub> production, a brief summary of the state of art in syngas production is summarized in the following section to create a basis to have a better understanding of the advantages and disadvantages of the proposed technology.

## 1.1 Syngas Production

Syngas is a mixture of gas containing mainly carbon monoxide and hydrogen in different ratios and generally distinguished from other industrial gases (composed of hydrogen and carbon monoxide) by its calorific value as seen in Table 1:1 [5].

Table 1:1 Classification of industrial gases based on their calorific values

<b>Gas Type</b>	<b>Calorific Value (kJ/m<sup>3</sup> STP)</b>
Water and producer gas	4,600 – 12,500
Synthesis and reduction gas	12,500
Town gas	16,700 – 20,000
Biogas and landfill gas	18,000 – 29,000
Substitute Natural Gas (SNG)	25,000 – 37,000

As it is an intermediate product, the method used to produce syngas is based on the raw material used and the desired end product. It can be produced from carbon sources like natural gas, heavy vacuum residue, naphtha, coal, any kind of carbon containing waste and biomass, yet natural gas and hydrocarbon based plants have been preferred due to their lower capital cost for the last few decades. It is mainly consumed by ammonia production (as 120 million ton/year), methanol production (as 30 million ton/year) and the refineries for the need of pure hydrogen. It is also used with methanol to produce higher alcohols, acetic acid, formaldehyde, dimethyl ether and methyl-tert-butyl ether [6].

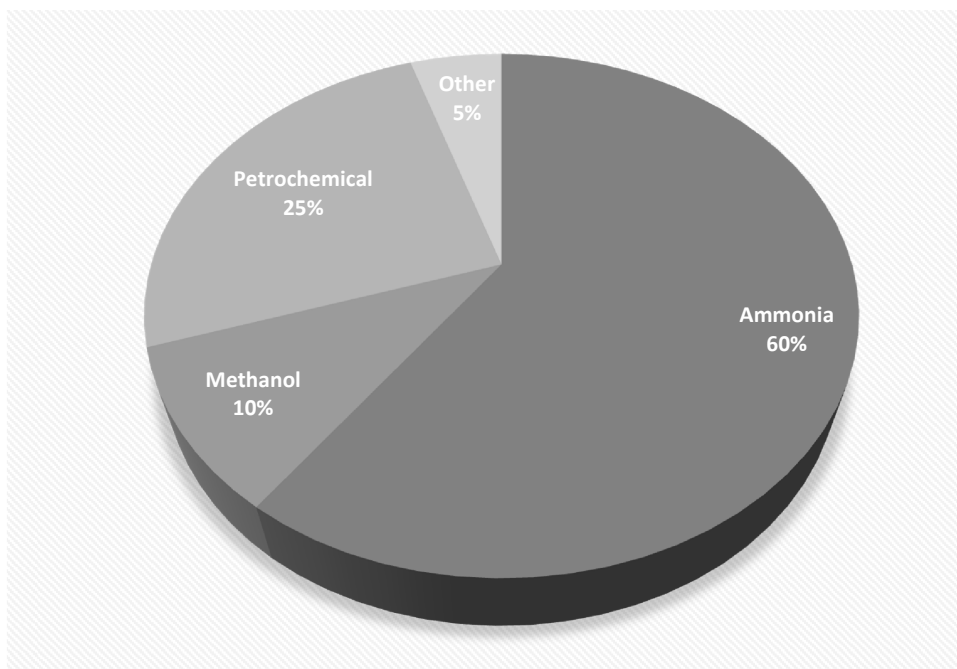


Figure 1:1 Syngas consumption in different industries in 2000

In principle, it is desired to produce a gaseous mixture rich in hydrogen and carbon monoxide. Depending on the process to be used in, the carbon monoxide to hydrogen ratio can be changed by the steam reforming reaction. Required compositions for the above end processes are listed in Table 1:2 [6].

Table 1:2 Syngas compositions for different industrial processes

<b>Process</b>	<b>Composition</b>
Ammonia	$H_2/N_2 \cong 3$
Methanol	$(H_2-CO_2)/(CO+ CO_2) \cong 2$
DME	$(H_2-CO_2)/(CO+ CO_2) \cong 2$
High-temperature Fischer–Tropsch	$(H_2-CO_2)/(CO+ CO_2) \cong 2$
Low-temperature Fischer–Tropsch	$H_2/CO \cong 2$
Higher alcohols	$H_2/CO = 1$
Acetic acid	CO

Since most of the above processes use syngas at elevated pressures like 20 bar or above, plants producing syngas are being designed to operate at pressures of 20-40 bar to eliminate the compression cost of higher volume syngas, which results in lower operating cost and even lower capital cost due to reduction in the designed capacity for smaller gas volumes at the expense of low conversions and yields because of thermodynamic equilibrium limitations.

Produced gas always needs to be purified and most likely it is required to be adjusted in  $H_2$  to CO ratio. Complexity of the purification steps increases from gaseous fuels to solid fuels and capital investment of the purification process can exceed the gasification itself [5] (Table 1:3). Based on the fuel used, a syngas plant might need to deal with dust, tar, carbon formation, cyanic compounds, oxygen,  $NO_x$ ,  $CO_2$ , organic sulfur and sulfides, ammonia, volatile metal-metal oxides and higher hydrocarbons.

Table 1:3 Cost and energy comparison for gaseous, liquid, and solid fuels

	<b>Natural Gas</b>	<b>Heavy Oil</b>	<b>Coal</b>
<i>Ammonia Plant</i>			
Capital Cost %	100	170	225
Energy Required %	100	115	135
<i>Methanol Plant</i>			
Capital Cost %	100	167	222
Energy Required %	100	111	132

### 1.1.1 Steam Reforming

In general, steam reforming is the conversion of hydrocarbons catalytically with steam to carbon monoxide and hydrogen. It is the most widely used method for producing syngas and hydrogen, which is to be used by various industrial facilities. The process was developed by BASF [7] and it was originally designed to operate at 4-10 bar and 800 °C unlike today's technology (20-40 bar).

At early years, steam reformers were built based on the need of hydrogen/syngas, usually near the ammonia and methanol plants. However, since the oil crisis in 1973, plants having high capacities were built near natural gas resources, eventually causing the fact that today natural gas is the main raw material among the hydrocarbon resources [5].

Steam reforming is a highly endothermic reaction ( $10 \text{ MJ/Nm}^3 \text{ CH}_4$  [6]) which is coupled by the water gas shift reaction (WGS) as seen in Table 1:4. High temperatures up to 950 °C is required over the catalyst to achieve significant methane conversion for a high steam to methane ratio to decrease the carbon formation (Figure 1:2). WGS reaction has been observed to be fast enough so that gas mixture in the reactor tubes is around its thermodynamic equilibrium.

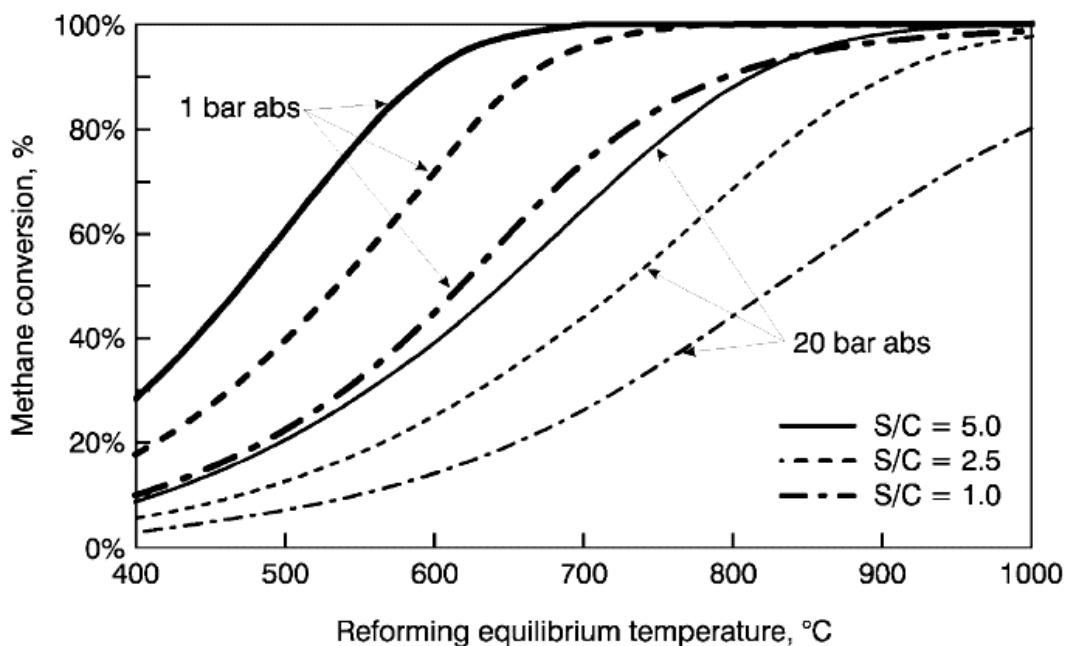


Figure 1:2 Methane conversion equilibrium for different steam to methane ratios

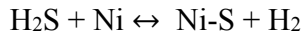
Table 1:4 Thermochemical data for steam reforming

Reaction	$\Delta H^{\circ}_{298}$ (kJ/mol)	$\Delta G^{\circ}_{298}$ (kJ/mol)	$\Delta G^{\circ}_{1000}$ (kJ/mol)
$\text{CH}_4 + \text{H}_2\text{O} \leftrightarrow \text{CO} + 3\text{H}_2$	206	142	-53
$\text{CO} + \text{H}_2\text{O} \leftrightarrow \text{CO}_2 + \text{H}_2$	-41	-29	1
$\text{CH}_4 + \text{CO}_2 \leftrightarrow 2\text{CO} + 2\text{H}_2$	247	171	-53

Reaction kinetics are limited by pore diffusion at those high operating temperatures. Nickel is the most widely used one with supports like alumina, magnesium alumina spinel oxide and zirconia [6]. They are prepared in shapes like rings with few holes to ensure highest available area. Catalysts are prepared by impregnation technique rather than precipitation due to its resistance to sintering and for its mechanical stability.

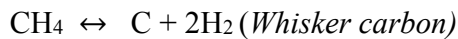
The catalyst might lose its activity from poisoning and carbon formation besides sintering. Ni catalyst is prone to poisoning by the presence of halogens, chlorine, alkali metals and

especially sulfur [5]. Even at low concentrations, sulfur reacts with metallic Ni in the form of sulfide as in the following reaction:



Sulfur appears in all hydrocarbon resources in various forms and treated accordingly. Hydrogen sulfide is handled via zinc oxide at temperatures around 400 °C while organic sulfur like mercaptan is treated by hydrogenation over Co-Mo or Ni-Mo to give H<sub>2</sub>S, which is to be captured by zinc oxide.

Carbon formation is another common problem in steam reforming, which is caused by the following reactions:



The most typical one is the Whisker carbon formation in which C accumulates around the Ni particle and eventually dissolves. As it reaches its saturation at the local temperature and pressure, it grows with the Ni particle at the tip of the structure [8]. This process can cause the deactivation and break down of the pellet and create an uneven flow field within the reactor tube decreasing the overall heat transfer coefficient as well as the energy consumed per volume which reduces the lifetime of the equipment significantly. Carbon formation by CO reactions can occur on both catalyst and reactor tube walls which leads to the corrosion due to the carbonization process. Carbon formation can be reduced by using a noble metal or adding some alkali metals like K which can re-gasify the carbon [9].

### 1.1.2 Dry Reforming

Methane reforming with CO<sub>2</sub> is a process developed to produce syngas containing lower H<sub>2</sub> to CO ratio. The reaction is more endothermic compared to steam reforming and it is

thermodynamically possible above 650 °C. Fe, Co, Ni and noble metals can be used as the catalyst and it is reported that catalytic activity for dry reforming follows the order Ru>Rh>Ni≈Ir>Pt>Pd as in steam reforming with a similar reaction mechanism [10]. Carbon formation is still a problem, especially at high pressures. A nickel based industrial process has been developed called *Calcor Process* operating around atmospheric pressure. It recycles the CO<sub>2</sub> from the downstream gas mixture and produces syngas with a H<sub>2</sub> to CO ratio of unity or less based on the chemical composition of the feedstock. It is also used with a H<sub>2</sub> – CO separation unit like PSA to remix them in a desired ratio [5].

Dry reforming is also used together with steam reforming to adjust the ratio. CO<sub>2</sub> from the downstream is recycled partially / totally or CO<sub>2</sub> is added externally. However, that increases the possibility of carbon formation requiring the adjustment of reaction parameters. *Midrex process* can be given as an industrial example for such a combination of steam and dry reforming.

### 1.1.3 Partial Oxidation

High hydrogen to carbon monoxide ratios in steam reforming, especially due to high steam ratio in the feed to suppress the carbon deposition on the catalyst, creates an important problem for the downstream processes. As an alternative, partial oxidation of methane was proposed in 1929 [11] for the ammonia synthesis and research on that route have been appealing since the oil crisis and studies have been continued on around non-noble transition metal catalysts. Partial oxidation is mildly exothermic, which is an important industrial advantage. More importantly, it has a molar ratio of H<sub>2</sub>: CO of 2 due to reaction stoichiometry as product, which usually has little CO<sub>2</sub>, making the technology a very suitable candidate for the processes given in Table 1:2. It also does not require high temperature & high pressure steam; however, it needs an air separation unit to get the oxygen if N<sub>2</sub> is not wanted in the mixture by design.

It is a high temperature-high pressure process in the application and gas phase reactions can become critical and threaten the safety of the operation due to explosions and thermal

runaway. Reactions (see Table 1.5 [12]) may occur homogeneously in the gas phase as well as on the catalyst surface to yield total combustion reactions or higher hydrocarbons like ethylene or ethane [13].

Partial oxidation reaction of hydrocarbons can be achieved without a catalyst as in hydrogen production unit of refineries or methanol plants. Methane is combusted substoichiometrically with oxygen in a well-mixed combustion chamber where flame temperature is adjusted by mixing some steam to the feed. Higher hydrocarbons like naphtha, heavy fuel, asphalt or tar may also be used as the feedstock. In fact, due to the air separation unit, cost of partial oxidation exceeds steam reforming so that it is preferred for heavy products ranging from fuel oil to asphalt. However, heavy metals and sulfur compounds are to be removed before the reactor and formed carbon is to be taken off before the downstream processes.

Table 1:5 Thermochemical data for methane partial oxidation

Reactions	$\Delta H^{\circ}_{298}$ (kJ/mol)	$\Delta G^{\circ}_{298}$ (kJ/mol)	$\Delta G_{1000}$ (kJ/mol)
$\text{CH}_4 + 2\text{O}_2 \rightarrow \text{CO}_2 + 2\text{H}_2\text{O}(\text{v})$	-800	-801	-801
$\text{CH}_4 + 1/2\text{O}_2 \rightarrow \text{CO} + 2\text{H}_2$	-36	-86	-240
$\text{CH}_4 + \text{O}_2 \rightarrow \text{CO}_2 + 2\text{H}_2$	-319	-344	-426
$\text{CO} + \text{H}_2\text{O}(\text{v}) \leftrightarrow \text{CO}_2 + \text{H}_2$	-77.2	-29	1
$\text{CH}_4 + \text{H}_2\text{O}(\text{v}) \leftrightarrow \text{CO} + 3\text{H}_2$	205.8	-142	-53
$\text{CH}_4 + \text{CO}_2 \leftrightarrow 2\text{CO} + 2\text{H}_2$	247	170	-53
$\text{CO} + \text{H}_2 \leftrightarrow \text{C} + \text{H}_2\text{O}(\text{v})$	-131.3	-91	22
$\text{CH}_4 \leftrightarrow \text{C} + 2\text{H}_2$	393.5	51	-30
$2\text{CO} \leftrightarrow \text{CO}_2 + \text{C}$	-172.5	-120	22
$\text{CO} + 1/2\text{O}_2 \rightarrow \text{CO}_2$	-283	-257	-187
$\text{H}_2 + 1/2\text{O}_2 \rightarrow \text{H}_2\text{O}(\text{v})$	-241.8	-229	-187

In catalytic oxidation, reactants are mixed in a mixing zone and react with the catalyst in the reaction zone. It can be operated with or without the steam based on the feedstock at atmospheric pressure or elevated pressures. Space velocity can be as high as  $500,000 \text{ h}^{-1}$  [14] for complete oxygen conversion, known as short contact time reactors. Lower and upper flammability limits are the primary design constraints in the mixing zone to prevent any explosions. As being an exothermic reaction, generated heat creates hot spots within the catalyst, especially at the beginning of the reaction zone such that back radiation is to be shielded between the mixing and reaction zones to avoid ignition.

Catalysts used in partial oxidation reactions are usually considered in three groups; Ni, Co and Fe catalysts, noble metals and metal carbides particularly Mo and W. Carbon deposition on the catalyst is still a problem and relative affinities are reported as [15]  $\text{Ni} > \text{Pd} > \text{Rh} > \text{Ru} > \text{Pt} \approx \text{Ir}$ .

Two routes to syngas synthesis from methane are generally accepted namely *Direct Partial Oxidation (DPO)* and *Combustion and Reforming Reactions (CRR)*. The former route is the dissociation of methane on the catalyst and synthesis of CO and H<sub>2</sub> directly. The latter one is the combustion of the methane to CO<sub>2</sub> and H<sub>2</sub>O at the inlet of the reactor and then reforming of those into syngas. It has been shown that depending on the catalyst used and operating conditions, CO-H<sub>2</sub> or CO<sub>2</sub>-H<sub>2</sub>O couple is found to be the primary products of the oxidation reactions [15-23].

#### **1.1.4 Autothermal Reforming**

Autothermal reforming is the combination of adiabatic steam reforming and partial oxidation reactions. Natural gas is fed to a combustion chamber with steam where it reacts with substoichiometric oxygen in open flame and all oxygen is used up in the chamber. Mixture is then passed through the catalyst bed where reforming reactions take place. Temperature at the entrance of reforming zone could be as high as 1100 °C.

The process has been used in the industry since 1950s. High steam to hydrocarbon ratio decreased in 1990s and steam to carbon ratio of 0.6 was set about in 2002. However low

steam to carbon ratio still possesses the risk of soot formation, which is actually determined by the operating conditions. By ensuring high temperature in the partial oxidation zone and adjustment of adequate amount of steam, soot formation had been suppressed in pilot scale experiments for steam to carbon ratios as low as 0.21 [24].

### **1.1.5 Alternative Technologies**

Due to the large reserves scattered around the world, methane is being considered as a strong candidate feedstock for various chemical processes. Known reserves are increasing and competes with the oil reserves for the last a few decades and it is expected to be increasing in the 21<sup>st</sup> century. In order to convert methane to valuable products, different methods have been developed, which can be grouped as indirect and direct methods.

Indirect methods depend on the production of carbon monoxide and hydrogen, namely syngas production. Steam reforming is a well-known technology; however, it needs high pressure and medium range temperature to be favorable thermodynamically. Additionally, Ni catalyst suffers from the coke formation. On the other hand, partial oxidation with pure oxygen eliminates the coke, yet this time separation of oxygen from air is required, which is an expensive technology. Additionally, oxygen methane mixture is needed to be handled with care to prevent explosions. Generated heat must also be handled as well. After the syngas production, Fischer Tropsch (F-T) synthesis is a possible indirect route to produce hydrocarbons and higher alcohols. Although it was developed for coal in early 1920s, now methane is considered and used as a feedstock for the process, which is based on iron or cobalt based catalysts. Another way to utilize the methane is synthesis of methanol, from which dimethyl ether, gasoline, ethylene and propylene can be produced.

Direct methods are expected to be more economically feasible than indirect methods; though yields are smaller, which creates a necessity of recycling resulting in separation costs. Direct methanol and formaldehyde conversion, oxidative coupling of methane to

ethane and ethylene and conversion to aromatic compounds like benzene or toluene without and oxidant can be listed as examples of direct production methods.

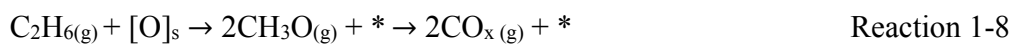
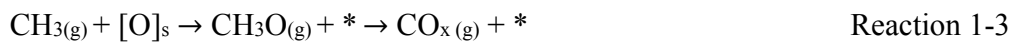
As explained above, today's technology for producing syngas is based on methods utilizing fixed bed reactors and fluidized bed technology has been considered as an alternative due to its characteristic advantages. It can be operated isothermally which can eliminate the temperature gradients. Pressure drop is expected to be less than fixed bed reactors of similar dimensions, which is an important advantage due to high operating pressures of downstream processes. It can also prevent a common risk of soot formation since the catalyst particles can be circulated between the combustion and reforming zones. Partial oxidation of methane with air had been achieved in a fluidized bed reactor with Platinum, Rhodium and Nickel catalyst [25] and it was seen that more than 90% of the feed was converted with a syngas selectivity of 95% on Rhodium-Alumina and Nickel-Alumina catalysts. Similar results – near the thermodynamic equilibrium at the operating conditions- were obtained for a fluidized bed reactor in which the catalyst is circulated as well [26]. In a comparable work [27], thermodynamic equilibrium was achieved with a residence time as low as 70 ms at 800 °C on Nickel-Alumina catalyst in a laboratory scale internally circulating fluidized bed reactor. However, carbon deposition on the catalyst was observed.

Utilization of O<sub>2</sub> for direct routes or indirect routes necessitates the separation from the air, which is costly. To avoid that, different solutions have been applied, which are depending on the utilization of the catalyst as the oxygen source. Out of those, membrane reactors seem to be an attractive alternative since they may provide high selectivity with air as oxidant.

Nozaki et al. achieved a 90 % selectivity of C<sub>2</sub> on lead oxide membrane [28] and showed that oxide ion transportation through PbO film participated in the oxidative coupling of methane. Tsai et al. used a dense perovskite [35] to separate air from the methane helium mixture in three different ways at 850 °C. They observed that if there is no catalyst, exit gas mixture composed of water and carbon dioxide. If a reformer catalyst like Nickel is added to the downstream, syngas was obtained. However, they got the highest conversion

(80% CH<sub>4</sub>) with a CO selectivity of 95% when H<sub>2</sub>: CO ratio was 2 if catalyst was applied on the membrane surface.

In another study, Cao et al. studied a perovskite membrane Ba<sub>0.5</sub>Sr<sub>0.5</sub>Co<sub>0.8</sub>Fe<sub>0.2</sub>O<sub>3-δ</sub> (BSCF) and they produced C<sub>2</sub> by introducing another reaction, water splitting so that they have overcome the thermodynamic limitations for the following reactions of methane coupling (OCM) [29];



They showed that as OCM reactions can be achieved via O<sub>2</sub> consuming & producing membranes previously [31, 32], it can also be done via thermal water splitting [33, 34] leading to the production of H<sub>2</sub> simultaneously.

By doing so, they [29] have achieved 26% methane to C<sub>2</sub> conversion with 9% water injected is converted to hydrogen, knowing that CO<sub>x</sub> formation on the surface from C<sub>2</sub> being the main reason for low yields [35]. Wolf et al. showed that rate constant of *Reaction 1-3* is 1.6 x 10<sup>-3</sup> mol / (kg cat. s) while it is 2.6 x 10<sup>-2</sup> mol / (kg cat. s) for *Reaction 1-8* on CaO/CeO<sub>2</sub> catalyst [30]. It was argued that produced C<sub>2</sub> is converted to CO<sub>x</sub> on the catalyst faster than it is produced and those encourages one to develop a medium in favor

of CO production as it is the most stable route due to the fact that it eventually leads to CO<sub>2</sub>.

In the literature, there are also studies available for different metal oxide couples like Fe<sub>2</sub>O<sub>3</sub>/Fe<sub>3</sub>O<sub>4</sub>, ZnO/Zn, Mn<sub>3</sub>O<sub>4</sub>/MnO, Co<sub>3</sub>O<sub>4</sub>/CoO, Nb<sub>2</sub>O<sub>5</sub>/NbO<sub>2</sub>, In<sub>2</sub>O<sub>3</sub>/In, WO<sub>3</sub>/W, CdO/Cd, SnO<sub>2</sub>/SnO, CeO<sub>2</sub>/Ce<sub>2</sub>O<sub>3</sub>, GeO<sub>2</sub>/GeO, MgO/Mg for hydrogen production and it has been stated that researchers at General Atomics (GA), Sandia National Laboratory (SNL) and University of Kentucky (UK) have developed 115 different thermochemical cycles for water splitting [36].



## **CHAPTER 2**

### **OBJECTIVES OF THE STUDY**

Syngas is a critical intermediate product for commodity chemicals like ammonia or methanol and consumed by various industrial applications. It is to be processed in specific ratios for each downstream application ranging from pure hydrogen to pure carbon monoxide and the most feasible syngas production technology is decided accordingly, which makes the development of a method to produce CO and H<sub>2</sub> at any desired ratio quite important. Furthermore, the proposed method was intended to contribute the sustainable development of the syngas production technology. Hence, combined aims of the study were set as seeking a candidate material for two step solar thermochemical heat storage applications and show the possibility and feasibility of utilizing that stored energy to produce CO from CO<sub>2</sub> and H<sub>2</sub> from H<sub>2</sub>O theoretically and experimentally.



## CHAPTER 3

### LITERATURE SURVEY

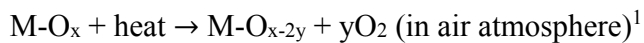
#### 3.1 Thermochemical Heat Storage on Reducible Metal oxides

Thermal decomposition of a compound is the chemical self-decomposition reaction that happens as the bond becomes instable at high temperatures. Oxides are multicomponent materials by nature and they tend to be at the most stable phase at any given thermodynamic coordinates; that is, having the lowest possible total free energy, which substantially brings about many opportunities.

Concentrated solar power plants have been used to produce electricity (reaches a total capacity of 1760 MW in 2011 [37]) and energy storage methods have always been a crucial step to the technology. In principle, solar heat can be stored either as sensible heat, latent heat or as a chemical bond. Heat storage in chemical bonds has numerous advantages over sensible/latent heat storage with oils, steam or molten salts as used in solar plants as seen in Table 3:1 (Note that battery and dam energy densities are reported as usable work while others are the heat of combustion.) [38]. It provides a lot higher energy density and heat can easily be stored for longer time durations at mild conditions. Chemical reaction can be selected as a phase change reaction, which means heat can be released at the phase change temperature giving a constant heat source. For metal-metal oxide reactions, oxygen/air is the only transported reactant in both oxidation and reduction

steps, which can also be used as the heat transfer medium. Separation of the air is not needed and process is easy to control and operate. If the oxide is chosen appropriately, the process is very environmentally friendly. Most importantly, work can be generated within 24 hours operation.

Energy storage as chemical bonds is composed of three stages: charge, storage and discharge. Charge is the following endothermic reaction where necessary energy is considered to be obtained from solar radiation:



Some of the reaction product,  $M-O_{x-2y}$ , is stored in day time and used according to following reaction at a lower temperature:

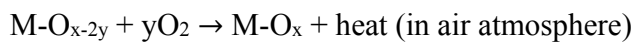


Table 3:1 Energy density based on heat storage medium

<b>Heat Storage Medium</b>	<b>Energy Density (kJ/kg)</b>
Gasoline	45,000
Sulfur	12,500
Cobalt Oxide	850
Lead Oxide	262
Molten Salt with latent heat	230
Molten Salt with sensible heat	155
Lithium Ion Battery	580
Water Dam at 100 m	1

---

<sup>1</sup> M: Metal, O: Oxygen

Those reactions are to be fast and reversible in a narrow range of temperature, which is expected to be high enough to achieve high thermal efficiency, stable, non-toxic and most importantly, economically feasible operation [39].

Table 3:2 Oxidation-reduction temperature ranges for various metal oxides

<b>Metal Oxides</b>	<b>Temperature Range (°C)</b>
Cr <sub>5</sub> O <sub>12</sub> , Li <sub>2</sub> O <sub>2</sub> , Mg <sub>2</sub> O	< 350
MnO <sub>2</sub> , Sb <sub>2</sub> O <sub>5</sub> , PtO <sub>2</sub> , PbO <sub>2</sub> , UO <sub>3</sub>	350 < T < 700
Co <sub>3</sub> O <sub>4</sub> , BaO, Mn <sub>2</sub> O <sub>3</sub> , Rh <sub>2</sub> O <sub>3</sub>	700 < T < 900
CuO	900 < T < 1100
Fe <sub>2</sub> O <sub>3</sub> , Mn <sub>3</sub> O <sub>4</sub> , V <sub>2</sub> O <sub>5</sub>	1100 <

Unlike water splitting via thermochemical operation, heat storage can be achieved at lower temperatures around 1000 °C while water splitting requires temperatures around 1400 °C. It should be noted that solar tower plants can reach around 1200 °C [40] which make the heat storage via chemical bonds possible.

In their extensive work, Wong at al. investigated 74 pure metal oxides [111] and several mixed oxides and narrowed down the list to the oxides given in Table 3:2. They stated that Cr<sub>5</sub>O<sub>12</sub> (110 °C), Li<sub>2</sub>O<sub>2</sub> (150 °C) and Mg<sub>2</sub>O (205 °C) has very low phase change temperature resulting in low reaction-diffusion rates and thermal efficiency and PtO<sub>2</sub>, Rh<sub>2</sub>O<sub>3</sub> and UO<sub>3</sub> are too expensive to be used as a heat storage medium. They made experiments for the rest for up to 50 redox cycles and found that only cobalt oxide is capable of going under redox reactions with fast kinetics (95% at 10 °C/min). They calculated the cost of produced electricity for a 150 MW plant as \$ 0.22-0.30/kWh for cobalt oxide, which they expected to decrease around \$ 0.15.

Agrafiotis et al. studied the cyclic redox characteristics of cobalt oxide powder [40] and showed that Co<sub>3</sub>O<sub>4</sub> can be used cyclically with a temperature range of 800 to 1000 °C

and the performance remains the same for 30 cycles. Oxidation was measured to be slower than the reduction step such that the extent of reoxidation changes with cooling/heating rate. They also found that addition of Ni, Cu or Mg does not create a difference in the process.

Block et al. worked on iron-cobalt oxide system to increase the stability [39] and decrease the cost related to cobalt by iron addition. However, iron rich samples required higher reduction and oxidation temperatures and stored less energy/kg. Sample having 87% Cobalt ( $\text{Co} / (\text{Co} + \text{Fe})$ ) was shown to be promising as added Fe increased the cyclic stability –stabilizes the reaction time as cycle number increases.

Carrillo et al. investigated manganese-cobalt oxide system with various ratios for 5 cycles [37] and compared their performances as a heat storage medium. They showed that pure oxides  $\text{Mn}_2\text{O}_3$  and  $\text{Co}_3\text{O}_4$  exhibit fastest reduction and oxidation rates yet mixed oxide of  $\text{Mn}_{0.03}\text{Co}_{2.97}\text{O}_4$  was found to be comparably fast with highest heat recovery between oxidation and reduction (86%, measured by DCS) although it has the lowest surface area.

Karagiannakis et al. studied manganese oxide and cobalt oxide separately [122] with a temperature range of 800-1000 °C in a monolithic reactor for ten redox cycles. They observed similar amounts of oxygen release and consumption yet redox reactions occurred faster in monolithic reactor due to better heat transfer characteristics. They also scanned a reduction range up to 1100 °C and oxidation range up to 900 °C and concluded that increasing the reduction temperature could not increase the amount of oxygen released while increasing oxidation temperature decreased total oxidation. Manganese oxide was found to be slower than cobalt oxide in both reactions and its energy storage density was five times less (per mass) compared to cobalt oxide.

### 3.2 Syngas Production on Reducible Metal Oxides

There are three main resources of hydrogen, namely, fossil fuels like natural gas, coal or petroleum, water with waste heat sources like nuclear power plants and water with renewable energy sources like photovoltaic cells or solar thermal systems. Those sources are to be processed with one of the three possible pathways to be converted into hydrogen: thermochemical, photochemical and electrochemical conversion.

Thermochemical conversion process is simply utilization of concentrated solar heat for thermal decomposition of water/carbon dioxide molecule. The easiest way to achieve the dissociation would be direct conversion of water to hydrogen and oxygen and carbon dioxide to carbon monoxide and oxygen yet those reactions require very high temperatures ( $\sim 2200$  °C for water and  $\sim 3300$  °C for carbon dioxide [41]) and a separation unit is necessary to get  $H_2 / CO$  while avoiding any possible combustion reactions. If those reactions; however, are carried out with an intermediate substance, redox reactions can be obtained at much lower temperatures without any need for oxygen separation and only heat is needed to continue with the cyclic operation, which can be supplied in various ways.

Early studies to produce hydrogen had focused on the utilization of waste heat, particularly from nuclear power plants due to their output temperature. A chemical cycle was developed in 1970s named Mark I for that purpose but it did not get much attention as the process includes substances like Hg and HBr. In 1990s, another successful cycle was presented in Germany called AGNES based on Fe and Mg cycles. A three-step cycle was reclaimed by General Atomics based on  $H_2SO_4$  decomposition and a four-step cycle was developed in Japan based on the hydrolysis of  $FeBr_2$  and  $CaBr_2$  [42-44].

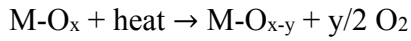
Those multistep processes are vulnerable to heat losses between unit operations and costly due to the need of separation at each step. However, two-step thermochemical cycles based on metal oxides minimize that disadvantage. Although they operate at higher temperatures, it has become possible to reach up to 1200 °C with the developed solar energy collectors.

Table 3:3 Reactions of cyclic hydrogen production technologies

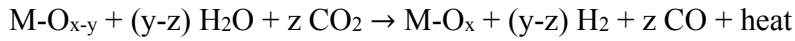
Process	Reactions
MARK I	$\text{CaBr}_2 + 2\text{H}_2\text{O} \rightarrow \text{Ca(OH)}_2 + 2\text{HBr} \text{ (730 }^\circ\text{C)}$ $\text{Hg} + 2\text{HBr} \rightarrow \text{HgBr}_2 + \text{H}_2 \text{ (250 }^\circ\text{C)}$ $\text{HgBr}_2 + \text{Ca(OH)}_2 \rightarrow \text{CaBr}_2 + \text{H}_2\text{O} + \text{HgO} \text{ (200 }^\circ\text{C)}$ $\text{HgO} \rightarrow \text{Hg} + \frac{1}{2} \text{O}_2 \text{ (600 }^\circ\text{C)}$
AGNES	$3\text{FeCl}_2 + 4\text{H}_2\text{O} \rightarrow \text{Fe}_2\text{O}_3 + 6\text{HCl} + \text{H}_2 \text{ (450-750 }^\circ\text{C)}$ $\text{Fe}_2\text{O}_3 + 8\text{HCl} \rightarrow \text{FeCl}_2 + 2\text{FeCl}_3 + 4\text{H}_2\text{O} \text{ (100-110 }^\circ\text{C)}$ $2\text{FeCl}_3 \rightarrow 2 \text{FeCl}_2 + \text{Cl}_2 \text{ (300 }^\circ\text{C)}$ $\text{Cl}_2 + \text{Mg(OH)}_2 \rightarrow \text{MgCl}_2 + \frac{1}{2} \text{O}_2 + \text{H}_2\text{O} \text{ (50-90 }^\circ\text{C)}$ $\text{MgCl}_2 + \text{H}_2\text{O} \rightarrow \text{Mg(OH)}_2 + 2\text{HCl} \text{ (350 }^\circ\text{C)}$
Sulfur Iodine Cycle	$\text{I}_2 + \text{SO}_2 + 2\text{H}_2\text{O} \rightarrow \text{H}_2\text{SO}_4 + 2 \text{HI} \text{ (97 }^\circ\text{C)}$ $2\text{HI} \rightarrow \text{H}_2 + \text{I}_2 \text{ (120 }^\circ\text{C)}$ $\text{H}_2\text{SO}_4 \rightarrow \text{H}_2\text{O} + \text{SO}_2 + \frac{1}{2} \text{O}_2 \text{ ( 870 }^\circ\text{C)}$
Calcium Bromine Iron Cycle	$\text{CaBr}_2 + \text{H}_2\text{O} \rightarrow \text{CaO} + 2\text{HBr} \text{ (725 }^\circ\text{C)}$ $\text{CaO} + \text{Br}_2 \rightarrow \text{CaBr}_2 + \frac{1}{2} \text{O}_2 \text{ (550 }^\circ\text{C)}$ $\text{Fe}_3\text{O}_4 + 8\text{HBr} \rightarrow 3\text{FeBr}_2 + 4\text{H}_2\text{O} + \text{Br}_2 \text{ (250 }^\circ\text{C)}$ $3\text{FeBr}_2 + 4\text{H}_2\text{O} \rightarrow \text{Fe}_3\text{O}_4 + 6\text{HBr} + \text{H}_2 \text{ (575 }^\circ\text{C)}$

Over 350 candidate materials have been reported to be active for water splitting reduction [45] yet few are two-step cycles. Some metal oxides go for a change in their physical state like Zn(g)-ZnO(s) couple known as volatile redox cycle. They are considered to be efficient due to their high oxygen storage capacity per mass yet they pose the inherent separation problem, which has been handled by quenching yet not to a desired extent [46]. In non-volatile oxides, two oxidative state remains in the solid form, which are classified as stoichiometric and non-stoichiometric redox cycles. Stoichiometric oxides go through a phase change like Co<sub>3</sub>O<sub>4</sub> to CoO, which is slower due to diffusion and kinetic limitations. However, non-stoichiometric redox reactions do not include a phase change but a change in the vacancy density in the lattice like CeO<sub>2</sub> to CeO<sub>2-δ</sub>. Reaction steps for are summarized in most general form below.

*Reduction Step (high temperature):*



*Oxidation Step (lower temperature):*



*Overall Reaction:*

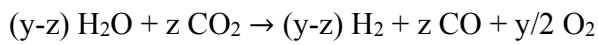


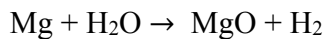
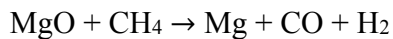
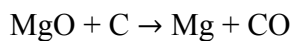
Table 3:4 Some examples for different types of redox cycles

Type	Oxide Couple
Volatile	ZnO → Zn(g) SnO <sub>2</sub> → SnO(g)
Non-volatile stoichiometric	Fe <sub>3</sub> O <sub>4</sub> → FeO M <sub>x</sub> Fe <sub>3-x</sub> O <sub>4</sub> → xMO + (3 - x)FeO Fe <sub>3</sub> O <sub>4</sub> + 3Al <sub>2</sub> O <sub>3</sub> → 3FeAl <sub>2</sub> O <sub>4</sub> M <sub>x</sub> Fe <sub>3-x</sub> O <sub>4</sub> + 3Al <sub>2</sub> O <sub>3</sub> → (3-x)FeAl <sub>2</sub> O <sub>4-x</sub> + xM-Al <sub>2</sub> O <sub>4</sub>
Non-volatile non-stoichiometric	CeO <sub>2</sub> → CeO <sub>2-δ</sub> M <sub>x</sub> Ce <sub>1-x</sub> O <sub>2</sub> → M <sub>x</sub> Ce <sub>1-x</sub> O <sub>2-δ</sub> ABO <sub>3</sub> → ABO <sub>3-δ</sub>

Two-step redox cycle was first studied by Nakamura et al. [47] who used Fe<sub>3</sub>O<sub>4</sub> to FeO couple with a temperature above 2000 °C, above the melting point temperature. Following studies on this couple have focused on reducing those high temperatures by decreasing oxygen partial pressure and substituting some Fe ions with Cu, Zn, Ni, Co or Mn while studies are also carried on with other candidate metal oxides like Mn<sub>3</sub>O<sub>4</sub>-MnO (decomposed at 1537 °C), Co<sub>3</sub>O<sub>4</sub>-CoO (decomposed at 900 °C), CdO-Cd (decomposed at 1400 °C), Nb<sub>2</sub>O<sub>5</sub>-NbO<sub>2</sub> (decomposed at 3327 °C), In<sub>2</sub>O<sub>3</sub>-In and WO<sub>3</sub>-W (higher than Fe

couple) [48, 50]. Although it suffers from being a volatile redox couple, one of the most studied samples is ZnO-Zn due to its high energy recovery potential, for which the details can be found in the literature [48, 49].

There are relatively more recent studies focusing on SnO<sub>2</sub>-SnO, GeO<sub>2</sub>-GeO and MgO-Mg couples due to their advantages over ZnO-Zn redox couple. SnO<sub>2</sub> can be reduced at temperatures around 1600 °C and re-oxidized up to 90% at around 600 °C. Although not as fast as ZnO reoxidation, it was shown to achieve much higher hydrogen yield [51]. GeO<sub>2</sub> is another candidate for ZnO due to its lower reduction temperature –around 1400 °C- enabling higher thermal efficiencies [52]. MgO-Mg redox couple has been studied with carbothermal reduction which leads to moderate reduction temperatures compared to its decomposition temperature of 3700 °C:



It was stated to be advantageous [53] over ZnO especially due to the fact that Zn is 2.7 times heavier than Mg. Yet this approach brings about pollution for downstream applications, particularly when the carbon source includes sulfur. Carbothermal redox cycle route has also been studied for ZnO and Fe<sub>3</sub>O<sub>4</sub> which decreased their reduction temperatures down to around 1200 °C and 1500 °C respectively [54,55].

Stoichiometric activation of ceria, as demonstrated by Abanades and Flamant in 2006, requires high temperatures above 2000 °C, where partial vaporization (>50%) was observed due to extensive sublimation and oxide cannot be reduced at high pressures. However, non-stoichiometric reduction does not require as high temperatures and it was demonstrated that syngas can be produced from CO<sub>2</sub> and H<sub>2</sub>O splitting reactions while the syngas ratio is to be adjusted by the ratio in the feedstock [58]. It is advantageous compared to other stoichiometric redox couples like Fe<sub>3</sub>O<sub>4</sub>-FeO due to higher diffusion

rates and its stability has been shown for 500 cycles [59]. However, non- stoichiometric nature leads to low oxygen storage capacity, which creates a significant disadvantage.

Performance comparison of some redox couples for hydrogen production were also summarized elsewhere [56], given in Table 3:5.

Table 3:5 Hydrogen Production capacities for several metal oxide couples

Redox Couple	Reduction Temperature °C	Re-oxidation Temperature °C	$\frac{H_2}{g \text{ material}} \cdot 10^{-4} g$	Conversion
$Fe_3O_4/m - ZrO_2$	1400	1100	5.7	33%
$Mn_{0.36}Fe_{2.64}O_4/m - ZrO_2$	1400	1100	3.9	26%
$NiFe_2O_4/m - ZrO_2$	1400	1100	11	69%
$Co_{0.9}Fe_{2.1}O_4/m - ZrO_2$	1450	1100	20	6%
$CoFe_2O_4/Al_2O_3$	1200	1000	31	7%
$Fe_3O_4$	1700	575	50	75%
$CeO_2$	1400	1100	2.6	5%
$Ce_{0.75}Zr_{0.25}O_2$	1400	1100	2.9	10%
$NiFe_2O_4$	1400	1100	8.6	1.7%
Sr -, Mn -doped $LaAlO_3$	1350	1000	61.4	78%

### 3.3 Noncatalytic Gas-Solid Reactions

Noncatalytic gas solid reactions (NGSr) are similar to heterogeneous catalytic reactions in principle; that is transport and kinetic resistances are to be considered simultaneously. However, in NGsr solid particles are also involved in reactions such that the process becomes transient by nature.

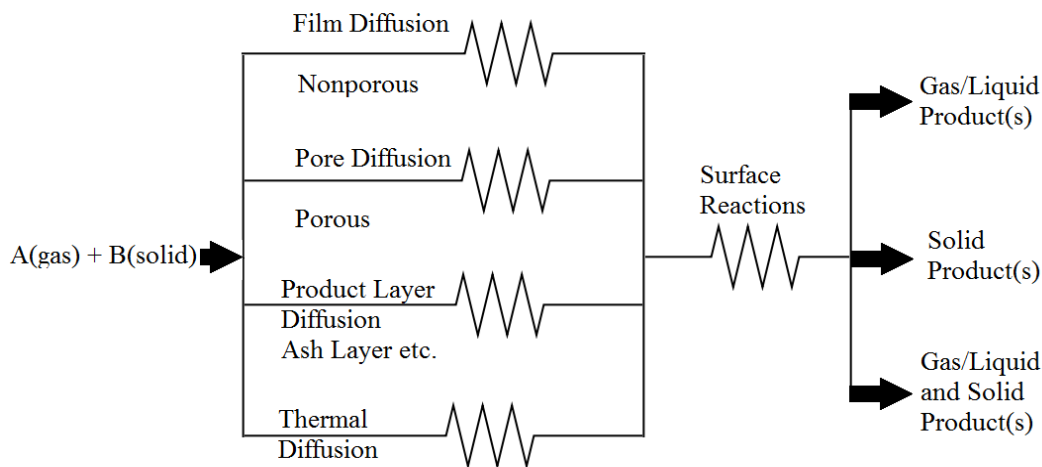


Figure 3:1 Schematic representation of various resistances in noncatalytic gas solid reactions

NGSr have industrially important applications in various fields, which can be grouped based on the behavior of the solid reactant, as presented in Table 3:6.

Table 3:6 Noncatalytic gas solid reaction examples from industry

<b>Significantly Affected Solid Geometry</b>	<b>Unaffected Solid Geometry</b>
<i>Combustion of Solid Fuels</i> $C(s) + O_2(g) \rightarrow CO_2(g)$	<i>Roasting of Metal Ores</i> $ZnS(s) + 3/2 O_2(g) \rightarrow ZnO(s) + S O_2(g)$
<i>Calcination of Limestone</i> $CaCO_3(s) \rightarrow CaO(s) + CO_2(g)$	<i>Cyanamide Production</i> $CaC_2(s) + N_2(g) \rightarrow CaCN_2(s) + C(s)$
<i>Gasification</i> $C(s) + H_2O(g) \rightarrow CO(g) + H_2(g)$	<i>Reduction of Magnetite</i> $Fe_3O_4(s) + 4H_2(g) \rightarrow Fe(s) + 4H_2O(g)$

Understanding and modeling of such a complex physical phenomenon is difficult yet can be approximated via mathematical models with different complexities. Simplest available

models do not include structural variations within the particle and treat the solid homogeneously where more complex models include structural variation during the chemical reactions.

For an isothermal nonporous particle, Yagi and Kunii built a simple model called *Shrinking Core Model (SCM)* [97] which assumes that rate of reaction layer movement towards to the center of the particle is comparable slower than the rate of transport of gaseous reactant such that the process becomes pseudo steady state. Gaseous reactant diffuses through a gas film and an inert reacted layer to the solid surface where reaction takes place. Then the products diffuse out to the bulk phase.

An important alternative perspective to SCM is to treat the process as if it is a catalytic reaction; that is introducing an effectiveness factor, which is a time dependent variable in this case. As Ishida and Wen [98-100] described, for high Thiele modulus values (meaning that the dominant resistance is the diffusion of gaseous reactant within the solid) process becomes analogous to SCM and equation of concentration profiles for gaseous and solid reactants can be solved numerically for arbitrary order of reactions [98-100] and analytical solutions are available for a first order reaction kinetics [96]. However, for low Thiele Modulus values ( $\sim 1$ ) where process is kinetically controlled and for values where resistances are comparable, SCM cannot approximate the real phenomenon [98-100]. When thermal diffusion is slower compared to mass diffusion, generated heat may change the temperature profile or the structure within the solid [101], which is not accounted of in SCM.

For a porous solid particle, a drastic change in gas concentration as shown in Figure 3:2 is not expected and reaction within a porous solid particle can be approximated by *Volume Reaction (Homogenous) Model*. It does not have analytical solutions for any arbitrary reaction order, yet some important and useful cases were discussed in the literature [102]. There also suggested models, which are in between: *zone models*. In two zone model, system is approximated via a homogeneous reacting core surrounding by a product shell layer [103]. A three zone model defines this reacting zone as an intermediate zone in between an unreacted core and a product shell [104].

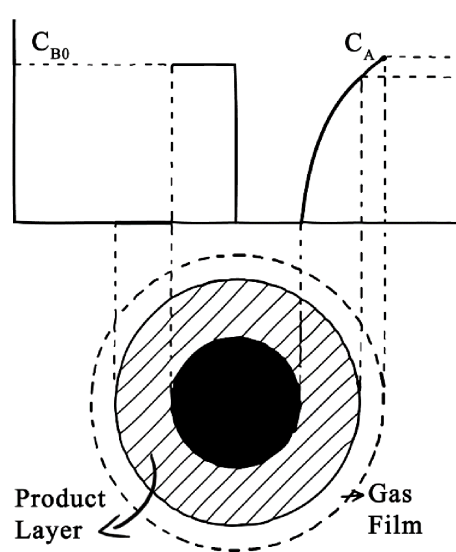


Figure 3:2 Shrinking Core Model

One step further from macroscopic models are the *grain models*, which explain the pore system within a solid particle with simplifying assumptions such as identical spherical grains where their sizes do not change and process can be approximated by SCM. Sohn and Szekely developed the original model [105] and presented approximate solutions for different geometries [106].

More advanced mathematical models can also be found in the literature yet with no analytically approximated solutions. As an example, Reyes and Jensen developed a model in which change in pore size distribution in time was calculated via *Population Balance Equations* and accessibility of pore surfaces and plugging possibilities are predicted via *Monte Carlo* simulations [107].

For phase transformation reactions in solids and crystallization where metal-metal oxide reaction interface becomes irregular, usually the model proposed by Avrami [108, 109] is applicable, which is an empirical approach and further explored in the following section.

### 3.3.1 Tools for Noncatalytic Gas Solid Reaction Mechanisms

Mathematical modeling of a system enables to obtain a phenomenological insight over the performance of a candidate metal oxide couple as well as the effect of process parameters, which inherently needs the derivation of rate equations.

Thermoanalytic methods namely *Differential Scanning Calorimetry* and *Thermogravimetry* are widely used to determine the heat of reaction and kinetic parameters, particularly for degradation reactions. Both measurement methods are analogical where DSC analysis monitors the change in heat reaction compared to total heat of reaction while TGA measures the change in the mass compared to possible total change of a sample mass.

There are different methods available in the literature to evaluate kinetic parameters based on TGA and DSC data. The most used methods have been compared experimentally [65] yet relatively since the true kinetics were unknown for the samples used in the experiment. Petrovic et al. derived synthetic curves according to arbitrarily selected kinetic data and back-calculated the estimated data with nine different methods [66] and proved that the *Kissinger method* shows good performance for first order reaction kinetics even with a single thermogram and it is very accurate (absolute error < 1%) with multiple thermograms for various orders of reaction.

Due to its ease of use and accuracy, *Kissinger method* has been the most popular method since 1950s among alternative methods. It has an exact solution for first order reactions and it gives less than 2% error for a wide range of activation energy-peak temperature couples [64].

The kinetics of the chemical reaction can be expressed with dimensionless conversion as follows<sup>2</sup>:

$$\frac{d\alpha}{dt} = k \cdot f(\alpha)$$

---

<sup>2</sup>  $W_i$ : Initial weight,  $W$ : Weight at any time,  $W_\infty$ : Final weight  
 $A_0$ : Pre-exponential factor,  $E_a$ : Activation energy,  $R$ : Gas constant,  $T$ : Temperature

Where

$$\alpha = \frac{W_i - W}{W_i - W_\infty}$$

$$k = A_0 \exp\left(-\frac{E_a}{RT}\right)$$

If the reaction kinetics are not complex, the working function  $f$  can be represented by *Avrami-Erofeev solid gas reaction model*:

$$f(\alpha) = (1 - \alpha)^n$$

where  $n$  shows the order of the reaction.

There are also other kinetic models available in the literature [68] as listed in Table 3:7

Table 3:7 Kinetic models for working function  $f$

<b>Kinetic Model</b>	<b><math>f(\alpha)</math></b>
Johnson Mehl Avrami Kolmogorov (JMAK)	$n(1-\alpha)(-\ln(1-\alpha))^{1-1/n}$
2D Reaction	$(1-\alpha)^{1/2}$
3D Reaction	$(1-\alpha)^{1/3}$
2D Diffusion	$1/(-\ln(1-\alpha))$
Jander	$3/2(1-\alpha)^{2/3}/(1-((1-\alpha)^{2/3}))$
Ginstling Brounshtein	$3/2((1-\alpha)^{-1/3}-1)$

### 3.4 Cobalt Oxide: Phases, Characterization and Kinetics

#### 3.4.1 Cobalt Oxide

In oxidation reactions, noble catalysts like Pt or Pd are considered to be the reference compounds since they exhibit high activities and other metals are usually seen to be less reactive. An exception to this is the bulk spinel cobalt oxide,  $\text{Co}_3\text{O}_4$ . It has been known that bulk cobalt oxide has even higher activity than noble metals on supports for oxidation of volatile organic compounds. When economic feasibility of the spinel cobalt oxide is considered; that cobalt salts cost 1/10-20 times of Pt or Pd salts, it becomes really attractive as a catalyst [69].

Cobalt oxide is already being used in important chemical reactions like Fischer-Tropsch synthesis [70], oxidation of CO [71], total oxidation of volatile organic compounds like propane, propylene and acetone [74-76], and some other industrial applications [72,73].

Recent studies on metal oxides show that the order and the size of the particles strongly effect the physical and chemical behavior of the materials [77-79]. Those changes are not only observed within their physical or electrical properties, but also within their band gaps [80], giving the materials unique properties and shifts in their thermodynamic equilibrium constants [81-85]. To illustrate, an interesting aspect of  $\text{Co}_3\text{O}_4$  is its ability to activate hydrocarbons at quite low temperatures based on particle size. Oxidation of ethylene to carbon dioxide has been achieved in nano scale preparation with a conversion of 30% at 0 °C, which was not possible before [86]. It has been stated that it is due to the development of (110) facet on cobalt oxide and addition of gold on that structure has increased the conversion up to 76%. Another study shows that propane is converted to propylene with oxygen at atmospheric pressure and temperature conditions with nano scale spinel cobalt oxide catalyst and at low conversion values (1%), the selectivity of propylene is found to be 100% [87]. Cobalt oxide is demonstrated to be successful in activating propane and propylene also in commercial bulk scale [76, 88]. That technological opportunity is not only important because of its economic importance, but

also its environmental contribution. Propylene is mainly produced via steam cracking reactions, which requires high amount of energy per product. It was reported that CO<sub>2</sub> emission is five times higher for propylene production compared to propane production [89].

### 3.4.2 Characterization, Thermal Analysis and Kinetics of Cobalt Oxides

There are five different cobalt oxide phases reported in the literature: CoO<sub>2</sub>, Co<sub>2</sub>O<sub>3</sub>, CoO(OH), Co<sub>3</sub>O<sub>4</sub> and CoO. Notedly, CoO(OH), Co<sub>3</sub>O<sub>4</sub> and CoO are the stable forms that are being used industrially [90].

Table 3:8 Locations of Co<sub>3</sub>O<sub>4</sub> and CoO diffraction lines

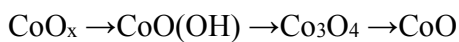
<b>Co<sub>3</sub>O<sub>4</sub> Diffraction Lines 2θ values</b>	<b>Plane</b>
31.4	(220)
36.9	(311)
38.5	(222)
44.9	(400)
55.7	(422)
59.5	(511)
65.4	(440)

<b>CoO Diffraction Lines 2θ values</b>	<b>Plane</b>
42.4	(200)
61.5	(220)

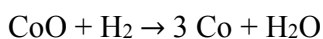
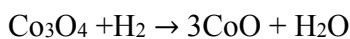
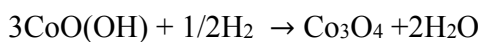
Table 3:9 Characterization of cobalt oxide phases by FTIR and Raman Spectroscopy

<b>Phase</b>	<b>FTIR</b> $\nu_{\text{Co-O}} \text{ (cm}^{-1}\text{)}$	<b>Raman Shift</b> $\text{(cm}^{-1}\text{)}$
Hexagonal CoO(OH)	584	367, 482, 599, 809
Spinel Co <sub>3</sub> O <sub>4</sub>	570, 661	482, 519, 621, 690
FCC CoO	507	455, 675

TPD studies on cobalt oxides for the above stable phases show the following decomposition reactions for oxidation states of +3, +8/3, +2 respectively:



TPR experiments for cobalt oxides also show those distinct phases with following reactions;



Above reactions are also justified quantitatively via TG-MS analysis. It has been shown that weight loss estimated by the reaction stoichiometry agrees within 2.5 wt % range with that of experimental measurements [90].

Kinetics of oxidation of metals into metal oxides have usually been investigated as a corrosion phenomenon rather than complete oxidation [62] such that there are a few studies on developing kinetic parameters on complete phase transformations from metal to different oxidation states. In the case of cobalt, modeling and simulation of complete oxidation process and finding the rate determining step between the possible interfaces of Co-CoO, CoO-Co<sub>3</sub>O<sub>4</sub>, Co<sub>3</sub>O<sub>4</sub>-air up to 900 °C has been presented based on *Avrami-Erofeev solid gas reaction model*, which is also used in this study. Oxidation of metallic cobalt to cobalt oxide was reported to be limited by diffusion of oxygen anions through

CoO-Co<sub>3</sub>O<sub>4</sub> interface, which has an activation energy of  $161 \pm 20$  kJ/mol with a pre-exponential factor of  $101.5 \pm 100$  min<sup>-1</sup> [93]. They found that the oxidation behavior is not as the parabolic law of diffusion predicted [94], which inherently assumes CoO has enough vacancies to be able to equilibrate itself with spinel cobalt oxide phase creating non stoichiometric Co<sub>1- $\delta$</sub> O phase.

Cobalt oxide surfaces of (100) of CoO and (110) and (111) of Co<sub>3</sub>O<sub>4</sub> are proven to be reactive towards oxygen and water by the study of Petitto et al. and they showed that water can react with both phases to introduce hydroxyl groups if enough energy for bond activation is available [95]. There also studies available in the literature for adsorption processes, some of which are presented in Table 3:10.

Table 3:10 Chemisorption of CO, CO<sub>2</sub>, H<sub>2</sub>O and O<sub>2</sub> on Cobalt Surfaces

<b>Gaseous State</b>	<b>Gaseous State Energy (eV)</b>	<b>Activation Energy for Adsorption (eV)</b>	<b>Adsorbed State</b>	<b>Adsorbed State Energy (eV)</b>	<b>Reference</b>
CO	0	0.25	C* + O*	-1.4	[125]
CO <sub>2</sub>	0	0.37	CO* + O*	-1.1	[126]
H <sub>2</sub> O	0	0	H <sub>2</sub> O*	-0.37	[127]
O <sub>2</sub>	0	0	O* + O*	-5.0	[128]

## CHAPTER 4

### METHODS AND MATERIALS

Following strategy was applied to fulfill the combined objectives of the study: looking for a candidate material to produce syngas via CO<sub>2</sub> and H<sub>2</sub>O splitting reactions and characterize the redox properties of that material:

- i. Compare candidate materials via a coarse thermodynamic analysis
- ii. Show the possibility and feasibility of syngas production over the selected material via thermochemical cycles with well-established methods theoretically
- iii. Demonstrate thermal reducibility of the material experimentally
- iv. Perform experiments to show syngas production from CO<sub>2</sub> and H<sub>2</sub>O
- v. Obtain the kinetic data of those reactions
- vi. Identify the ranges where mass and heat transfer limitations prevail for the selected material
- vii. Identify the rate determining step
- viii. Develop fundamental and realistic reactor models

Necessary background and preliminary work done for those work steps are presented in the following sections.

## 4.1 Thermodynamic Analysis

Metal oxides can be used as an oxygen source for an oxidation reaction which can selectively lead to a desired product or total combustion. Reactivity of the metal oxide depends on relative magnitudes of its own metal-oxygen bond strength and the strength of new possible bonds and thermodynamic equilibrium analysis can give clues about whether those reactions are expected to take place.

A system is said to be at equilibrium at a given temperature and pressure when the chemical composition and the total mass is constant if the system has the lowest free energy.

$$dG = 0 \qquad \text{Equation 4-1}$$

For any given system, equilibrium composition can be then calculated giving the minimum total free energy for a given temperature and pressure. Gibbs free energy minimization is a method that can be used for that purpose without the need of reaction kinetics. In this method, the compounds and starting amounts are given for the selected temperature and pressure and the working function, total Gibbs free energy, is to be minimized by changing the ratios of the amounts of possible chemical compounds with certain constraints by introducing a mathematical tool, Lagrange multipliers method. Then, performance of any metal-metal oxide couple can be investigated at various temperatures and pressures at equilibrium conditions.

$$\Delta G = \Delta H - T\Delta S \qquad \text{Equation 4-2}$$

Gibbs free energy can reveal whether a reaction is spontaneous for given conditions or not. Ellingham diagrams are graphical representations of the change in Gibbs free energy

with respect to temperature and oxygen partial pressure while the slope of the line is determined by the change in the entropy. It is a very popular method, especially for iron-steel production technology. During the construction of the plots, all reactions are stoichiometrically arranged such that they all consume one mole of O<sub>2</sub> and equilibrium partial pressure for a given temperature can be found accordingly.



$$\Delta G^0 = RT \ln(P_{O_2}) \quad \text{Equation 4-4}$$

$$P_{O_2} = \exp\left(\frac{\Delta G^0}{RT}\right) \quad \text{Equation 4-5}$$

Ellingham diagrams are also prepared for other oxidants such as water vapor and carbon dioxide in the same plot and one can find the ratios of H<sub>2</sub>:H<sub>2</sub>O and CO:CO<sub>2</sub> for a specific equilibrium temperature for a metal-metal oxide couple. Relative positions of the lines give information about the stability of the reactions. The ones having higher free energies are said to be less stable and easily reduced by the ones with lower free energy.

Another tool that can be used is the predominance diagrams which are simply a different way to represent thermodynamic equilibrium conditions between stable phases in a multicomponent reactive system. It is used when the system includes more than one metal-metal oxide couple and more than one gaseous phase or there is an alloy system with a gaseous species. A detailed example on how to produce predominance diagrams has been given in a previous study done by Çalışan [121].

#### 4.1.1 Selection of Metal Oxide Candidates

Free energy changes for possible reactions in syngas production were investigated with different metal oxides via constructing an Ellingham Diagram from temperature averaged enthalpy and entropy data collected from the literature as given in Appendix A. The ones around the desired reactions, between water splitting and total combustion of methane, which leads to the most stable form, are determined from the plot. Particularly, oxides around the water splitting and well above the methane to syngas reaction –to include the possible carbothermal reduction reactions- are highlighted after comparing heat of reactions, slopes (entropy change), availability and cost. Finally, cobalt oxide was selected to be further investigated in this study.

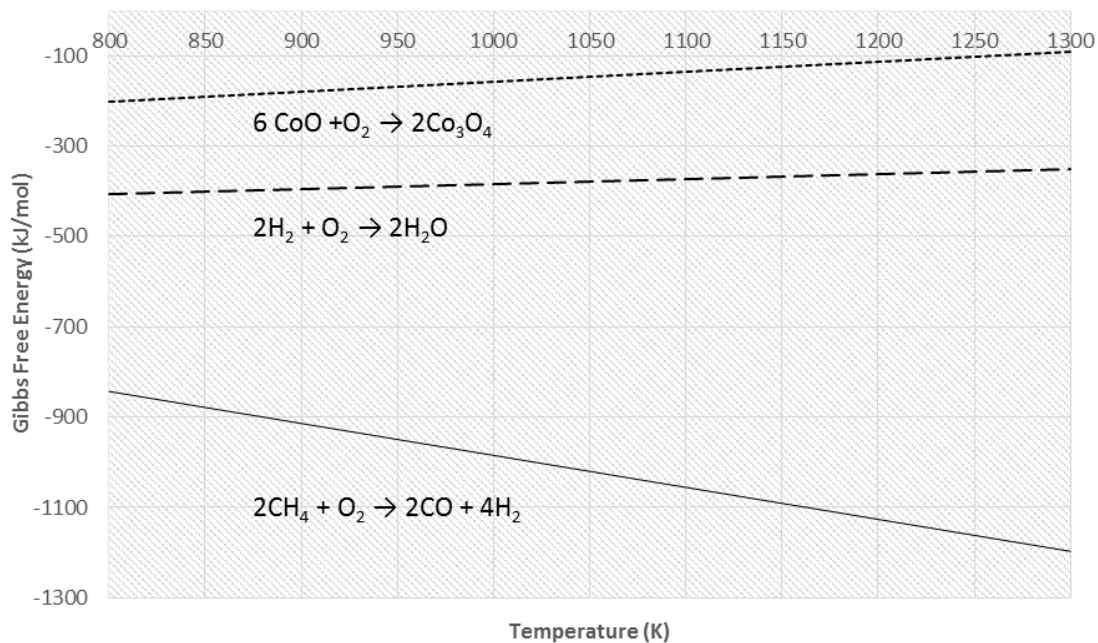
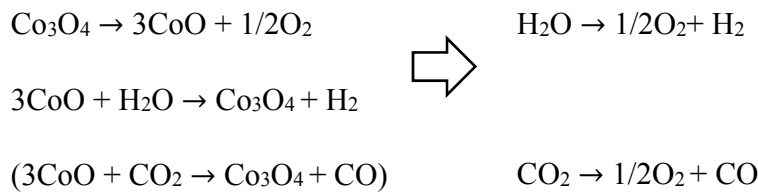


Figure 4:1 Free energy change with respect to temperature for selected formation reactions

#### 4.1.1.1 Theoretical Thermodynamic Efficiencies of Metal Oxides

Thermodynamics can predict whether a reaction takes place under certain conditions as well as how efficient a process can be.



In thermodynamic point of view, sum of individual reactions is the same as the overall reactions and that enables to define  $\Delta G$  and  $\Delta H$  for any redox couple by simply considering the thermodynamics of splitting reactions at the process temperature and pressure. So, effect of reduction and oxidation temperatures on thermodynamic efficiency can be estimated from the properties of  $\text{H}_2\text{O}$  and  $\text{CO}_2$  splitting experiments.

Efficiency of those splitting reactions can be stated as the ratio of free energy change at oxidation temperature to heat of reaction for the reduction step:

$$\text{Efficiency} = \left( \frac{\Delta G_{T_{\text{oxidation}}}}{\Delta H_{T_{\text{reduction}}}} \right) \times 100 \quad \text{Equation 4-6}$$

It is to be compared with an alternative way of producing usable work between the high temperature process and low temperature process as the first step of the feasibility analysis by checking the Carnot efficiency of a closed cycle at those temperatures as follows:

$$\text{Carnot Efficiency} = 1 - \frac{T_{\text{oxidation}}}{T_{\text{reduction}}} \quad \text{Equation 4-7}$$

At the beginning of the study, those two efficiencies of redox pairs given in Table 3:5 were compared as summarized in Appendix A.  $\Delta G$  and  $\Delta H$  values were evaluated for water splitting reaction at the given reoxidation and thermal reduction temperatures of the related studies. It was seen that efficiency of thermochemical water splitting is around 70% while Carnot efficiency was found to be around 20% (for the same temperatures).

As the next step, water splitting and  $\text{CO}_2$  splitting to  $\text{CO}$  and  $\text{O}_2$  were investigated for different thermal reduction and reoxidation temperatures between 1000 and 1800 K. It was found that efficiency is not a strong function of thermal reduction temperature while it increases as the oxidation temperature decreases. Additionally, water splitting reaction was found to be more efficient compared to  $\text{CO}_2$  splitting under the same conditions (see Figure 4:2).

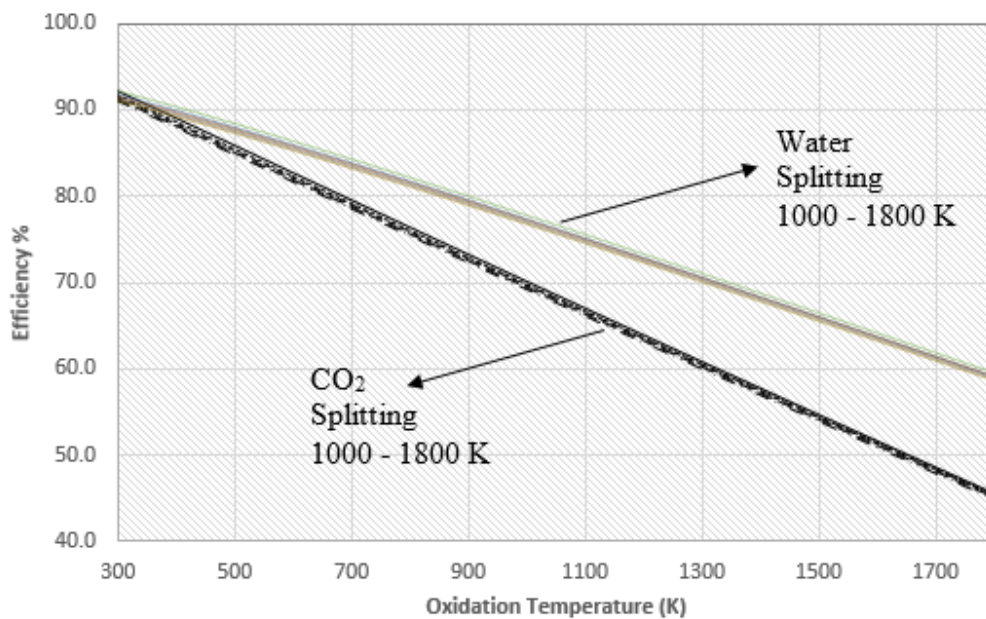


Figure 4:2 Efficiency for the splitting reactions at various thermal reduction and re-oxidation temperatures (1000 – 1800 K) for water and  $\text{CO}_2$

## **4.2 Experimental Methods and Materials**

### **4.2.1 Experimental Methods**

#### **4.2.1.1 Procurement of the Material**

Technical grade cobalt oxide was obtained from *Ege Ferro Company* and all experiments were done with this oxide.

#### **4.2.1.2 Material Characterization**

Technical grade cobalt oxide was analyzed for chemical analysis via *Rigaku ZSX Primus II X-ray fluorescence (XRF)* analysis. Procured cobalt oxide was also examined with *X-ray diffractometer (Rigaku XRD, -30kV, 15mA- with Cu K $\alpha$  radiation,  $\lambda=1.54\text{\AA}$ )* for scattering angle  $5^\circ$  to  $90^\circ$ . Diffraction lines were compared with literature [90-92].

#### **4.2.1.3 BET Experiments**

Technical grade bulk  $\text{Co}_3\text{O}_4$  is taken as the reference sample (CA-0913-0) and it was calcined at different temperatures as given in Table 4:1.

Next, samples are dried in vacuum oven at  $120^\circ\text{C}$  for 12 hours. Immediately after drying, they were analyzed via *Micromeritics Gemini 2380 Surface Area Analyzer*, which is normally used to measure the surface area of a given substance, to obtain adsorption-desorption isotherms for oxygen. Instead of nitrogen at 77 K, experiments were done by introducing pure oxygen to vacuumed chamber at room temperature up to 695 mmHg in three consecutive adsorption-desorption cycles.

Table 4:1 Calcination Temperatures and Durations

Sample Name	Calcination Temperature (°C)	Duration (hr)
CA-0913-0	-	-
CA-0913-1	800	24
CA-0913-2	800, then 900	24, 24
CA-0913-3	800, then 1000	24, 24
CA-0913-4	800, then 1100	24, 24
CA-0913-1(2)	800	24

#### 4.2.1.4 TGA Experiments

*Thermogravimetric Analysis* is a method monitoring the weight change of a sample with time/temperature, which can give information about thermal stability of a material, phase transitions, kinetics of decomposition reactions or chemisorption processes and change in chemical composition of a given sample.

TGA of spinel cobalt oxide was made under dry air and N<sub>2</sub> flow from room temperature up to 1100 °C by 10°/min to observe, compare and quantify the phase change in oxidative and inert atmospheres. Analysis was also done with 5°/min and 15°/min heating rates to derive the DTA curves and kinetic data of phase change from spinel cobalt oxide to FCC cobalt oxide via *Kissinger Method*.

#### 4.2.1.5 TPR and Water Splitting Experiments

*Temperature Programmed Reduction* is a method in which the sample is reduced by adsorbing a compound and desorbing as temperature increases. Desorbed compound is to be detected via mass spectroscopy (MS) or by a thermal conductivity detector (TCD) *etc.* In the experimental setup, a thermal conductivity detector was used to monitor the change

in H<sub>2</sub> signal. Ar and hydrogen gases were used with two mass flow controller (MFC, Teledyne Hastings 200) with a mass flow control station (MFCS, TRL Instrument). Water injections were done via a syringe pump.

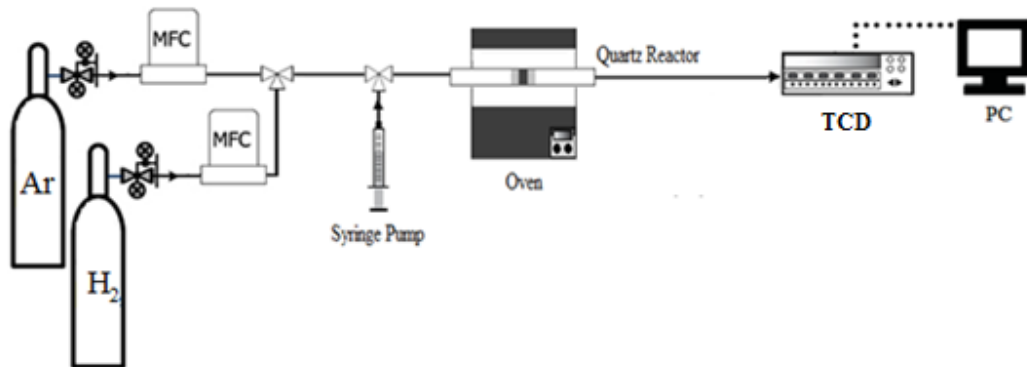


Figure 4:3 Experimental setup for water splitting experiments

#### Reduction by Hydrogen

Reduction by hydrogen was done to observe phase changes from spinel oxide to metallic Co and quantify the reducibility of the sample. 0.3 g technical grade  $Co_3O_4$  were put into 75 cm long quartz reactor. Oxide was heated up to 700 °C from room temperature by 10 °C/min. Carrier gas flow rate was kept constant at 47.5 ccpm with 2.5 ccpm H<sub>2</sub> flow.

#### Re-oxidation by Water

0.3 g technical grade  $Co_3O_4$  were put into a 75 cm long quartz reactor. First oxide is heated up to 925 °C from room temperature by 10 °C/min. Then it is cooled down to 725 °C under Ar flow.

250 µl of water was injected via syringe pump with a rate of 100 µl/min for 16<sup>th</sup> times. Each cycle was recorded separately for high resolution of the data. Unused water was

captured by anhydrous calcium sulfate (Drierite®) so as to eliminate the probable disturbances in the TCD signal.

#### **4.2.1.6 Thermal Decomposition and CO<sub>2</sub> Splitting Experiments**

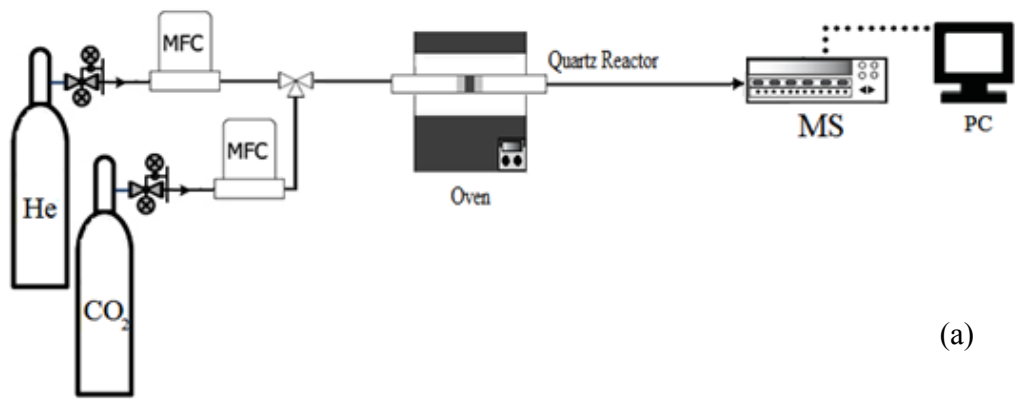
Thermal decomposition of spinel oxide was demonstrated with the experimental setup shown in Figure 4:4 where exit gas from the reactor was analyzed by *Mass Spectrometry*. Reduced oxide then was further reacted with CO<sub>2</sub> to produce CO.

##### Thermal Decomposition of Co<sub>3</sub>O<sub>4</sub>

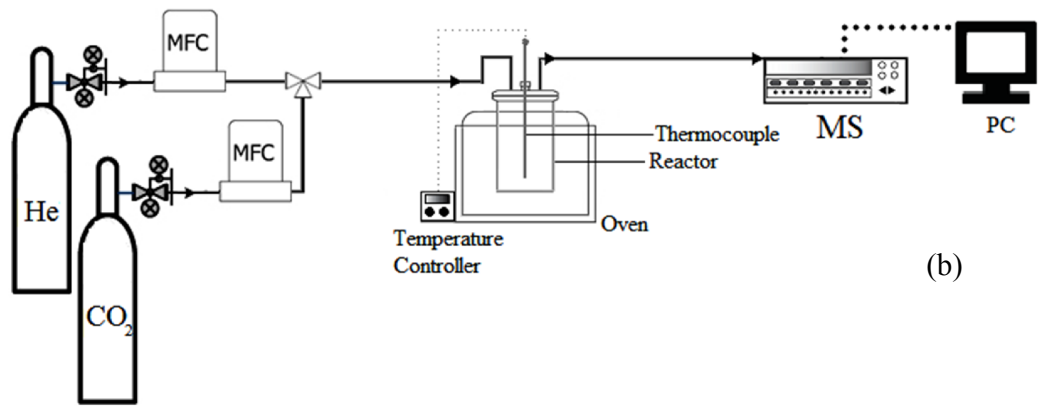
In the first part, 1 g technical grade Co<sub>3</sub>O<sub>4</sub> was put into the quartz reactor (Figure 4:4-a). Reactor was heated under the flow of 50ccpm He up to 1000 °C. Same experiment was repeated with 15 g sample as well in 400 cc stainless steel reactor (Figure 4:4-b)

##### Re-oxidation by Carbon Dioxide

After the thermal decomposition experiment under the flow of 50ccpm He for 15 g sample, gas was switched to 20ccpm CO<sub>2</sub> (99.9%) until the reactor cools down to room temperature (took approximately 3hours). After cooling, gas was switched to the 50ccpm He again and heating period was started. The exit stream was sent to the MS. Experiment was conducted until 770 °C. Same procedure was repeated for the second run right after the first run.



(a)



(b)

Figure 4:4 Setup for the CO<sub>2</sub> Splitting Experiments

### 4.3 Kinetic Analysis

In a nonisothermal experiment for measuring the kinetics of phase transformation (TGA-DTA), as the temperature is increased, reaction rate is expected to increase and pass through a maximum point due to the depletion of the reactants. If the temperature increase rate is constant, then the following equation can be integrated as a function of temperature as described by Kissinger [67].

$$\frac{d\alpha}{dt} = k \cdot f(\alpha)$$

At the maximum rate point, derivative becomes zero and followings are obtained<sup>3</sup>,

$$\frac{1}{n-1} \left( \frac{1}{(1-\alpha)^{n-1}} - 1 \right) = \frac{A_0 RT_{max}^2}{E_a Q} \exp\left(-\frac{E_a}{RT_{max}}\right) \left(1 - \frac{2RT_{max}}{E_a}\right)$$

$$\frac{E_a Q}{RT_{max}^2} = A_0 ((1-\alpha)^{n-1}) n \exp\left(-\frac{E_a}{RT_{max}}\right)$$

where Q is the heating rate.

For the special case n=1,

$$\ln\left(\frac{1}{1-\alpha}\right) = \left(1 - \frac{2RT}{E_a}\right)$$

One can find the order of the reaction from the symmetrical behavior of the DTA curve. As n decreases, the curve becomes more asymmetric and amount of asymmetry can be measured from the inflection points as shown below or can be evaluated from

$$Shape\ Index = \frac{\left(\frac{d^2\alpha}{dt^2}\right)_{inflection\ point\ 1}}{\left(\frac{d^2\alpha}{dt^2}\right)_{inflection\ point\ 2}}$$

---

<sup>3</sup> The idea is based on the following: As the temperature increases, reaction rate coefficient (k) increases which can be also seen in its explicit Arrhenius form. Meanwhile, concentration of the converted material decreases such that rate of change in reaction rate passes through a maximum. The same principle is also used in similar method in *Thermal Desorption Spectroscopy*, Redhead Method.

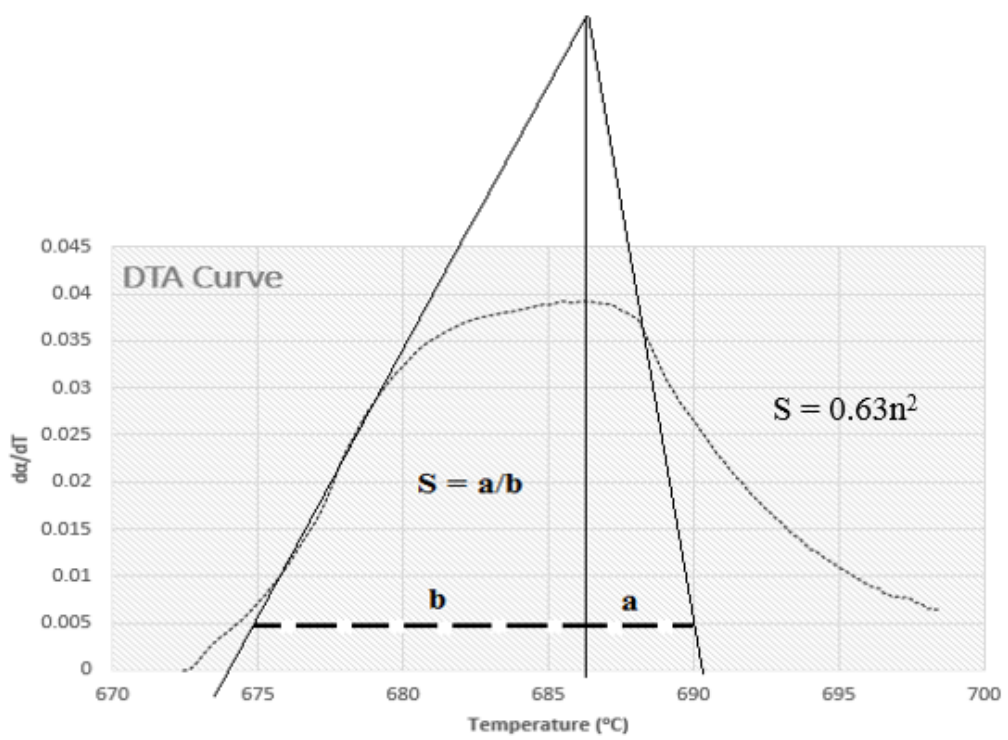
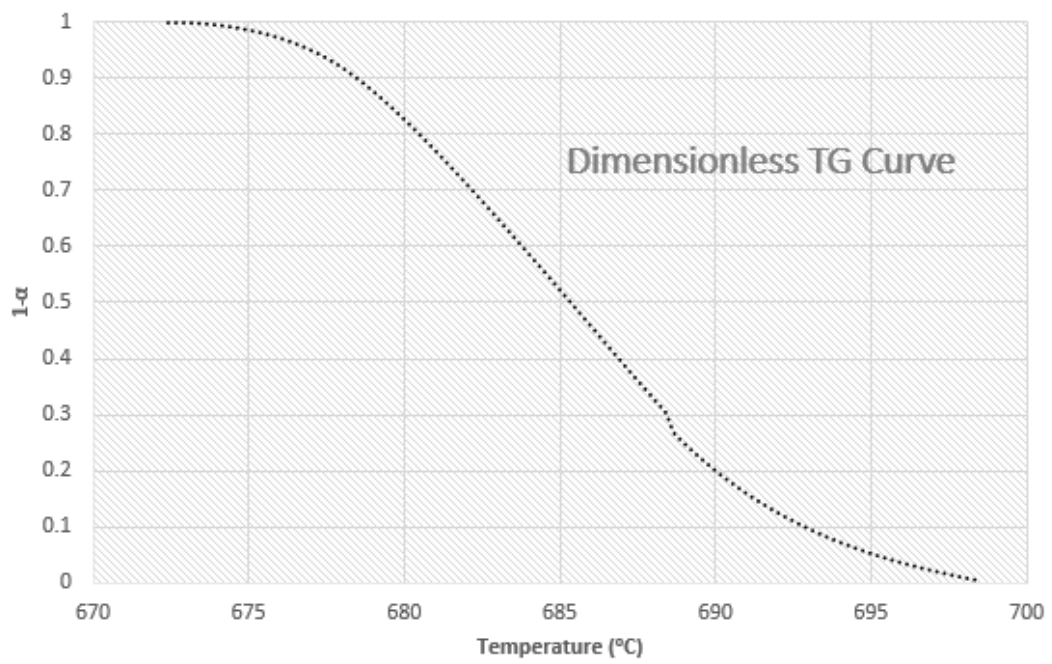


Figure 4:5 Determination of shape index

It has been shown that the shape index is a function of reaction order only and that relationship can be used to estimate the order of reaction. Once the order of reaction is determined, activation energy can be found easily.

For multiple heating rates, following analysis can also be done to obtain the order of reaction with pre-exponential factor<sup>4</sup>.

$$\frac{d\alpha}{dt} = k \cdot f(\alpha) \quad \text{Equation 4-8}$$

$$\frac{d\alpha}{dt} = A \exp\left(-\frac{E_a}{RT}\right) f(\alpha) \quad \text{Equation 4-9}$$

$$Q \frac{d\alpha}{dT} = A \exp\left(-\frac{E_a}{RT}\right) f(\alpha) \quad \text{Equation 4-10}$$

$$\ln\left(Q \frac{d\alpha}{dT}\right) = \ln(Af(\alpha)) + \left(-\frac{E_a}{R}\right) \frac{1}{T} \quad \text{Equation 4-11}$$

So, if  $\ln\left(Q \frac{d\alpha}{dT}\right)$  data is plotted against  $1/T$  for different  $\alpha$  values for any reaction,  $\ln(Af(\alpha))$  points can be obtained. It was shown that  $f(\alpha)$  can be expressed as;

$$f(\alpha) = (1 - \alpha)^n \quad \text{Equation 4-12}$$

giving

$$\ln(A(1 - \alpha)^n) \quad \text{Equation 4-13}$$

or

$$\ln A + n \cdot \ln(1 - \alpha) \quad \text{Equation 4-14}$$

So, if obtained points of  $\ln(Af(\alpha))$  is plotted against  $\ln(1 - \alpha)$ , both the order and the pre-exponential factor can be derived from experimental data.

---

<sup>4</sup> Since temperature is increased linearly in the experiment ( $T = a + b.t$ ), one can easily change the independent time variable to temperature from the derivative of the linear temperature relationship ( $dt = 1/b \cdot dT$ ).

## 4.4 Mass and Heat Transfer Limitations

### 4.4.1 Mass Transfer

Diffusion is the only mode of mass transfer within a solid, in which atoms/ions/molecules move through the lattice due to either a chemical potential gradient or random walk. There are different diffusion mechanisms which can be grouped as interstitial and substitutional, both depend on the existence of lattice defects in various forms. In an interstitial solution, most of the available sites for the solute are vacant such that they can jump between based on the probability designated by its momentary free energy. In substitutional diffusion, atoms can replace their sites directly or an atom can move to a vacant site. It is also possible that a number of atoms move within the lattice in a cooperative way as in ring diffusion. At high temperatures, vacancy concentration increases significantly, becoming the dominant mechanism, and species are formed and move with available thermal energy present, namely intrinsic diffusion, giving higher activation energies [95]. In the case of cobalt oxide, as explained in part 3.4.2, the process is found to be limited by diffusion of cobalt cations and oxygen anions within the lattice and at the working temperature range, around 800 °C ~ 950 °C, possible mechanism is to be intrinsic diffusion. Model derived by Metz (2010) et al. assumes a steady state approximation with first order kinetics to describe the phenomenon, which fits quite well with oxidation kinetics of cobalt oxide. Based on same assumptions, adaptation of *Deal Grove Model* can be built up to have a broad insight for the oxidation process, which is to guide a better modeling strategy, as described below.

#### 4.4.1.1 Growth Model

System considered consists of three main domains: bulk gas phase where oxygen/oxidizing agent is present, oxidized zone and reduced zone. Oxygen concentration is considered to reach a certain value,  $C_{O_s}$ , by either solution of oxygen following a form

similar to *Henry's Law* or a first order reaction where oxidizing agent reacts with the surface. Then oxygen atoms diffuses through the oxidized zone, explained by *Fick's law of diffusion* and react at the interface between two phases with *first order reaction kinetics*. In time, oxidized zone grows in the x direction as shown below.

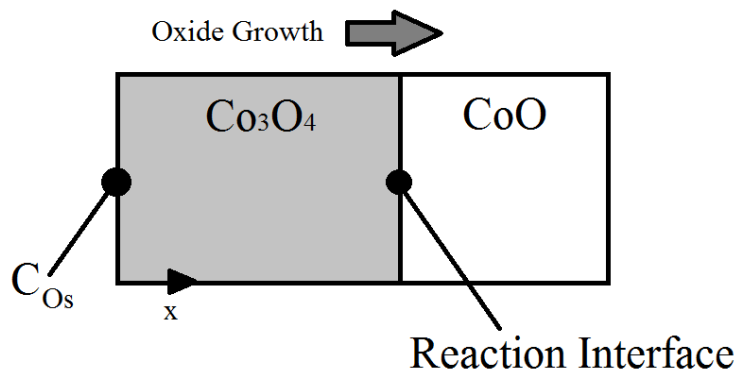


Figure 4:6 Schematic representation of the growth model

If mass fluxes at the gas-solid and solid-solid interfaces are considered to be equal, there is no accumulation of oxygen in any solid domain, change in the oxide thickness with time can be derived from this equality:

$$j_I = H_{oxygen}(C_{bulk} - C_{O_s})$$

$$j_{II} = D_{oxygen} \frac{(C_{O_s} - C_{O_i})}{\delta}$$

$$j_{III} = k_{rxn} C_{O_i}$$

$$j_I = j_{II} = j_{III}$$

where;

- $H_{oxygen}$ : Oxygen Solubility (m/s)

- $D_{oxygen}$ : Diffusivity of oxygen ( $m^2/s$ )
- $\delta$ : Oxide thickness in x direction (m)
- $C_{O_i}$ : Oxygen concentration at the interface ( $mol/m^3$ )
- $k_{rxn}$ : Oxidation reaction rate constant (m/s)

At the reaction interface;

$$k_{rxn}C_{O_i} = D_{oxygen} \frac{(C_{O_s} - C_{O_i})}{\delta}$$

$$C_{O_i} = \frac{(C_{O_s})}{1 + \delta \frac{k_{rxn}}{D_{oxygen}}}$$

Although fluxes are considered to be equal to one another, thickness of the oxide layer changes with time. To describe this phenomenon, one can say:

$$\frac{d}{dt}(\delta) = \frac{k_{rxn}C_{O_i}}{\rho_m}$$

where  $\rho_m$  is molecules per unit volume of formed oxide layer ( $mol/m^3$ )

$$\frac{d}{dt}(\delta) = \left( \frac{k_{rxn}}{\rho_m} \right) \left( \frac{(C_{O_s})}{1 + \delta \frac{k_{rxn}}{D_{oxygen}}} \right)$$

$$\frac{d}{dt}(\delta) = \frac{(C_{O_s})D_{oxygen}}{\rho_m \left( \delta + \frac{D_{oxygen}}{k_{rxn}} \right)}$$

If integrated between  $t = 0$ ;  $\delta = 0$  and  $t = t$ ;  $\delta = \delta$ , following is obtained:

$$\left( \frac{\rho_m}{2(C_{O_s})D_{oxygen}} \right) \delta^2 + \frac{\rho_m}{k_{rxn}(C_{O_s})} \delta - t = 0$$

$$\delta = \frac{2(C_{O_s})D_{oxygen}/\rho_m}{2 k_{rxn}(C_{O_s})/\rho_m} \left( \sqrt{1 + \frac{4(k_{rxn}(C_{O_s})/\rho_m)^2}{2(C_{O_s})D_{oxygen}/\rho_m} t} - 1 \right)$$

$$\alpha = 2(C_{O_s})D_{oxygen}/\rho_m; \quad \beta = k_{rxn}(C_{O_s})/\rho_m;$$

$$\delta = \frac{\alpha}{2\beta} \left( \sqrt{1 + \frac{4t(\beta)^2}{\alpha}} - 1 \right)$$

Where  $\alpha$  gives the diffusive term and  $\beta$  gives the reactive term in the equation. If the governing differential equation is considered, two limiting cases are obtained:

$$\frac{d}{dt}(\delta) = \left( \frac{k_{rxn}}{\rho_m} \right) \left( \frac{(C_{O_s})}{1 + \delta \frac{k_{rxn}}{D_{oxygen}}} \right)$$

For small  $\delta$  values; that is the oxide layer is thin, following is found:

$$\frac{d}{dt}(\delta) = \left( \frac{k_{rxn}}{\rho_m} \right) (C_{O_s}) = \beta$$

meaning that oxidation process is within the kinetically controlled regime. For large  $\delta$  values:

$$\frac{d}{dt}(\delta) = \left( \frac{k_{rxn}}{\rho_m} \right) \left( \frac{(C_{O_s})}{\delta \frac{k_{rxn}}{D_{oxygen}}} \right) = \frac{\alpha}{2\delta}$$

meaning that oxidation process is within the diffusion controlled regime.

To investigate the oxidation process in either of the zones or in a regime where both mechanisms are significant,  $C_{O_s}$ ,  $\rho_m$  and  $k_{rxn}$  are needed to be defined and some correlations were collected from the literature, as given in Appendix B.6. Diffusivities of oxygen and cobalt in cobalt oxide has been given in the literature are tabulated below [95-97]. Diffusivities of oxygen in other oxides/metals are given in the Appendix B.1 for comparison.

Table 4:2 Diffusivities of oxygen and cobalt in cobalt oxide

<b>Diffusing Species</b>	<b>Temperature Range (K)</b>	<b>Pre-exponential (m<sup>2</sup>/s)</b>	<b>Activation Energy (kJ/mol)</b>	<b>Diffusivity at 1000 K (m<sup>2</sup>/s)</b>
[O]	1440-1830	$50 \times 10^{-4}$	95± 5	$5.4 \times 10^{-8}$
[Co]	1373-1673	$4.8 \times 10^{-7}$	150	$7.0 \times 10^{-15}$
[Co]	1236-1911	$5.0 \times 10^{-4}$	161± 1	$1.9 \times 10^{-8}$

With this preliminary approach, it is seen that mass transfer rates by diffusion are slow and penetration of oxide layers of order of centimeters takes hours with the conditions defined in Appendix B.6. Radial mass transport in a micrometer-scale, however, seems to be completed in seconds.

#### 4.4.2 Heat Transfer

In mass transfer analysis, a basic approach has been developed to understand the order of magnitude of rate of mass transfer within the solid such that a starting point for a noncatalytic gas solid reactor model to be built could be obtained. A similar analysis is to be done to characterize heat transfer rates in simple but representative physics as well as simultaneous heat and mass transfer interactions to conclude a perspective to decide on reactor modeling strategy for more realistic simulations.

To do so, a few basic cases were investigated as presented below, for which the details were given in the Appendix B.3, and it was deduced that heat transfer rates are fast for micro-scale solid domains while it becomes significant as local high/low temperature zones have the dimensions in the order of millimeters.

#### 4.4.2.1 Fundamental Calculations

In the simplest case, the lattice structure cobalt oxide was considered to be perfectly repeated over a  $1 \text{ m}^2$  surface and it was assumed that all available Co atoms on the surface were oxidized to spinel oxide, which gives an approximation to a heat flux,  $2.294 \text{ J/m}^2$ . Adiabatic increase in temperature when 1 mol of  $\text{Co}_3\text{O}_4$  is formed at 1000 K was also calculated for both oxidation of Co and CoO and found as 3456.13 K and 1780.59 K respectively. Roughly estimated heat flux was then used as an instantaneous heat source, it was seen that temperature profile returns to its initial state in less than milliseconds.

Transient temperature profiles were also derived with constant wall temperature (1780.59 K) and constant heat flux ( $2.294 \text{ J/m}^2$ ) boundary conditions and results are given in Appendix B.3. It was seen that if local temperature is increased and kept at the new temperature even for a few seconds, that energy can diffuse to noticeable distances and create local hot spots in the range of millimeters.

#### 4.4.2.2 Time Scales for the Heating/Cooling of Finite Geometries

Based on above deductions, theoretical analysis was based on temperature increases/decreases rather than on heat fluxes. Model details and results are given in Appendix B.4.

Firstly, it was considered what would be time scale of the thermal response for the reduction of a 1 unit cell of  $\text{Co}_3\text{O}_4$  within a larger volume. To do so, endothermic reduction reaction was considered to take place in the small cube and energy balance calculations give a temperature decrease to 338 K from 1000 K. Then, transient conservation of energy equation was solved to determine how fast colder small cell reaches to thermal equilibrium with the larger volume. Results imply that instantaneous temperature drop at a local point can be compensated very fast ( $\sim 10^{-10}$  seconds).

Secondly, transient heat transfer rates were investigated within a plate having a more practical scale ( $\sim$ cm). A step change was introduced to a small fraction of the plate and heat dissipation to the colder zone was monitored. Temperature increase was selected as 50 K based on the results given in fundamental analysis. Problem was solved for seven different lengths of the heated zone and it was found that as the percentage of the heated portion is increased ( $\sim$ 1% of total length), thermal response time is seen to be in the order of minutes.

#### **4.4.3 Nonisothermal Effects: Simultaneous Heat and Mass Transfer within a Spherical Particle**

As explained briefly in *Noncatalytic Gas–Solid Reactions* (Section 3.3), simultaneous heat and mass transfer problem can be analyzed by introducing an effectiveness factor. Derivation of effectiveness factor has been presented in Appendix B.5 with its numerical solution via COMSOL software for first order reaction kinetics. Non-dimensional term  $\beta$  is a key parameter for the effectiveness factor, which shows the ratio of the maximum possible temperature increase to the surface temperature. It becomes positive for exothermic reactions leading to effectiveness factors larger than unity such that it can affect the performance of the particle significantly especially for reactions with high temperature sensitivity. For cobalt oxidation reaction, this value is found practically zero (see the Appendix B.5.3); it is because of the ratio of the mass diffusivity to thermal conductivity) meaning that no significant thermal effects are expected within the particles.



## **CHAPTER 5**

### **RESULTS**

#### **5.1 Investigating the Feasibility of Redox Reactions through Thermodynamic Analysis**

##### **5.1.1 Understanding the State of Art in Syngas Production**

Syngas is produced via steam reforming, partial oxidation and with the combination of those, namely, autothermal reforming and the objective of this analysis is to define a method which accurately estimates the product distribution for those reactions. To do so, two questions were answered in the following text:

- (1) What controls the governing mechanisms for syngas production from methane?
- (2) How can those mechanisms be represented with reasonable accuracy?

After answering those two questions, findings were analyzed in light of a relatively new approach, membrane reactors.

The answer of the first question is rather obvious if one is only interested in the product distribution. It has been stated by many researchers that product distribution of steam reforming and partial oxidation of methane can be precisely estimated by thermodynamic equilibrium of gas phase products at elevated temperatures [112-120]. The reaction mechanism; however, is debatable at those temperatures for partial oxidation and

autothermal reforming of methane. Mechanism for oxidation is reported to be either total combustion followed by steam and dry reforming reactions (Combustion and Reforming Reaction-CRR) or direct partial oxidation of methane (DPO). CRR mechanism has been experimentally shown by monitoring the reactor bed temperature. Temperature profiles (macroscopic scale) demonstrate an exothermic zone, which is followed by an endothermic zone. It should be noted that those experiments were performed with undiluted methane and oxygen mixtures for various catalysts [117,118]. Experimental validity of DPO mechanism has been instantiated with short contact time reactors such that CO and H<sub>2</sub> are found to be the primary products [114, 115, 117, 118]. There are also some studies in the literature which has spotted a quite remarkable point in CRR and DPO mechanisms; that is an experimentally observed temperature difference between the catalyst and exit gas temperature [113,117,120]. That temperature difference, about 400 °C, was observed for various space times as well [113]. It is known that non-catalytic partial oxidation of methane can be achieved at temperatures from and above 1000 – 1300 °C [116, 117, 118, 112] and that spotted temperature difference becomes significant as non-catalytic partial oxidation reactions could be an important contribution to produced syngas. In fact, an important work was published by Chang and Heinemann [120] in which they made temperature measurement on catalysts given in the literature for validity of DPO mechanism. They first made experiments on methane oxidation without any catalyst and they observed conversion for temperatures above 925 °C yet with less H<sub>2</sub> selectivity. With the Co-MgO catalyst, they obtained high CO and H<sub>2</sub> selectivity for temperatures above 700°C while they detect a temperature difference of ~100 °C via thermocouples. What they do different than the others was they removed the furnace used and they discovered that measured temperature could not drop below 450 °C while the catalyst was glowing. Then they switched the temperature measurement technique IR radiation thermometer and they recorded a temperature exceeding 1250 °C giving a difference with a thermocouple more than 800 °C. They conducted further experiments and proved that at high space velocities system behaves like an adiabatic process which can results in local temperatures as high as 2400 °C depending on CO selectivity. So, they concluded that at high methane and oxygen flow rates, local temperatures may go up to 1300 °C where non-catalytic oxidation becomes significant and one can get quite different

selectivities and yields for identical residence times and inlet compositions (92% to 5% selectivity in H<sub>2</sub> and 89% to 1% selectivity in CO in their study).

Based on above, it was concluded that thermodynamic equilibrium analysis can be a practical tool to estimate the effect of reaction conditions and reactant ratios on the product distribution. Cobalt oxide has been selected as the candidate material which has a potential activity for syngas production and its interaction with the reacting medium at equilibrium conditions should also be investigated. Gibbs free energy minimization method was used to fulfill that objective and obtain thermodynamic limitations for different possible reactions of cobalt, oxygen, water and methane inlet streams at different ratios and equilibrium temperatures. Results are presented in the following sections for atmospheric pressure based on the data given in the Appendix A.

Table 5:1 Chemical reactions in syngas production

<b>Reactions</b>	<b><math>\Delta H^{\circ}_{298}</math> (kJ/mol)</b>
$\text{CH}_4 + 2\text{O}_2 \rightarrow \text{CO}_2 + 2\text{H}_2\text{O}(\text{v})$	-800
$\text{CH}_4 + 1/2\text{O}_2 \rightarrow \text{CO} + 2\text{H}_2$	-36
$\text{CH}_4 + \text{O}_2 \rightarrow \text{CO}_2 + 2\text{H}_2$	-319
$\text{CO} + \text{H}_2\text{O}(\text{v}) \leftrightarrow \text{CO}_2 + \text{H}_2$	-77
$\text{CH}_4 + \text{H}_2\text{O}(\text{v}) \leftrightarrow \text{CO} + 3\text{H}_2$	205
$\text{CH}_4 + \text{CO}_2 \leftrightarrow 2\text{CO} + 2\text{H}_2$	247
$\text{CO} + 1/2\text{O}_2 \rightarrow \text{CO}_2$	-283
$\text{H}_2 + 1/2\text{O}_2 \rightarrow \text{H}_2\text{O}(\text{v})$	-241

For the results presented from 5.1.1.2 to 5.1.1.4, it was found that Co remains in the metallic form until all C and H available are totally combusted to CO<sub>2</sub> and H<sub>2</sub>O for almost the entire range studied so that Co data is not presented in the reported plots.

Indirectly defined syngas production reactions with side reactions are given in Table 5:1.

### 5.1.1.1 Cobalt –Cobalt Oxide Phase Transformation

First analysis was done on cobalt-oxygen mixture at different ratios. The aim of this calculation was to show the accuracy of the method as cobalt oxide phases are known experimentally and transition between those states is well established. It was found that Co prefers to be in CoO form if there is not stoichiometrically enough oxygen for the  $\text{Co}_3\text{O}_4$  phase (Figure 5.1-a) and  $\text{Co}_3\text{O}_4$  phase is reduced to CoO after 1200 K, which was the case in TGA analysis in inert atmosphere (Figure 5.1-b).

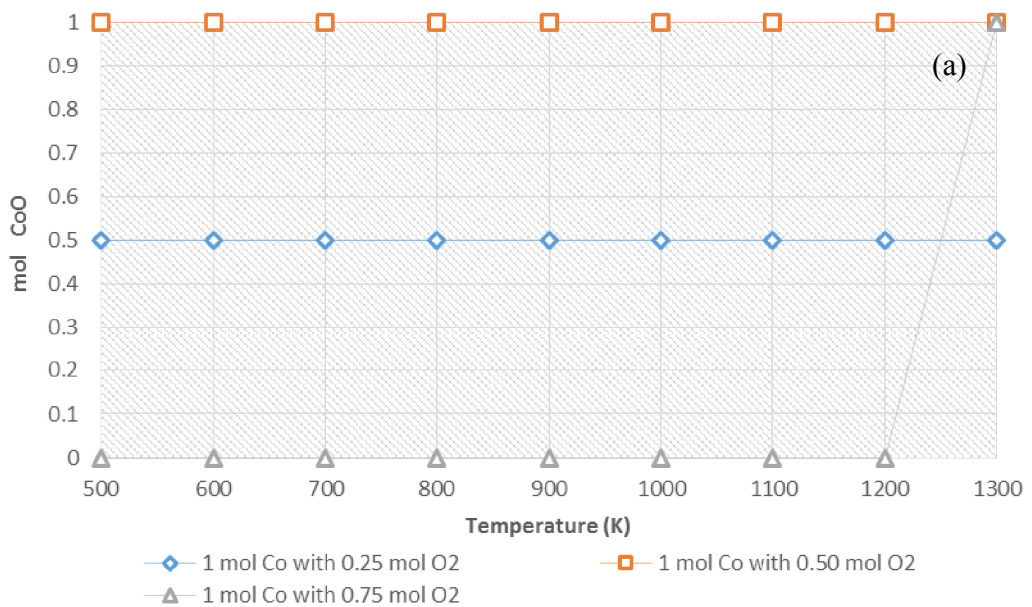


Figure 5:1 Equilibrium composition for Co-O system

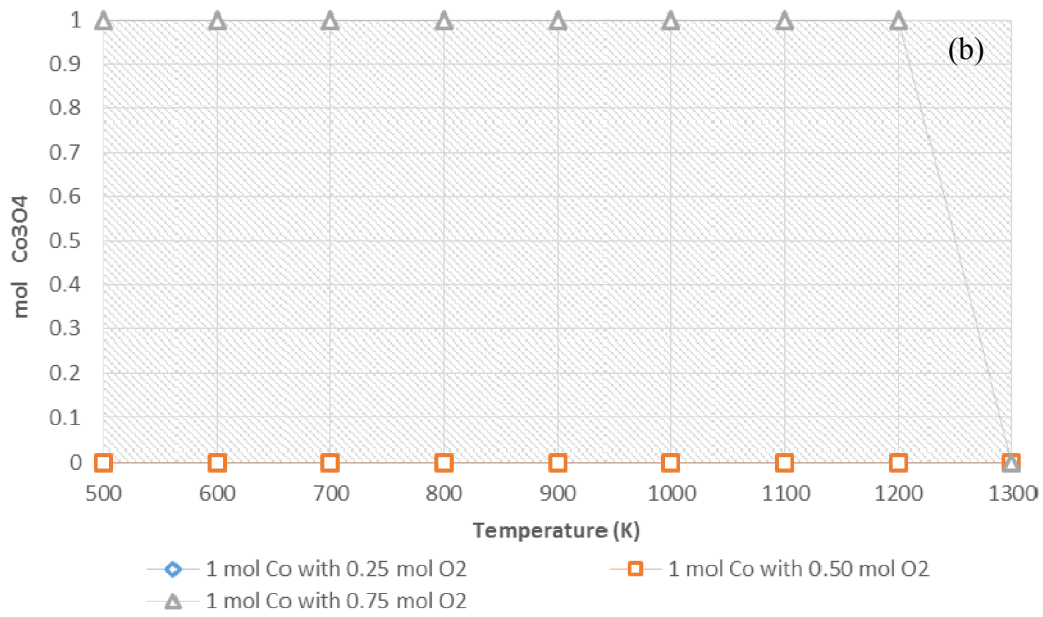


Figure 5:1 Equilibrium composition for Co-O system (continued)

In the following sections, free energy minimization results obtained for partial oxidation, steam reforming and autothermal reforming of methane are given respectively.

### 5.1.1.2 Partial Oxidation of Methane in the Presence of Cobalt

Equilibrium calculations show that high temperature operation is favorable as it gives higher methane conversions. For temperatures above 1000 K, both CO and H<sub>2</sub> selectivities up to 100% can be obtained based on the ratio of the oxygen and methane available. It is also seen that H<sub>2</sub>:CO ratio of two, which is the desired value for many downstream applications, can be achieved for temperatures above 1000 K for O<sub>2</sub>:CH<sub>4</sub> ratios below the stoichiometric feed (when ratio is 0.4) as seen in Figure 5.2-d. Additionally, H<sub>2</sub>:CO ratio can be increased as high as 5, implying that ratios higher than 2 can also be achieved (Figure 5.2-d), which is needed for processes like ammonia synthesis. However, it should be noted that conversion of methane (Figure 5.2-a) is low for sub-stoichiometric O<sub>2</sub> feed. So, high selectivities can be obtained (Figure 5.2-b,c) at the expense of methane conversion, or vice versa.

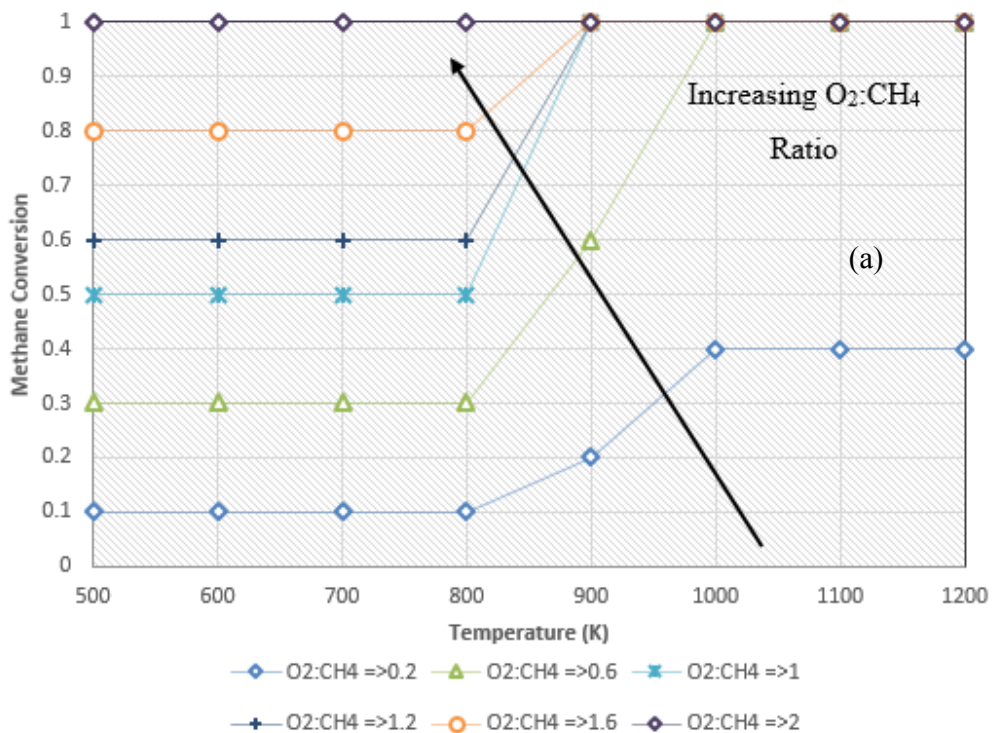


Figure 5.2 Equilibrium conversion and selectivity for partial oxidation of methane

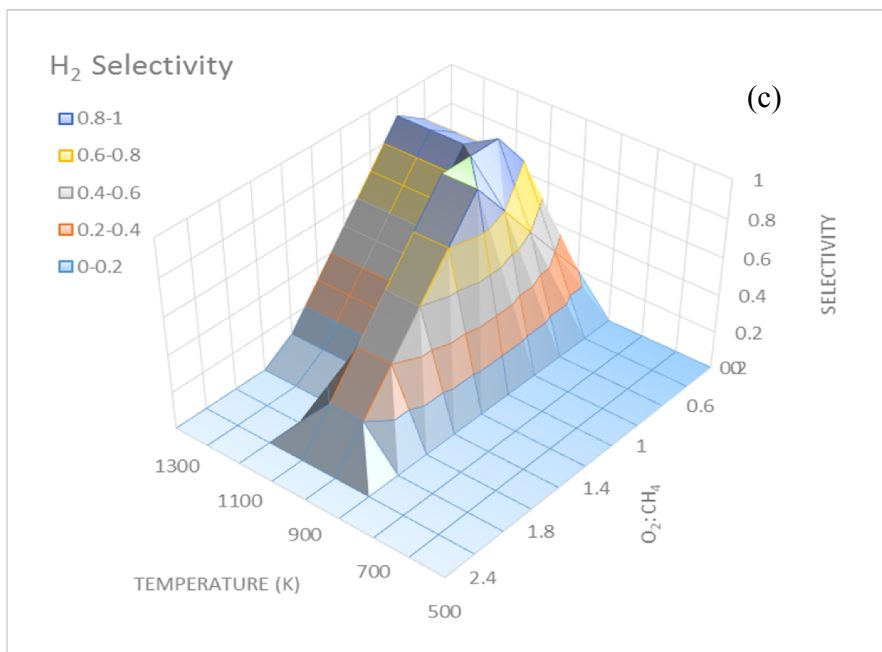
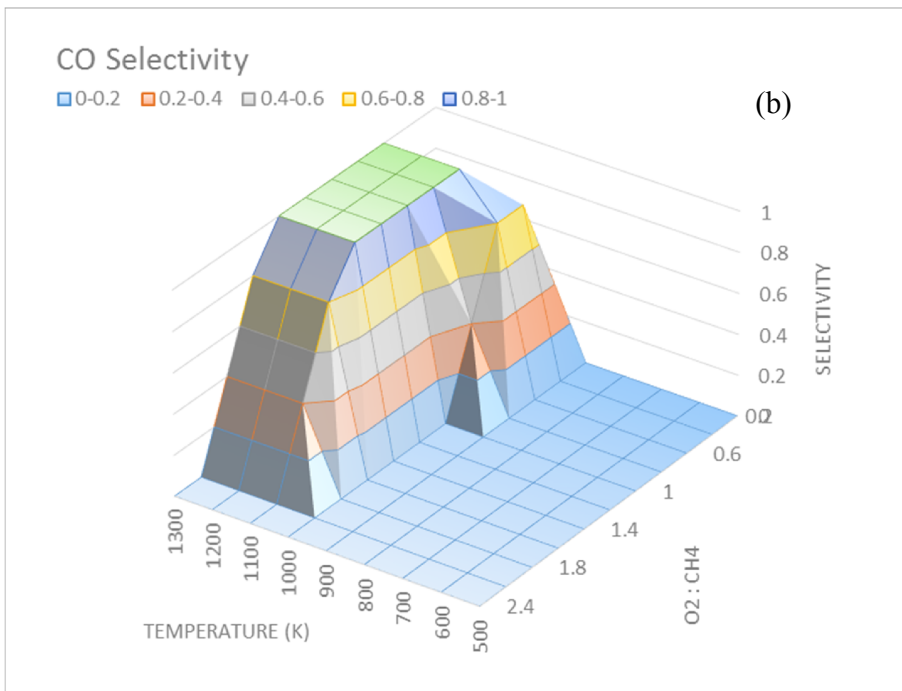


Figure 5:2 Equilibrium conversion and selectivity for partial oxidation of methane (continued)

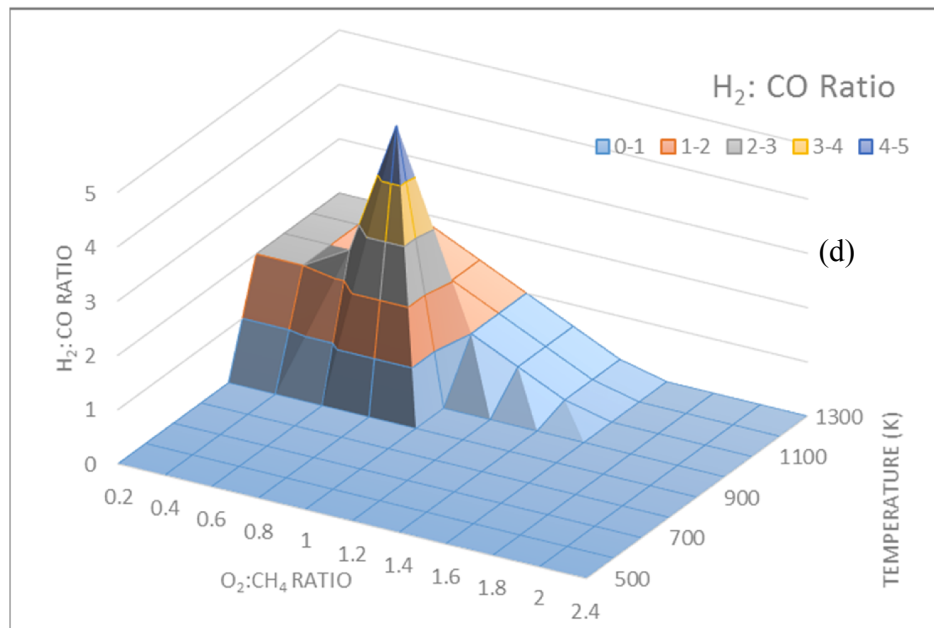


Figure 5:2 Equilibrium conversion and selectivity for partial oxidation of methane (continued)

### 5.1.1.3 Steam Reforming of Methane in the Presence of Cobalt

For steam reforming of methane, no reaction is observed below 800 K. With the stoichiometric feed, methane can be completely converted for temperature above 1000 K (Figure 5.3-a). CO<sub>2</sub> selectivity is found to be highest around 900 K and it decreases with increasing temperature (Figure 5.3-b). H<sub>2</sub>O and CH<sub>4</sub> can be converted completely to H<sub>2</sub> and CO above 1000 K and for stoichiometric feed, exit stream is practically composed of syngas only (Figure 5.3-c, d). It is also seen that expected H<sub>2</sub>: CO ratio is above three at around 1100 K (Figure 5.3-e). It should be noted that those results are found for atmospheric pressure.

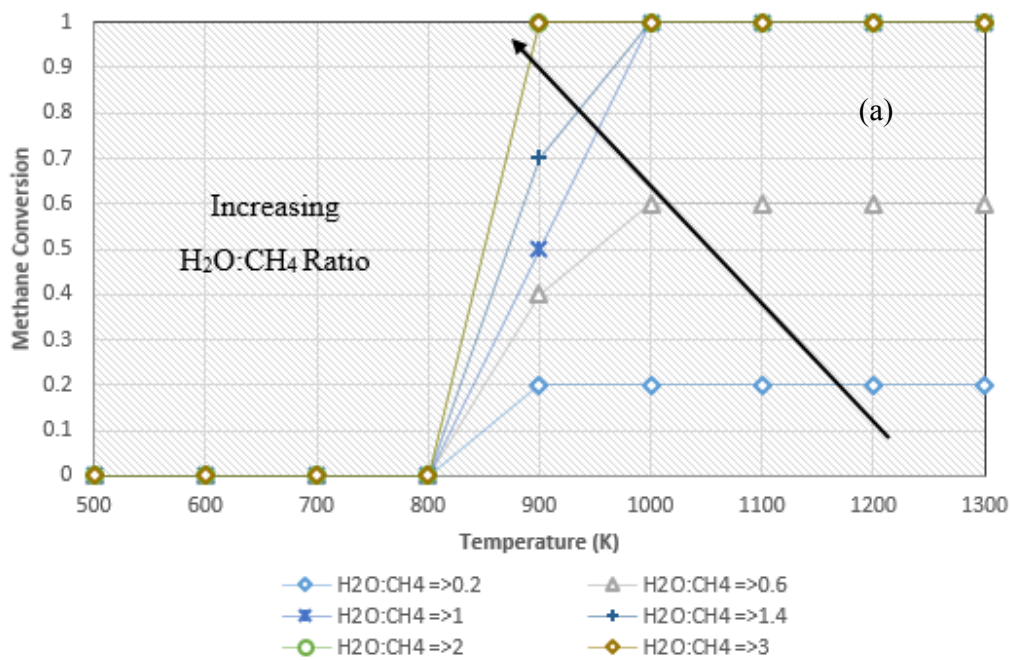


Figure 5.3 Equilibrium conversion and selectivity for steam reforming of methane

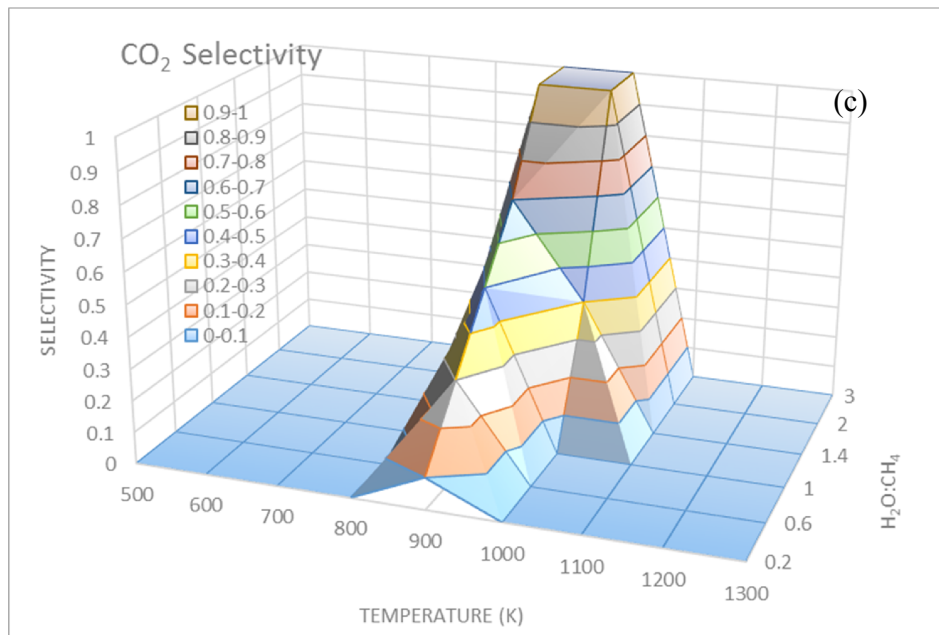
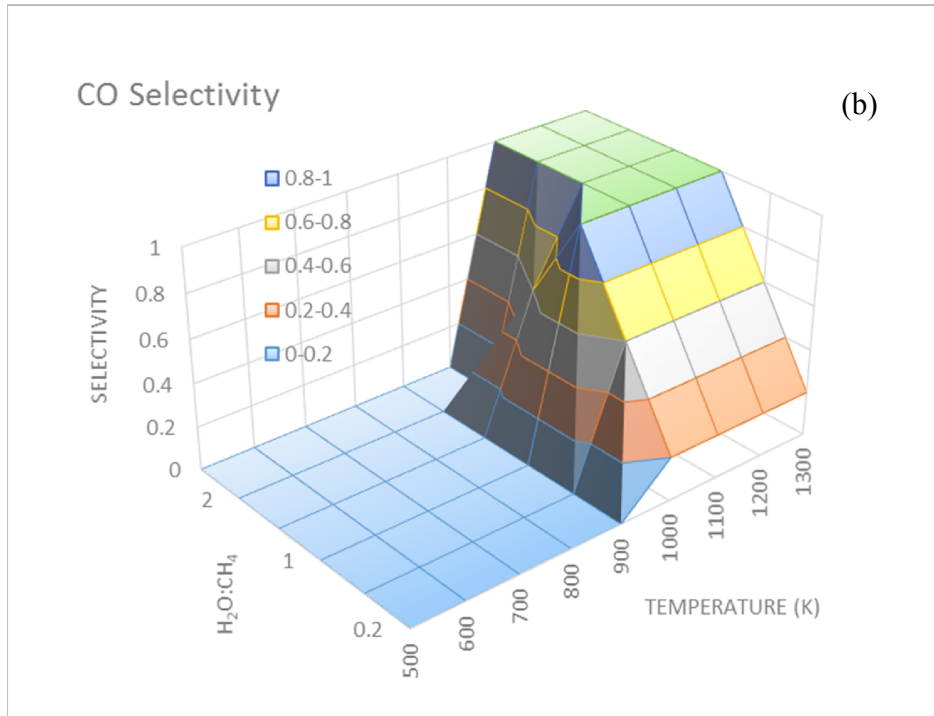


Figure 5:3 Equilibrium conversion and selectivity for steam reforming of methane (continued)

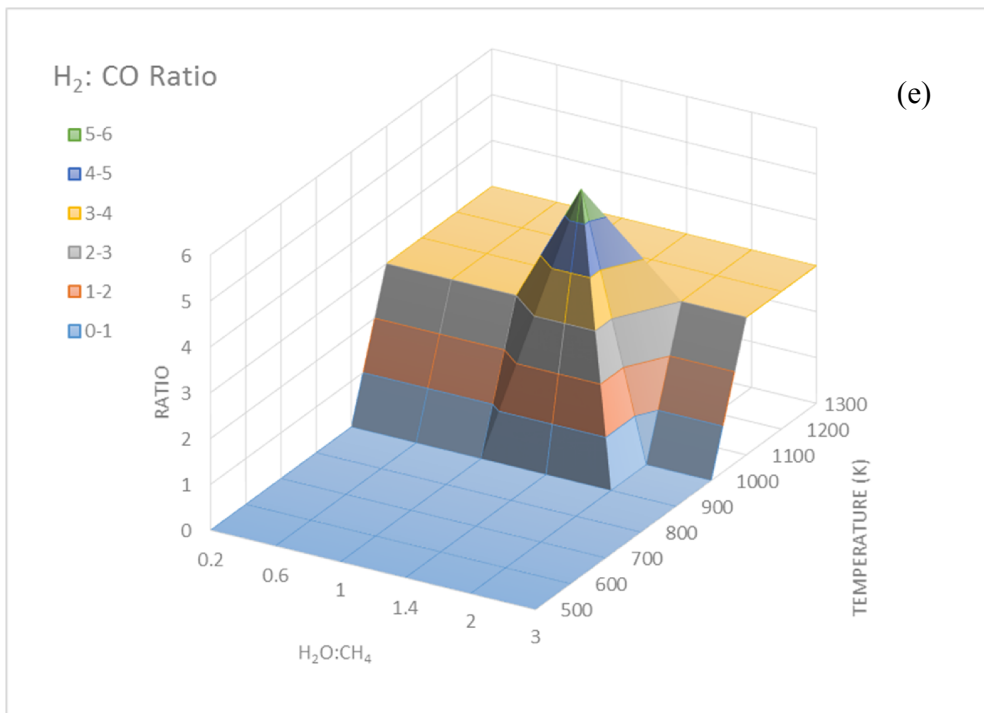
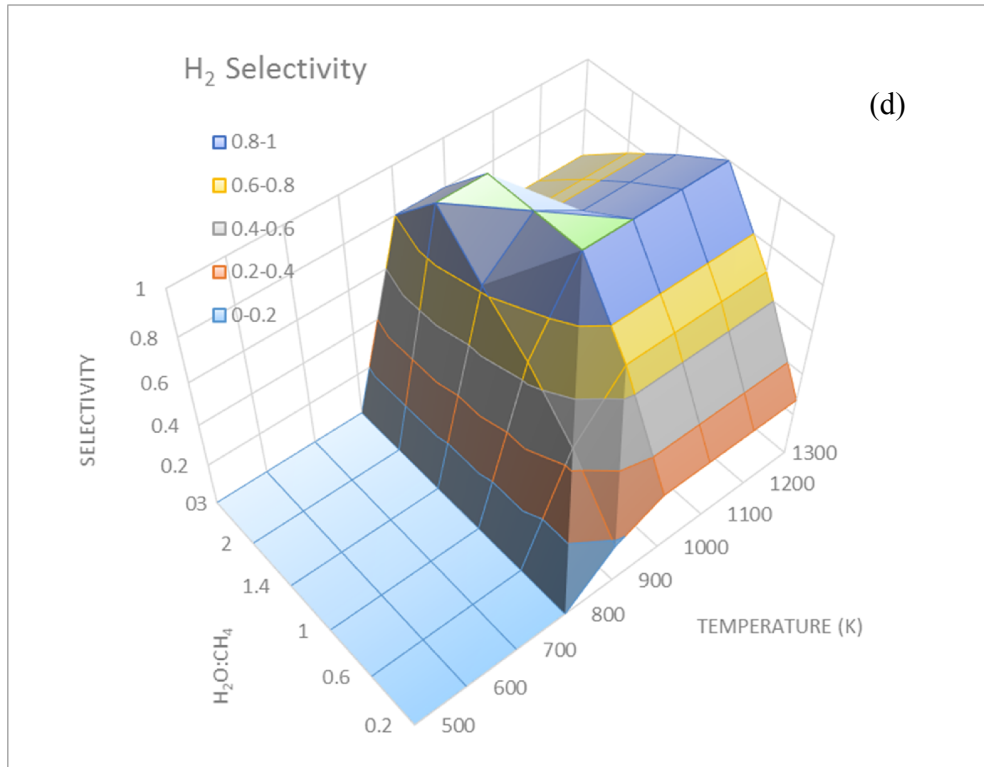


Figure 5:3 Equilibrium conversion and selectivity for steam reforming of methane (continued)

#### 5.1.1.4 Autothermal Thermal Reforming of Methane in the Presence of Cobalt

In this part, increasing the ratio of oxygen in autothermal thermal reforming of methane reactions for various water: methane ratios is investigated at different temperatures.

CO cannot be produced until temperatures reach around 1000 K and selectivity of CO is found to be shifting towards to higher temperature values compared to steam reforming reactions (Figure 5.4). On the other hand, CO<sub>2</sub> can be found in the product mixture even at 500 K and maximum selectivity is spotted to be around 900 K. No CO<sub>2</sub> is seen above 1000 K (Figure 5.5). Additionally, H<sub>2</sub> starts to be found at 900 K, where there is no CO and its selectivity is maximum around 1000 K. As O<sub>2</sub> amount increases, selectivity to H<sub>2</sub> decreases significantly (Figure 5.6). Methane is found to be converted completely after 900 K and CH<sub>4</sub> increases as O<sub>2</sub> amount increases for lower temperatures (Figure 5.7). As expected, as the oxygen amount increases, steam reforming reaction becomes less preferable and water conversion decreases (Figure 5.8). It should be noted that conversion increase of water and increase in CO<sub>2</sub> and H<sub>2</sub> selectivity signifies the effect of water gas shift reaction at those temperatures.

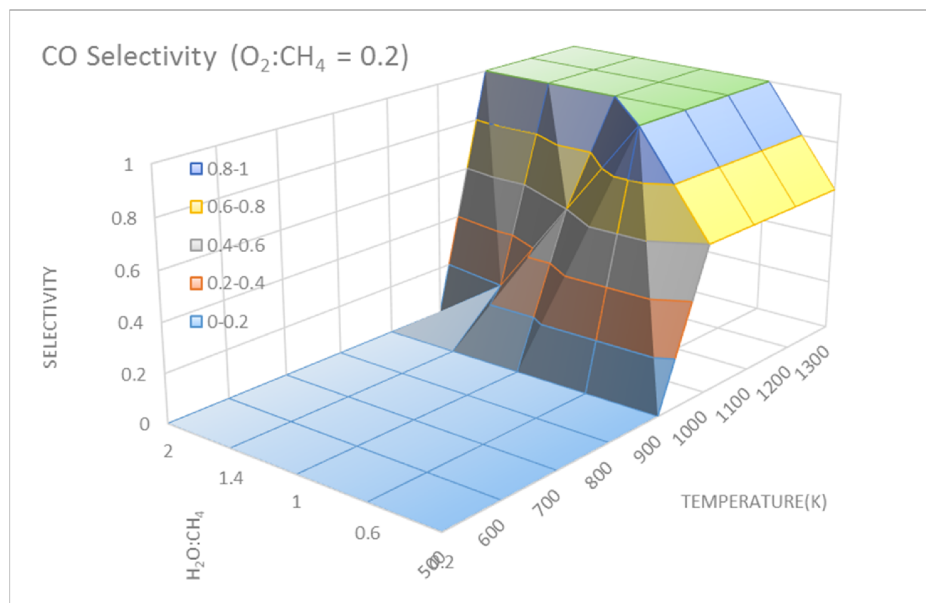


Figure 5:4 Effect of oxygen addition to CO selectivity in autothermal thermal reforming of methane

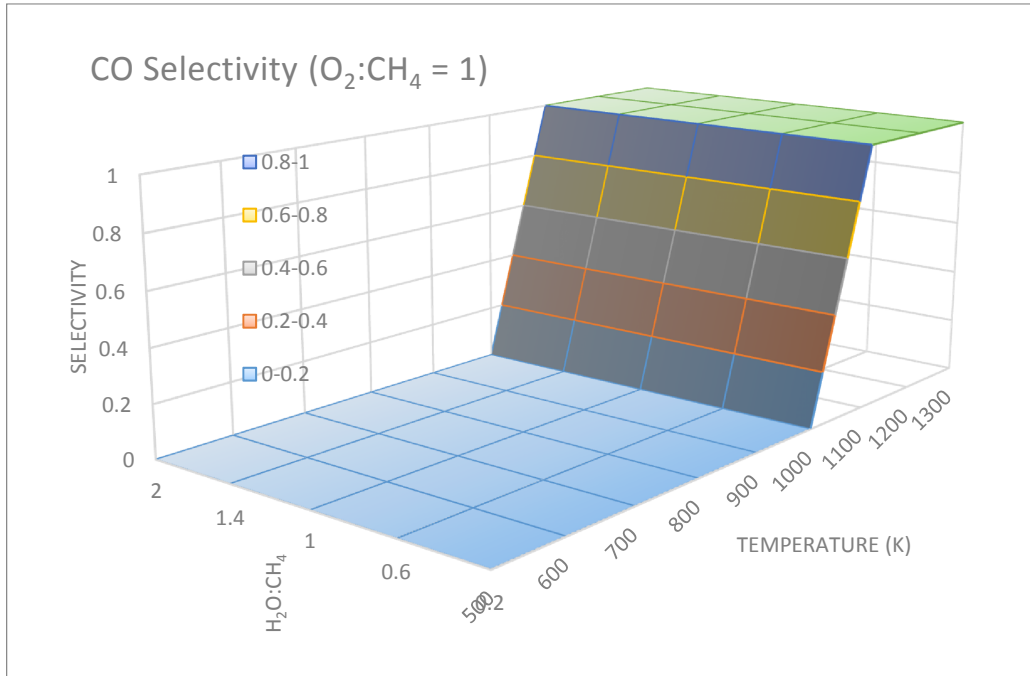
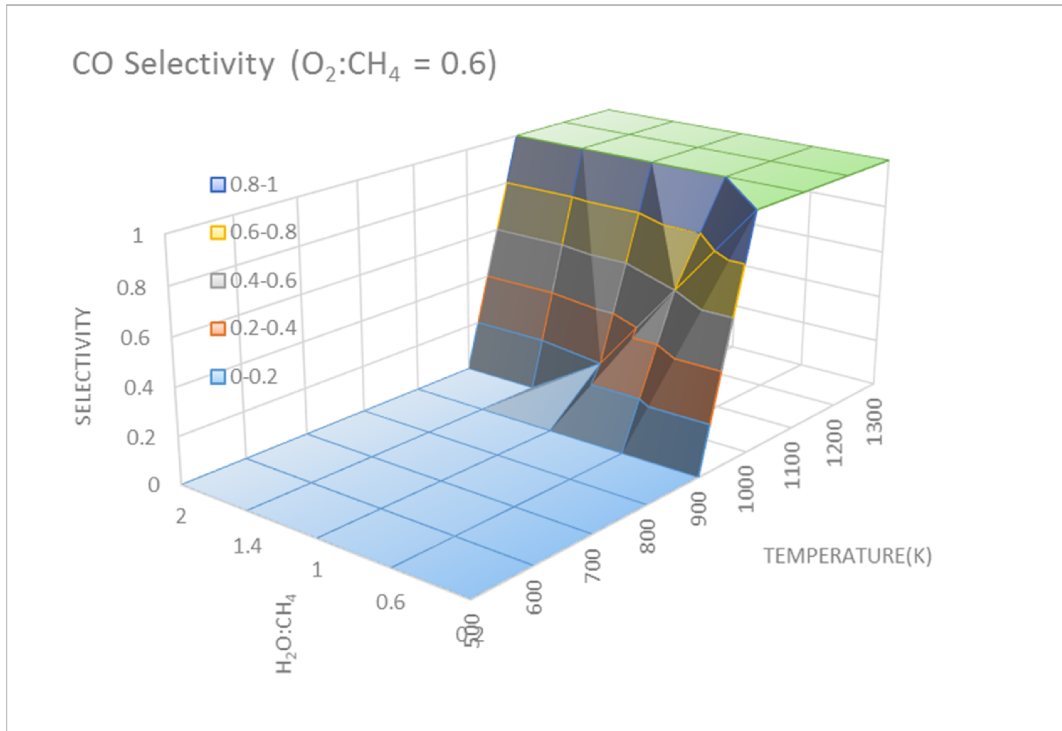


Figure 5:4 Effect of oxygen addition to CO selectivity in autothermal thermal reforming of methane (continued)

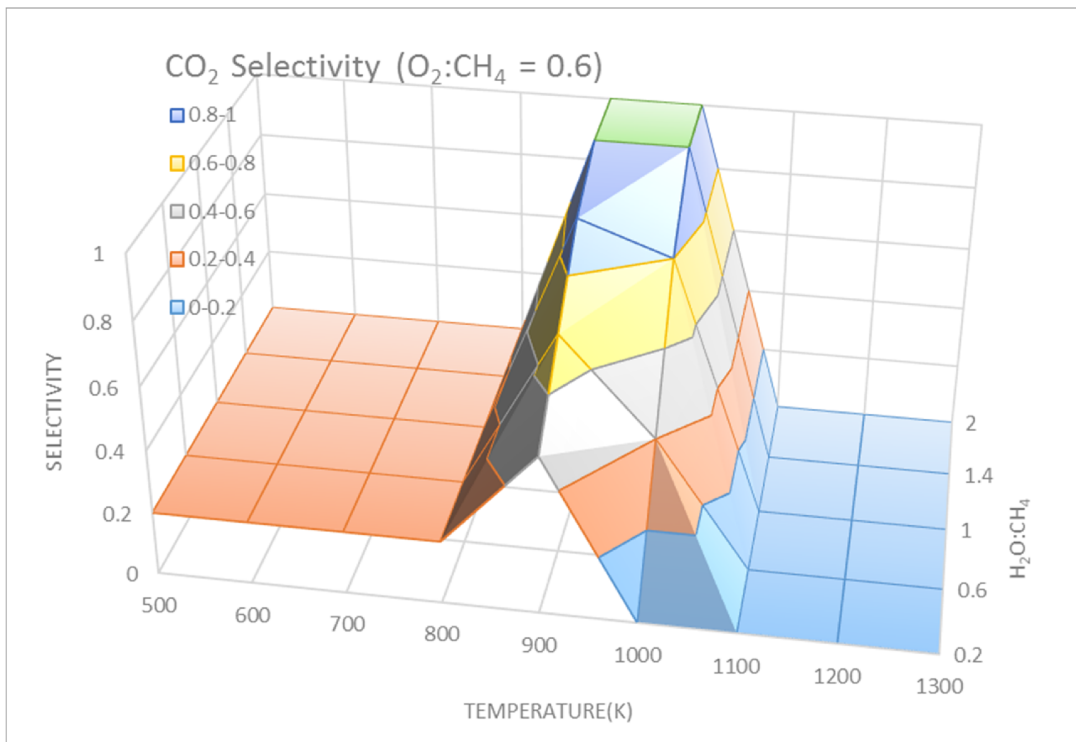
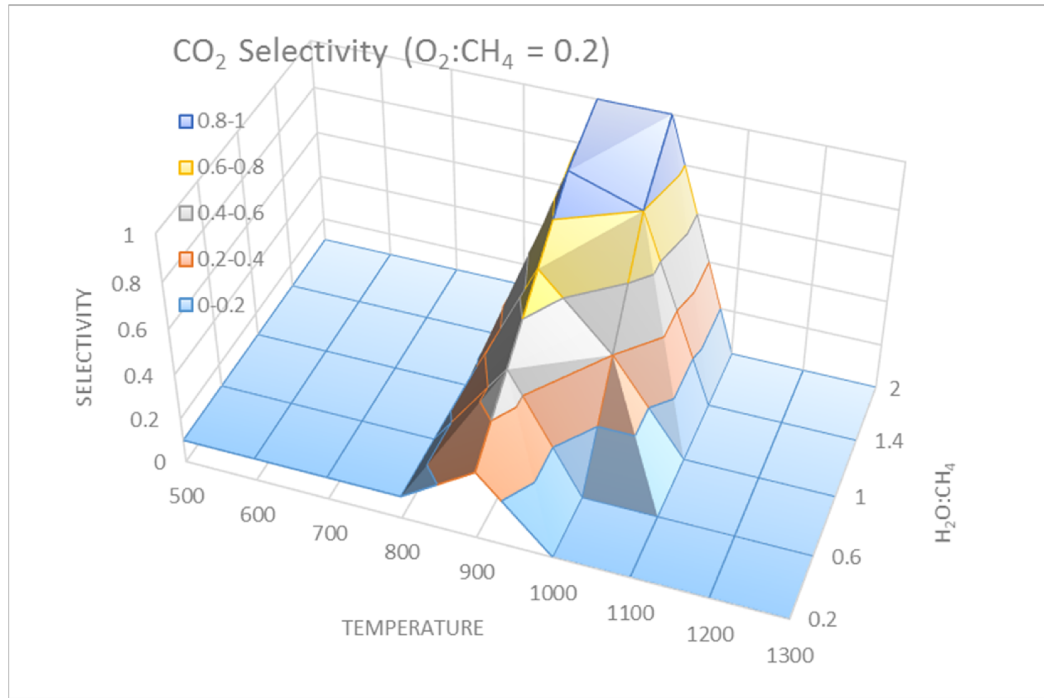


Figure 5:5 Effect of oxygen addition to CO<sub>2</sub> selectivity in autothermal thermal reforming of methane

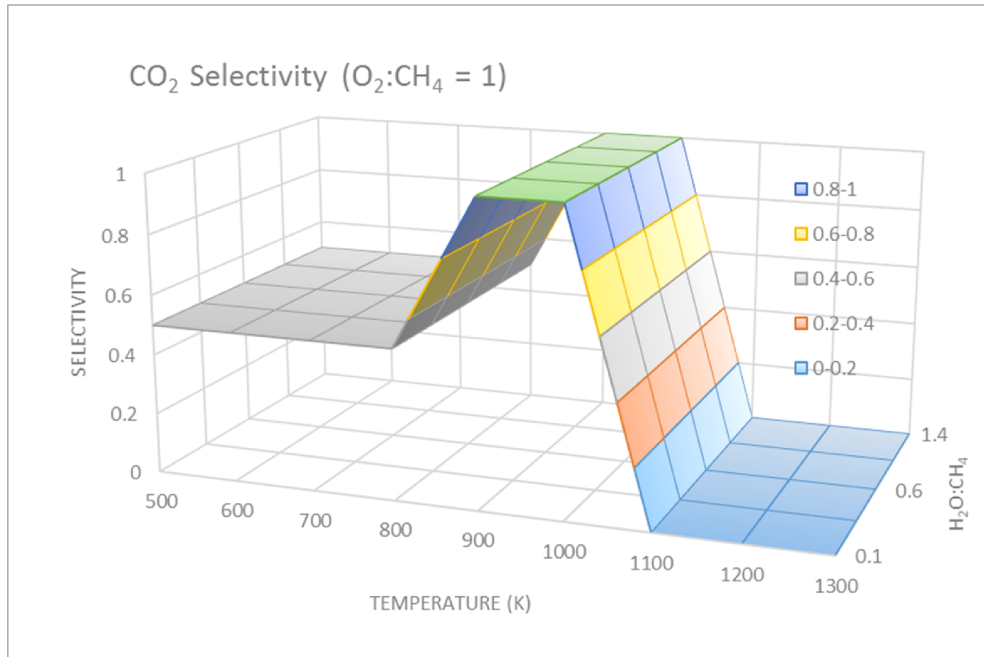


Figure 5:5 Effect of oxygen addition to CO<sub>2</sub> selectivity in autothermal thermal reforming of methane (continued)

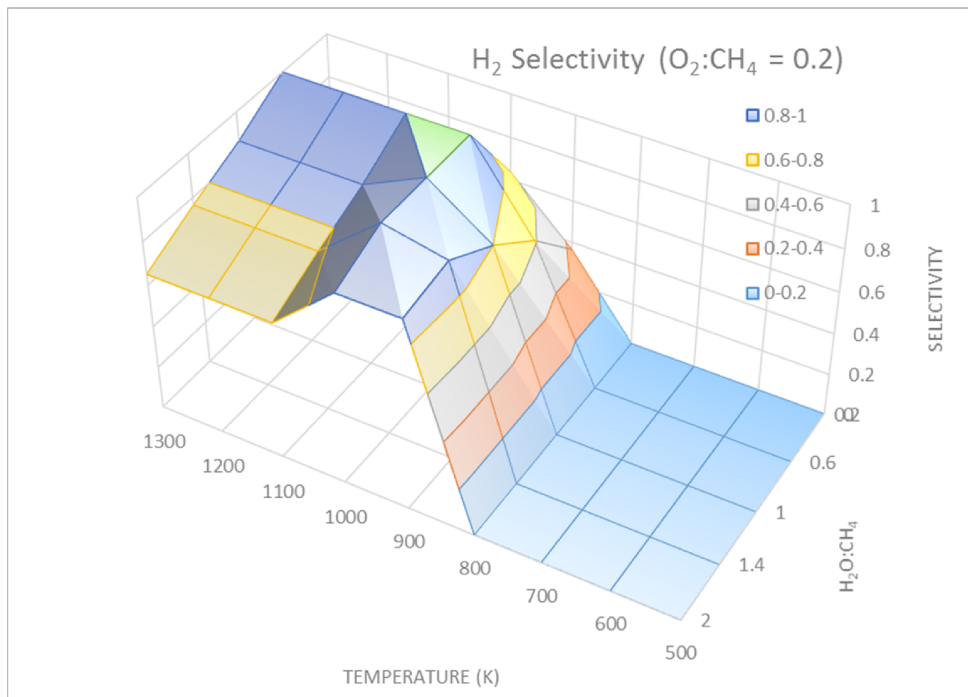


Figure 5:6 Effect of oxygen addition to H<sub>2</sub> selectivity in autothermal thermal reforming of methane

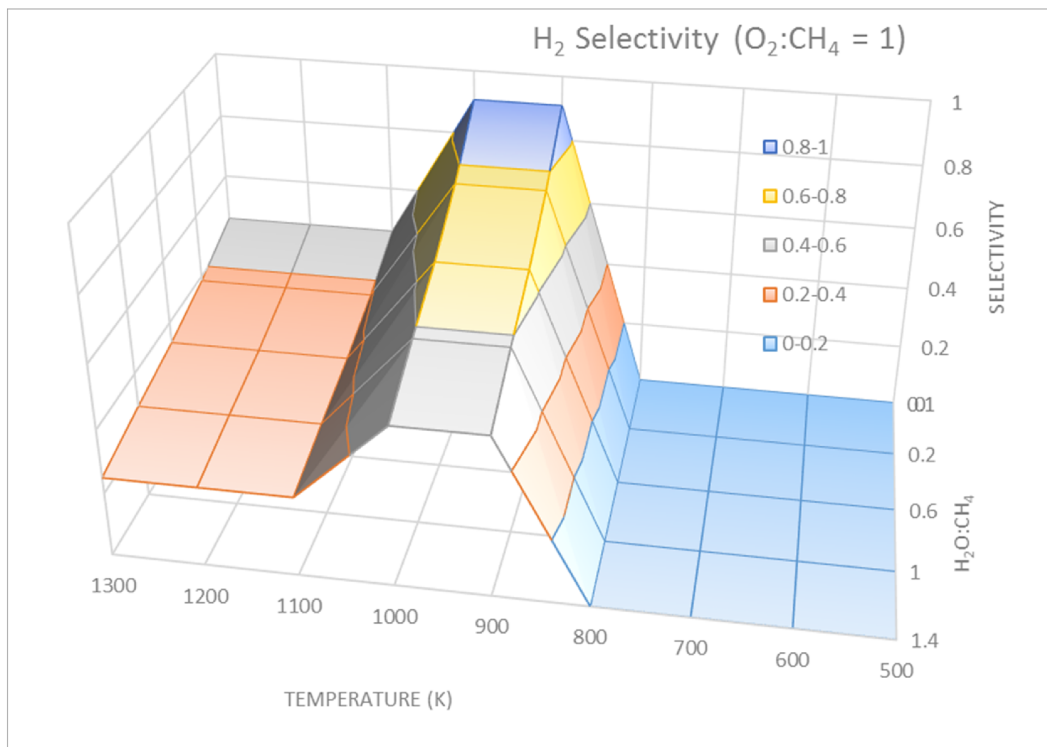
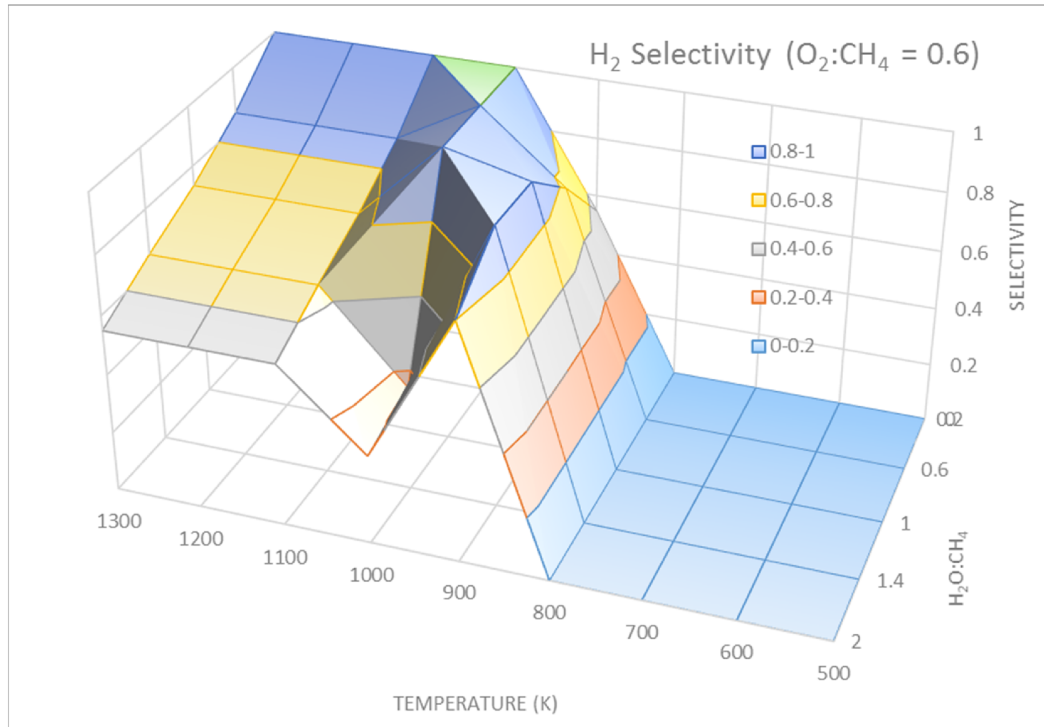


Figure 5:6 Effect of oxygen addition to H<sub>2</sub> selectivity in autothermal thermal reforming of methane (continued)

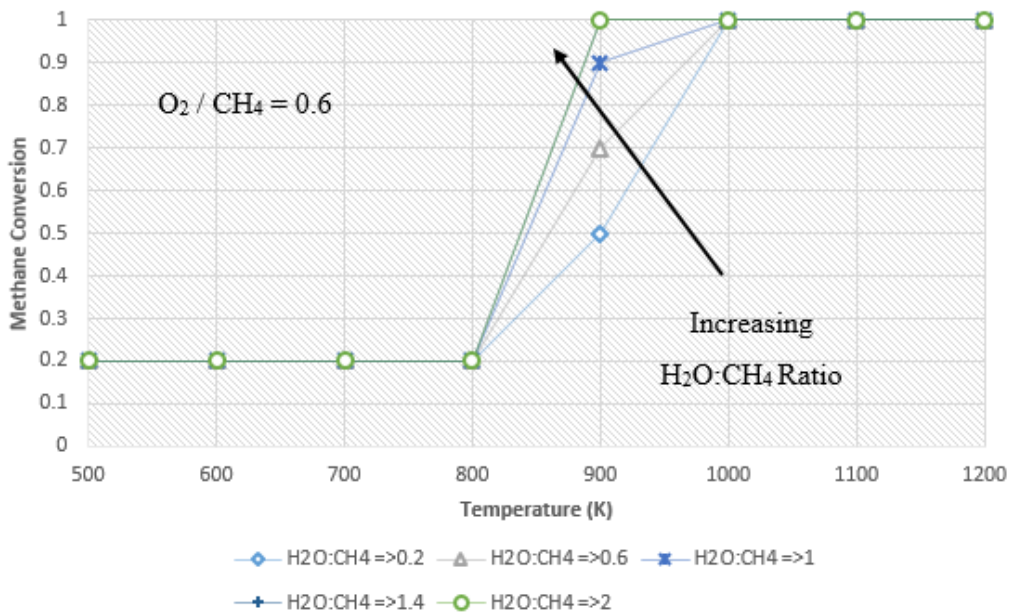
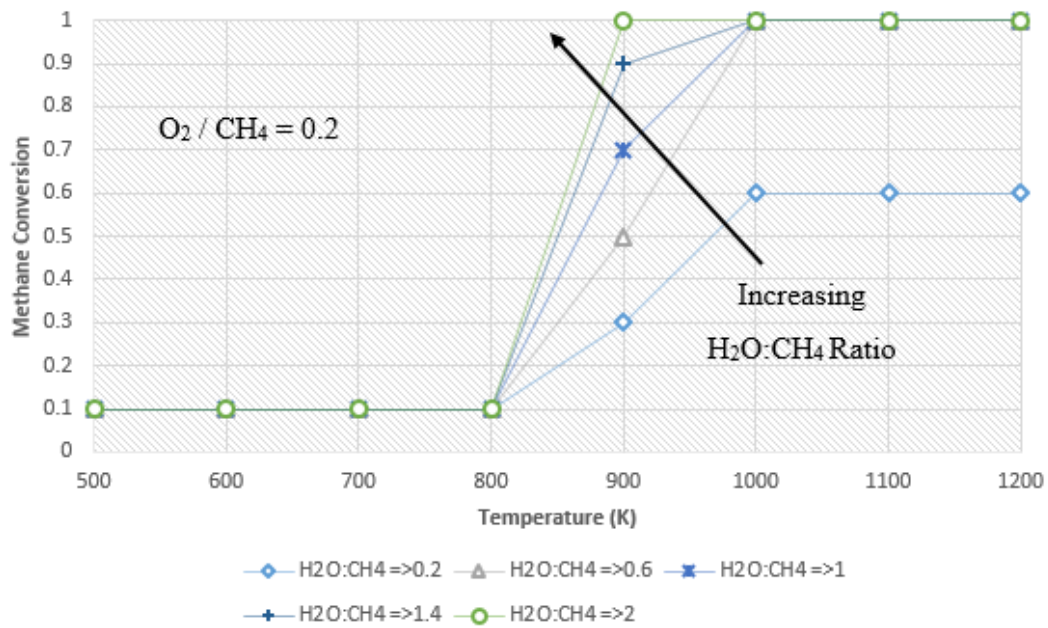


Figure 5:7 Effect of oxygen addition to methane conversion in autothermal thermal reforming of methane

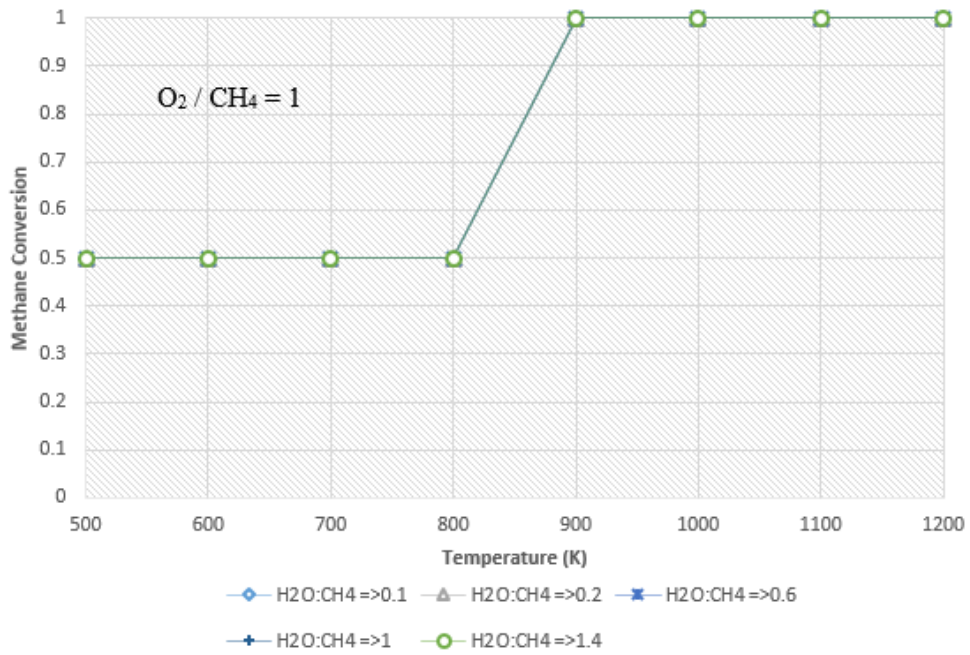


Figure 5:7 Effect of oxygen addition to methane conversion in autothermal thermal reforming of methane (continued)

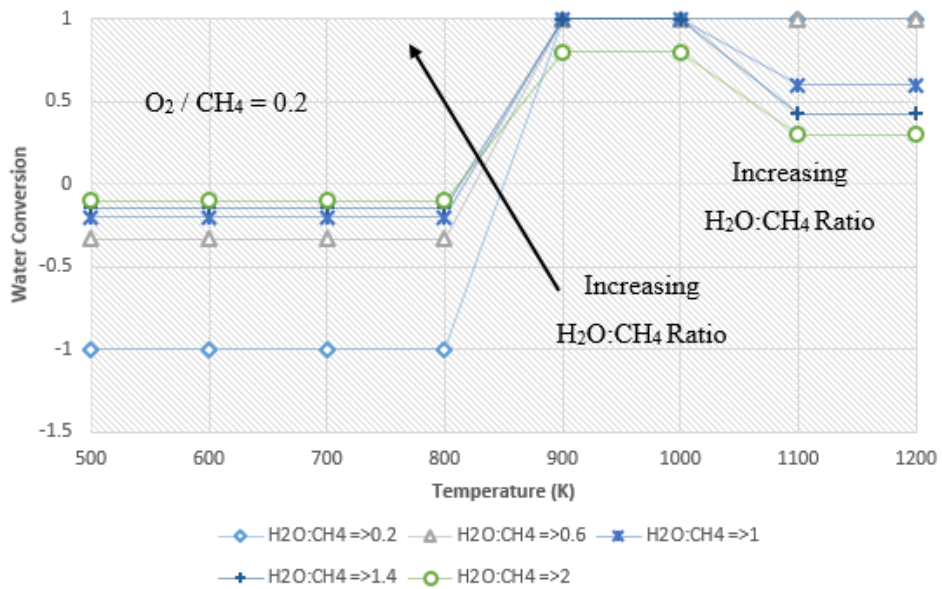


Figure 5:8 Effect of oxygen addition to water conversion in autothermal thermal reforming of methane

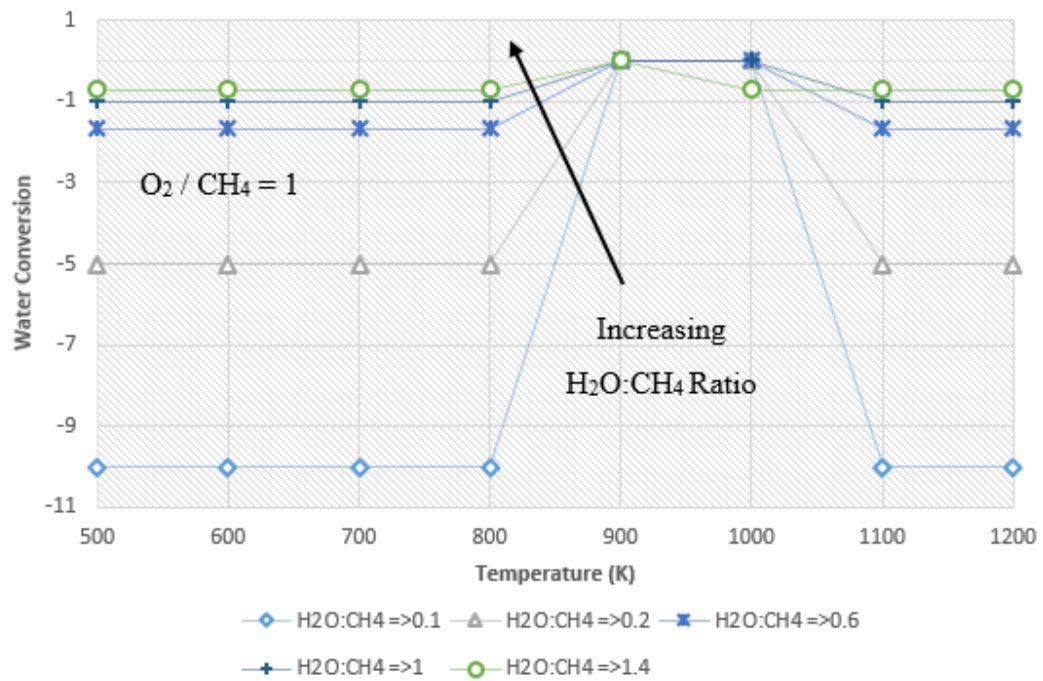
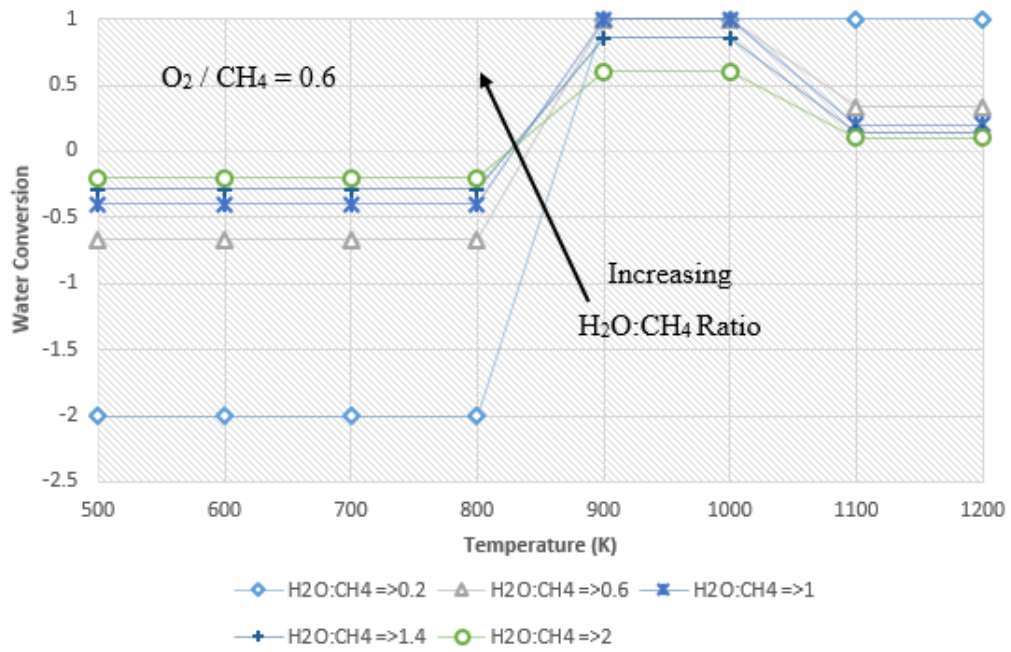


Figure 5:8 Effect of oxygen addition to water conversion in autothermal thermal reforming of methane (continued)

### 5.1.1.5 Concluding Remarks

Objective of this section was to define a method which accurately estimates the product distribution for syngas production from methane and it was shown that thermodynamic equilibrium of gaseous products can provide that information. To do so, *Gibbs Free Energy Minimization* was selected as the method of the analysis. It was found that ratio of the produced H<sub>2</sub> to CO is strongly dependent on the oxygen source and partial oxidation is favorable as it gives a ratio of around 2. In addition to that, the operating temperature is to be kept high for reasonable methane conversions. The most critical point here is the ratio of oxygen to methane and it has to be sub-stoichiometric or at least around stoichiometric for selective operation, which can indeed be ensured by membrane reactors. Autothermal reforming seems to be combining the advantages of both methods when the oxygen ratio is kept small. Based on the results presented above, it can be said that for a temperature of operation around 1000 K, auto thermal reforming with a sub-stoichiometric oxygen feed to the medium may give selectivities of CO and H<sub>2</sub> around 100% with a complete methane conversion.

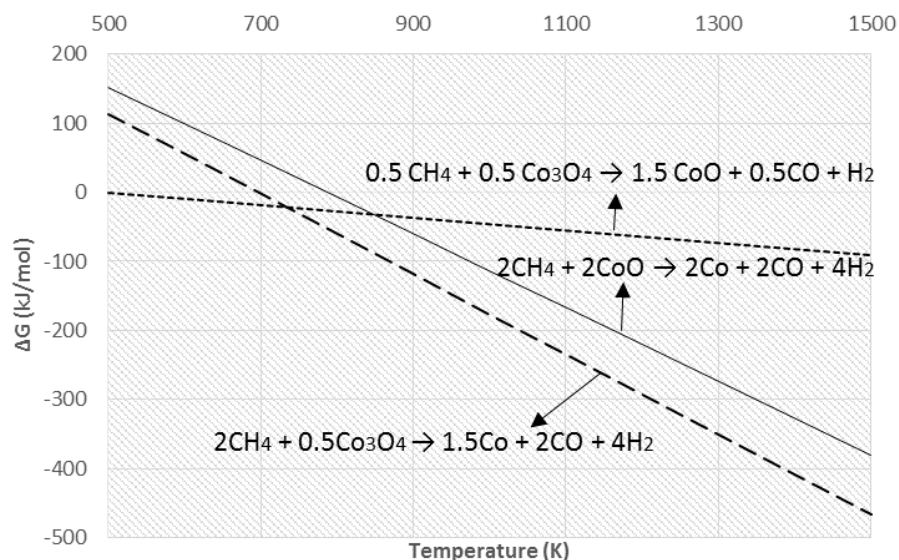


Figure 5:9 Free energy comparison of syngas production reaction when oxygen is supplied from cobalt oxide

Another important result is the state of cobalt at the thermodynamic equilibrium under steam reforming / methane oxidation conditions. It was found that cobalt is not oxidized until all available hydrogen and carbon are totally combusted in the environment for almost the entire range studied. Based on this result, it can be claimed that cobalt can be kept in the metallic form if thermodynamic equilibrium is achieved. That argument can be illustrated with the free energy analysis given in Figure 5:9. It was found that Co remains in metallic phase for temperatures above ~800 K for both CoO and Co<sub>3</sub>O<sub>4</sub> phases.

That result becomes particularly important if a membrane reactor arrangement is considered to be used. If the surface contacting with methane is said to be at thermodynamic equilibrium for a temperature of operation around 1000 K (see Figure 5:10), surface cobalt is expected to give any oxygen transported from the bulk by diffusion to methane. That outcome will be further investigated in part 5.4.3 from the mass and heat transfer limitations perspective.

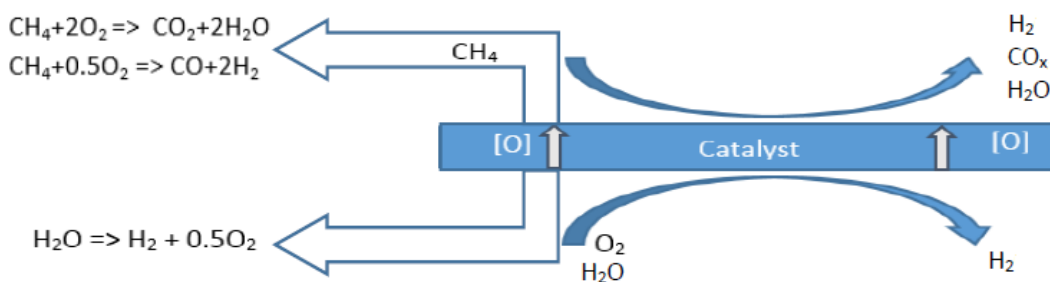


Figure 5:10 Schematic representation of a membrane reactor for syngas production

### 5.1.2 Possibility of Syngas Production from CO<sub>2</sub> and H<sub>2</sub>O over Cobalt Oxide

Phase transitions of the selected metal oxide between different oxidative states give important clues about the equilibrium limits for the reduction and oxidation reactions; oxygen storage capabilities and their reducibility under different atmospheric conditions. In this part, this was investigated via predominance diagrams from the collected data for different temperatures given in the Appendix A. Then, the possibility of producing CO and H<sub>2</sub> over that reduced oxide is shown with the same method at various temperatures.

As the starting point, phase transitions between those oxides are shown as a function of temperature and pressure as given below. It was easily seen that given plot is remarkably consistent with the analysis presented in part 5.1.1 and TGA results given in part 5.2.3. The diagram demonstrates that Co<sub>3</sub>O<sub>4</sub> can be reduced to CoO at temperatures around 800-900 °C based on the oxygen partial pressure. It also shows that a cycle between Co and CoO is not practically possible as it requires very high temperatures.

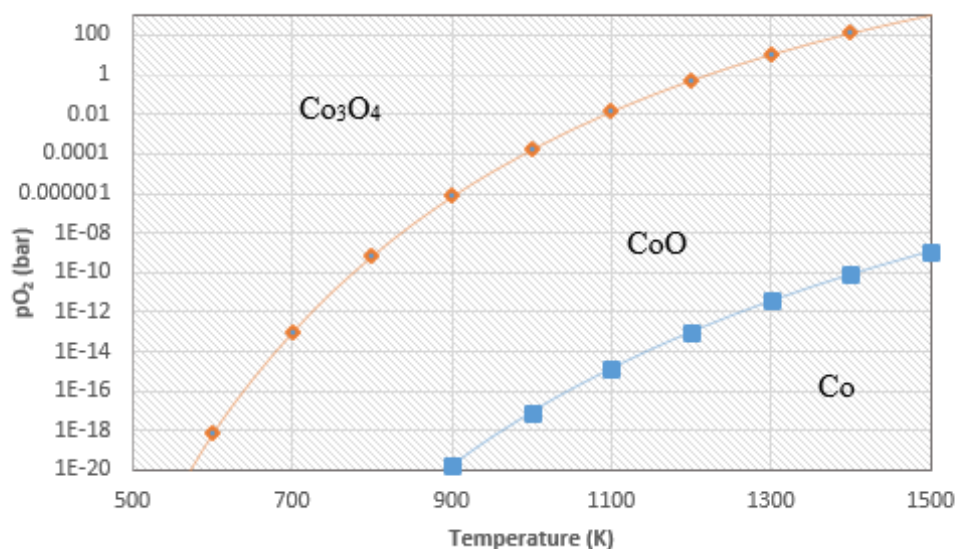


Figure 5:11 Cobalt oxide phase transitions in oxygen environment at various temperatures and pressures

Equilibrium partial pressures for CO produced from CO<sub>2</sub> was determined at 500 K, 1000 K and 1200 K and results are given below. The first thing noticed is the cycle between Co and CoO seems like a better choice yet it not feasible as it requires very high reduction temperatures and CO partial pressures obtained are found to be low for the spinel-FCC cycle. Yet those calculations are based on bulk thermodynamics. Surface oxidation reactions may exhibit quite differently as stated in the previous sections and may not be limited by the gaseous bulk thermodynamics. At this point, that result can be said to be satisfactory, which is proven to be accurate with the experimental results given in the next section. Same is also valid for water splitting reaction.

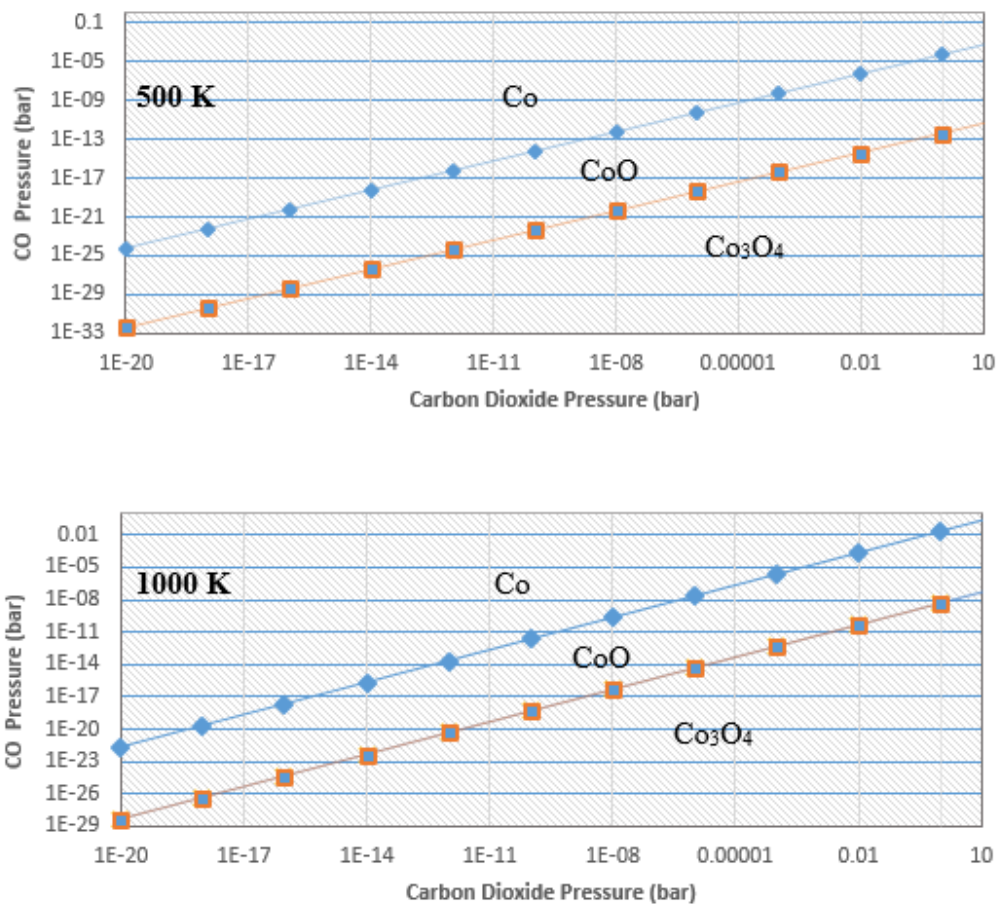


Figure 5:12 CO-CO<sub>2</sub> equilibrium for cobalt oxidation reactions for various pressures at 500, 1000 and 1200 K

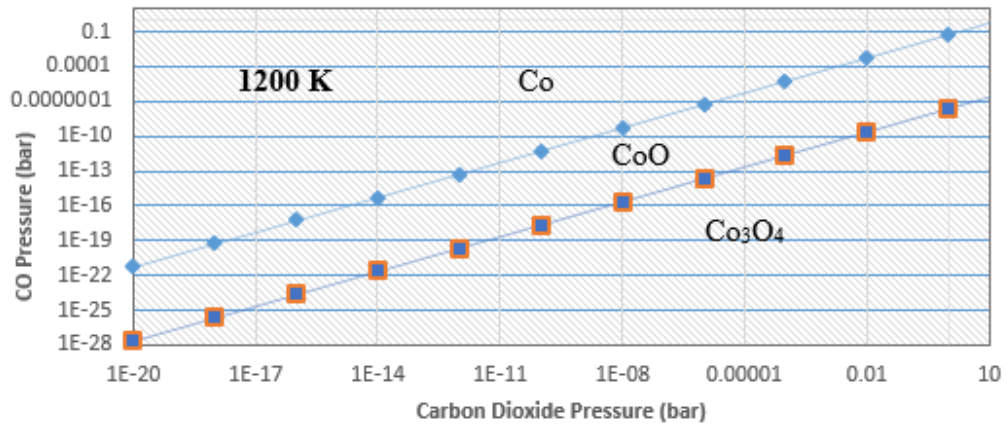


Figure 5:12 CO-CO<sub>2</sub> equilibrium for cobalt oxidation reactions for various pressures at 500, 1000 and 1200 K (continued)

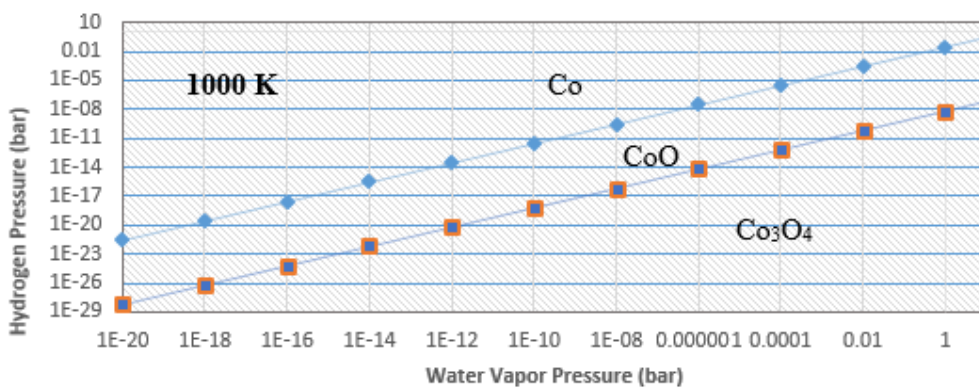
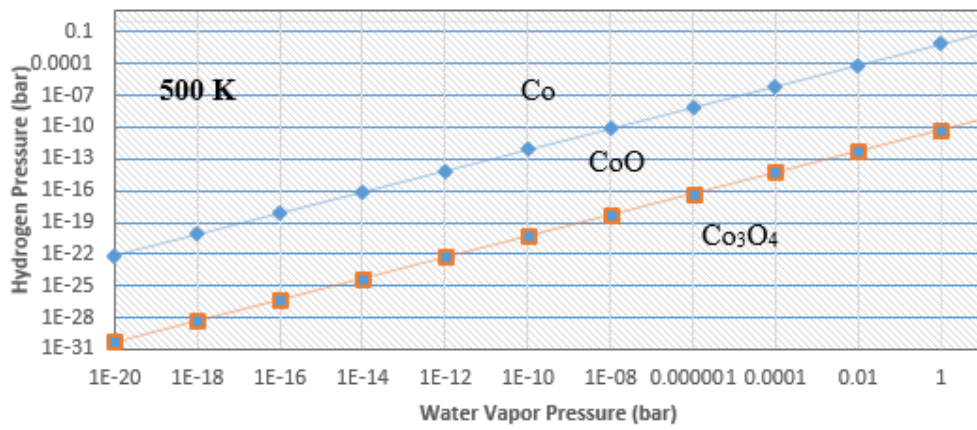


Figure 5:13 H<sub>2</sub>O-H<sub>2</sub> equilibrium for cobalt oxidation reactions for various pressures at 500, 1000 and 1200 K

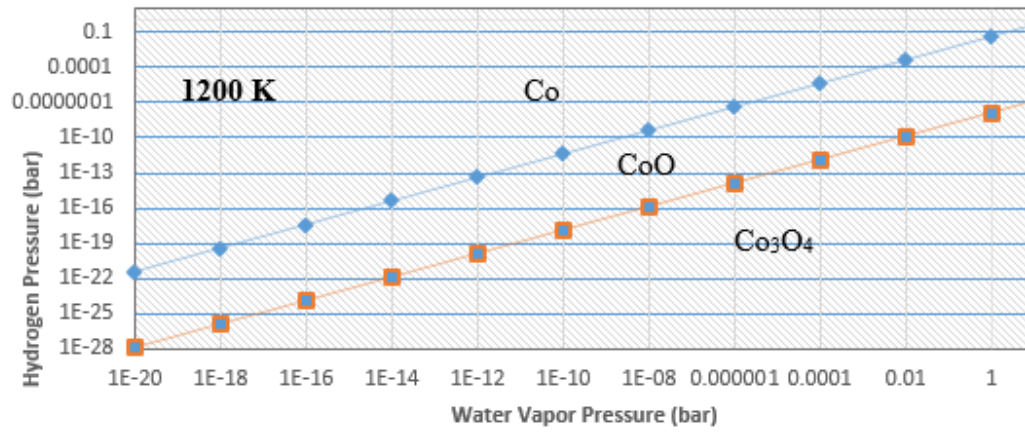


Figure 5:13 H<sub>2</sub>O-H<sub>2</sub> equilibrium for cobalt oxidation reactions for various pressures at 500, 1000 and 1200 K (continued)

## 5.2 Experimental Results

In thermodynamic analysis, it has been shown that cobalt oxide is a significant candidate for syngas production from methane or from carbon dioxide and water. In this section, experimental evidence on reduction and oxidation reactions for thermochemical syngas production from carbon dioxide and water is presented.

### 5.2.1 Material Characterization

Technical grade cobalt oxide was firstly analyzed via X-ray fluorescence (XRF). Cobalt oxide was found to be 97.1 % (mass) where the rest is MgO, Al<sub>2</sub>O<sub>3</sub>, SiO<sub>2</sub>, SO<sub>3</sub>, CaO, Cr<sub>2</sub>O<sub>3</sub>, MnO, Fe<sub>2</sub>O<sub>3</sub>, NiO, CuO, ZnO, MoO<sub>3</sub> and PbO in trace amounts.

All samples prepared for further analysis via BET (CA-0913-0- CA-0913-4) were also examined with X-ray diffractometer for scattering angle between 5° to 90°. Diffraction lines were compared with literature [90-92] and it is seen that all characteristic peaks namely 31.4°, 36.9°, 44.9°, 59.5° and 65.4° were detected in all samples as seen in Figure 5:14

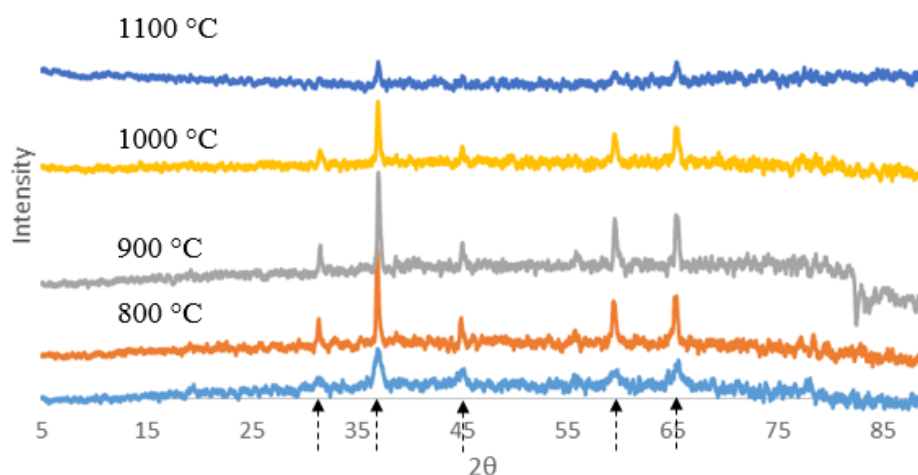


Figure 5:14 XRD patterns for Cobalt oxide samples

XRD patterns of those samples show that heat treatment in oxidizing atmosphere can change the morphology of the material. As the calcination temperature increases, size of the crystallites changes. Calcination increases the size to 30 nm and 32 nm from 10 nm for heat treatment at 800 °C and 900 °C respectively. After the phase change temperature (~940 °C), further increase in calcination temperature causes a noticeable decrease in size to 27 nm and 23 nm for 1000 °C and 1100 °C. It may be also stated that ratio of the highest peak (222) /2<sup>nd</sup> highest peak (440) and highest peak (222) /3<sup>rd</sup> highest peak (511) decrease with increasing calcination temperature.

Sample CA-0913-1 was selected as the candidate material to see any possible time effects. XRD analysis of that sample and a freshly prepared sample CA-0913-1(2) was done after three months from the initial measurement to compare with its three months old pattern. It was seen that relative magnitudes of the highest three characteristic peaks (38.5°, 59.5° and 65.4°) do not change for those three results, as seen in Figure 5:15.

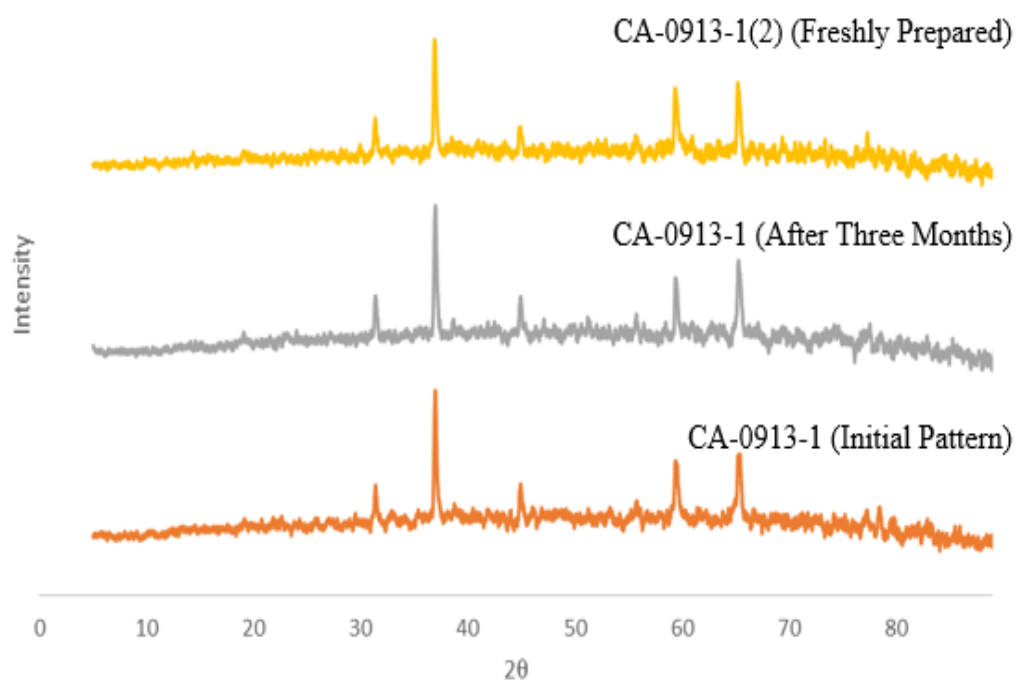
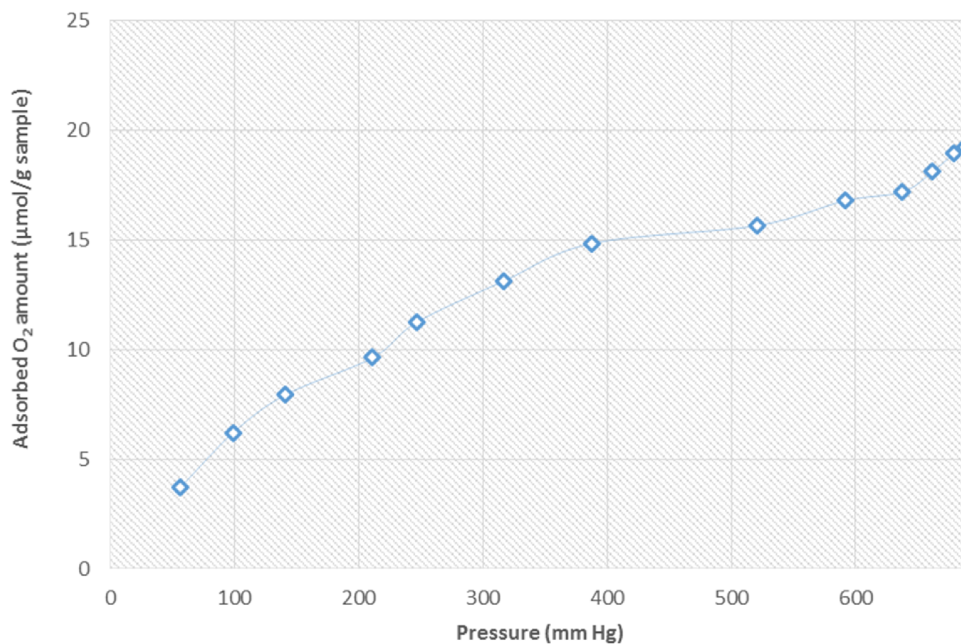


Figure 5:15 XRD patterns for sample CA-0913-1 before and after three months

## 5.2.2 Adsorption-Desorption of Oxygen on Cobalt Oxide

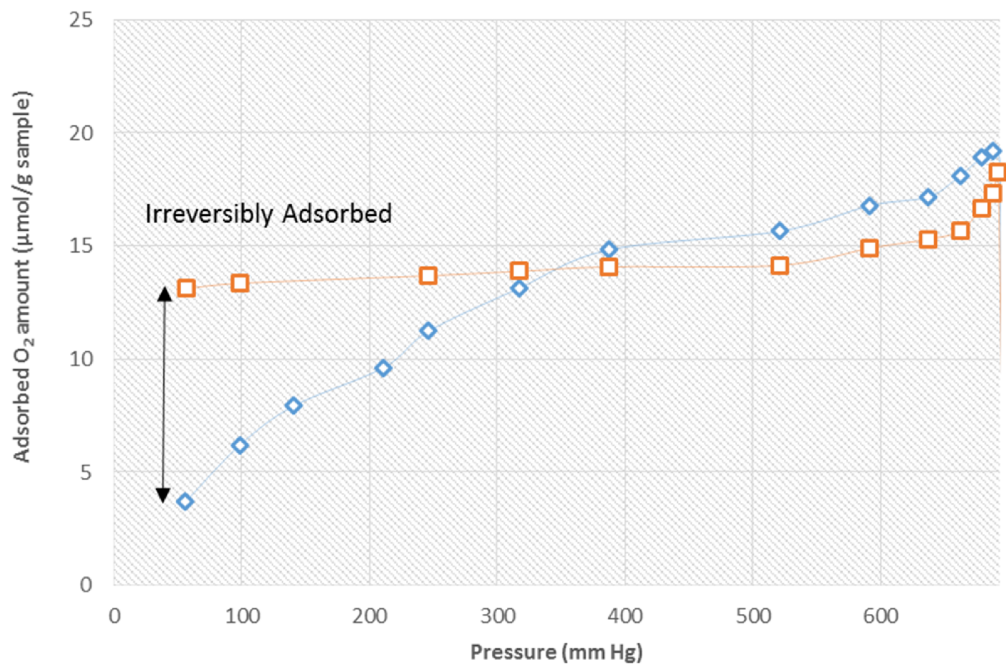
Samples are then analyzed via BET, which is normally used to measure the surface area of a given substance, to obtain adsorption-desorption isotherms for oxygen. Instead of using it with nitrogen, experiments were done by introducing oxygen at room temperature and the following results are obtained.

Results are tabulated below for three consecutive adsorption desorption cycles as explained in the experimental methods to find out how the amount of irreversibly adsorbed oxygen changes when sample is subjected to high temperatures. Adsorption-desorption isotherms for CA-0913-1(2) is given in Figure 5.16 as an example. Oxygen was introduced to the sample gradually until the pressure reaches to 688 mmHg (Figure 5.16-a). Sample chamber was then vacuumed and it was seen that some of the oxygen was irreversibly adsorbed on the oxide (Figure 5.16-b). Same procedure was repeated for two more times (Figure 5.16-c, d).

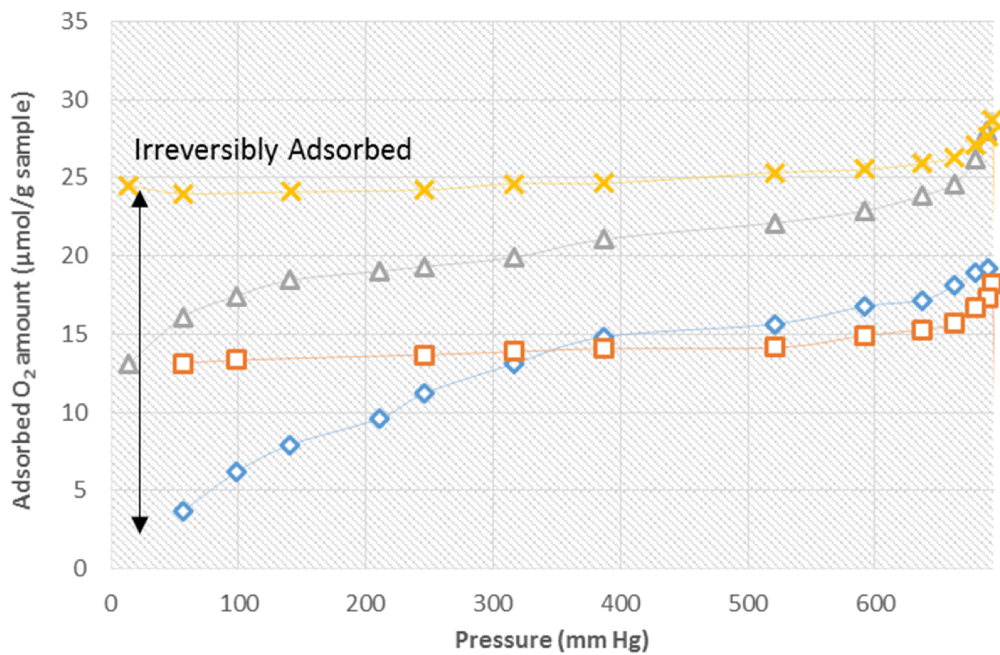


*a. First adsorption isotherm*

Figure 5:16 Irreversible adsorption of oxygen on cobalt oxide

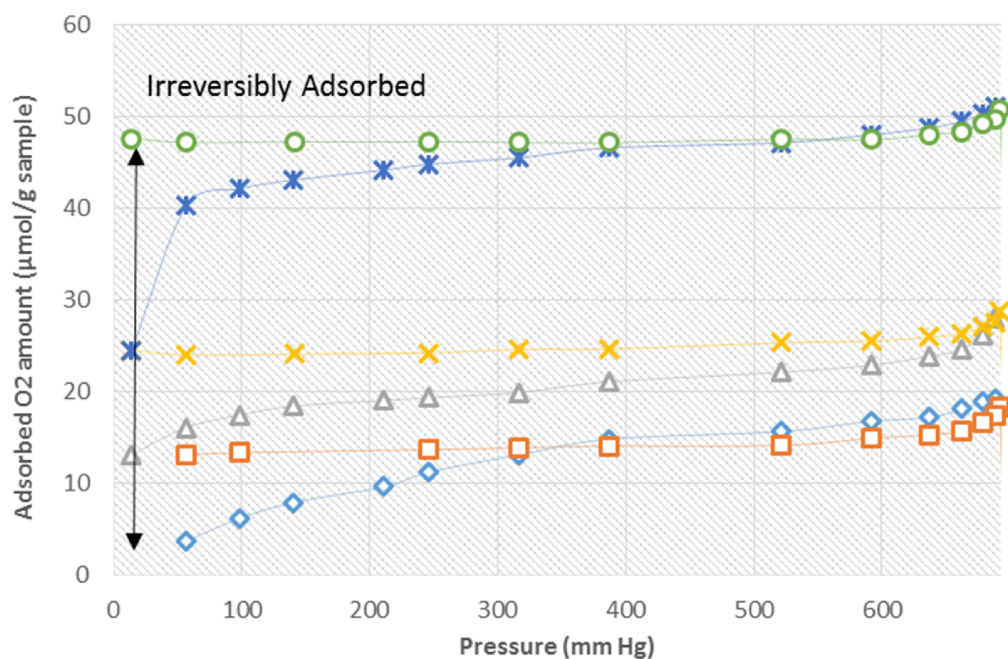


*b. End of first adsorption-desorption cycle*



*c. End of second adsorption-desorption cycle*

Figure 5:16 Irreversible adsorption of oxygen on cobalt oxide (continued)



*d. End of third adsorption-desorption cycle*

Figure 5:16 Irreversible adsorption of oxygen on cobalt oxide (continued)

Table 5:2 Irreversibly Adsorbed O<sub>2</sub> on Co<sub>3</sub>O<sub>4</sub> samples after three adsorption-desorption cycles

<b>Sample</b>	<b>Calcination Temperature (°C)</b>	<b>Irreversibly Adsorbed O<sub>2</sub> (μmol)/gsample</b>
CA-0913-0	-	11.56
CA-0913-1	800	9.14
CA-0913-2	900	8.31
CA-0913-3	1000	2.65
CA-0913-4	1100	~0
CA-0913-1(2)	800	47.57

At the first glance, it is seen that as the calcination temperature increases, the ability to adsorb oxygen irreversibly decreases (note that sample CA-0913-0 was not subjected to heat treatment). However, those BET analyses could not be performed just after the calcination. To be on the safe side, analysis was repeated for the sample CA-0913-1 and BET analysis was done just after the calcination process (named as CA-0913-1(2)). As given in the table, amount of irreversibly adsorbed O<sub>2</sub> was found to be about four times higher than the untreated sample. This result actually give important hints on the effect of heat treatment on the cobalt oxide. As shown in the XRD analysis, those two samples have identical peaks and intensities indicating that there is not a structural difference. It can be argued that the difference may be due to the relative amount of oxygen deficiencies on the surface of the material. At those high temperatures, some of the surface oxygen is expected to be removed and those vacancies can be filled up with atmospheric oxygen in time. At this point, the question of how the sample CA-0913-1 then can adsorb oxygen after 3 months is to be asked. A probable answer might be the difference in oxygen pressures of BET experiment (100% O<sub>2</sub>) and the atmosphere itself (21% O<sub>2</sub>). In fact, when the adsorbed amount of oxygen was checked for sample CA-0913-1, there is no significant amount of adsorption until O<sub>2</sub> pressure reaches to ~0.21 atm while it certainly increases for CA-0913-1(2), as seen in Appendix C.1.

Those coarse results indicate that significant increase in lattice vacancy can be expected for a reactor with cobalt oxide operating at temperatures around 800 °C, which can be used for CO<sub>2</sub> and H<sub>2</sub>O reduction in short contact time operations even in an oxidative environment; that is even if there is no phase change.

### 5.2.3 Thermal Decomposition of Cobalt Oxide

TGA analysis gives evidence about the possible phase change of cobalt oxide as well as the necessary data to be used in kinetic analysis.



$$\frac{\text{CoO}}{\text{Co}_3\text{O}_4} \sim 93.35 \% \text{ wt}$$

That phase change was found to occur at around 940 °C for oxidizing atmosphere which can also be shown by the phase change equilibrium curve as shown in the thermodynamic analysis. Phase change in N<sub>2</sub> atmosphere occurs at temperatures lower than the oxidizing atmosphere. It is found that mass loss is 99.9% same with the one calculated from stoichiometric calculations.

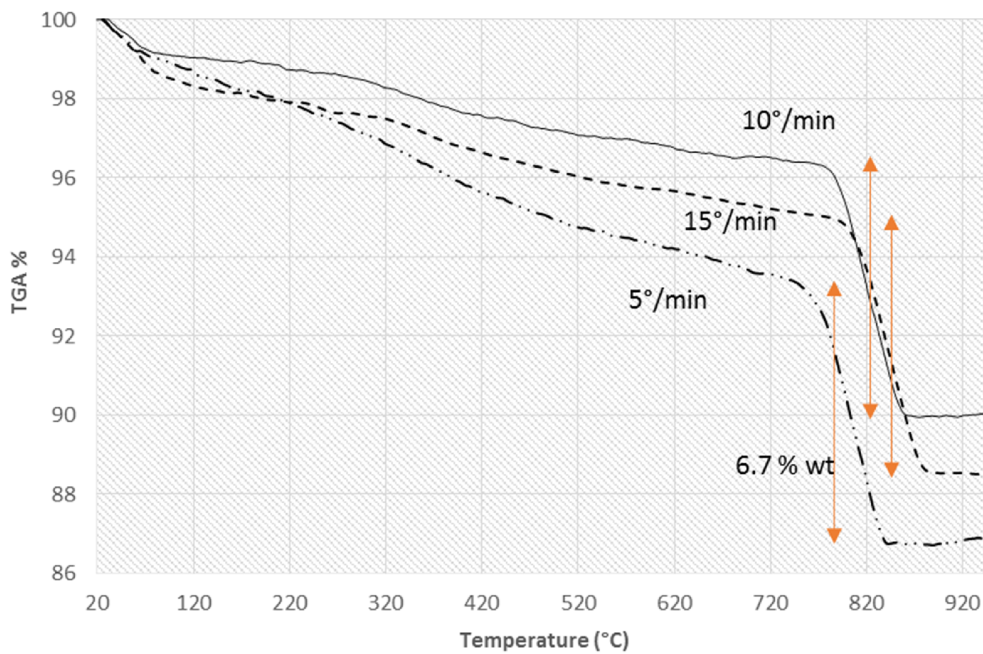


Figure 5:17 TGA curves for cobalt oxide in nitrogen atmosphere at different heating rates

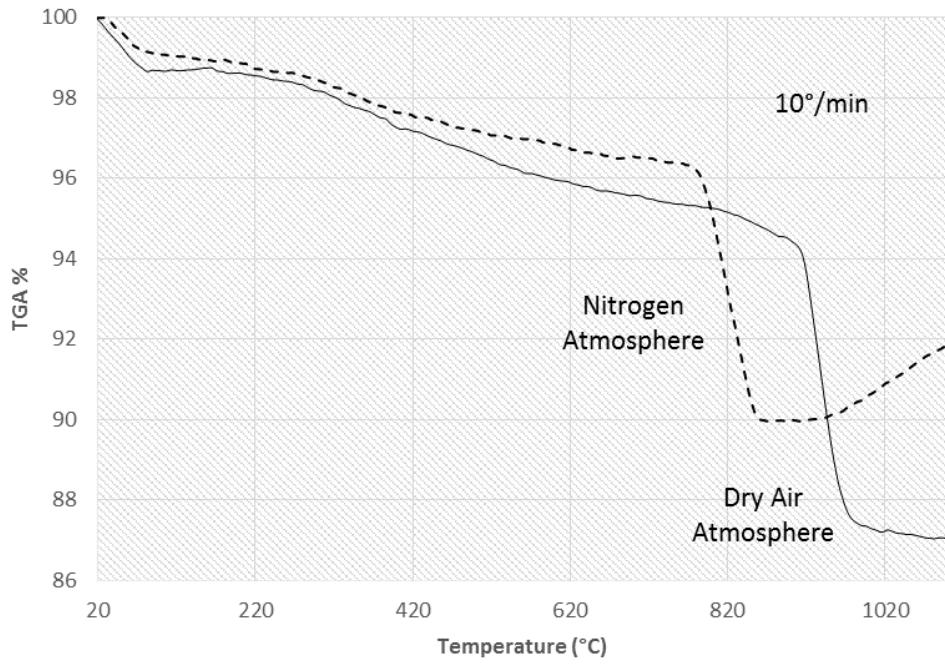


Figure 5:18 Cobalt decomposition in inert and oxidative environment

## 5.2.4 Production of Hydrogen over Reduced Cobalt Oxide

### 5.2.4.1 Reducibility of Spinel Cobalt Oxide

Reducibility of the cobalt oxide was tested with the experimental setup given in part 3.2.1.5 before performing the water splitting experiments. The objectives were to see the phase transformations from spinel oxide to metallic cobalt and to compare the calibration of the setup with a known reaction.

First, TCD signal for hydrogen was calibrated for TPR experiments and experimental results are compared with stoichiometric calculation to ensure the reliability of the setup. To do so, 100  $\mu\text{l}$ , 150  $\mu\text{l}$  and 200  $\mu\text{l}$  of pure hydrogen was injected to Ar flow of 47.5 ccpm three times and averaged. It was seen that there is a linear relationship between the amount injected and area under the TCD signal. Then, 0.3 g technical grade  $\text{Co}_3\text{O}_4$  was reduced as explained in part 4.2.1.5 and phase change from spinel oxide to metallic Co was achieved experimentally.

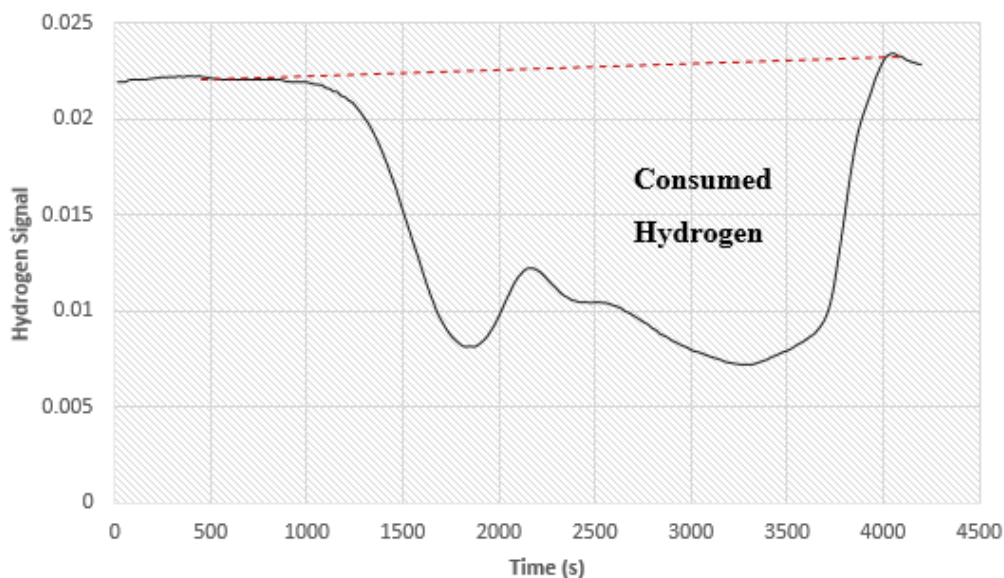


Figure 5:19 Reduction of  $\text{Co}_3\text{O}_4$  to Co via  $\text{H}_2$  in Ar flow ( $10^\circ/\text{min}$ )

Consumed hydrogen amount was calculated via numerical integration and it was compared with the stoichiometric hydrogen amount to reduce  $\text{Co}_3\text{O}_4$  completely to Co. It was found that there is a 4% difference.

#### 5.2.4.2 Water Splitting over Reduced Cobalt Oxide

A fresh sample of CA-0913-0 was placed in the TPR setup as explained in part 4.2.1.5 and  $\text{Co}_3\text{O}_4$  was reduced to CoO. Thermal decomposition temperature was selected as such based on TGA analysis. 250  $\mu\text{l}$  of water was injected via syringe pump with a rate of 100  $\mu\text{l}/\text{min}$  for 16<sup>th</sup> times. Each cycle was recorded separately for high resolution of the data. For the first two injections, no liquid water droplets were observed at the entrance of the quartz reactor and hydrogen peaks could not be observed. At the third injection, reactor inlet got wet and  $\text{H}_2$  peaks started to be observed. Data obtained were plotted and the baseline shifts were corrected for each cycle. Area under the hydrogen peaks were calculated by Simpson's Rule. Results for each peak is given in the Appendix C.2. When TCD signals were converted to amount of hydrogen produced, following is obtained.

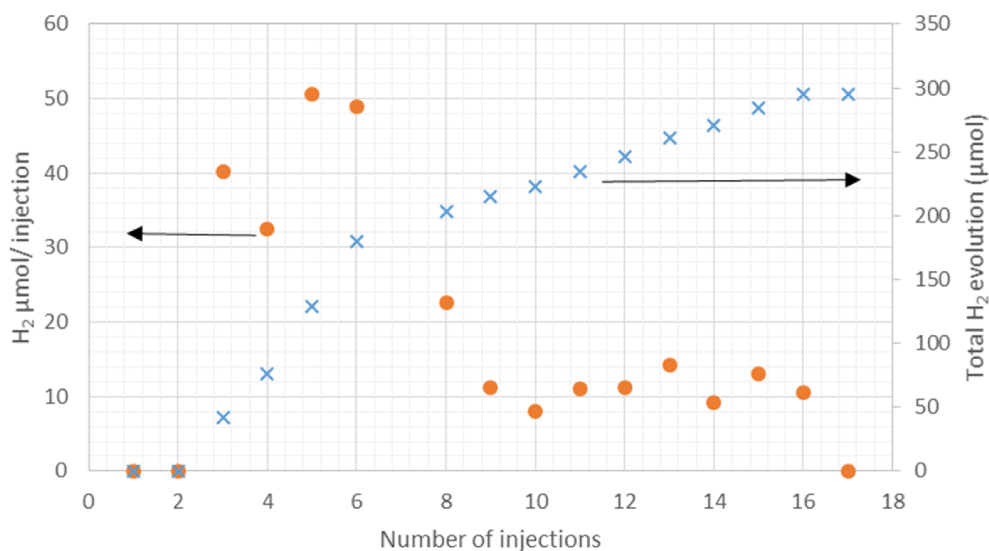


Figure 5:20 Hydrogen production over reduced cobalt oxide with water splitting reaction

At the end of 16<sup>th</sup> injection, amount of hydrogen produced was calculated to be 295.8  $\mu\text{mol}$ , which is equal to 23.7 % of the maximum amount of hydrogen that can be produced from 300 mg of  $\text{Co}_3\text{O}_4$  sample; that is  $19.7 \times 10^{-4} \text{ g H}_2 / \text{g Co}_3\text{O}_4$ .

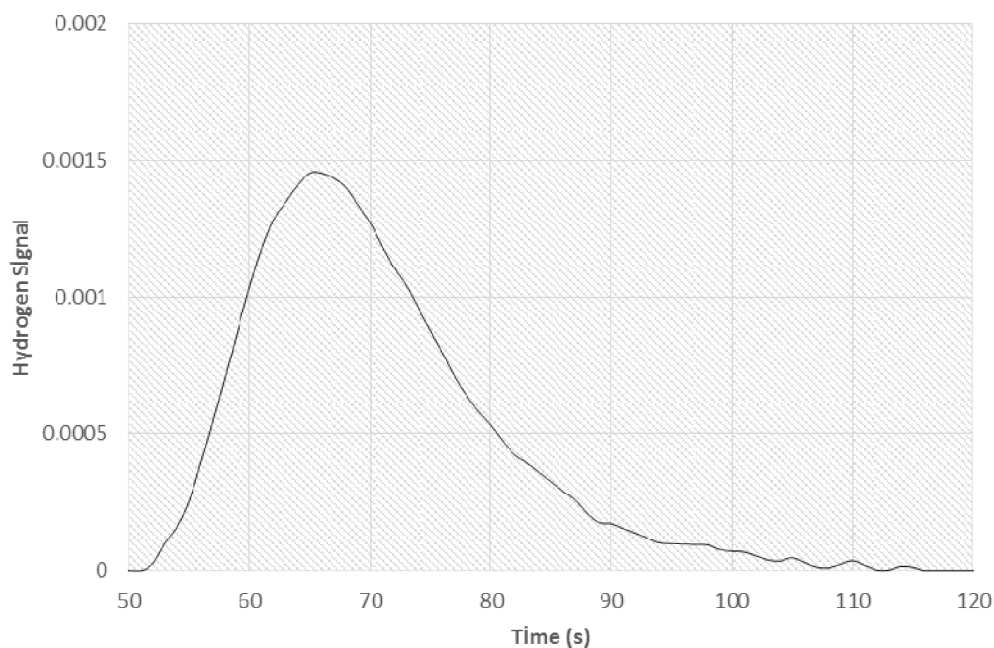


Figure 5:21 Hydrogen peak obtained for the third injection during the water splitting reaction

### 5.2.5 Production of CO over Reduced Cobalt Oxide

CO production over reduced cobalt oxide from carbon dioxide was studied as explained in part 4.2.1.6. In the first part of the experiment,  $\text{Co}_3\text{O}_4$  was reduced to  $\text{CoO}$  and oxygen release (32 amu) was monitored via MS for two different setup, shown schematically in Figure 5:22.

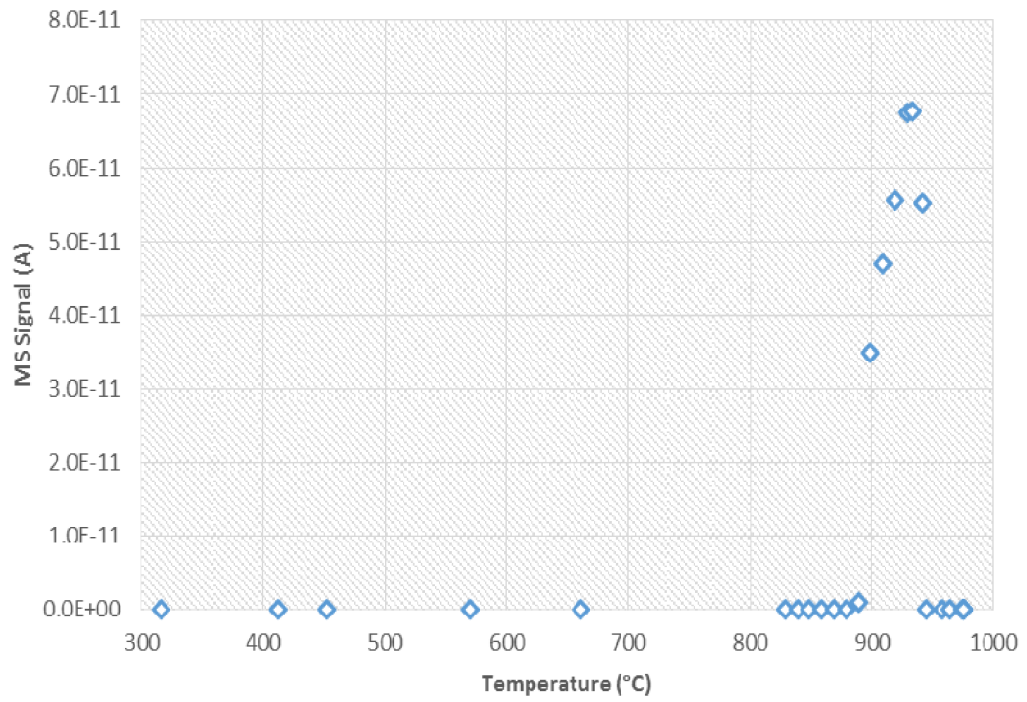


Figure 5:22 O<sub>2</sub> signal for Co<sub>3</sub>O<sub>4</sub> reduction for 1 g of sample CA-0913-0

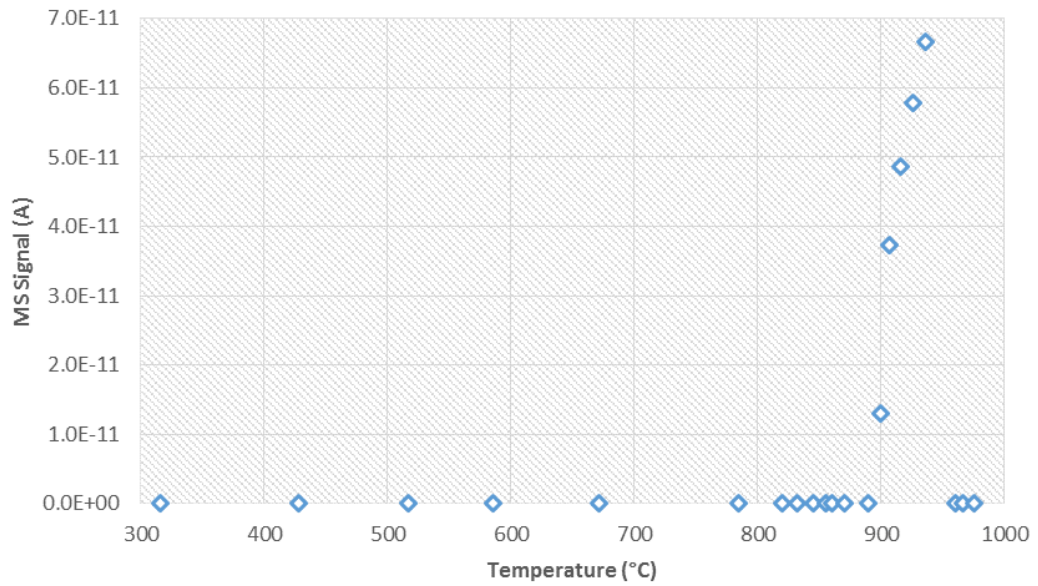


Figure 5:23 O<sub>2</sub> signal for Co<sub>3</sub>O<sub>4</sub> reduction for 1 g of sample CA-0913-0 for second run

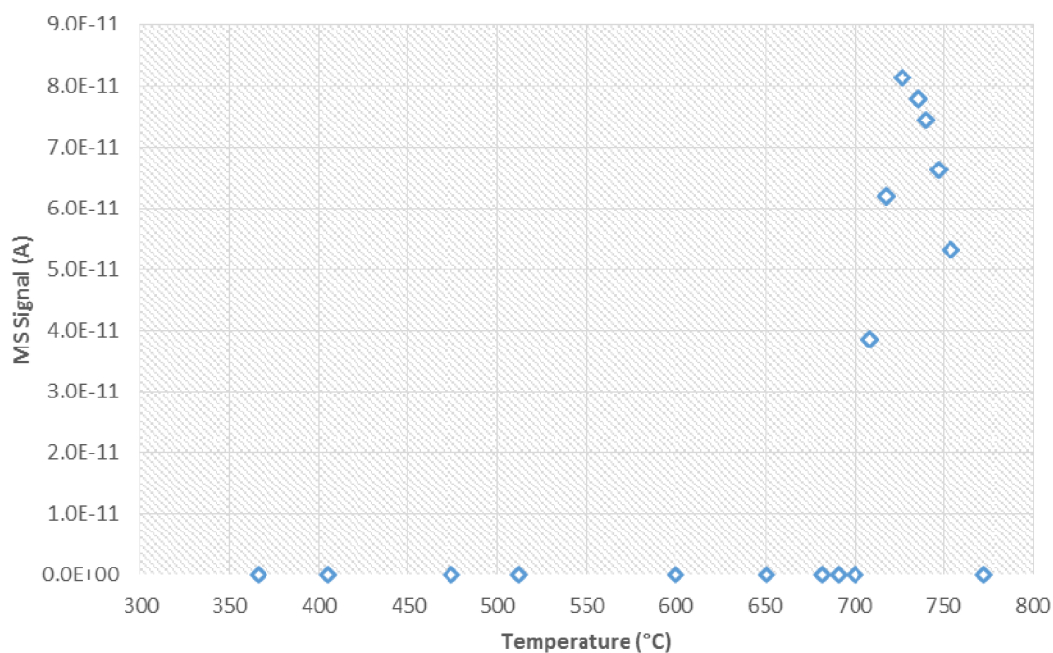


Figure 5:24 O<sub>2</sub> signal for Co<sub>3</sub>O<sub>4</sub> reduction for 15 g of sample CA-0913-0

In the second part of the experiment, 15 g of sample CA0913-0 was put into the stainless steel reactor shown in Figure 4:4(b). During the CO<sub>2</sub> flow that is the oxidation of CoO, expected signal of formed CO was not distinguishable from the signal of CO<sub>2</sub> as CO<sub>2</sub> also gives a signal at 28 amu. It was considered that if CO<sub>2</sub> oxidized CoO, O<sub>2</sub> signal during the thermal decomposition should be obtained if the sample is heated again (under He flow), which is verified with the figure given below. Significant CO formation was observed during thermal decomposition, considered to be due to deposited carbon / adsorbed CO. Onwards from the thermal decomposition point (see Figure 5:24), CO<sub>2</sub> peaks were started.

After the signal of CO was disappeared, reactor was heated up to 770 °C (as seen above) under the ongoing flow of 50ccpm He. Then, reactor was cooled again under 20ccpm CO<sub>2</sub> (99.9%) down to 100 °C (approximately 2hours). After cooling, gas was switched to the 50ccpm He again and heating period was started. The exit stream was sent to the MS and following figure was obtained.

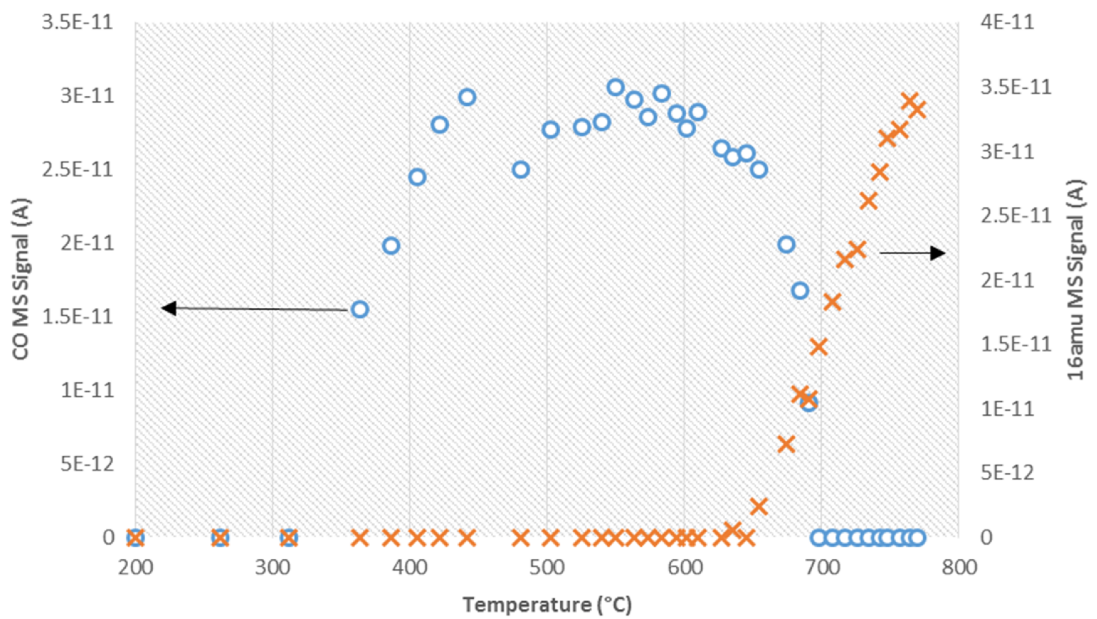


Figure 5:25 CO production (left - o) and oxygen signal (right - x) for 15 g of sample CA0913-0

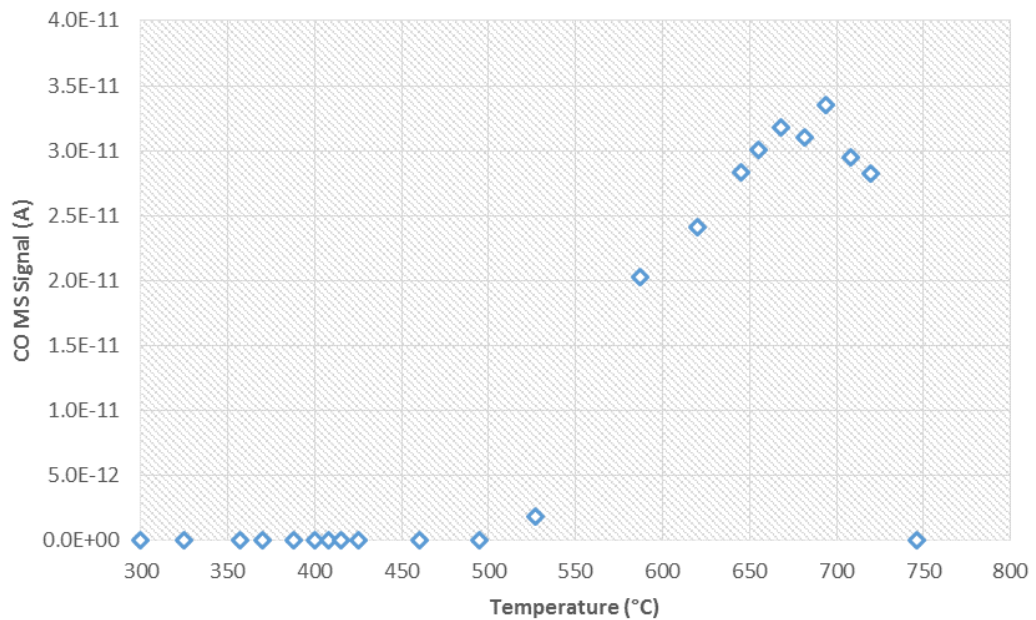


Figure 5:26 CO production for 15 g of sample CA0913-0 in the second consecutive run

### **5.2.5.1 Simulation of Heat Transfer Problem in the Reactors Used for CO Production**

In the thermal decomposition experiments with the quartz reactor and stainless steel reactor shown in Figure 4:4, it was spotted that decomposition process begins at different measured temperatures, which might signify a possible heat transfer problem. To have a better understanding, numerical simulations of those setups for heat transfer was done via COMSOL Multiphysics software. For the steel reactor, it was found that cooled upper surface of the reactor (cooled to prevent the rubber seal from burning) dominates other heat losses and reactor reaches steady state in a few seconds. For the quartz reactor, a temperature difference about 30 °C was observed between the measured oven temperature and the temperature of the reactor during the heating process. Results are given in Appendix B.7. Although numbers obtained in those simulations cannot be used in a quantitative analysis, it can deduced that thermal response of the steel reactor is expected to be a lot faster than the quartz reactor.

### 5.3 Kinetic Analysis

Kinetic analysis of the thermal decomposition of cobalt oxide was done via application of Kissinger Method on TGA data. As the very first step, DTA curves were derived for three different heating rates. Experimental data is presented in Appendix C.3.

Table 5:3 DTA peak temperatures at the heating rates of 5°, 10° and 15° per minute for spinel cobalt oxide thermal decomposition

Heating Rate (C°/min)	DTA Peak Temperatures (°C)
5°	799.4
10°	819.8
15°	839.4

As explained, Kissinger method can be applied for single DTA curve or from multiple DTA curves, which is shown to be more accurate, from the following relationship [67]:

$$\frac{d\left(\ln\frac{Q}{T_{max}^2}\right)}{d\left(\frac{1}{T_{max}}\right)} = -\frac{E_a}{R}$$

From DTA curves, a mean value of 252.24 kJ/mol was obtained for the activation energy as shown in the following table.

Table 5:4 Calculated Activation Energies from Kissinger Method via DTA couples

Heating Rate (K/min)	DTA Peak Temperatures (K)	$\ln(Q/T_{max}^2)$	$1000/T_{max}$	$E_a/R$	$E_a$ (kJ/mol)
5	1072.35	-12.35	0.93	37631.42	312.87
10	1092.76	-11.69	0.92		
5	1072.35	-12.35	0.93	30521.95	253.76
15	1112.42	-11.32	0.90		
10	1092.76	-11.69	0.92	22865.47	190.10
15	1112.42	-11.32	0.90		

To be able to calculate the order and pre-exponential factor, method explained in part 4.3 is used for heating rates of 5°, 10° and 15° per minute.  $\ln\left(Q \frac{d\alpha}{dT}\right)$  values were found at some dimensionless mass conversions as shown below where decomposition reaction takes place.

From the slope of  $1/T$  and  $\ln(Q(d\alpha/dT))$  lines, activation energy was confirmed to be 252.09 kJ/mol, which closed to the one found before, where the  $\ln(Af(\alpha))$  intercepts were found to be 25.35, 25.31 and 25.03 for alpha values of 0.55, 0.65 and 0.75 respectively. For those  $\ln(Af(\alpha))$ , A and order of reaction was derived as explained in part 4.3. From Figure 5:29, n and A were found as 0.56 and  $1.658 \times 10^{11}$  respectively.

Table 5:5  $\ln\left(Q \frac{d\alpha}{dT}\right)$  values for different heating rates (Q) at various  $\alpha$  values

$\alpha$	T(K) 5°/min	T(K) 10°/min	T(K) 15°/min	Q = 5 $\ln(Q(d\alpha/dT))$	Q = 10 $\ln(Q(d\alpha/dT))$	Q = 15 $\ln(Q(d\alpha/dT))$
0.5	1020.03	1075.81	1084.06			
0.6	1055.18	1086.46	1099.85	-4.25	-2.37	-2.35
0.7	1069.53	1096.95	1111.95	-3.36	-2.35	-2.09
0.8	1082.79	1107.35	1124.1	-3.28	-2.34	-2.09

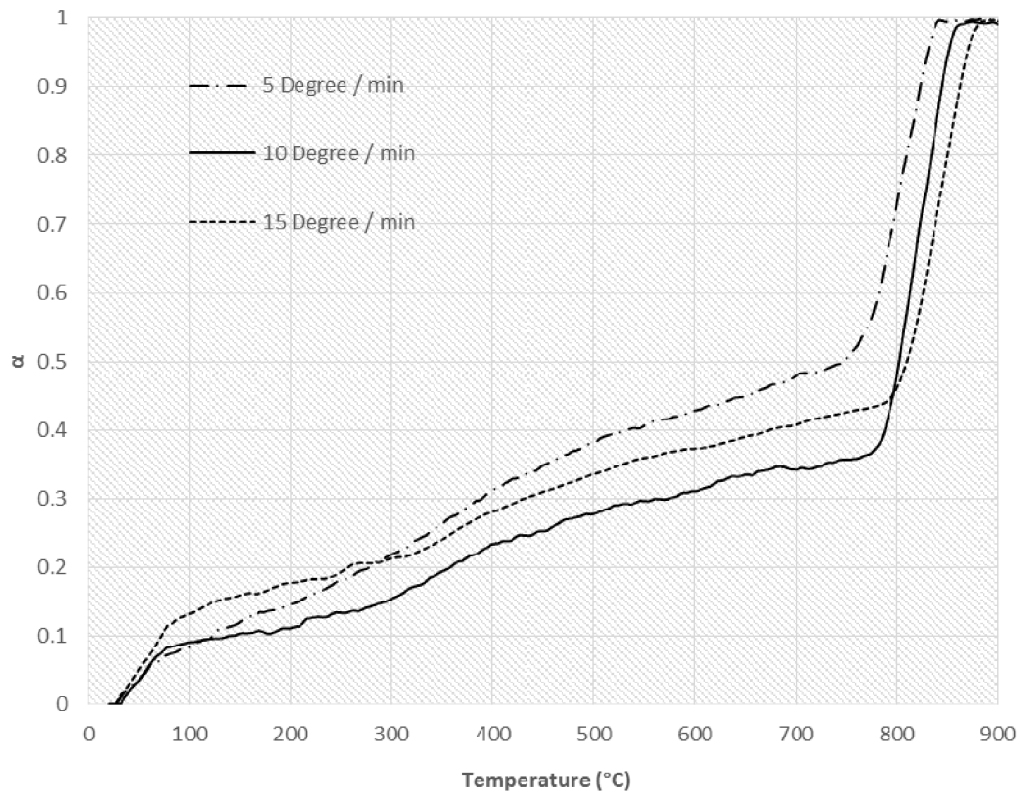


Figure 5:27 Change of  $\alpha$  with temperature for different heating rates

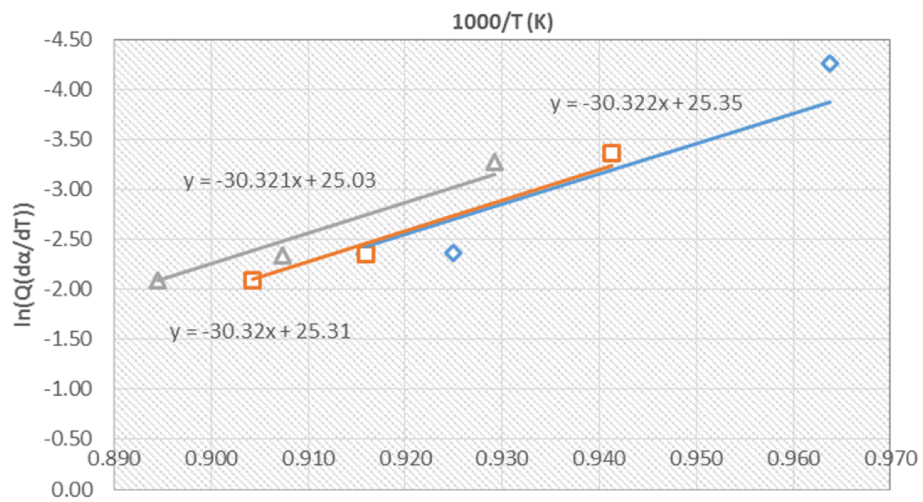


Figure 5:28 Derivation of  $\ln(Af(\alpha))$  values at mean alpha values

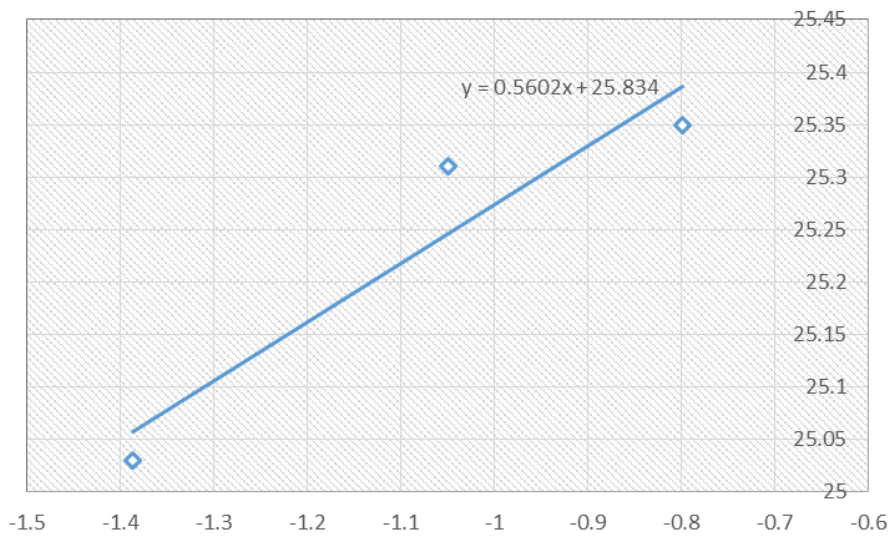


Figure 5:29 Derivation of order of reaction and pre-exponential factor

## 5.4 Mathematical Modeling of Thermal Decomposition of Cobalt Oxide

Mathematical models and solution of those models for thermal decomposition of  $\text{Co}_3\text{O}_4$  is presented here. Two modeling strategies were applied. In the first one, reaction was investigated in a gradientless reactor; that is the local temperatures and compositions are identical at any point within the reactor. In the second one, transient decomposition was studied in a 3D reactor where changes in temperatures and compositions are monitored at each local point.

### 5.4.1 1-D Modeling: Transient Reduction of Cobalt Oxide in a Gradientless Reactor

In part 4.4, it was seen that heat and mass transfer limitations seem to be the bottleneck of the design where the derived rate equation is expected to include diffusion resistances within the solid particles for the material size studied experimentally. In order to have an idea of how reaction proceeds in a reactor where there is no heat transfer limitations, a batch reactor was built as follows.

In the first case, reactor was considered to be isothermal at 1123 K and defined by the following governing equation:

$$\frac{d\alpha}{dt} = A \exp\left(-\frac{E_a}{RT}\right) (1 - \alpha)^n$$

$$\alpha(0) = 0$$

$$T = 1123 \text{ K}$$

$$E_a = 252090 \text{ J/mol}$$

$$R = 8.314$$

$$A = 1.658 \times 10^{11}$$

$$n = 0.56$$

When the ODE is solved, it was seen that reaction is completed in seconds, which clearly demonstrate the easiness of complete conversion when there are not any heat transfer resistances as previously predicted in part 4.4.1.

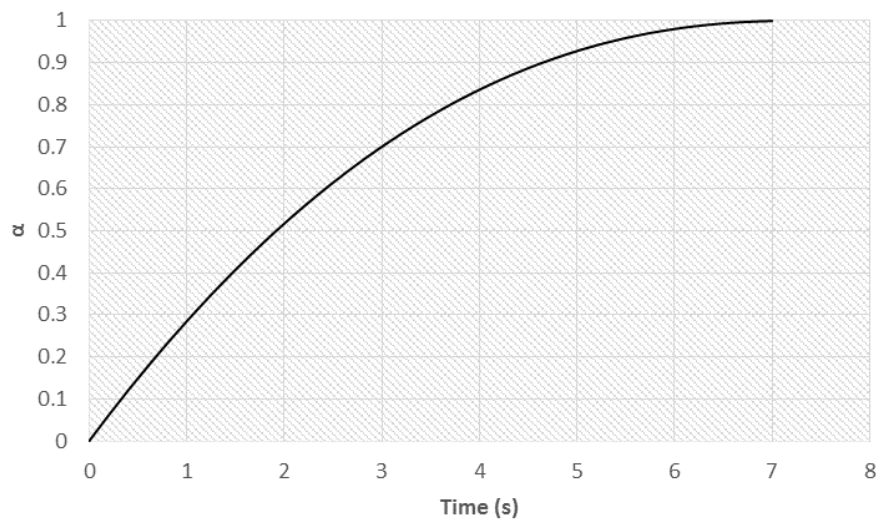


Figure 5:30 Dimensionless conversion of cobalt oxide reduction in isothermal batch reactor

In the second step, a reactor of a certain size was then operated under transient non isothermal conditions. To do so, a reactor volume was defined and a heat flux of 1000 kW/m<sup>2</sup> was supplied from one side of the volume, which is an average value that can be supplied from a source which is based on concentrated solar energy. Conservation of energy equation was built based on the conversion of mass as follows where the derivation is given in Appendix D.

$$\frac{dT}{dt} = \frac{Q + (-\Delta H_{rxn}(T) \times A \exp\left(-\frac{E_a}{RT}\right) (1 - \alpha)^n (W_{initial} - W_{final})) / (16)}{Cp_{Co_3O_4} W + Cp_{CoO} (W_{initial} - W)}$$

$$T(0) = 1073 \text{ K}$$

$$MW_{Co_3O_4} = 240.8 \text{ g/mol}$$

$$MW_{CoO} = 74.933 \text{ g/mol}$$

$$Volume = 1 \text{ m}^3$$

$$Surface \text{ Area} = Volume^{2/3}$$

$$Q = 10^6 \frac{W}{m^2} \times Surface \text{ Area}$$

It is seen that even if the reactor is well-mixed, complete conversion can be achieved in almost two hours for a 1 m<sup>3</sup> of reactor and temperature profiles agrees with the preliminary heat transfer limitation simulations that is there would be local temperature drops due to endothermic reduction reaction. It can also be concluded that introducing a heat flux within the range of concentrated solar radiation can sustain the need of energy if there would be no heat transfer problems.

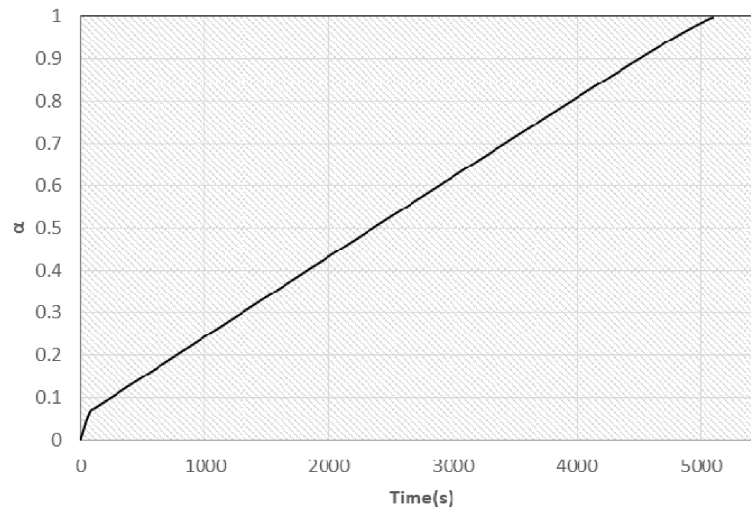


Figure 5:31 Dimensionless conversion of cobalt oxide reduction in non-isothermal batch reactor

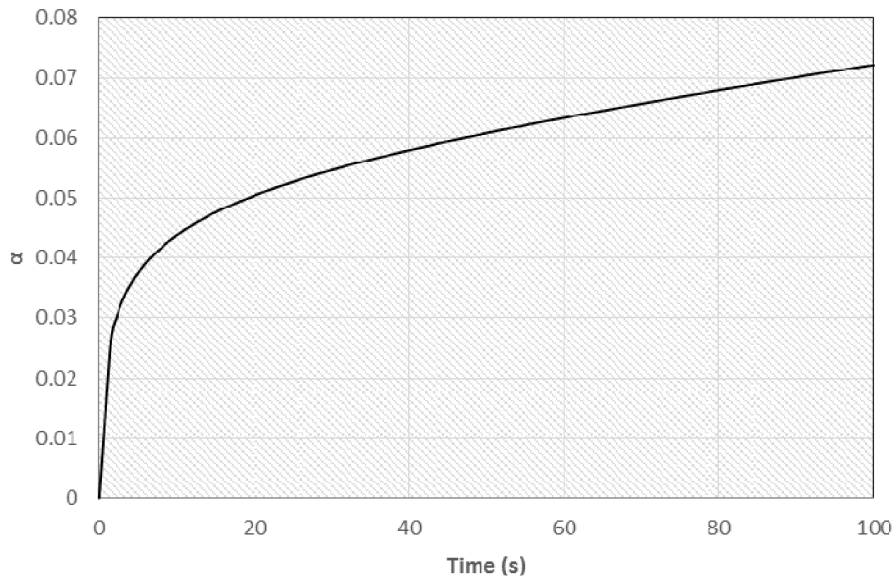


Figure 5:31 Dimensionless conversion of cobalt oxide reduction in non-isothermal batch reactor (continued)

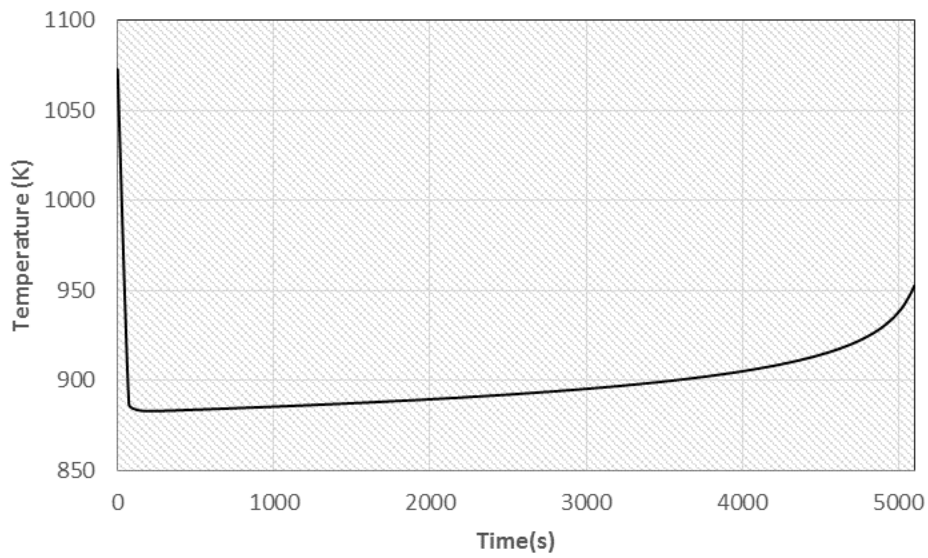


Figure 5:32 Change in temperature of the non-isothermal batch reactor during the reduction of cobalt oxide

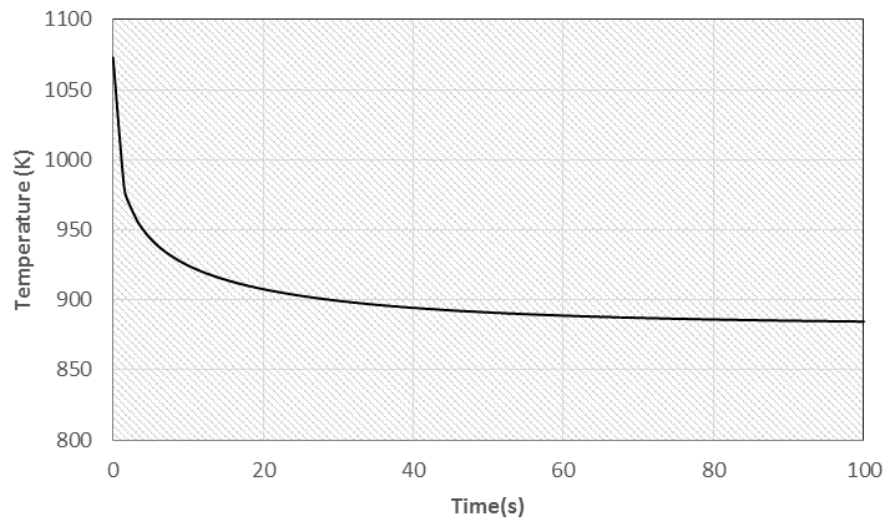


Figure 5:32 Change in temperature of the non-isothermal batch reactor during the reduction of cobalt oxide (continued)

To see the effect of the volume on average operating temperature and time required for complete conversion, above equations were solved at different volumes. Results are given in Figure 5:33.

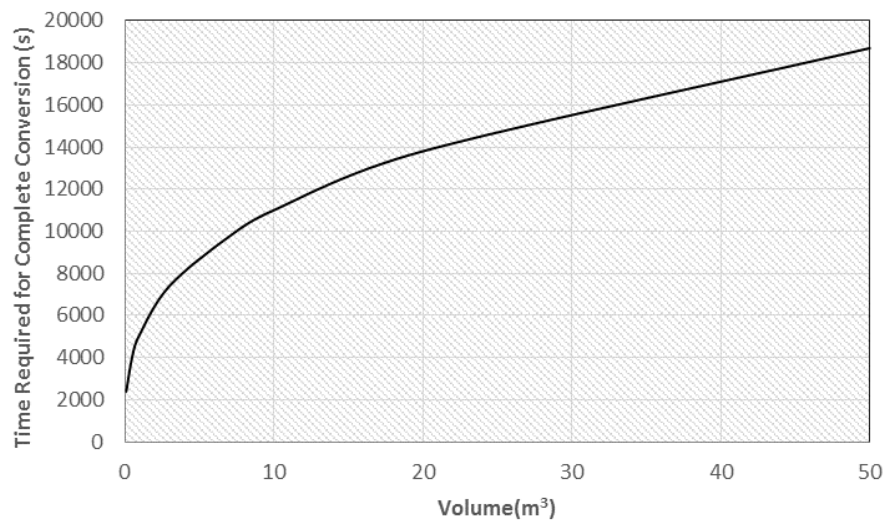


Figure 5:33 Change in thermal decomposition time and average temperature for the non-isothermal batch reactor at various sizes

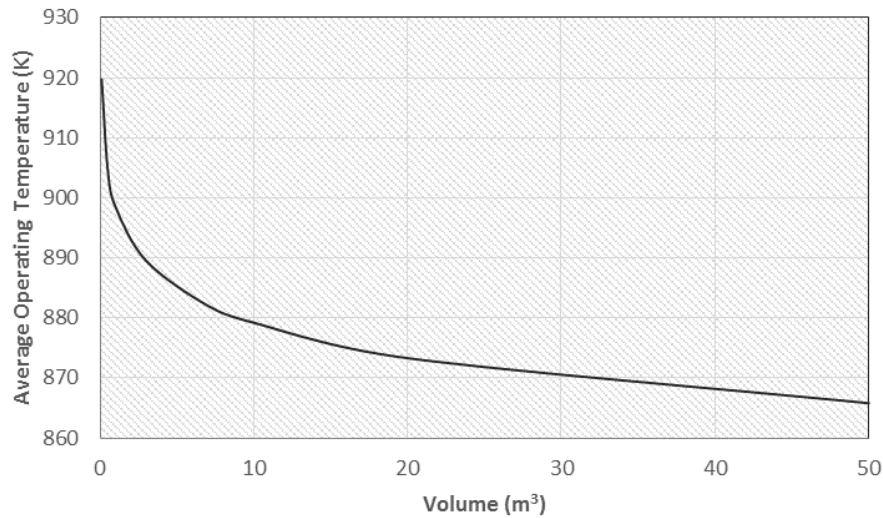


Figure 5:33 Change in thermal decomposition time and average temperature for the non-isothermal batch reactor at various sizes (continued)

It was deduced that heat transfer limitations are quite critical and increases the time scale of reduction significantly even for a well-mixed medium. To be able to obtain more accurate results on the estimation of time scale for the reduction of cobalt oxide, heat transfer resistances within the reacting medium is also needed to be introduced to the model. It was also concluded that the expected time scale might be in the order of hours.

Lastly, adiabatic transient case was solved for a few cases where initial temperature of the oxide was altered in each case. It is seen that available energy at high temperatures was used in minutes and temperature drops below 800 K and phase change stops, which is consistent with fundamental heat calculations given in the appendices as well as the phase change thermodynamics. Results of the calculations are given for a few initial temperatures. It should be noted that even at the maximum temperature, selected as 1773 K previously, available energy is not sufficient to complete the thermal decomposition.

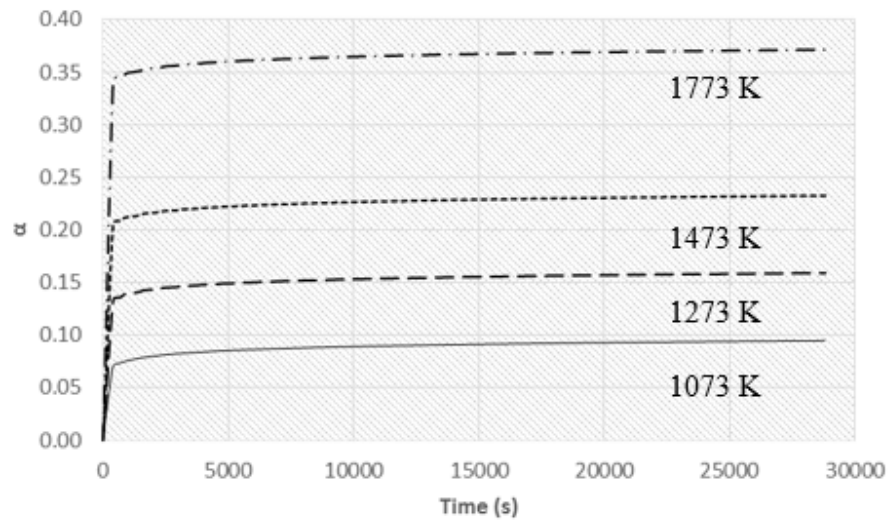


Figure 5:34 Dimensionless conversion of cobalt oxide reduction in adiabatic batch reactor at various initial temperatures

### 5.4.2 3D Modeling: Transient Response of a Reactor with a Finite Geometry

In this part, a finite rectangular volume of 0.1 m<sup>3</sup> was investigated to see the thermal response of the reaction medium to a heat flux of 100 kW/m<sup>2</sup> and to estimate the time for complete reduction of the process. To do so, reactor was selected as cubic and heat flux is considered to be fed from the top surface. Transient convection diffusion equation was coupled with the conservation of energy and solved via COMSOL with the following parameters, variables and initial conditions. All physical properties are taken from the literature as given in Appendix B.8 and rate equation derived in the kinetic analysis part was used. Equations given below were solved from t=0 to t = 28440 s (8 hours).

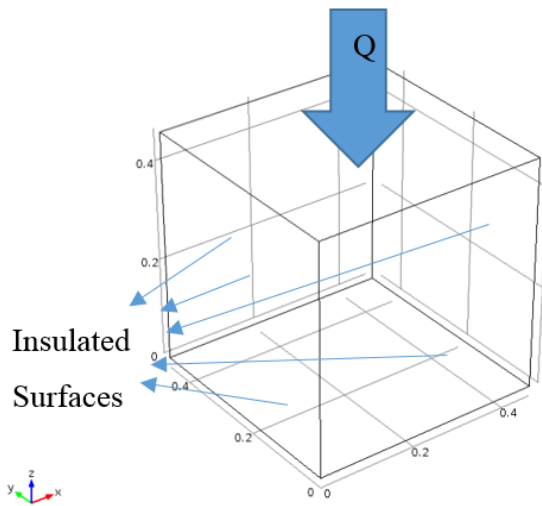


Figure 5:35 Schematic representation of the reactor used in 3D modeling

$$\frac{\delta\alpha}{\delta t} + \nabla \cdot (-D\nabla\alpha) + u \cdot \nabla\alpha = k(1 - \alpha)^n \cdot S(\alpha - 1)$$

$$((1 - \alpha)Cp_A + \alpha Cp_B)((1 - \alpha)\rho_A + \alpha\rho_B) \frac{\delta T}{\delta t} + \nabla \cdot (-k_c \nabla T) = -Q_g$$

where

A:  $\text{Co}_3\text{O}_4$

B:  $\text{CoO}$

$$\alpha(0) = 0$$

$$T_0 = 1073 \text{ K}$$

$$S(t) = 1; t < 0$$

$$= 0; t \geq 0$$

$$u = 0 \text{ m/s}$$

$$Q = 100 \frac{\text{kW}}{\text{m}^2}$$

$$MW_A = 240.8 \text{ g/mol}$$

$$MW_B = 74.933 \text{ g/mol}$$

$$\rho_A = 6110 \text{ kg/m}^3$$

$$\rho_B = 6440 \text{ kg/m}^3$$

$$Cp_A = (0.1322T + 78.032)/MW_A \text{ J/K/kg}$$

$$Cp_B = (0.0102T + 45.789)MW_B \text{ J/K/kg}$$

$$\Delta H_{rxn} = \frac{(-5)10^{-5}T^2 + 0.0758T + 178.72}{MW_A} \frac{\text{kJ}}{\text{kg } A_{reacted}}$$

$$k_c = 150.4892 - 0.1903T + (8.9428)10^{-5}T^2 \text{ W/m/K}$$

$$D = 10^{-29} \text{ m}^2/\text{s}$$

$$k = 1.658 \cdot 10^{11} \cdot \exp\left(-\frac{252090}{8.314T}\right) \text{ 1/s}$$

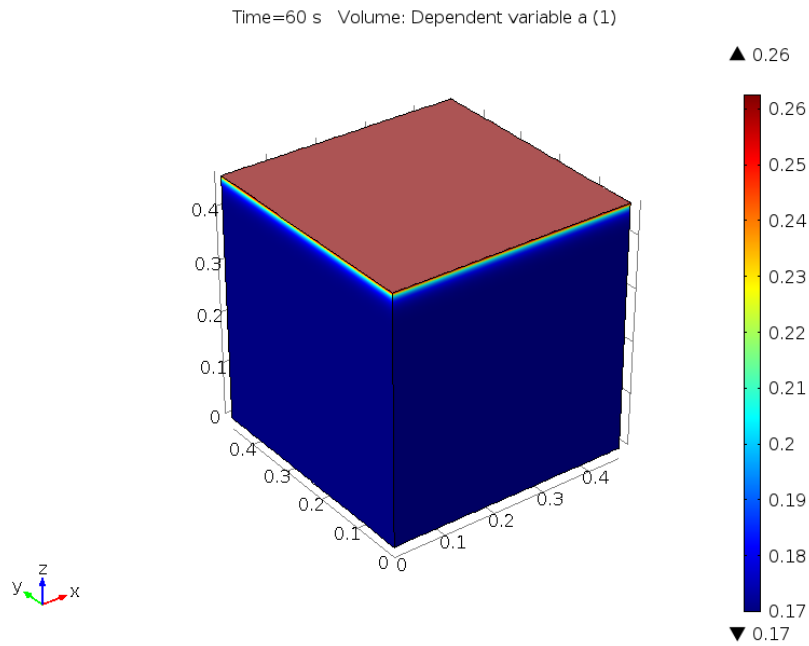
$$Q_g = \rho_A(-\Delta H_{rxn}) \frac{\delta\alpha}{\delta t}$$

Volume was meshed with the specifications presented below.

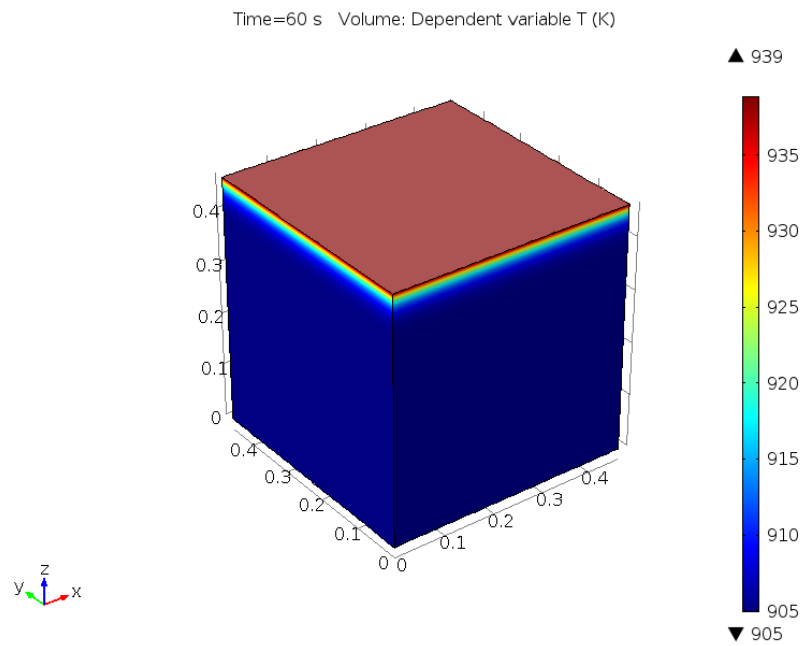
Table 5:6 Mesh size of the cubic reactor

<b>Mesh Elements</b>	<b>Heated Surface</b>	<b>Cube</b>
Type	Free triangular	Swept triangular
Max. Element Size	0.0371	0.00928
Min. Element Size	0.00464	$9.28 \times 10^{-5}$
Max. Element Growth Rate	1.45	1.3
Curvature Factor	0.5	0.2
Resolution of narrow regions	0.6	1

Simulation results were found to be quite different than the 1-D models predicted. In the first minute, It was seen that energy stored at  $t = 0$  (sample is at 1073 K) is used by the decomposition reaction and temperature drops as reaction proceeds in the whole reaction domain. Then, reaction only continues at the heated surface (which is at a higher temperature) and that reaction interface goes inwardly as decomposition reaction is completed. This phenomenon leads to a very important outcome: decomposition reaction zone here is at a higher temperature than it is in a gradientless reactor so that rate of reaction becomes much higher. As a result, conversion of  $\text{Co}_3\text{O}_4$  to  $\text{CoO}$  can be completed much more rapidly. Concentration and temperature profiles are given for both the reactor presented here and nonisothermal gradientless reactor with identical amount of supplied heat ( $100 \text{ kW/m}^2$ ).

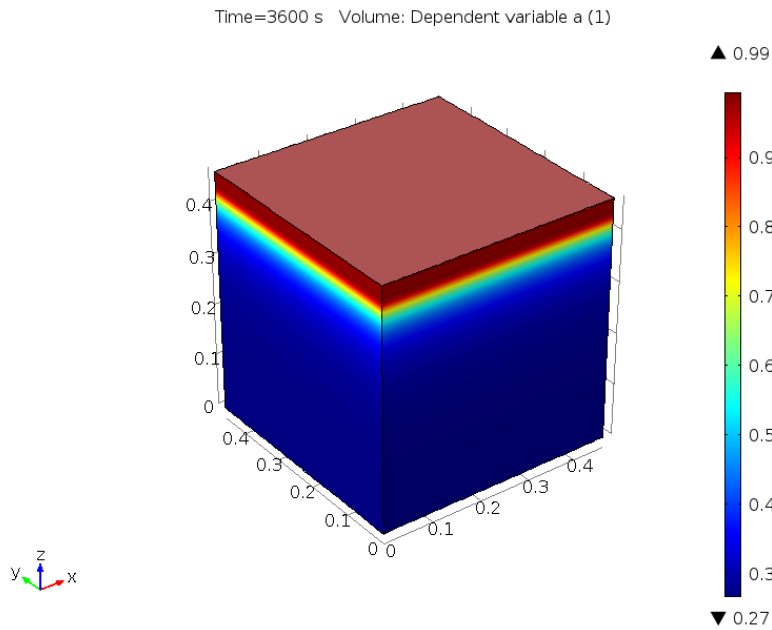


(a) Concentration profile after one minute

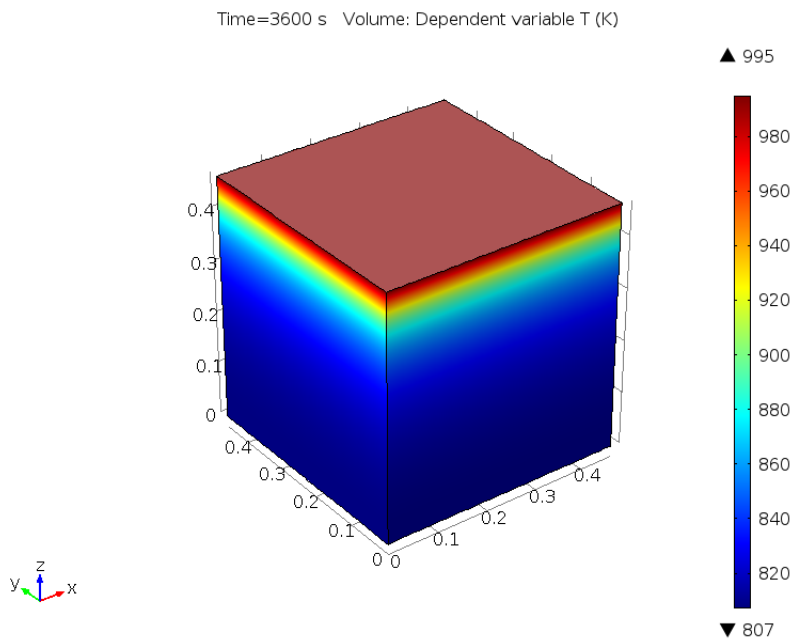


(b) Temperature profile after one minute

Figure 5:36 Concentration and temperature profiles for 3D reactor and comparison with a gradientless reactor with identical conditions

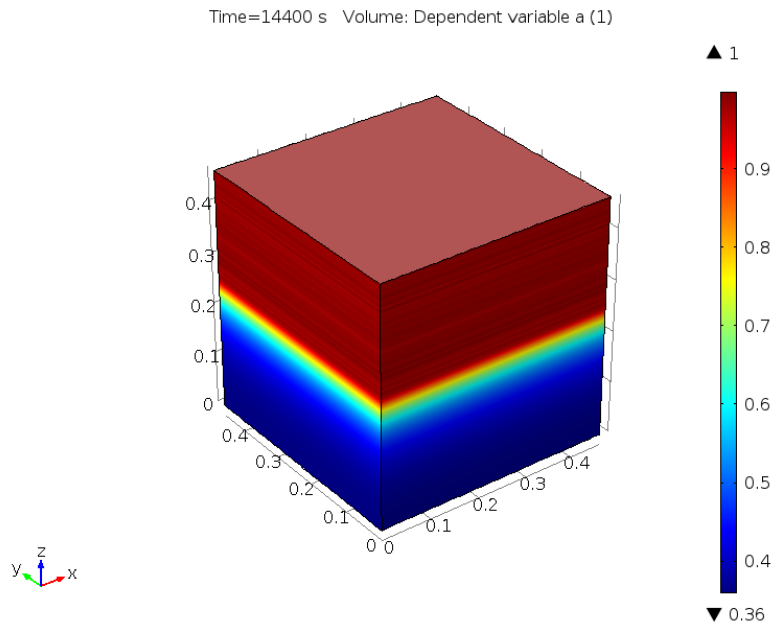


(c) Concentration profile after one hour

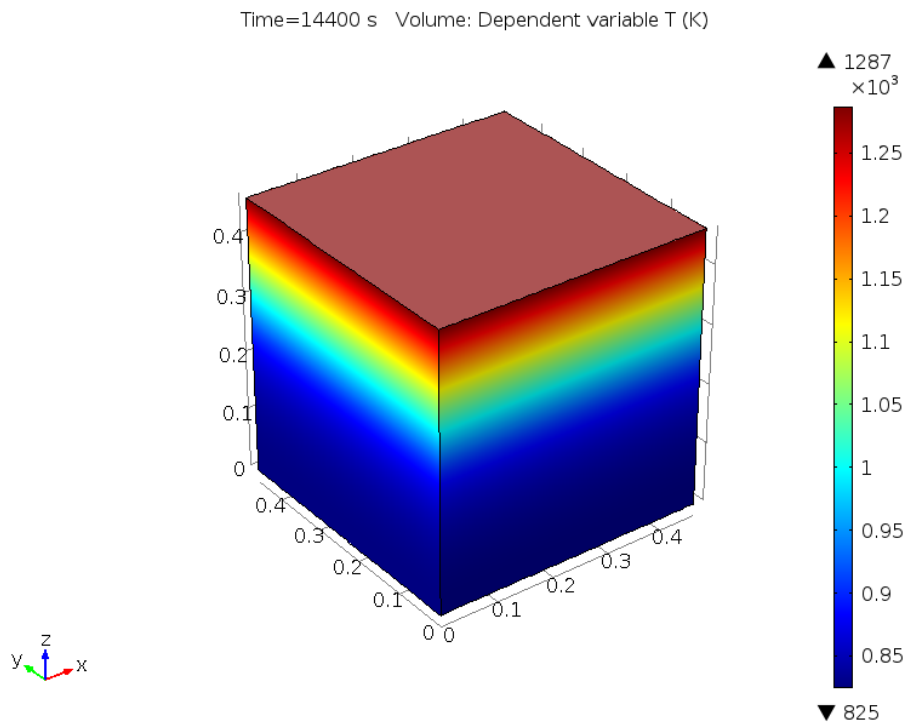


(d) Temperature profile after one hour

Figure 5:36 Concentration and temperature profiles for 3D reactor and comparison with a gradientless reactor with identical conditions (continued)

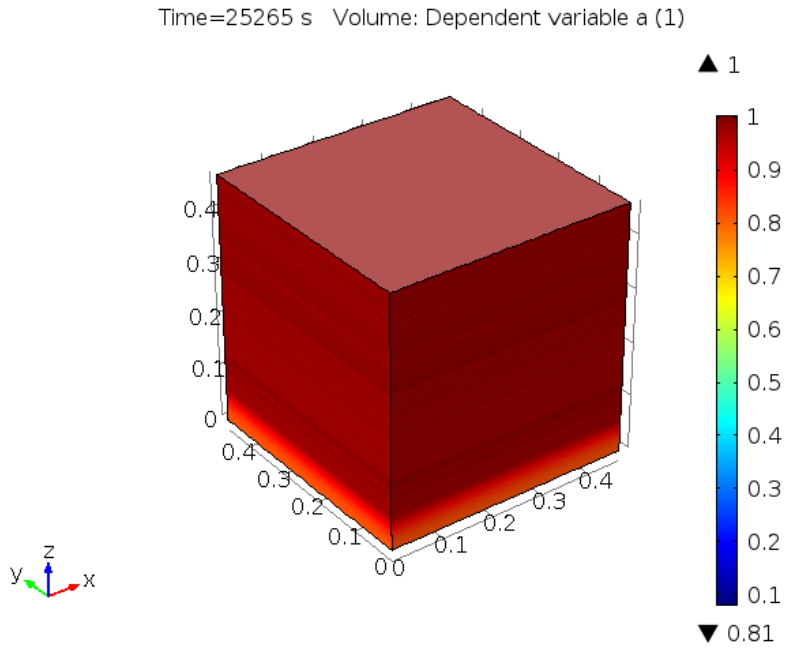


(e) Concentration profile after four hours

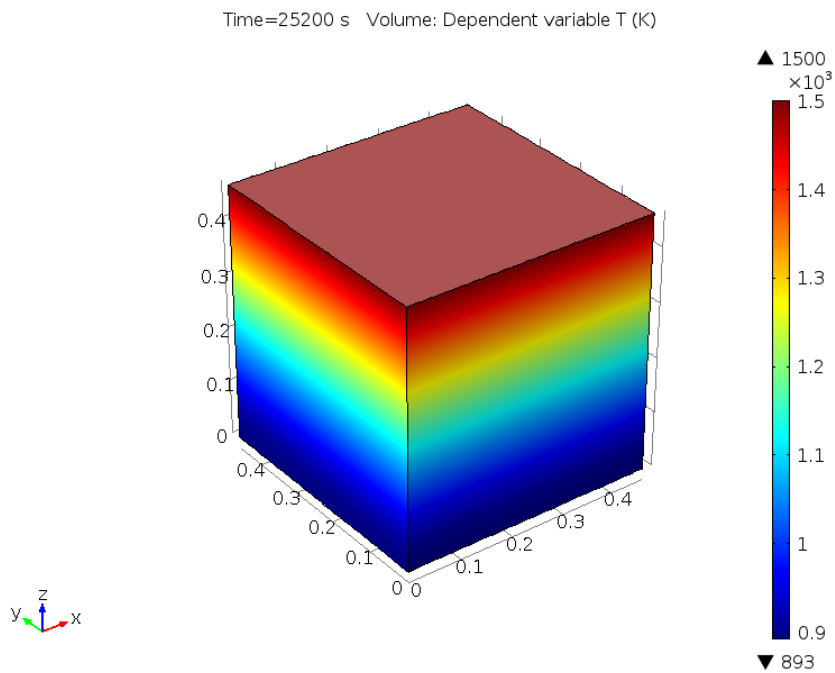


(f) Temperature profile after four hours

Figure 5:36 Concentration and temperature profiles for 3D reactor and comparison with a gradientless reactor with identical conditions (continued)

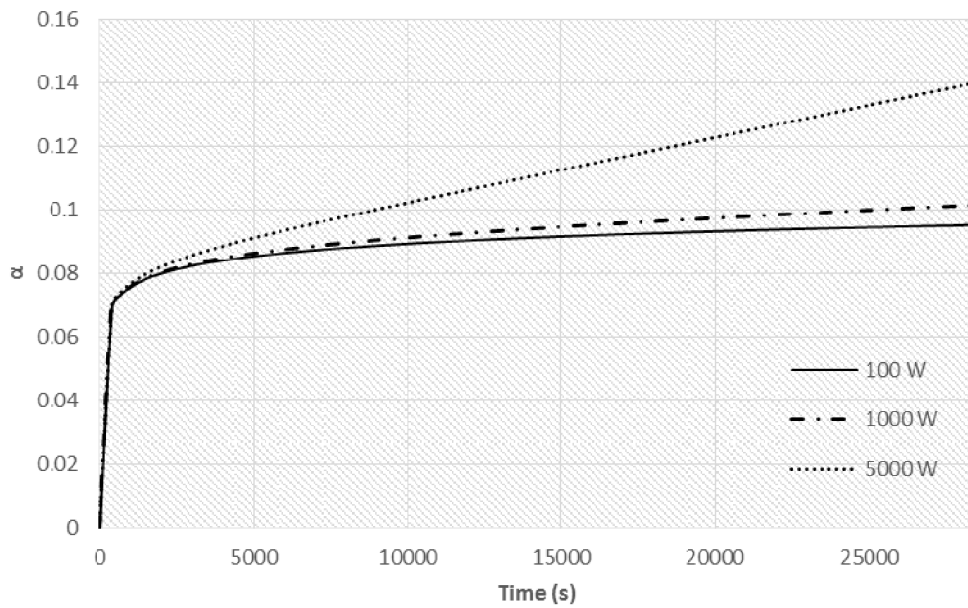


(g) Concentration profile after seven and a half hours

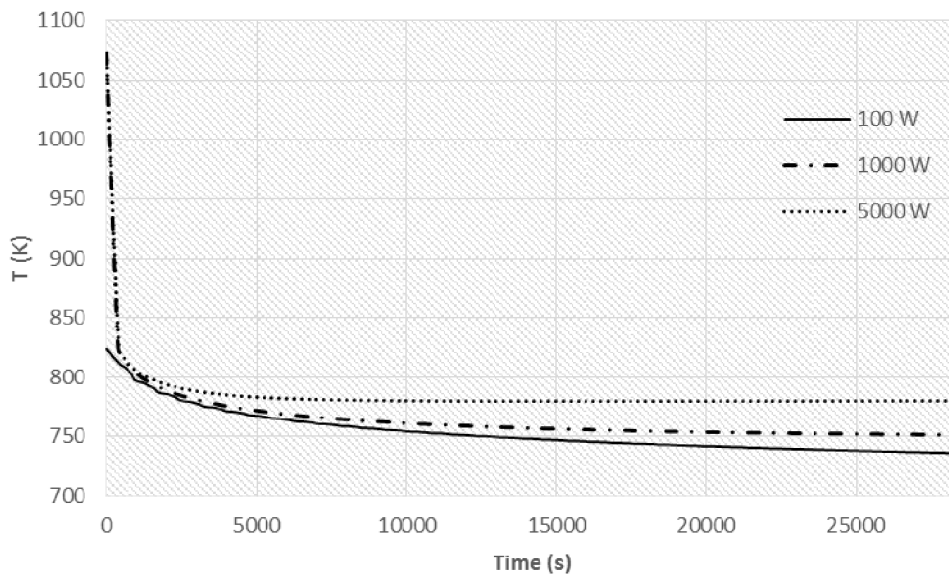


(h) Temperature profile after seven and a half hours

Figure 5:36 Concentration and temperature profiles for 3D reactor and comparison with a gradientless reactor with identical conditions (continued)



(i) Change in dimensionless conversion in gradientless reactor for various heat sources



(j) Change in temperature in gradientless reactor for various heat sources

Figure 5:36 Concentration and temperature profiles for 3D reactor and comparison with a gradientless reactor with identical conditions (continued)

As seen in Figure 5.36, there is a temperature difference of around 250 degree Kelvin between the reactors: one with a resistance to heat transfer and one with no thermal resistance. Interestingly, having a heat transfer resistance enables the former to have achieve high reaction rates. In fact, thermal decomposition was completed in the former one while conversion was less than 10% in the latter for the same heat input. It was also noticed that conversion cannot be increased significantly even if the heat input was increased fifty times (Figure 5.36-i, j). As a result, it was found that decomposition reaction can be completed with a reasonable heat flux ( $100 \text{ kW/m}^2$ ) within 8 hours with the aid of heat transfer resistances.

## 5.5 Membrane Reactors: Heat and Mass Transfer Limitations

Membrane reactors are one of the alternatives for syngas production from methane as explained in part 1.1.5. In thermodynamic analysis, it has been concluded that cobalt may give all the oxygen transported by diffusion to methane at around 1000 K if thermodynamic equilibrium is achieved (see 4.1.1).

Objective of this section is to investigate a membrane reactor (Figure 5:10) operating at thermodynamic equilibrium in terms of mass and heat transfer limitations at the operational limits.

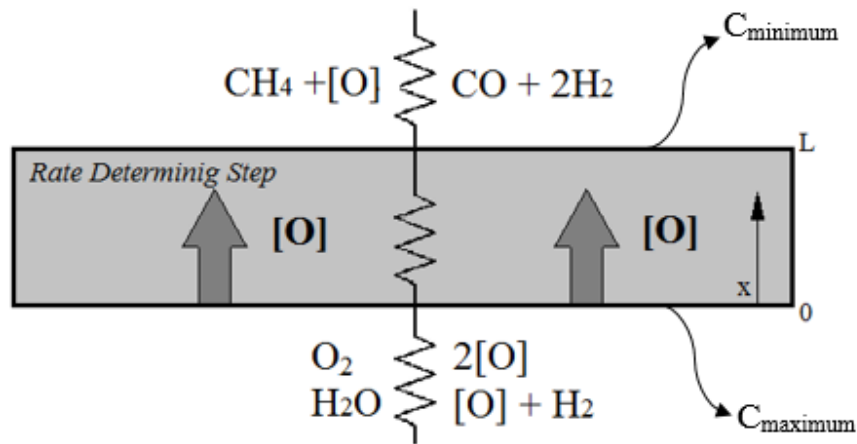


Figure 5:37 Resistances for partial oxidation (steam reforming) of methane via membrane reactor

To be able to see the effect of mass transfer resistance, it is assumed that oxidation of lower surface ( $x = 0$ ) and methane oxidation ( $x = L$ ) on the upper surface are faster compared to the diffusion of oxygen ions within the cobalt oxide. Temperature was selected to be 1000 K so that methane can be converted to syngas completely at thermodynamic equilibrium conditions. To maximize the rate of mass transfer, boundary conditions were selected as the highest and lowest possible values at 1000 K. At that temperature, cobalt phase was found to be  $Co_3O_4$  and its maximum oxygen concentration was stated to be  $0.1 \text{ mol/cm}^3$  (see Appendix B.6). For  $x = L$ ,  $C_{\text{minimum}}$  was selected to be

$\approx 0 \text{ mol/cm}^3$  by assuming that it gives all of its oxygen to methane at the equilibrium conditions. Based on those assumptions, concentration profile and rate of oxygen (A) transport within the membrane was found as follows:

$$C_A(x) = (C_{\text{maximum}} - C_{\text{minimum}})x/L + C_{\text{maximum}}$$

$$\dot{n}_A(L) = D_{AB} \frac{(C_{\text{maximum}} - C_{\text{minimum}})}{L} \times \text{Area}$$

$$\text{Area} = 1 \text{ m}^2$$

Table 5:7 Hydrogen production via membrane reactor with changing thickness

L(cm)	g-Co <sub>3</sub> O <sub>4</sub>	mol O <sub>2</sub> /m <sup>2</sup> s	max g H <sub>2</sub> x 10 <sup>4</sup> / g-Co <sub>3</sub> O <sub>4</sub>
0.0001	0.6	2725.65	3.57 x 10 <sup>5</sup>
0.0005	3.1	545.13	1.43 x 10 <sup>4</sup>
0.001	6.1	272.57	3.57 x 10 <sup>3</sup>
0.005	30.6	54.51	1.43 x 10 <sup>2</sup>
<b>0.01</b>	<b>61.1</b>	27.26	<b>3.57 x 10<sup>1</sup></b>
0.02	122.2	13.63	8.92 x 10 <sup>0</sup>
0.03	183.3	9.09	3.97 x 10 <sup>0</sup>
0.07	427.7	3.90	7.28 x 10 <sup>-1</sup>
0.1	611.0	2.73	3.57 x 10 <sup>-1</sup>
1	6,110.0	0.27	3.6 x 10 <sup>-3</sup>
3	18,330.0	0.09	4 x 10 <sup>-4</sup>
5	30,550.0	0.06	1 x 10 <sup>-4</sup>
7	42,770.0	0.04	~0
10	61,100.0	0.03	~0

So, amount of oxygen transported is stated as function of membrane thickness for a unit square surface area. From the reaction stoichiometry given in Figure 5:37, amount of

hydrogen produced was calculated per gram of cobalt oxide used. Results are tabulated in Table 5.7. Same equation was also solved for  $C_{A, x=L} = 0.086$ , which is the oxygen concentration of CoO.

It was found that even for the highest possible concentration gradient, thickness of a cobalt oxide membrane reactor is to be built very thin ( $\sim 100 \mu\text{m}$ ) to be compatible with the values reported in the literature. As seen from the table below, the oxygen flux found is compatible with the experimental results found from the literature for both upper surface boundary conditions.

Table 5:8 Comparison of membrane model results with the literature

<b>Membrane Studied</b>	<b>Membrane Thickness (mm)</b>	<b>Temperature (K)</b>	<b><math>\frac{\text{mol O}_2 \times 10^4}{\text{m}^2 \text{ sample}}</math></b>
PbO [35]	0.1	1000	1
$\text{Ba}_{0.5}\text{Sr}_{0.5}\text{Co}_{0.8}\text{Fe}_{0.2}\text{O}_{3-\delta}$ [29]	0.07	1200	50
$\text{Co}_3\text{O}_4$ (max)	0.1	1000	27.25
$\text{Co}_3\text{O}_4$ (when $C_{A, x=L} = 0.086$ )	0.1	1000	7.63

Temperature gradient within the membrane in x direction is expected to be insignificant for the thicknesses mentioned above. However, there is a huge difference between the heat of reactions of methane partial oxidation and water splitting reaction, which might create a temperature difference within the membrane.

The overall reaction takes place is the methane steam reforming reaction, which is endothermic. In the studied model, necessary amount of heat was introduced into the membrane volumetrically as a heat source. Conservation of energy and conservation of mass equations were solved simultaneously with the following boundary conditions.

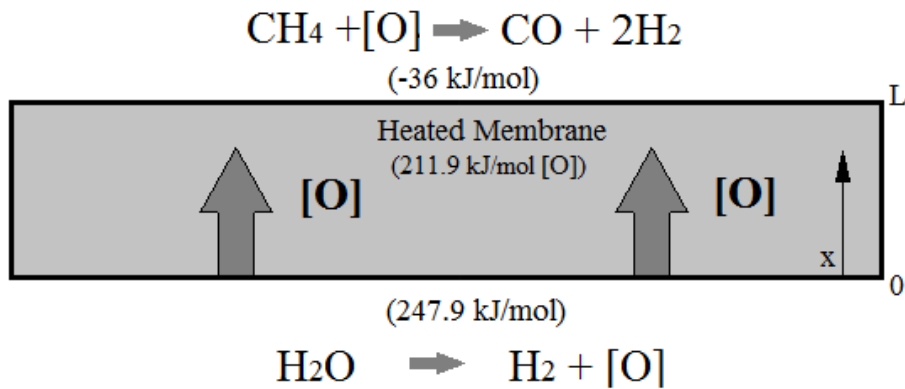


Figure 5:38 Schematic representation of the model used for identifying heat transfer limitations in the membrane reactor

$$\frac{d}{dx} \left( D \frac{d}{dx} C_A \right) = 0$$

$$x = 0 \text{ cm}; C_A = 0.1 \text{ mol/cm}^3$$

$$x = 0.01 \text{ cm}; C_A = 0.1 \text{ mol/cm}^3$$

$$D = 50 \times \exp \left( \frac{-95,000 \frac{\text{J}}{\text{mol}}}{8.314 \frac{\text{J}}{\text{molK}} T} \right) \text{ cm}^2/\text{s}$$

where A represents [O]

$$\frac{d}{dx} \left( k_c \frac{dT}{dx} \right) + Q = 0$$

$$x = 0 \text{ cm}; -k_c \frac{dT}{dx} = -247,900 N''_{Ax=0}$$

$$x = 0.01 \text{ cm}; -k_c \frac{dT}{dx} = 36,000 N''_{Ax=L}$$

$$k_c = 150.4892 - 0.1903T + (8.9428)10^{-5}T^2 \text{ W/m/K}$$

$$Q = 211,900 N''_{Ax=L}$$

Results show that there is little temperature gradient within the membrane even for the given boundary conditions such that a membrane with the specified thickness can be considered as isothermal.

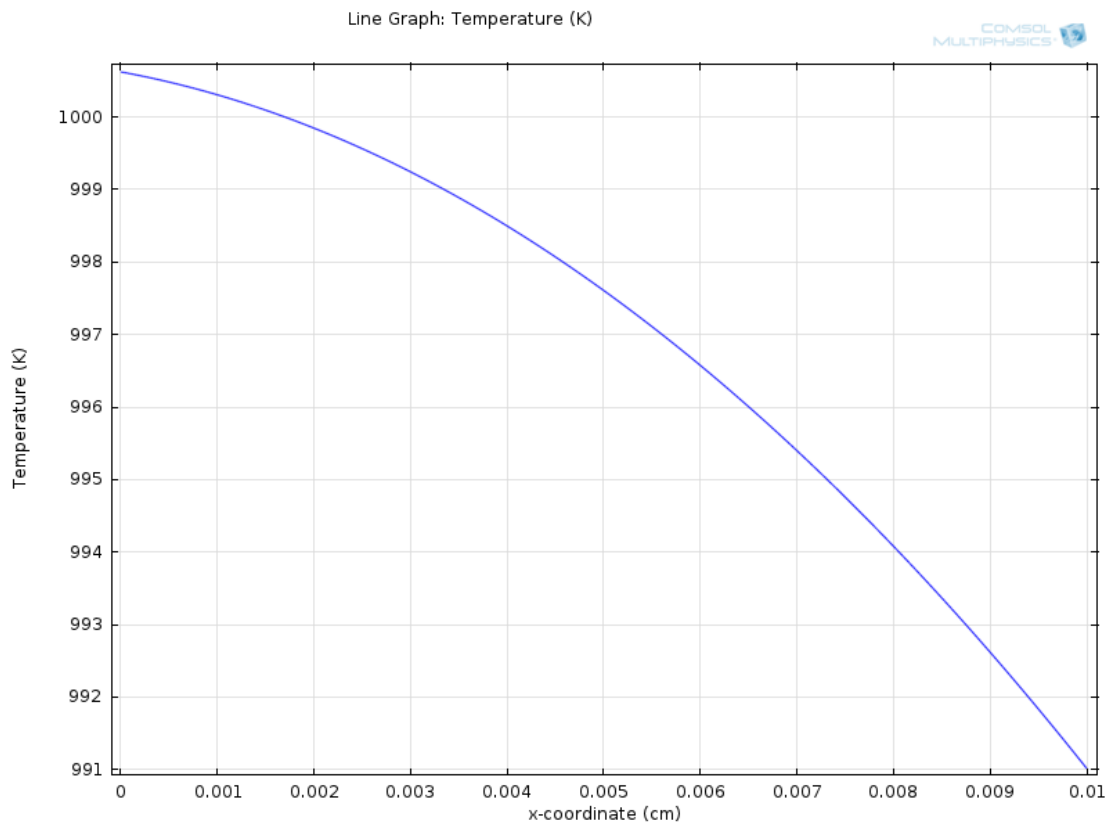


Figure 5:39 Temperature profile of the membrane during the steam reforming reaction



## CHAPTER 6

### SUMMARY OF THE RESULTS AND FUTURE PROSPECTS

Increase in energy demand of the modern society with the developments in accessible technology and growing world population has depleted the fossil energy reserves noticeably in the last century [123]. As solar energy has the theoretical potential to meet that energy demand of the world [124], utilization and storage of solar energy is a very appealing topic studied by various disciplines of science and technology [49]. Among the known methods, thermochemical heat storage as chemical bonds has numerous advantages as stated in part 3.1. Particularly, non-volatile stoichiometric metal oxides were shown to be successful for their high solar energy storage capacity [45-59]. Besides being a good candidate for solar energy carrier, thermal decomposition of those oxides substantially brings about a very important opportunity: chemical potential to facilitate reactions involving partial oxidation of methane and splitting of water/carbon dioxide. Motivation of the study was set in that perspective and we aimed for stating a candidate material for syngas production of any ratio by combining produced CO from CO<sub>2</sub> and produced H<sub>2</sub> from water via reducible metal oxides at mild conditions through thermodynamic analysis and characterization of related redox reaction kinetics on those oxides experimentally.

The study presented contributes to the research area in a few perspectives and further discussed in that order;

- Developing a methodology to select a candidate material
- Understanding and modeling of solar thermal decomposition kinetics of the selected oxide for thermochemical energy storage applications
- Showing the possibility and feasibility of syngas production over the selected material and providing experimental evidence
- Identifying the ranges where mass and heat transfer limitations prevail for the selected material

First of all, feasibility of the splitting reactions were investigated via theoretical thermodynamic efficiencies. Solar thermochemical energy storage is composed of two major steps which are charge and discharge operating different temperatures. Basically, we are considering to utilize two events at different temperatures, which might have been used to produce useful work via thermodynamic cycles. So, as the first step of the analysis, efficiency of the thermochemical energy storage was compared with Carnot efficiency that could have been achieved from those high and low temperature sinks. It was seen that thermochemical energy utilization through splitting reactions are about four times more efficient, which makes the approach worth to study. Secondly, material comparison was done based on the spontaneity of the interested reactions. Free energy changes for possible reactions in syngas production were investigated with temperature averaged data and candidate materials were highlighted. After comparing heat of reactions per oxygen, slopes (entropy change), availability and cost, cobalt oxide was considered to be further studied. Next, literature was searched out and it was seen that most of the reported materials with promising results (given in part 3.1 and 3.2) are within the highlighted candidates, which is an indirect measure of the applied methodology.

Although there are studies showing that  $\text{Co}_3\text{O}_4$  is a promising candidate for thermochemical energy storage applications, there is need for experimental data on decomposition and oxidation kinetics as well as the determination of the rate determining step; that is when heat and mass transfer prevails. In this study, it was desired to establish thermal decomposition kinetics with credible methods and utilize this information to probe into the effect of heat transfer limitations on decomposition rate via mathematical

modeling. As a start, charge stage of the thermochemical heat utilization was studied theoretically. Both free energy minimization method (

Figure 5:1) and built predominance diagrams (Figure 5:11) predicted the phase change reactions accurately and give important clues on the effect of oxygen presence and phase change temperature. Those results are found to be almost identical to experimental findings, presented in part 5.2.3. To be able to build a proper model, alternative approaches to non-catalytic gas solid reactions were scanned from the literature and Avrami model was found to be applicable. Decomposition kinetics for cobalt oxide were also needed and obtained experimentally (part 5.3). Kissinger method was selected as the starting point of the derivation among various empirical methods in the literature for phase transformation kinetics due to its proven reliability.

Operating hours of the charge stage of a thermochemical heat storage unit is naturally limited to effective insolation time slot. Being a high temperature endothermic reaction, charge stage is expected to be limited by energy transfer rate for relatively fast kinetics. After defining the kinetics of thermal decomposition, an analysis was conducted to compare reaction kinetics to heat transfer rate based on that hypothesis. To do so, two modeling strategies were applied. Firstly, rate determining step was investigated in a gradientless reactor; that is the local temperatures and compositions are identical at any point within the solved domain. Secondly, transient decomposition was modeled in a 3D reactor where changes in temperatures and compositions are monitored at each local point to see how the heat transfer limitations effect the rate of conversion. Obtained results were interesting. Heat transfer resistance due to conduction found to decrease decomposition time required for a certain amount compared to the case where there is no thermal resistance. In fact, the reason for this outcome is a fundamental principle. At the heated surface, temperature is higher than the below layers which causes an increase in the rate of reaction. As being an endothermic reaction, supplied heat is consumed and heat consumption is faster than it is conducted. As a result, practically heat is conducted to lower layers after the decomposition reaction is completed on the heated surface. This thermal resistance also brings about another important consequence. During the simulations, it was spotted that if the supplied heat flux was increased, temperature of the

converted upper layers can go beyond the melting point of the CoO easily before the reaction is completed in the whole domain. This results imply the importance of an optimization study including variations in the heat flux applied, reactor depth and conductivity of the medium to maximize the heated surface/volume ratio while minimizing the time required for complete conversion.

The major objective of the study was the production of syngas on thermally reduced metal oxide from water and carbon dioxide, which is the discharge step of the two step redox cycle. Before that, three major syngas production technologies were investigated to create a basis from the state of art. It was found that (see part 5.1.1) methane conversion and syngas selectivity (as well as the CO: H<sub>2</sub> ratio) is thermodynamically limited and this fact was used as the starting point of the analysis. Free energy minimization method was used to investigate various conditions for partial oxidation, steam reforming and autothermal reforming reactions where cobalt oxide was used as the oxygen source. The most fascinating result was the state of cobalt at temperatures above ~850 K. Operating temperature was found to be kept around 1000 K for highest syngas selectivity with complete methane conversion. When these two results were combined, an important outcome has been revealed. If a membrane surface contacting with methane is said to be at thermodynamic equilibrium for a temperature of operation around 1000 K (see Figure 5:10), surface cobalt is expected to give any oxygen transported from the bulk by diffusion to methane. This result was further used for modeling a membrane reactor where syngas was produced from autothermal /steam reforming of methane (see part 5.5). Simulation of heat and mass transfer within the membrane showed that cobalt seems to be compatible with other metal oxide membranes in terms of oxygen transfer rates and practically membrane can operate isothermally even at the most drastic conditions (when water is the source of oxygen). This deduction is promising for the future studies on membrane reactors with cobalt/cobalt oxide as cobalt oxide is stable, in solid state and nonvolatile at those temperatures unlike lead or bismuth oxides. Additionally, cobalt/cobalt oxide manufacturing is easier compared to perovskite membranes, one of the most studied membranes for similar applications. However, those results are derived with a very important assumption that is the membrane operates at thermodynamic equilibrium, which leads to a reactor design problem focusing on optimum residence time for the

reactants. Nevertheless, oxygen adsorption desorption experiments (see part 5.2.2) give important clues on significant lattice deficiencies created at elevated temperatures, which will bring about enhanced concentration gradient for membrane applications.

As stated, providing evidence on CO production from CO<sub>2</sub> and H<sub>2</sub> production from H<sub>2</sub>O on reduced cobalt oxide is one of the main objectives of the study. After going through applied syngas production methods and discussing the appealing possibility of cobalt utilization in membrane reactors, possibility of syngas production from CO<sub>2</sub> and H<sub>2</sub>O was investigated theoretically.

Equilibrium partial pressures were investigated by building predominance diagrams where water and carbon dioxide was the oxidant and phase transformations between different oxidative states were derived at different temperatures. It was seen that Co-CoO transformation requires very high reduction temperatures and partial pressures obtained were too low for the CoO-Co<sub>3</sub>O<sub>4</sub>, which might be considered as disappointing. Same analysis was also done for a previously studied material (see ref. 121) by which CO was produced to compare equilibrium partial pressures and they found to be close one another. In fact, those calculations are based on bulk thermodynamics. Surface oxidation reactions may exhibit quite differently as stated in the previous sections and may not be limited by the gaseous bulk thermodynamics. At that point, result was considered to be satisfactory.

Verification of those claims was done by several experiments as given in parts 5.2.4 and 5.2.5. First of all, thermal decomposition of cobalt oxide was examined parallel to analysis done in part 5.2.3 at each run for both CO and H<sub>2</sub> production experiments. However, phase change temperatures was found to be different for two reactors used in the experiments, which might signify a possible heat transfer / temperature measurement problem. To have a better understanding, both reactors were simulated via mathematical modeling (see Appendix B.7) and a temperature difference was found between the oven and the reactor for quartz reactor. Qualitatively, it can be argued that thermal response of the steel reactor is expected to be a lot faster than the quartz reactor.

During the hydrogen production, water could not be fed to the reactor in a heated line continuously. Instead, it was injected via a syringe pump (enabling constant feed rate). For the first two injections, no hydrogen was observed via TCD. At the third injection, it

was spotted that entrance of the reactor got wet and that water droplet was being boiled for a few seconds. That event continued until the last injection. As the rate of water and the fraction of water vapor meeting the reduced oxide could not be controlled, only qualitative results could be derived. Nevertheless, 23.7 % of the maximum amount of hydrogen that can be produced from 300 mg of  $\text{Co}_3\text{O}_4$  sample which is equivalent to  $19.7 \times 10^{-4} \text{ g H}_2 / \text{g Co}_3\text{O}_4$ . This value is better than most of the results presented in the literature (see Table 3:5) even though the rates are expected to be lower for CoO oxidation (since evaporation of the water will decrease the temperature of oxidation).

Experimental evaluation of CO production could not be observed due to instrumental limitations for low metal oxide amounts. So, 15 gr of  $\text{Co}_3\text{O}_4$  was analyzed in steel reactor via MS. To begin with, the way produced CO was observed was unexpected. After thermal decomposition and cooling down to room temperature under inert atmosphere,  $\text{CO}_2$  was introduced while temperature was being increased. However, no CO was detected. It was first considered that CO evaluation was suppressed by the presence of  $\text{CO}_2$  which also gives a peak at 28 amu. So, a hypothesis was claimed: if  $\text{CO}_2$  oxidizes CoO to  $\text{Co}_3\text{O}_4$ , that oxygen addition could be observed indirectly via heating the sample in inert atmosphere. When this was done, CO peak starts to be observed at around 350 °C instead of oxygen peak. In addition to that, when temperature reaches to thermal decomposition temperature, CO release turned into  $\text{CO}_2$ , probably due to available excess oxygen. These results clearly show that  $\text{CO}_2$  can easily oxidize CoO. What is interesting is the state of carbon under the reaction conditions. It is not clear for now whether it is adsorbed as C or CO or where it is adsorbed; on metal oxide or on the reactor walls.

In the light of experimental studies, it is now clear that CoO can produce  $\text{H}_2$  and CO from  $\text{H}_2\text{O}$  and  $\text{CO}_2$ . However, it was understood that the reaction mechanisms cannot be obtained with the built experimental setups. To be able to derive the necessary kinetic data, specific gas sensors have been purchased which will enable us to investigate the change in gas compositions accurately. This data is indeed critical to define discharge step of the cycle, which will lead the study to a pilot scale reactor design.

A deep understanding of the physical phenomena for two step thermochemical cycles is inseparable from inherent mass and heat transfer limitations due to the nature of non-

catalytic gas solid reactions. At the each step of the study, that factor had always kept in mind and obtained results were attributed to a conclusion while bearing those transport limitations in mind. Rates of conversion in both charge and discharge steps are functions of reactant concentration and medium temperature. So, it is important to characterize the effect of mass and heat transfer rates on reaction kinetics. Nonisothermal effects were investigated for a wide range from nanometer to meter via different approaches as presented in Appendix B. It was seen that heat transfer resistances are negligible up to hot spot formations in the range of millimeters, which indeed shows itself in thermal decomposition simulations. As stated in part 3.3, non-isothermal effects can be expected for gas-solid reactions. That possibility might create a boost in reaction rate compared to normal surface conditions. In the case cobalt that effect is not expected as seen in Appendix B.5.3 where  $\beta$  is practically zero. Another critical result was obtained from the growth model solved in Appendix B.6. That model predicts that oxidation of CoO can be completed in seconds for particles in micrometer scales, which is the case for the oxide used in TGA experiments. Time scale predicted is not expected to be exact but somehow close to the reality, at least in the order of magnitude. Phase change kinetics were derived from a time interval of at least 15 minutes by Kissinger method and predicted diffusion rate was quite small comparably. So, kinetics used in the thermal decomposition modeling was considered to be representing the kinetics of reaction in a coarse sense.

The most important and encouraging result obtained in this study was the raised self-awareness on the easiness of cobalt oxide redox reactions. Unlike its alternatives (see Table 3:5), thermal decomposition of cobalt oxide can be achieved at a much lower temperature (about 500 K in general). Temperature decrease in the charge stage inherently simplifies the process design and decreases the required capital investment cost. Especially, when concentrated solar energy is considered, that decrease becomes much more significant. The most conspicuous aspect of cobalt is the fact that experimentally obtained hydrogen production rates were better than most of the alternatives reported in the literature while sustaining a narrow temperature shift range between the charge and discharge steps.

Although cobalt oxide has shown good performance in cyclic operation under air atmosphere as shown in the literature review, there is no data for its cyclic performance in water splitting and carbon dioxide splitting atmospheres. Furthermore, powder cobalt oxide can agglomerate in time. This would increase the size of the particles, which directly increase the diffusive resistances. In the future, cyclic performance of the cobalt oxide must be tested to investigate its durability and stability for water and carbon dioxide splitting reactions.

## CHAPTER 7

### CONCLUSIONS

Syngas production with two step thermochemical cycles via reducible metal oxides was studied both theoretically and experimentally in this study. A methodology was built based on the laws of thermodynamics to select a candidate material for that purpose and  $\text{Co}_3\text{O}_4$  was considered worthy to further investigate. Charge step of the thermochemical cycle was investigated by free energy minimization analysis and by constructing predominance diagrams to examine the phase transformation equilibria. Transition temperatures were found to be consistent with decomposition experiments, from which reaction kinetics were estimated via Kissinger Method. All those findings were used to create mathematical models to identify the ranges where mass and heat transfer limitations prevail. It was diagnosed that there is not any significant mass or heat transfer limitations at the microscopic scale while heat transfer is the rate determining step at the macroscopic scale. That resistance was spotted to create non-isothermal contribution and increases the reaction rate significantly. Tools related to thermodynamic equilibria were also used to show the possibility and feasibility of syngas production over the selected material from  $\text{CO}_2$  and  $\text{H}_2\text{O}$ . Water splitting and carbon dioxide splitting experiments show the evidence for the discharge step of the thermochemical cycle and experimentally produced hydrogen amount per gram oxide was found to be better than many alternatives presented in the recent literature. Finally, syngas production via autothermal reforming of methane was studied theoretically with a novel approach. Membrane reactors were modeled by combining thermodynamic equilibria with the conservation laws and it was shown that cobalt-cobalt oxide structure is a promising candidate for such applications.



## REFERENCES

1. National Research Council Panel on New Directions in Catalytic Sciences and Technology, *Catalysis Looks to the Future*, National Academy Press, Washington D.C., 1992.
2. Hutchings, G.J., *J. Matter. Chem.*, 19(9), 1222-1235, 2009.
3. Ertl, G., Knözinger, H., Schüth, F., Weitkamp J., *Handbook of Heterogeneous Catalysis*, Wiley-VCH Verlag GmbH & Co. KGaA, Weinheim, Germany, 2008.
4. Richardson, J. T. , *Principles of Catalyst Development*, Plenum Press, New York, 1989.
5. Gas Production, Ullmann's Encyclopedia of Industrial Chemistry, 7th ed., Wiley-VCH Verlag GmbH & Co. KGaA, Weinheim, 2007.
6. Rostrup Nielsen, J.R., Sehested, J., Nørskov, J.K., *Hydrogen and synthesis gas by steam-and CO<sub>2</sub> reforming*, *Adv.Catal.* 47, 65-139, 2002.
7. BASF, DRP 296 866, 1912.
8. Rostrup-Nielsen, J.R., Sehested, J., *Whisker Carbon Revisited*, *Stud. Surf. Sci. Catal.*, 139, 1, 2001.
9. Twigg, M.V., Carbon Formation on Reforming Catalyst, *Catalyst Handbook*, 2<sup>nd</sup> ed., Manson Publishing, 1996.

10. Rostrup-Nielsen, J.R. and Bak Hansen, J.H., *J. Catal.*, 144, 38, 1993.
11. Zhu, Q., Zhao, X., Deng, Y., *J. Nat. Gas. Chem.* 13, 191, 2004.
12. Enger B.C., Lødeng R. and Holmen A., *Applied Catalysis A: General*, 346, 1–27, 2008.
13. Berger R.J., Marin G.B., *Ind. Eng. Chem. Res.*, 38, 2582-2592, 1999.
14. Hickman, D.A. and Schmidt, L.D., *Science* 259, 343-346, 1993.
15. Claridge, J.B., Green, M.L.H., Tsang, S.C., York, A.P.E., Ashcroft, A.T., Battle, P.D., *Catal. Lett.*, 22, 299, 1993.
16. Hickmann, D.A. and Schmidt, L.D., *J. Catal.*, 138, 267, 1992.
17. Hickmann, D.A., Hauptfear E.A. and L.D. Schmidt, *Catal. Lett.*, 17, 223, 1993.
18. Hickmann, D.A. and Schmidt, L.D., *AIChE J.*, 39, 1164, 1993.
19. Prettre, M., Eichner Ch. and Perrin, M., *Trans. Faraday Soc.*, 42, 335, 1946.
20. Vermeiren, W.J.M., Blomsma, E. and Jacobs, P.A., *Catal. Today*, 13, 427, 1992.
21. W. Weng, W., Chen, M., Yan, Q., Wu, T., Chao, Z., Liao, Y. and Wan, H., *Chin. Sci. Bull.*, 45, 2236, 2000.
22. W. Weng, W., Chen, M., Yan, Q., Wu, T., Chao, Z., Liao, Y. and Wan, H., *Catal. Today*, 63, 317, 2000.

23. Weng, W., Yan, Q. G., Luo, C.R., Liao, Y.Y. and Wan, H.L., *Catal. Lett.* 74, 37, 2001.
24. Aasberg-Petersen, K., Christensen, T.S., Stub Nielsen, C., Dybkjaer, I., *Recent developments in autothermal reforming and prereforming for synthesis gas production in GTL Applications, Fuel Process. Technol.*, 83, 253, 2002.
25. Bharadwaj, S.S. and Schmidt L.D., *Synthesis gas formation by catalytic oxidation of methane in fluidized bed reactors, J. Catal.*, 146, 11-21, 1994.
26. Pugsley, T.S. and Malcus, S., *Partial oxidation of methane in a circulating fluidized-bed catalytic reactor, Ind. Eng. Chem. Res.*, 35, 4567-4571, 1997.
27. Marschall, K.-J. and Mleczko, L., *Short-contact-time reactor for catalytic partial oxidation of methane, Ind. Eng. Chem. Res.*, 38, 1813-1821, 1997.
28. Nozaki T. and Fujimoto K., *AIChE Journal*, 40, 870, 1994.
29. Caoa, Z., Jiangb, H., Luo, H., Baumannc, S., Meulenbergc, W.A., Vossd, H., Caroa J., *Catalysis Today*, 193, 2–7, 2012.
30. Wolf, D., Slinko, M., Kurkina Baerns, E., *Applied Catalysis A: General*, 166, 47-54, 1998.
31. Dittmeyer, R., Hollein, V., Daub, K., *J. Mol. Catal. A: Chem.*, 173, 135–184, 2001.
32. van de Graaf, J.M., Zwiép, M., Kapteijn, F., Moulijn, J.A., *Chem. Eng. Sci.* 54, 1441–1445, 1999.

33. Jiang, H.Q., Wang, H.H., Liang, F.Y., Werth, S., Schirrmeister, S., Schiestel, T., Caro, J., *Catal. Today*, 156, 187–190, 2010.
34. Evdou, A., Zaspalis, V., Nalbandian, L., *Fuel*, 89, 1265–1273, 2010.
35. Nozaki T. and Fujimoto K., *AIChE Journal*, 40, 870, 1994.
36. K. Schultz, *Thermochemical Production of Hydrogen from Solar and Nuclear Energy*, Presentation to the Stanford Global Climate and Energy Project, 2003.
37. Carrillo, A.J., Moya, J., Bayón, A., Jana, P., A. de la Peña O’Shea, v., Romero, M., Gonzalez-Aguilar, J., P. Serrano, D., Pizarro, P. and M. Coronado J., *Solar Energy Materials & Solar Cells*, 123, 47, 2014.
38. Kuravi, S., Trahan, J., Goswami, D.Y., Rahman, M.M., Stefanakos, E.K., *Thermal energy storage technologies and systems for concentrating solar power plants*, *Prog. Energy Combust. Sci.*, 39, 285, 2013.
39. Block, T., Knoblauch, N. and Schmücker M., *Thermochimica Acta*, 577, 25, 2014.
40. Agrafiotis, C., Roeb, M., Schmücker, M. and Sattler C., *Solar Energy*, 102, 189, 2014.
41. Millera, J.E., Ambrosinia, A., Cokera, E.N., Allendorfb, M.D. and McDanielb, A.H., *Advancing oxide materials for thermochemical production of solar fuels*, *Energy Procedia*, 49, 2019, 2014.
42. Penner, S.S., *Energy*, 31, 33, 2006.

43. O'Keefe, D., Allen, C., Besenbruch, G., Brown, L., Norman, J., Sharp, R. and McCorkle, K., *Preliminary results from bench-scale testing of a sulfur–iodine thermochemical water-splitting cycle*, *Int. J. Hydrogen Energy*, 7, 381, 1982.
44. Sakurai, M., Bilgen, E., Tsutsumi, A. and Yoshida, K., *Solar UT-3 thermochemical cycle for hydrogen production*, *Solar Energy*, 57, 51, 1996.
45. Perret, R., *Solar Thermochemical Hydrogen Production Research (STCH)*, *Sandia National Laboratories Report*, 2011.
46. Alxneit, I., *Solar Energy*, 82, 959, 2008.
47. Nakamura, T., *Solar Energy*, 19, 467, 1977.
48. Xiao, L., Wu, S.Y. and Li Y.R., *Renewable Energy*, 41, 1, 2012.
49. Steinfeld A., *Solar thermochemical production of hydrogen e a review*. *Solar Energy* 78, 603, 2005.
50. Scheffe, J.R. and Steinfeld, A., *Mater. Today*, article in press, 2014.
51. Chambon, M., Abanades, S. and Flamant, G., *Kinetic investigation of hydrogen generation from hydrolysis of SnO and Zn solar nanopowders*, *International Journal of Hydrogen Energy*, 34, 5326, 2009.
52. Kang, K-S., Kim, C-H., Cho, W-C., Bae, K-K., Kim, S-H. and Park, C-S., *Novel two-step thermochemical cycle for hydrogen production from water using germanium oxide: KIER 4 thermochemical cycle*, *International Journal of Hydrogen Energy*, 34, 4283, 2009.
53. Gálvez, M.E., Frei, A., Albisetti, G., Lunardi, G. and Steinfeld, A., *Solar hydrogen production via a two-step thermochemical process based on MgO/Mg*

- redox reactions thermodynamic and kinetic analyses, International Journal of Hydrogen Energy*, 33, 2880, 2008.
54. Steinfeld, A., *Solar hydrogen production via a 2-step water-splitting thermochemical cycle based on Zn/ZnO redox reactions, Int. J. Hydrogen Energy*, 27, 611, 2002.
55. Steinfeld, A. and Fletcher, E.A., *Theoretical and experimental investigation of the carbothermic reduction of Fe<sub>2</sub>O<sub>3</sub> using solar energy, Energy*, 16, 1011, 1991.
56. Calisan, A., Ates, C., Kincal, S. and Uner D., *Using nonstoichiometric Co-Pb mixed metal oxides for solar thermal synthesis of hydrogen and CO, 249th ACS National Meeting, Chicago, 2014.*
57. Abanades, S. and Flamant, G., *Thermochemical hydrogen production from a two-step solar-driven water-splitting cycle based on cerium oxides, Solar Energy*, 80, 1611, 2006.
58. Furler, P., Scheffe, J.R. and Steinfeld, A., *Energy Environ. Sci.*, 5, 6098, 2012.
59. Chueh, W.C. and Haile, S.M., *Philos. Trans. R. Soc. A: Math. Phys. Eng. Sci.*, 368, 3269, 2010.
60. Campbell, F.C., *Phase Diagrams Understanding the Basics*, ASM International the Materials Information Society, Ohio, 2012.
61. Kubaschewski, O. and Alcock, C. B., *Metallurgical thermochemistry*, Pergamon Press, New York 1979.
62. Kubaschewski, O. and Hopkins, B. E., *Oxidation of metals and alloys*, London, Butterworths, 1962.

63. Barin, I., *Thermochemical properties of Pure Substances*, Weinheim, Basel, 1989.
64. Budrugaec, P., and Segal, E., *Applicability of the Kissinger equation in thermal analysis revisited*, *J. Therm. Anal. Calorim.*, 88, 703, 2007.
65. Nishizaki, H., Yoshida, K. and Wang, J. H., *J. Appl. Polym. Sci.*, 25, 2869, 1980.
66. Petrovic Z.S. and Zavargo Z.Z., *Journal of Applied Polymer Science*, 32, 4353, 1986.
67. Kissinger H.E., *Analytical Chemistry*, 29, 11, 1702, 1957.
68. Sestak, J. and Malek J., *Phenomenological models of heterogeneous reactions*, *Solid State Ionics*, 63-65, 245, 1993.
69. Gelin P., Primet M., *App. Catal.* 39, 1-37, 2002.
70. Bezemer G.L., Falke U., Van Dillen A.J., De Jong K.P., *Chem. Commun.*, 6, 731, 2005.
71. Pollard M.J., Weinstock B.A., Bitterwolf T.E., Griffiths P.R., Newbery A.P., Paine J.B., *J. Catal.* 254, 218-225, 2008.
72. Backman L.B., Rautiainen A., Lindblad M., Jylha O., Krause A.O.I., *Appl. Catal. A*, 208, 223-234, 2001.
73. Petyk J., Kolakowska E., *App. Catal., B*, 24, 121-128, 2000.
74. Yan Ma C., Mu Z., Jun Li J., Gang Yin Y., Cheng J., Qing Lu G., Ping Hao Z., Zhang Q., *J. Am. Chem. Soc.*, 132, 2608-2613, 2010.

75. Davies T., Garcia T., Solsona B., Taylor S.H., *Chem. Commun.* 32, 3417-3419, 2006.
76. Finocchio E., Busca G., Lorenzelli V., Sanchez E.V., *J. Chem. Soc., Faraday Trans.*, 92(9), 1587-1593, 1996.
77. Waychunas, G.A., Zhang, H.Z. *Structure, chemistry, and properties of mineral nanoparticles*, *Elements*, 4, 381-387, 2008.
78. Auffan, M., Rose, J., Bottero, J-Y., Lowry, G. V., Jolivet, J-P., Wiesner, M. R., *Towards a definition of inorganic nanoparticles from an environmental, health and safety perspective*, *Nature Nanotechnology*, 4, 634-641, 2009.
79. Navrotsky, A., Mazeina, L., Majzlan, J., *Size driven structural and thermodynamic complexity in iron oxides*, *Science*, 319, 1635-1639, 2008.
80. Madden, A.S., Hochella, Jr., M.F., *A test of geochemical reactivity as a function of mineral size: Manganese oxidation promoted by haematite nanoparticles*, *Geochimica et Cosmochimica Acta*, 69, 389-398, 2005.
81. Chen, L.X., Rajh, T., Jager, W., Nedeljkovic, J., Thurnauer, M.C., *X-ray absorption reveals surface structure of titanium dioxide nanoparticles*. *Journal of Synchrotron Radiation* 6, 445-447, 1999.
82. Section 14, *Does Size Matter? The Effect of Size on Nanoparticle Structure and Properties Geochemical Perspectives*, 611-627, 2012.
83. J. M. McHale, A. Auroux, A. J. Perrotta, A. Navrotsky, *Science*, 277 (5327), 788-791, 1997.
84. Navrotsky A., Ma C., Lilova K., Birkner N., *Science*, 330, 199, 2010.

85. Lu, F., Zhang, J, Navrotsky, A., Ewing, R.C., and Lian, J., *Temperature And Size Effects On Radiation-Induced Phase Transformation In Monoclinic Nano-Sized Zirconia, Microscopy and Microanalysis*, 16, 1624-1625, 2012.
86. Yan Ma C., Mu Z., Jun Li J., Gang Yin Y., Cheng J., Qing Lu G., Ping Hao Z., Zhang Qiao S., *J. Am. Chem. Soc.*, 132, 2608-2613, 2010.
87. Davies T., Gracia T., Solsana B., Taylor S.H., *Chem. Commun.*, 32, 3417-3419, 2006.
88. Finocchio E., Busca G., Lorenzelli V., Sanchez E.V, *J.Chem. Soc., Faraday Trans.*, 92, 1587-1593, 1996.
89. Dubois, J.L., *Catal. Today*, 99, 5-14, 2005.
90. Tanga, C-W., Wang, C-H. and Chien, S-H., *Thermochimica Acta*, 473, 68, 2008.
91. Tucakovic, B., Majstorovica, D., Jelic, D. and Mentus, S., *Thermochimica Acta*, 541, 15, 2012.
92. Jaffari, G.H., Lin, H-Y., Ni, C. and Shah, S. I., *Materials Science and Engineering: B*, 164, 23, 2009.
93. Metz, R., Jonathan, M., Delalu, H., Ananthakumar, S. and Hassazadeh, M., *Ceramics International*, 36, 855, 2010.
94. Lafleurielle, M, Millot, F., Dhalenne, G. and Revcolevschi, A., *Solid State Ionics*, 89, 139, 1996.
95. Treybal, R.E., *Mass Transfer Operations, Diffusion in Solids*, McGraw-Hill, Inc., 3<sup>rd</sup> Edition, 1980.

96. Joshi, J. B. and Doraiswamy, L. K., *Chapter 11 Chemical Reaction Engineering*, Albright's chemical engineering handbook, Taylor & Francis Group, LLC, 2009.
97. Levenspiel, O., *Chemical Reaction Engineering*, Third Ed., John Wiley & Sons, 1999.
98. Wen, C. Y., *Ind. Eng. Chem.*, 60 (9), 34, 1968.
99. Ishida, M. and Wen, C. Y., *Chem. Eng. Sci.*, 26, 1031, 1971.
100. Ishida, M., Wen, C. Y. and Shirai, T., *Chem. Eng. Sci.*, 26, 1043, 1971.
101. Wen, C. Y., and Wang, S. C., *Ind. Eng. Chem.*, 62 (8), 30, 1970.
102. Doraiswamy, L. K. and Sharma, M. M., *Heterogeneous Reactions: Analysis, Examples, and Reactor Design*, vol. 1, Gas-Solid and Solid-Solid Reactions, vol. 2, Fluid-Fluid and Fluid-Fluid-Solid Reactions. New York: John Wiley & Sons, 1984.
103. Ishida, M. and Wen, C. Y., *AIChE J.*, 14, 311, 1968.
104. Bowen, J. H. and Cheng, C. K., *Chem. Eng. Sci.*, 24, 1829, 1969.
105. Sohn, H.Y. and Szekely, J., *Chem. Eng. Sci.*, 27, 763, 1972.
106. Sohn, H.Y. and Szekely, J., *Chem. Eng. Sci.*, 29, 630, 1974.
107. Reyes, S., and Jensen, K.F., *Chem. Eng. Sci.*, 42, 565, 1987.
108. Avrami, M., *J. Chem. Phys.* 7, 1103, 1939.

109. Avrami, M., *J. Chem. Phys.*, 8, 212, 1940.
110. Miller, J.E., Ambrosini, A., Coker, E.N., Allendorf, M.D. and McDaniel, A.H., *Energy Procedia*, 49, 2019, 2014.
111. Wong, B., *Thermochemical Heat Storage for Concentrated Solar Power*, U.S. Department of Energy under DE-FG36-08GO18145, GENERAL ATOMICS PROJECT 30314, 2011.
112. Song, X. and Guo, Z., *Energy Conversion and Management*, 47, 560–569, 2006.
113. Bizzi, M., Basini, L., Saracco, G. and Specchia, V., *Chemical Engineering Journal*, 90, 97–106, 2002.
114. Liu, T., Snyder, C. and Veser, G., *Ind. Eng. Chem. Res.* 46, 9045-9052, 2007.
115. Veser, G., Frauhammer, J. and Friedle, U., *Catalysis Today*, 61, 55–64, 2000.
116. Vernon, P.D.F., Green, M. L.H., Cheetham, A.K. and Ashcroft A.T., *Catalysis Letters*, 6, 181-186, 1990.
117. York, P.E.A., Xiao, T., Green, M.L.H. and Claridge, J.B., *Catalysis Reviews: Science and Engineering*, 49:4, 511-560, 2007.
118. York, P.E.A., Xiao, T. and Green, M.L.H., *Topics in Catalysis*, 22, 3–4, 345-358, 2003.

119. Tsang S.C, Claridge, J.B. and Green, M.L.H., *Catalysis Today*, 23, 3-15, 1995.
120. Chang, Y.F. and Heinemann, H., *Catalysis Letters*, 21, 215-224, 1993.
121. Çalışan, A., *Syngas Production over Reducible Metal Oxides*, 2013.
122. Karagiannakis, G., Pagkoura, C., Zygoianni, A. Lorentzou, S. and Konstandopoulos, A.G., *Energy Procedia*, 49,820, 2014.
123. Charvin, P., Stephane, A., Florent, L. and Gilles, F., *Analysis of solar chemical processes for hydrogen production from water splitting thermochemical cycles*, *Energy Conversion and Management*, 49(6),1547, 2008.
124. Lewis, N.S. and Nocera, D.G., *Powering the planet: chemical challenges in solar energy utilization*, *Proceedings of the National Academy of Sciences USA* 103(43), 15729, 2006.
125. Jiang, T., Mowbray, D. J., Dobrin, S., Falsig, H., Hvolbæk, B., Bligaard, T. and Nørskov J. K., *J. Phys. Chem. C*,113 (24), 10548, 2009.
126. *Catal. Lett.* 141,3,370,2011.
127. *Phys. Chem. Chem. Phys.*, 13, 20760, 2011
128. *CatApp BEP*.

## APPENDIX A

### THERMODYNAMICS

Table A:1 Temperature averaged thermodynamic data for various oxides

Temperature Range (K)	Compound	Phase	Enthalpy kJ/mol	Entropy J/mol/K
298-1000	Ag <sub>2</sub> O	Solid	-28.1	-60.6
298-933	Al <sub>2</sub> O <sub>3</sub>	Solid	-1675.1	-313.2
933-2315	Al <sub>2</sub> O <sub>3</sub>	Solid	-1682.9	-323.2
723-2316	B <sub>2</sub> O <sub>3</sub>	Gas	-1229	-210
298-1002	BaO	Solid	-568.2	-97
298-1560	BeO	Solid	-608	-97.7
545-1097	Bi <sub>2</sub> O <sub>3</sub>	Solid	-590.2	-292.6
298-2500	CO	Gas	-112.9	86.5
298-2500	CO <sub>2</sub>	Gas	-394.8	0.836
298-1112	CaO	Solid	-633.1	-99
594-1040	CdO	Solid	-263.2	-104.9
1040-1500	CdO	Solid	-356.7	-198.5
298-1071	CeO <sub>2</sub>	Solid	-1084	-212
298-1071	Ce <sub>2</sub> O <sub>3</sub>	Solid	-1788	286.6
298-1400	CoO	Solid	-233.9	-70.7
1938-2023	CrO	Liquid	-334.2	63.8
1173-1923	Cr <sub>2</sub> O <sub>3</sub>	Solid	-1110.1	-249.3
1923-1938	Cr <sub>3</sub> O <sub>4</sub>	Solid	-1355	-265

Table A:1 Temperature averaged thermodynamic data for various oxides (continued)

298-1356	Cu <sub>2</sub> O	Solid	-168.4	-71.2
298-1356	CuO	Solid	-152.5	-85.3
298-1643	Fe <sub>0.947</sub> O	Solid	-263.7	-64.4
298-1650	FeO	Solid	-264	-64.6
298-1870	Fe <sub>3</sub> O <sub>4</sub>	Solid. α	-1103.1	-307.4
298-1735	Fe <sub>2</sub> O <sub>3</sub>	Solid. α	-815	-251.1
303-2068	Ga <sub>2</sub> O <sub>3</sub>	Solid	-1089.9	-323.6
298-1210	GeO <sub>2</sub>	Solid	-575	-188
298-2500	H <sub>2</sub> O	Gas	-247.4	-55.8
298-1973	HfO <sub>2</sub>	Solid	-1060	-174
298-773	HgO	Solid. red	-90.8	-70.3
298-1193	La <sub>2</sub> O <sub>3</sub>	Solid	-1790	-278
454-1620	Li <sub>2</sub> O	Solid	-603.8	-136.6
298-922	MgO	Solid	-601.2	-107.6
922-1378	MgO	Solid	-609.6	-116.5
1378-2000	MgO	Solid	-732.7	-206
298-1517	MnO	Solid	-388.9	-76.3
298-1517	Mn <sub>3</sub> O <sub>4</sub>	Solid. α	-1384.9	-344.4
298-1517	Mn <sub>2</sub> O <sub>3</sub>	Solid	-953.9	-255.2
298-783	MnO <sub>2</sub>	Solid	-519	-181
298-2273	MoO <sub>3</sub>	Solid	-1164.1	77.82
298-2210	NbO	Solid	-415	-87
298-2175	NbO <sub>2</sub>	Solid. α	-784	-167
298-1785	Nb <sub>2</sub> O <sub>5</sub>	Solid	-1888	-420
298-1728	NiO	Solid. α	-235.8	-86.2
298-1728	NiO	Solid. β	-235.8	-86.2
298-1728	NiO	Solid. γ	-235.8	-86.2
600-1473	Pb <sub>3</sub> O <sub>4</sub>	Solid	-702.5	-368.9
600-762	PbO	Solid. red	-221.5	-104.6
762-1170	PbO	Solid. yellow	-218.1	-100.2
298-904	Sb <sub>2</sub> O <sub>3</sub>	Solid	-687.6	-241.1
958-1973	SeO <sub>2</sub>	Gas	-178	-66.1
298-1685	SiO <sub>2</sub>	Solid	-907.1	-175.7

Table A:1 Temperature averaged thermodynamic data for various oxides (continued)

505-1973	SnO <sub>2</sub>	Solid	-574.9	-198.4
298-1943	TiO	Solid. $\alpha$	-514.6	-74.1
298-1943	TiO	Solid. $\beta$	-514.6	-74.1
298-1943	Ti <sub>2</sub> O <sub>3</sub>	Solid. $\alpha$	-1502.1	-258.1
298-1943	Ti <sub>2</sub> O <sub>3</sub>	Solid. $\beta$	-1502.1	-258.1
298-1943	Ti <sub>3</sub> O <sub>5</sub>	Solid. $\alpha$	-2435.1	-420.5
298-1943	Ti <sub>3</sub> O <sub>5</sub>	Solid. $\beta$	-2435.1	-420.5
298-1943	TiO <sub>2</sub>	Solid. rutile	-941	-177.6
298-1405	UO <sub>2</sub>	Solid	-1079.5	-167.4
298-2073	VO	Solid	-425	-80
298-1633	VO <sub>2</sub>	Solid. $\alpha$	-706	-155
298-1633	VO <sub>2</sub>	Solid. $\beta$	-706	-155
298-2343	V <sub>2</sub> O <sub>3</sub>	Solid	-1203	-238
298-2500	0.5O <sub>2</sub> + CO $\rightarrow$ CO <sub>2</sub>		-281.9	-85.664
298-2500	O <sub>2</sub> + C $\rightarrow$ CO <sub>2</sub>		-394.8	0.836
298-2500	C + 0.5O <sub>2</sub> $\rightarrow$ CO		-112.9	86.5
298-2500	H <sub>2</sub> + 0.5O <sub>2</sub> $\rightarrow$ H <sub>2</sub> O		-247.4	-55.8
298-2500	CH <sub>4</sub> +2O <sub>2</sub> $\rightarrow$ CO <sub>2</sub> +2H <sub>2</sub> O		-802.2	-2.064
298-2500	2CH <sub>4</sub> +0.5O <sub>2</sub> $\rightarrow$ C <sub>2</sub> H <sub>6</sub> +H <sub>2</sub> O		-156.4	-12.473
298-2500	C <sub>2</sub> H <sub>6</sub> +0.5O <sub>2</sub> $\rightarrow$ C <sub>2</sub> H <sub>4</sub> +H <sub>2</sub> O		-111.1	64.609
298-2500	CH <sub>4</sub> +1/2O <sub>2</sub> $\rightarrow$ CO+2H <sub>2</sub>		-138.4	353.9

Table A:2 Thermodynamic data at different temperatures used in thermodynamic analysis

Temperature (K)	CO		CO <sub>2</sub>		H <sub>2</sub> O	
	$\Delta H$ (kJ/mol)	$\Delta G$ (kJ/mol)	$\Delta H$ (kJ/mol)	$\Delta G$ (kJ/mol)	$\Delta H$ (kJ/mol)	$\Delta G$ (kJ/mol)
500	-110.00	-155.414	-393.666	-394.939	-243.896	-219.069
600	-110.15	-164.486	-393.803	-395.182	-244.797	-214.018
700	-110.47	-173.518	-393.983	-395.398	-245.658	-208.819
800	-110.91	-182.497	-394.188	-395.586	-246.461	-203.501
900	-111.42	-191.416	-394.405	-395.748	-247.198	-198.086
1000	-111.98	-200.275	-394.623	-395.886	-247.868	-192.593
1100	-112.59	-209.075	-394.838	-396.001	-248.468	-187.035
1200	-113.22	-217.819	-395.05	-396.098	-249.004	-181.426
1300	-113.87	-226.509	-395.257	-396.177	-249.479	-175.775
1400	-114.54	-235.149	-395.462	-396.24	-249.899	-170.09
1500	-115.23	-243.74	-395.668	-396.288	-250.269	-164.376
Temperature (K)	CoO		Co <sub>3</sub> O <sub>4</sub>		CH <sub>4</sub>	
	$\Delta H$ (kJ/mol)	$\Delta G$ (kJ/mol)	$\Delta H$ (kJ/mol)	$\Delta G$ (kJ/mol)	$\Delta H$ (kJ/mol)	$\Delta G$ (kJ/mol)
1600	-235.343	-198.632	-909.774	-716.825	-80.802	-32.741
1700	-234.402	-191.381	-908.999	-678.302	-83.303	-22.887
1800	-233.625	-184.275	-907.802	-639.941	-85.452	-12.643
1900	-233.428	-177.207	-907.337	-601.601	-87.238	-2.115
2000	-232.97	-170.209	-905.043	-563.516	-88.692	8.616
2100	-232.709	-163.251	-902.293	-525.712	-89.849	19.942
2200	-232.656	-156.309	-899.139	-488.203	-90.75	30.472
2300	-232.827	-149.363	-895.639	-450.998	-91.437	41.524
2400	-233.353	-142.39	-892.206	-414.087	-91.945	52.626
2500	-234.348	-135.357	-889.197	-377.422	-92.308	63.761
2600	-243.217	-128.288	-881.838	-341.108	-92.553	74.918



## A.2 Free Energy Minimization

### A.2.1 Methodology Used

Total Gibbs free energy of a system can be evaluated with;

$$G = \sum_{i=1}^P \sum_{j=1}^C n_j^i g_j^i$$

Where

$$g_j^i = g_j^0 + RT \ln(a_j^i)$$

$$a_j^s = \gamma_j^s x_j^s \quad \text{for solids,}$$

$$a_j^l = \gamma_j^l x_j^l \quad \text{for liquids,}$$

$$a_j^g = P y_j \quad \text{for gases.}$$

If the activity coefficients are taken as one, the function to be minimized becomes,

$$f = \frac{G}{RT} = \sum_{j=1}^C n_j^i (g_j^0 + RT \ln(x_j^s)) / RT + \sum_{j=1}^C n_j^i (g_j^0 + RT \ln(x_j^l)) / RT + \sum_{j=1}^C n_j^i (g_j^0 + RT \ln(P y_j)) / RT$$

### A.2.2 Lagrange Multipliers Method

For a function to be minimized,  $f$ , that is;

$$f(x_1, x_2, \dots, x_n) \rightarrow \min$$

If it is related to a function  $\phi$  such that,

$$\phi_k(x_1, x_2, \dots, x_n) = 0 \quad k = 1, 2, \dots, m; \quad m < n$$

Then the function to be minimized becomes,

$$\varphi = f + \sum \lambda_k \phi_k$$

Where  $\lambda_k$  is, Lagrange Multipliers, computed thorough minimization process, which relies on,

$$\frac{\delta \varphi}{\delta x_i} = 0 \quad i = 1, 2, 3, \dots, n$$

### A.2.3 Lagrange Multipliers for Free Energy Minimization

Since elements are to be conserved within the system, related  $\phi_k$  for total free energy can be expresses as follows,

$$\begin{aligned} \phi &= (\text{Amount of an element}) \\ &\quad - (\text{Amount of that element in an compound})(\text{amount of compound}) \end{aligned}$$

$$\phi = \alpha - \beta \cdot \gamma$$

For more than one phase and species, for element k,

$$\phi_k = \alpha_k - \sum_{i=1}^P \sum_{j=1}^C \beta_j^i \gamma_j^i = 0$$

### A.2.4 Other Constraints

Besides the above constraints, n value for any species cannot be less than zero. In other words, lower limit has to be set so that none of the compounds has a negative amount after minimization.

### A.2.5 Procedure

- i. All possible chemicals and necessary free energy data are introduced.
- ii. Feed composition and feed conditions are set.
- iii. Initial composition is given as an initial guess and lower boundary is set.
- iv. By using Lagrange Multipliers method, total free energy is minimized by changing the compositions of the species while satisfying the conservation of species and other constraints.
- v. Final compositions are printed out.

### A.2.6 MATLAB Code

#### Main Program

```
%% MAIN PROGRAM %%

global Gj T R P Po i

fileID = fopen('gibbs.txt','w');
fprintf(fileID,'%12s %12s %12s %12s %12s %12s %12s %12s
%12s\r\n','Co','CoO','Co3O4','CO','CO2','CH4','H2','O2','H2O');

for i=1:9

Gj = [ 0 -198.632 -716.825 -155.414 -394.939 -32.741 0 0 -219.069
      0 -191.381 -678.302 -164.486 -395.182 -22.887 0 0 -214.018
      0 -184.275 -639.941 -173.518 -395.398 -12.643 0 0 -208.819
      0 -177.207 -601.601 -182.497 -395.586 -2.115 0 0 -203.501
      0 -170.209 -563.516 -191.416 -395.748 8.616 0 0 -198.086
      0 -163.251 -525.712 -200.275 -395.886 19.492 0 0 -192.593
      0 -156.309 -488.203 -209.075 -396.001 30.472 0 0 -187.035
```

```

0 -149.363 -450.998 -217.819 -396.098 41.524 0 0 -181.426
0 -142.390 -414.087 -226.509 -396.177 52.626 0 0 -175.775 ];

T = [500
600
700
800
900
1000
1100
1200
1300]; %K

R = 8.314; % kJ/mol/K
P = 1; % atm, this is the total pressure in the medium
Po = 1; % atm, this is the standard state pressure

% gibbs free energy of species

species = {'Co' 'CoO' 'Co3O4' 'CO' 'CO2' 'CH4' 'H2' 'O2' 'H2O'};

% Atoms for species
Aeq = [ 1 1 3 0 0 0 0 0 0      %Co
        0 1 4 1 2 0 0 2 1      %O
        0 0 0 0 0 4 2 0 2      %H
        0 0 0 1 1 1 0 0 0 ];   %C

% Feed Information
beq = [0      % mol Co
       17     % mol O
       30     % mol H
       5];    % mol C

%lower limit
LB = [0 0 0 0 0 0 0 0 0];

```

```

% initial guess
x0 = [0.5 0.5 0.5 0.5 0.5 0.5 0.5 0.5 0.5];

options = optimset('Algorithm','sqp','TolX',1e-6);
x = fmincon(@func,x0,[],[],Aeq,beq,LB,[],[],options)

fprintf(fileID,'%12.8f %12.8f %12.8f %12.8f %12.8f %12.8f %12.8f %12.8f
%12.8f\r\n',x);
fclose(fileID);

end

```

## Function 1

```

function G = func(nj)
%% SUB PROGRAM %%
%nj= [0.5 0.5 0.5 0.5 0.5 0.5 0.5 0.5 0.5];

%% gibbs free energies:
%% rows    =>  temperatures from 500 to 1300 with 100K increments
%% columns =>  show compounds in the order of species given in the code
% species = {'Co','CoO','Co3O4','CO','CO2','CH4','H2','O2','H2O'};

global Gj T R P Po i

% Gibbs energy
Enj = sum(nj(1,4)+nj(1,5)+nj(1,6)+nj(1,7)+nj(1,8)+nj(1,9));
G = nj(1,1)*Gj(i,1)/R/T(i) ...
+nj(1,2)* Gj(i,2)/R/T(i) ...
+nj(1,3)* Gj(i,3)/R/T(i) ...
+nj(1,4)*(Gj(i,4)/R/T(i) + log(nj(1,4)/Enj*P/Po)) ...% ln(P_i)
+nj(1,5)*(Gj(i,5)/R/T(i) + log(nj(1,5)/Enj*P/Po)) ...
+nj(1,6)*(Gj(i,6)/R/T(i) + log(nj(1,6)/Enj*P/Po)) ...
+nj(1,7)*(Gj(i,7)/R/T(i) + log(nj(1,7)/Enj*P/Po)) ...
+nj(1,8)*(Gj(i,8)/R/T(i) + log(nj(1,8)/Enj*P/Po)) ...

```

```
+nj(1,9)*(Gj(i,9)/R/T(i) + log(nj(1,9)/Enj*P/Po));
end
```

## Function 2

```
function G = func(nj)
%% SUB PROGRAM %%
%nj= [0.5 0.5 0.5 0.5 0.5 0.5 0.5 0.5 0.5];

%% gibbs free energies:
%% rows    =>  temperatures from 500 to 1300 with 100K increments
%% columns =>  show compounds in the order of species given in the code
% species = {'Co' 'CoO' 'Co3O4' 'CO' 'CO2' 'CH4' 'H2' 'O2' 'H2O'};

global Gj T R P Po i

% Gibbs energy
Enj = sum(nj(1,4)+nj(1,5)+nj(1,6)+nj(1,7)+nj(1,8)+nj(1,9));
G = nj(1,1)*Gj(i,1)/R/T(i) ...
+nj(1,2)* Gj(i,2)/R/T(i) ...
+nj(1,3)* Gj(i,3)/R/T(i) ...
+nj(1,4)*(Gj(i,4)/R/T(i) )...% ln(P_i)
+nj(1,5)*(Gj(i,5)/R/T(i) ) ...
+nj(1,6)*(Gj(i,6)/R/T(i) ) ...
+nj(1,7)*(Gj(i,7)/R/T(i) ) ...
+nj(1,8)*(Gj(i,8)/R/T(i) ) ...
+nj(1,9)*(Gj(i,9)/R/T(i) );
end
```

### A.3 Thermal Efficiency Comparison

Table A:3 Thermal efficiencies of various metal oxides

Redox Couple	Decomposition Temperature of Metal Oxide (K)	Reoxidation Temperature with Water (K)	Carnot Efficiency %	$\Delta G_{\text{water}}$ at Reoxidation Temp. (kJ/mol)	$\Delta H_{\text{water}}$ at Decomposition Temp. (kJ/mol)	Efficiency %
$\text{Fe}_2\text{O}_4/\text{m} - \text{ZrO}_2$	1673	1373	17.9	-171.6	-250.7	68.4
$\text{Mn}_{0.36}\text{Fe}_{2.64}\text{O}_4/\text{m} - \text{ZrO}_2$	1673	1373	17.9	-171.6	-250.7	68.4
$\text{NiFe}_2\text{O}_4/\text{m} - \text{ZrO}_2$	1673	1373	17.9	-171.6	-250.7	68.4
$\text{Co}_{0.9}\text{Fe}_{2.1}\text{O}_4/\text{m} - \text{ZrO}_2$	1723	1373	20.3	-171.6	-250.8	68.4
$\text{CoFe}_2\text{O}_4/\text{Al}_2\text{O}_3$	1473	1273	13.6	-177.0	-250.1	70.8
$\text{Fe}_3\text{O}_4$	1973	848	57.0	-200.1	-251.2	79.7
$\text{CeO}_2$	1673	1373	17.9	-171.6	-250.7	68.4
$\text{Ce}_{0.75}\text{Zr}_{0.25}\text{O}_2$	1673	1373	17.9	-171.6	-250.7	68.4
$\text{NiFe}_2\text{O}_4$	1673	1373	17.9	-171.6	-250.7	68.4
Sr-, Mn-doped $\text{LaAlO}_3$	1623	1273	21.6	-177.0	-250.6	70.6

## APPENDIX B

### MASS AND HEAT TRANSFER CALCULATIONS

#### B.1 Diffusivity of Oxygen in Different Mediums

Table B:1 Diffusivities of oxygen in various metal-metal oxides

Specimen	Temperature Range (K)	Pre-exp. (m <sup>2</sup> /s)	Activation Energy (kJ/mol)	Diffusivity at 1000 K
Nb [1]	348 to 368	$4.2 \pm 0.3 \times 10^{-7}$	107.2 ± 0.4	-
Si [2]	623-1473	$2.8 \times 10^{-7}$	250.39	$1.1 \times 10^{-12}$
Ge [2]	623-1473	$3.9 \times 10^{-7}$	198.18	$2.3 \times 10^{-20}$
Nb-O [7]	873–1373	$17 \pm 0.2 \times 10^{-7}$	108 ± 1	$1.7 \times 10^{-17}$
Ta-O [7]	873–1873	$3.5 \pm 0.3 \times 10^{-7}$	99.3 ± 0.7	$3.9 \times 10^{-12}$
CuO [7]	873–1273	$5.8 \times 10^{-7}$	57.4 ± 11.6	$2.3 \times 10^{-12}$
Ni [3]	950-1600	$392 \times 10^{-7}$	192.38	$5.8 \times 10^{-10}$
WO <sub>3</sub> [4]	841-1181	$0.68 \times 10^{-7}$	125.06	$3.5 \times 10^{-15}$

Table B:1 Diffusivities of oxygen in various metal-metal oxides (continued)

ZnO (single crystal 90 deg.) [5]	1190-1315	$1.2 \times 10^8$	571±28	$2 \times 10^{-14}$
ZnO (single crystal parallel) [5]	1190-1315	$1.5 \times 10^5$	491±50	$1.8 \times 10^{-22}$
Pure (poly) [5]	1190-1315	$5 \times 10^{-3}$	298±91	$3.4 \times 10^{-21}$
Al-doped (poly) [5]	1190-1315	7	361±75	$1.4 \times 10^{-18}$
Co- doped (poly) [5]	1190-1315	0.2	332±77	$9.7 \times 10^{-19}$
Mn-doped (poly) [5]	1190-1315	$1 \times 10^{-8}$	165±237	$9.1 \times 10^{-19}$
Li- doped (poly) [5]	1190-1315	$2 \times 10^{-11}$	123±27	$2.4 \times 10^{-17}$
PbO [6]	973-1123	$10^{-14}$	RT	$10^{-14}$
Pt [8]	1700-1780	$9.3 \pm 1.8 \times 10^{-4}$	78± 25	$7.8 \times 10^{-08}$
CoO [9]	1440-1830	$50 \times 10^{-4}$	95± 5	$5.4 \times 10^{-08}$
Ni [10]	1173			$2.30 \times 10^{-12}$
Th [11]	1100-1800	$5.73 \times 10^{-6} // 10^{-10}$	49.9 // 17.6	$1.41 \times 10^{-8} // 1.2 \times 10^{-11}$
MgO [12]	1023-1248	$2.12 \times 10^{-11}$	327	$1.8 \times 10^{-28}$
Sc <sub>2</sub> O <sub>3</sub> [13]	1380-1571	$7.72 \times 10^{-8}$	160.094	$3.3 \times 10^{-16}$
Y <sub>2</sub> O <sub>3</sub> [13]	1337-1514	$6.06 \times 10^{-10}$	81.844	$3.2 \times 10^{-14}$
Dy <sub>2</sub> O <sub>3</sub> [13]	1360-1508	$1.63 \times 10^{-9}$	109.683	$3.0 \times 10^{-15}$
Ho <sub>2</sub> O <sub>3</sub> [13]	1323-1547	$7.18 \times 10^{-7}$	169.415	$1.0 \times 10^{-15}$
Er <sub>2</sub> O <sub>3</sub> [13]	1333-1565	$1.31 \times 10^{-8}$	125.902	$3.5 \times 10^{-15}$
Tm <sub>2</sub> O <sub>3</sub> [13]	1288-1508	$1.14 \times 10^{-6}$	190.441	$1.3 \times 10^{-16}$

Table B:1 Diffusivities of oxygen in various metal-metal oxides (continued)

Lu <sub>2</sub> O <sub>3</sub> [13]	1293-1570	$1.88 \times 10^{-8}$	124.397	$6 \times 10^{-15}$
Zr [14]	673-858	$9.4 \times 10^{-4}$	$216.440 \pm 0.92$	$4.6 \times 10^{-15}$
PbO [15]	773-923	$5.39 \times 10^{-9}$	22.4	$3.6 \times 10^{-10}$

1. Masa-Aki Okamoto. An elasticity study on mobility of interstitial oxygen in niobium. *Acta Metallurgica*. Volume 31. Issue 8. August 1983. Pages 1169–1175.
2. Gusakov. V. *Solid State Phenomena*. Volume 108-109. 2005. Pages 413-418.
3. Garruchet. S S.Politano. O ; Arnoux. P Vignal. *Solid State Communications*. Volume 150. Issue 9-10. Pages: 439-442 2010.
4. V.K. Sikka. C.J. Rosa. *Corrosion Science*. Volume 20. Issues 11–12. 1980. Pages 1201–1219.
5. Hajime Haneda. Isao Sakaguchi. Akio Watanabe. Takamasa Ishigaki & Junzo Tanaka. *Journal of Electroceramics* 4:S1. Pages 41-48. 1999.
6. Takao Nozaki and Kaoru Fujimoto. *AIChE Journal*. 1994 Vol. 40. No. 5. pages 870-878.
7. R. Kirchheim. *Acta Metallurgica*. Volume 27. Issue 5. May Pages 869–878. 1979.
8. Velho L.R.. Bartlett R.V.. *Metallurgical Transactions*. Volume 3. 65. 1972.
9. Chen W.K. Jackson R.A.. *Journal of Physics and Chemistry of Solids*. Volume 30. 1309-1314. 1969.
10. C. J. Smithells and C. E. Ransley. *Proceedings of the Royal Society of London. Series A. Mathematical and Physical Sciences*. Vol. 157. No. 891. pp. 292-302. 1936.
11. Ando K.. Oishi Y.. Hidaka Y.. *J. Chem. Phys.*. 65. 2751. 1976.
12. *Diffusion in Oxides. Reviews in Mineralogy & Geochemistry*. Vol. 72 pp. 757-825. 2010.

13. M. F. Berard, C. D. Wirkus, and D. R. Wilder. *Journal of The American Ceramic Society*. 51. 643. 1968.

14. Pemsler J.P. *Journal of the Electrochemical Society*. 105. 315. 1958.

15. Robert L . Strong, Barbara A. Thoxpson. *Self-Diffusion of Oxygen in Lead Oxide*. 1963.

## B.2 Metal-Oxygen Bond Energies

Table B:2 Metal-oxygen bond energies for various metal oxides

<b>Bond</b>	<b>Energy (kJ/mol)</b>	<b>Method</b>
Cu-O	287.4±11.6	GIB MS
Cu-O (100)	452.7	Review
Cu-O (110)	465.3	Review
Cu-O (111)	431.0	Review
Cu-O <sub>2</sub>	63±29	Kinetics
Cu-O <sub>2</sub> (plate surface)	21.8	Calorimetry
Cu-O <sub>2</sub> (polycryst. Surface)	326	Review
Pb-O	382.0±12.6	Review
Pb-O <sub>2</sub>	<155 (181)	PD ( $\Delta H_f$ )
PbO-PbO	263.6±21	Review
Nb-Nb	513	CID
Nb-O	756 (726.5±10.6)	Spectroscopy(Derived)
NbO-O	648	$\Delta H_f$
Nb <sub>2</sub> -O	>357±48	GIB MS
Si-O	793.2±16.4	Spectroscopy
SiO-O	454.2	$\Delta H_f$
SiO-SiO	222±42	Review
Ge-O	652.7±8.4	MS
GeO-O	318	$\Delta H_f$
GeO-GeO	188.3±12.6	Review
Ta-O	793.9±16.4	Spectroscopy
TaO-O	643	$\Delta H_f$
Ta-O <sub>2</sub> (polycr. Surf.)	886	Calorimetry

Table B:2 Metal-oxygen bond energies for various metal oxides (continued)

WO-O	598	$\Delta H_f$
WOO-O	619	$\Delta H_f$
W-O (polycs. Surf.)	543	FEM
W-O (100)	523-569	Review
W-O (110)	540	Review
W-O (111)	96.7	TD
W-O (211)	42-59	FEM
W-O (311)	100	FEM
W-O (411)	220	FEM
W-O <sub>2</sub> (polycr. surface)	570	Review
Ni-O	366±30	HT MS
Ni-O (100)	505.4	Review
Ni-O (110)	519.7	Review
Ni-O (111)	481	Review
Ni-O <sub>2</sub>	239	Kinetics
Ni-O <sub>2</sub> (polycr. surf.)	448	Review
Ni-O <sub>2</sub> (100)	536	Calorimetry
Ni-O <sub>2</sub> (110)	550±7.5	Calorimetry
Ni-O <sub>2</sub> (111)	475±11	Calorimetry
Ni-O <sub>2</sub> (211)	440±19	Calorimetry
NiO-O <sub>2</sub> (polycr. surf.)	226	Review
Zn-O	<250 (159)	MS (GIB MS)
ZnO-O <sub>2</sub>	460	Review

Adopted from: Yu Ran Luo, Comprehensive Handbook of Chemical Bond Energies, CRC Press, 2007.

## B.3 Fundamental Calculations in Heat Transfer

### B.3.1 Number of molecules per $1\mu\text{m} \times 1\text{cm}$ surface

Normal spinel structure  $\text{Co}_3\text{O}_4$  has a lattice constant of  $8.08\text{ \AA}$  and has the following structure [1],

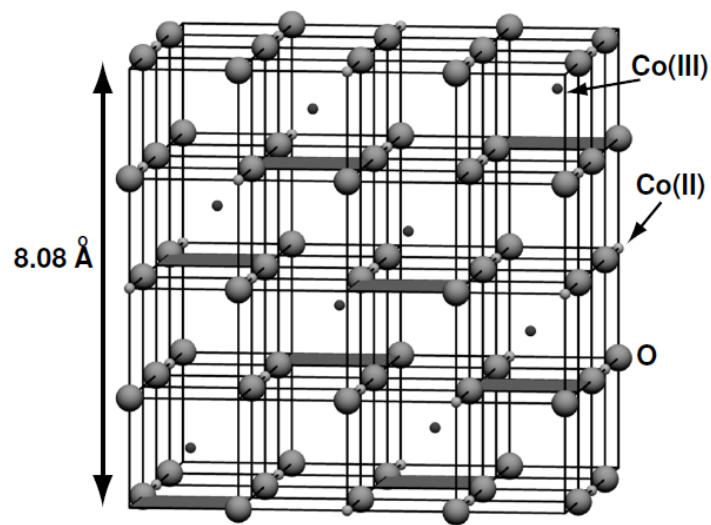


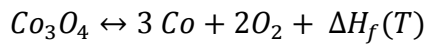
Figure B:1 Lattice structure of spinel cobalt oxide

[1] Wang, J., Low Energy Electron Di@raction Studies of Transition Metal Oxide Surfaces and Films, obtained from <http://nbn-resolving.de/urn/resolver.pl?urn=nbn%3Ade%3Agbv%3A3-000007962>, 2005.

For a unit cell surface, there are approximately 3 Co atoms giving one  $\text{Co}_3\text{O}_4$  and for a perfect surface, following is found,

$$\frac{1 \text{ Co}_3\text{O}_4}{0.653 \text{ nm}^2} \times 1\mu\text{m} \times 1\text{cm} = \frac{1 \text{ Co}_3\text{O}_4 \times 10^{-8} \text{ m}^2}{0.653 \times 10^{-18} \text{ m}^2} = 1.531 \times 10^{10} \text{ Co}_3\text{O}_4$$

### B.3.2 Heat released/m<sup>2</sup>



At 1000 K;

$$\Delta H_f(1000 \text{ K}) = 9.024 \times 10^5 \text{ J/mol}$$

# mols/m<sup>2</sup> is found as;

$$\frac{1 \text{ Co}_3\text{O}_4}{0.653 \text{ nm}^2} \times 1 \text{ m}^2 \times \frac{10^{18} \text{ nm}^2}{1 \text{ m}^2} \times \frac{1 \text{ mol}}{6.022 \times 10^{23}} = 2.542 \times 10^{-6} \frac{\text{mol Co}_3\text{O}_4}{\text{m}^2}$$

So heat released/m<sup>2</sup> is found as;

$$q = 2.542 \times 10^{-6} \frac{\text{mol Co}_3\text{O}_4}{\text{m}^2} \times 9.024 \frac{\text{J}}{\text{mol}} = 2.294 \frac{\text{J}}{\text{m}^2}$$

### B.3.3 Increase in Temperature when 1 mol of Co<sub>3</sub>O<sub>4</sub> is formed at 1000 K

$$Q = 9.024 \frac{\text{J}}{\text{mol}} \times 1 \text{ mol Co}_3\text{O}_4 = 9.024 \times 10^5 \text{ J}$$

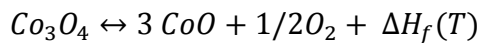
$$Cp_{\text{Co}_3\text{O}_4}(T) = 0.1263T + 86.002 \quad \text{in J/mol/K};$$

Energy balance gives;

$$Q + 1 \int_{1000}^T Cp_{\text{Co}_3\text{O}_4}(T) dT = 0 \text{ (Adiabatic)}$$

$$T = 3456.13 \text{ K}$$

For the adiabatic oxidation of CoO,



At 1000 K;

$$\Delta H_f(1000 \text{ K}) = 2.042 \times 10^5 \text{ J/mol}$$

$$T = 1780.59 \text{ K}$$

### B.3.4. Instantaneous Infinite Plane Source Emitting Half Space

For a wide plate, temperature profile when an instantaneous source introduced to the system is as follows;

$$T(x, t) = q/(\rho C_p)/(\pi \alpha t)^{0.5} \cdot \exp(-(x^2)/(4\alpha t))$$

For such a system, followings are found for  $\text{Co}_3\text{O}_4$  formed at 1000 K.

Given

$$\frac{\text{W}}{\text{m}\cdot\text{K}}$$

$$k(T) := \frac{\left(150.4892 - \frac{1.903T}{10} + \frac{8.9428T^2}{10^5}\right)}{100}$$

$$\rho := 6110$$

$$\frac{\text{kg}}{\text{m}^3}$$

$$C_p(T) := \frac{(0.1263T + 86.002)}{0.2408}$$

$$\frac{\text{J}}{\text{kg}\cdot\text{K}}$$

$$\alpha(T) := \frac{k(T)}{\rho \cdot C_p(T)}$$

$$q := 2.294 \text{ J/m}^2$$

$$k_{\text{av}} := \frac{\int_{1000}^{1500} k(T) dT}{500} = 0.542$$

$$C_{p_{av}} := \frac{\int_{1000}^{1500} C_p(T) dT}{500} = 1.013 \times 10^3$$

$$\alpha_{av} := \frac{\int_{1000}^{1500} \alpha(T) dT}{500} = 8.752 \times 10^{-8}$$

$$T(x,t) := \frac{\frac{q}{\rho \cdot C_{p_{av}}}}{(\pi \cdot \alpha_{av} \cdot t)^{0.5}} \cdot \exp\left(\frac{-x^2}{4 \cdot \alpha_{av} \cdot t}\right)$$

$$T_r(x,t) := 1000 + T(x,t)$$

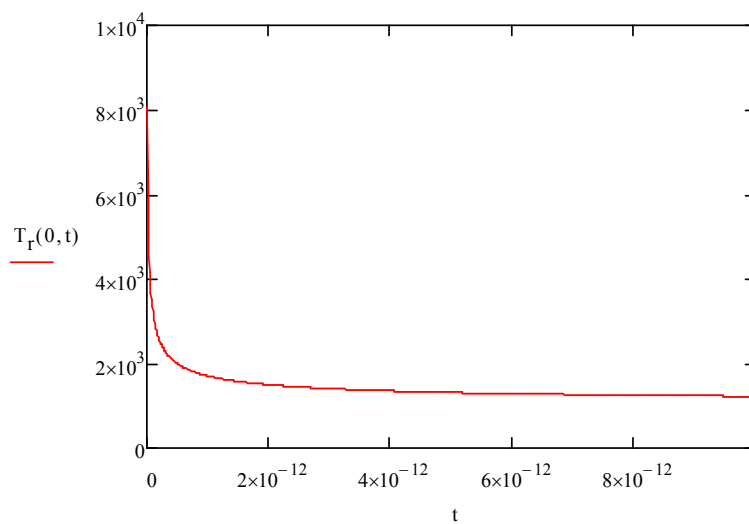


Figure B:2 Transient temperature profile for infinite plane source emitting half space

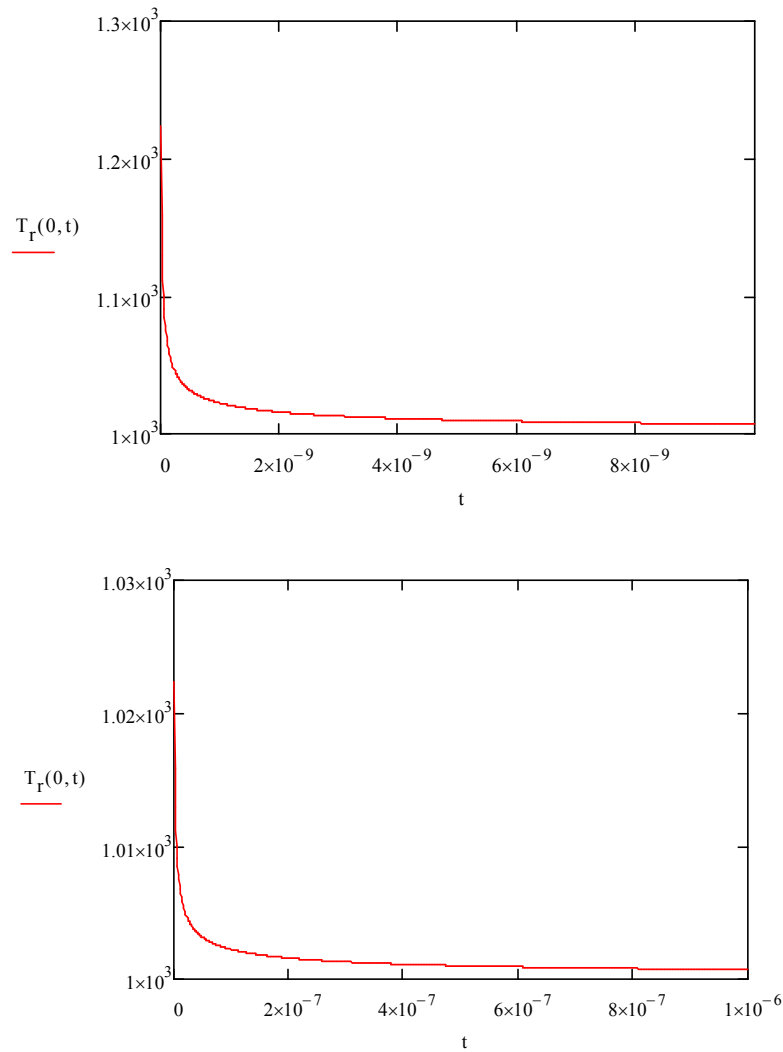


Figure B:2 Transient temperature profile for infinite plane source emitting half space (continued)

### B.3.5 Constant Surface Temperature and Heat Flux in a Semi-Infinite Plate

Solutions of thermal diffusion into a semi-finite plane was also done for the cases of constant surface temperature and heat flux with the same conditions in part 9.2.3.4 where  $T_s$  and  $q$  are taken from fundamental analysis. All temperatures are in K and where time scale is seconds.

### Constant Surface Temperature

$$T_s := 1780.59 \quad T_i := 1000$$

$$T(x,t) := T_s + (T_i - T_s) \cdot \operatorname{erf}\left[\frac{x}{2(\alpha_{av}t)^{0.5}}\right]$$

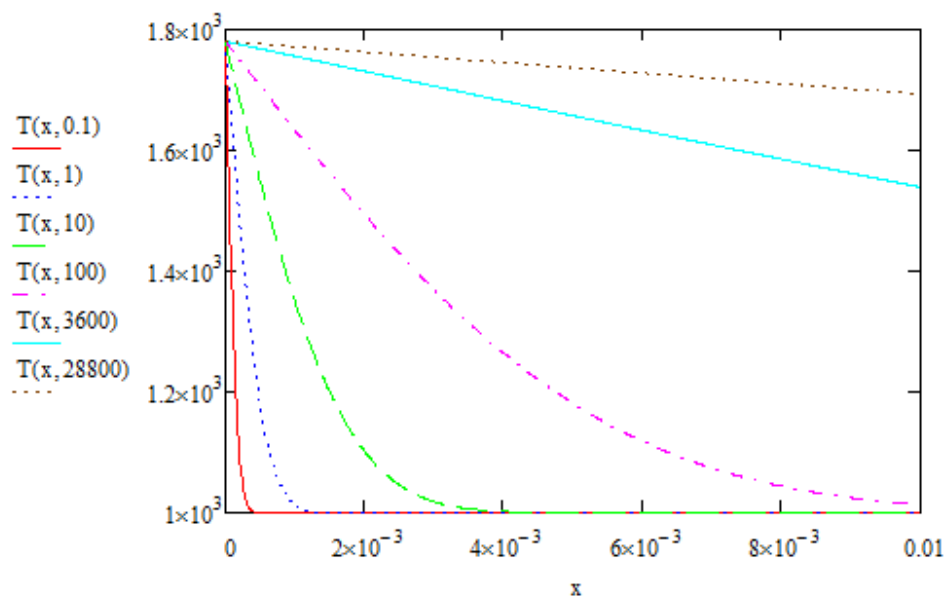


Figure B:3: Transient temperature profiles for constant surface temperature boundary condition

### Constant Heat Flux

$$T_f(x,t) := T_i + \frac{2 \cdot q \cdot \left(\frac{\alpha_{av} \cdot t}{\pi}\right)^{0.5}}{k_{av}} \cdot \exp\left(\frac{-x^2}{4 \cdot \alpha_{av} \cdot t}\right) - \frac{q \cdot x}{k_{av}} \cdot \operatorname{erfc}\left[\frac{x}{2(\alpha_{av} \cdot t)^{0.5}}\right]$$

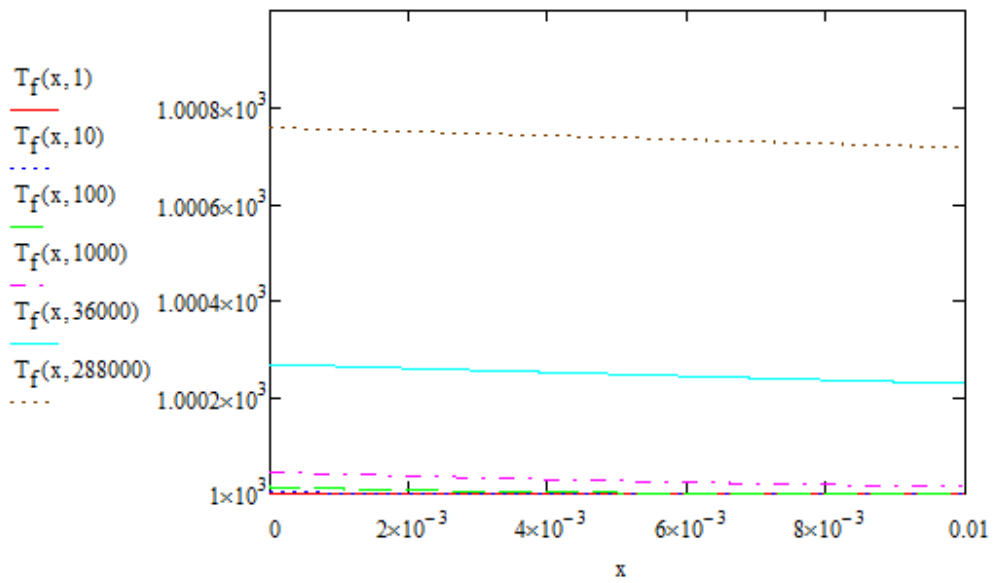


Figure B:4: Transient temperature profiles for constant surface flux boundary condition

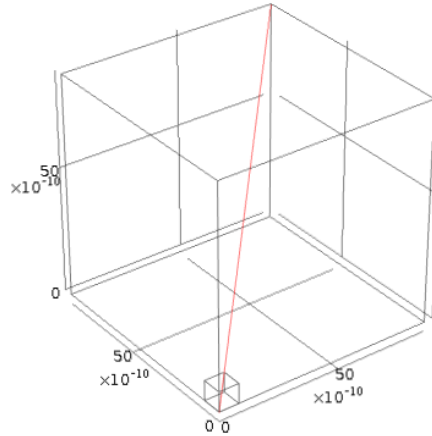
## B.4 Heating/Cooling of a Finite Geometry

### B.4.1 Cube of Co<sub>3</sub>O<sub>4</sub>: Heating Problem

#### Schematics:

Inner Cube Edge: 8.08 Å

Outer Cube Edge: 8.08 nm



#### Physics:

##### Variables:

$$k = (150.4892[\text{W/m/K}] - 1.903[\text{W/m/K/K}]/10 \cdot T + 8.9428[\text{W/m/K}^3]/100000 \cdot T \cdot T) / 100$$

$$C_p = 0.1263[\text{J/mol/K}^2] \cdot T + 86.002[\text{J/mol/K}]$$

$$\rho = 6110[\text{kg/m}^3]$$

$$C_{p2} = c_p / m_w$$

$$MW = 0.24080[\text{kg/mol}]$$

##### Equation to be solved:

$$\rho C_p \frac{\partial \text{temp}}{\partial t} + \rho C_p \mathbf{u} \cdot \nabla \text{temp} = \nabla \cdot (k \nabla \text{temp}) + Q$$

##### Initial Values:

##### *Evaluation of Temperature for one unit cell*

Since 1 molecule of Co<sub>3</sub>O<sub>4</sub> does not have enough energy to decompose, 1 unit cell (8 atoms) are taken as the system. The dimensions are arranged accordingly.

$$h(T) := 0.0251 \cdot T^2 - 23.318 \cdot T - 904189$$

$$q_0 := h(1000) = -9.024 \times 10^5 \quad \text{joule/mol}$$

$$cp(T) := 0.1263T + 86.002$$

$$cp(1000) = 212.302 \quad \text{J / K/mol}$$

$$A_N := 6.02 \cdot 10^{23}$$

$$q := \frac{q_0}{A_N} = 0$$

$$q - \frac{8}{A_N} \left[ \left( \frac{0.1263}{2} \cdot tt^2 + 86.002 \cdot tt \right) - \left( \frac{0.1263}{2} \cdot 1000^2 + 86.002 \times 1000 \right) \right] \text{ solve, tt} \rightarrow \begin{pmatrix} 338.52779601737667356 \\ -1700.3963629215730314 \end{pmatrix}$$

T<sub>inner cube</sub> = 338.528 K

T<sub>outer cube</sub> = 1000 K

### Results:

Change in the temperature as a function of time for the diagonal line (see schematics) is given below.

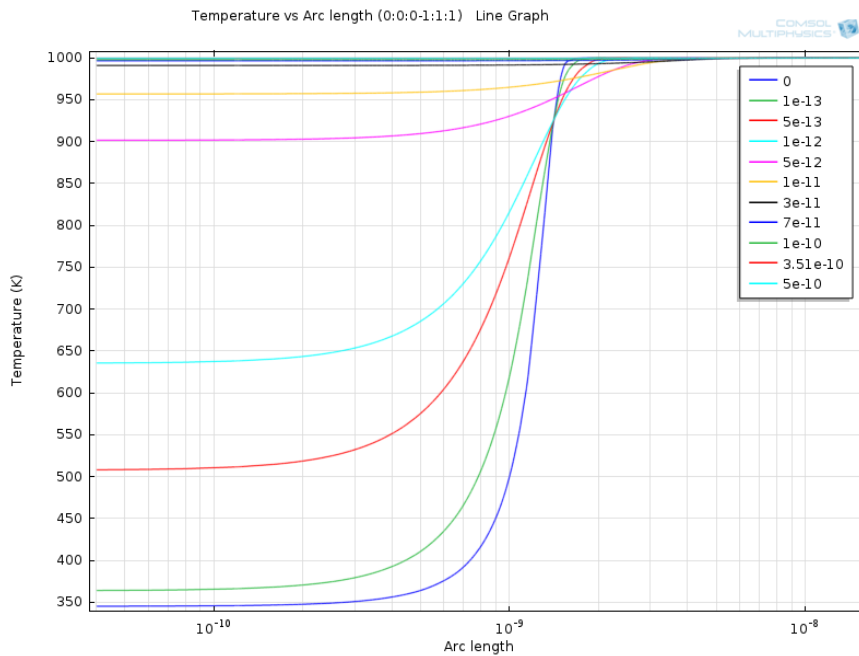


Figure B:5 Diagonal transient temperature profile

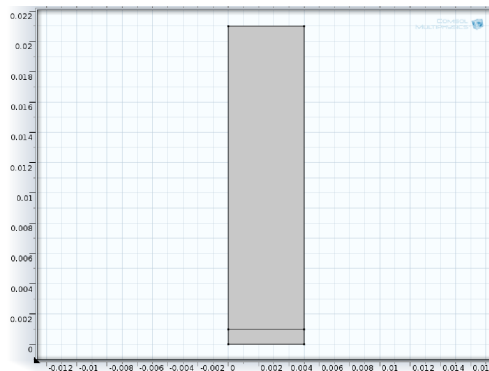
## B.4.2 Cooling of a Plate

Here, it desired to solve a hypothetical case where a thin slab temperature has increased by 50 degree and that somehow generated heat is distributed over a longer plate. Solution is done for different thickness of heated thin slab.

### Schematics:

Slab: 5mm x 20 mm

Thin Slab: 5mm x (0.01, 0.1, 0.25, 0.5, 0.75, 1, 1.5) mm (in which temperature is increased)



### Physics:

#### Variables:

$$k = (150.4892[\text{W/m/K}] - 1.903[\text{W/m/K/K}] \cdot T + 8.9428[\text{W/m/K}^3] / 100000 \cdot T^2) / 100$$

$$C_p = 0.1263[\text{J/mol/K}^2] \cdot T + 86.002[\text{J/mol/K}]$$

$$\rho = 6110[\text{kg/m}^3]$$

$$C_{p2} = c_p / m_w$$

$$MW = 0.24080[\text{kg/mol}]$$

#### Equation to be solved:

$$\rho C_p \frac{\partial \text{temp}}{\partial t} + \rho C_p \mathbf{u} \cdot \nabla \text{temp} = \nabla \cdot (k \nabla \text{temp}) + Q$$

#### Initial Values:

$$T_{\text{thin}} = 1050 \text{ K}$$

$$T_{\text{slab}} = 1000 \text{ K}$$

**Results:**

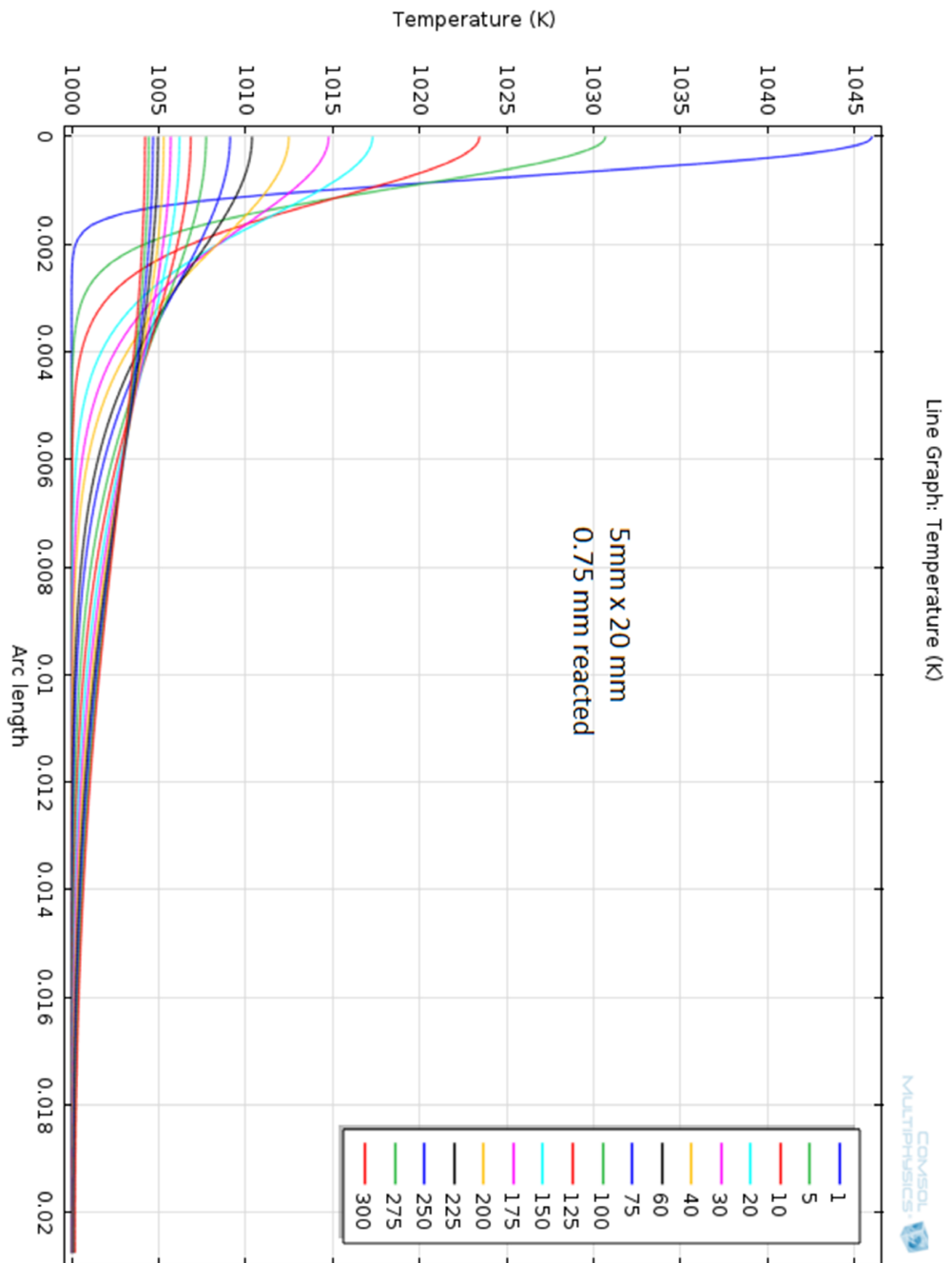


Figure B:6 Temperature profiles at different time steps for 0.75 mm thin slab

Temperatures (x, y, t) for the point P (0, 0) for different thicknesses of the high temperature zone are given below.

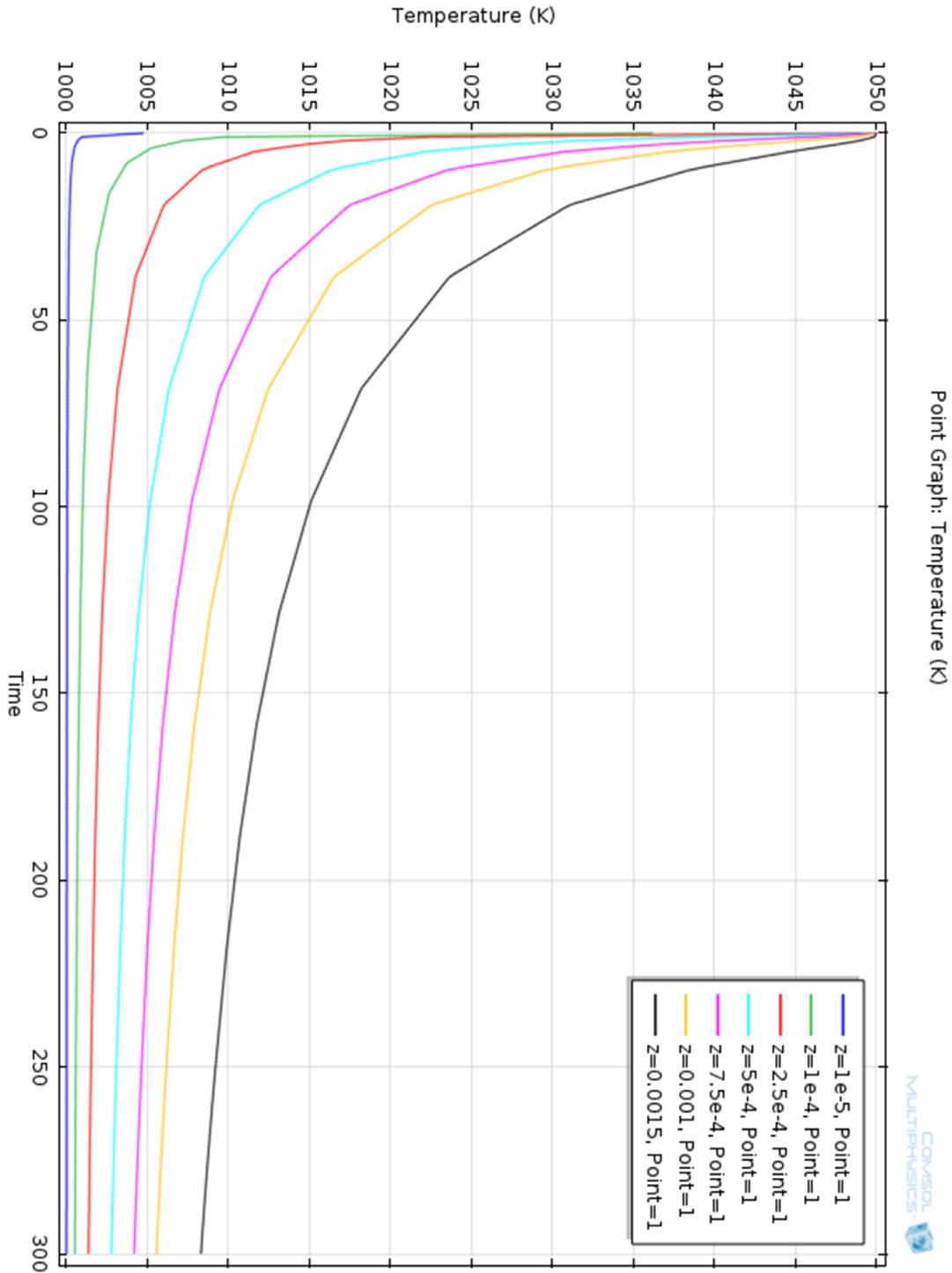


Figure B:7 Transient temperature profiles as a function of slab thickness

## B.5 Numerical Solution of Simultaneous Mass and Heat Transfer within a Spherical Particle and Effectiveness Factor

If the noncatalytic gas solid reaction  $A \rightarrow P$  under non isothermal conditions where heat is transferred via conduction only is considered to be analogous with a catalytic reaction to derive an effectiveness factor, temperature profile can be found from conservation of energy,

$$\frac{d}{dr} \left( r^2 k \frac{dT}{dr} \right) + r^2 (\Delta H_{rxn} k' C_A) = 0$$

Which requires the concentration profile;

$$\frac{d}{dr} \left( r^2 D_{AB} \frac{dC_A}{dr} \right) + r^2 (k'(T) C_A) = 0$$

Where

$$k'(T) = k_0 \cdot \exp \left( -\frac{E_a}{RT} \right)$$

Or

$$k'(T) = k_0(T_s) \exp \left( -\frac{E_a}{RT_s} \left( \frac{T_s}{T} - 1 \right) \right)$$

Which is a function of temperature, indicating the simultaneous solution of those two mechanisms. To do so, boundary conditions are to be determined;

$$C_A = C_{As} \text{ at } r = R; \quad \frac{dC_A}{dr} = 0 \text{ at } r = 0$$

$$T = T_s \text{ at } r = R; \quad \frac{dT}{dr} = 0 \text{ at } r = 0$$

In their study, Weisz and Hicks (1961) lumped those equations into one equation and normalized as follows,

$$D_{AB} \left( \frac{d^2 C_A}{dr^2} + \frac{2}{r} \frac{dC_A}{dr} \right) = k_0 \frac{C_A}{C_{As}} \exp\left(\frac{E_a}{RT_s} \cdot \frac{C_{As} \Delta H_{rxn} D_{AB}}{kT_s} \left( \frac{1 - C_A/C_{As}}{1 + \frac{C_{As} \Delta H_{rxn} D_{AB}}{kT_s} (1 - C_A/C_{As})} \right)\right)$$

$$\frac{d^2 y}{dx^2} + \frac{2}{x} \frac{dy}{dx} = \phi_0^2 y \exp\left(\gamma \beta \frac{1 - y}{1 + \beta(1 - y)}\right)$$

Where

$$y = \frac{C_A}{C_{As}}, x = \frac{r}{R}, \gamma = \frac{E_a}{RT_s}, \beta = \frac{C_{As} \Delta H_{rxn} D_{AB}}{kT_s}, \phi_0^2 = R^2 \frac{k_0}{D_{AB}}$$

$$y = 1 \text{ at } x = 1; \frac{dy}{dx} = 0 \text{ at } x = 0$$

### B.5.1 Definition of Nonisothermal Effectiveness Factor

Rate within the pellet can be found from

$$r_A = \int_0^R k'(T) C_A(r) (4\pi r^2) dr$$

If above dimensionless relationship is used,

$$r_A = \frac{4}{3} \pi R^3 k_s C_{As} \left( 3 \int_0^1 x^2 y(x) \exp\left(\gamma \beta \frac{1 - y(x)}{1 + \beta(1 - y(x))}\right) dx \right)$$

effectiveness factor becomes,

$$r_A = \eta \left( \frac{4}{3} \pi R^3 \right) k_s C_{As}$$

$$\eta = 3 \int_0^1 x^2 y(x) \exp\left(\gamma \beta \frac{1 - y(x)}{1 + \beta(1 - y(x))}\right) dx$$

## B.5.2 Solution of the ODE

Solution of the ODE is done via COMSOL Multiphysics ODE solver package.

Definition of the Problem: Geometry is defined as a sphere of radius 1 with a general diffusion-convection definition,

$$d_a \frac{\partial u}{\partial t} + \nabla \cdot (-c \nabla u) + \beta \cdot \nabla u = f$$

$$\nabla = \left[ \frac{\partial}{\partial r}, \frac{\partial}{\partial y}, \frac{\partial}{\partial z} \right]$$

Where

$$\beta = d_a = 0$$

$$f = \phi_0^2 u \exp\left(\gamma \beta \frac{1-u}{1+\beta(1-u)}\right)$$

$$u = 0 \text{ at } t = 0$$

$$u = 1 \text{ at } r = 1$$

$$du/dr = 0 \text{ at } r = 0$$

$$\eta = 3 \int_0^1 r^2 u(r) \exp\left(\gamma \beta \frac{1-u(r)}{1+\beta(1-u(r))}\right) dr$$

Mesh Definition: To create a fast converging and accurate mesh, surface of the sphere is divided into triangular elements with following specifications:

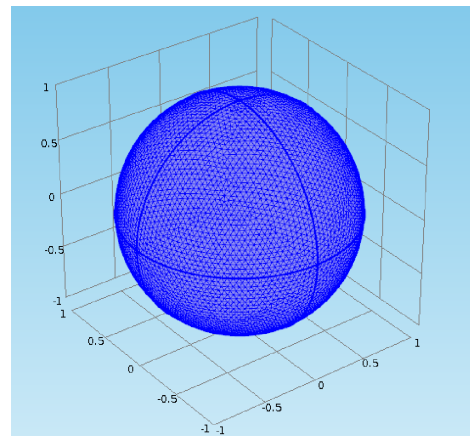
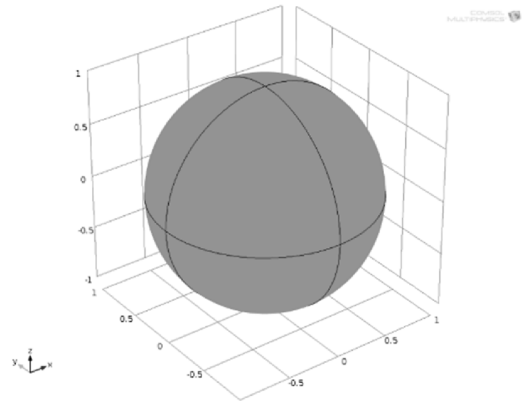
Maximum element size: 0.046

Minimum element size: 0.0030

Maximum element growth rate: 1.08

Resolution of curvature: 0.30

Resolution of narrow regions: 0.95



After that, surface is set to grow inward with following constraints:

Maximum element size: 0.2

Minimum element size: 0.0036

Maximum element growth rate: 1.50

Resolution of curvature: 0.60

Resolution of narrow regions: 0.5

By doing so, 41624 elements are created with 7322 boundary elements.

Solver Configurations: Relative tolerance is set to be 0.0010 and number of iteration is limited to 25. Minimum dumping factor is given as  $10^{-5}$ .

Solution: For the solution,  $\gamma$  is fixed for 10 and for different fixed  $\beta$  values,  $\phi_0$  are swept to solve u distribution within the pellet. As an example  $\beta = 0.8$ , which changes most drastically is to be shown here.

To be able to compute the effectiveness factor, line integration method is used with an integration order of 4.

Since the change from one Thiele modulus to another can be great, parametric swept options could not be used. Instead, different  $\phi$  values are fed one by one and  $\eta$  is found accordingly.

Following  $\eta$  values are obtained for  $\gamma = 10$  and  $\beta=0.8$ .

Table B:3 Effectiveness factors for several Thiele modulus values

$\phi$	$\eta$
0.3	1.05
0.5	1.15
0.6	1.26
0.7	1.49
0.77	421
0.8	4.99
0.9	5.76
1	5.91
3	3.11
5	1.98
10	1.03
50	0.2

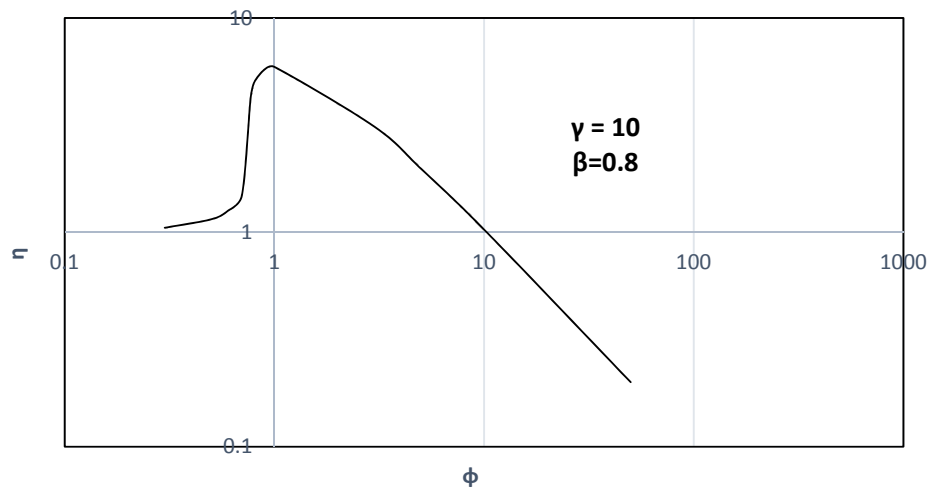


Figure B:8 Nonisothermal effectiveness factor

### B.5.3 Calculation of $\beta$ for Cobalt Oxide

$\beta$  value for the cobalt oxide reaction was found at a practical temperature; that is 1000 K, as follows via Mathcad:

$$k(T) := \frac{\left(150.4892 - \frac{1.903 \cdot T}{10} + \frac{8.9428 \cdot T^2}{10^5}\right)}{100} \frac{\text{W}}{\text{m} \cdot \text{K}}$$

$$\frac{\int_{1000}^{1300} k(T) \, dT}{300} = 0.506$$

$$\Delta H_{\text{rxn}} := h_{\text{Co}_3\text{O}_4} - 3 \cdot h_{\text{CoO}} \quad \frac{\text{kJ}}{\text{mol}}$$

$h_{\text{CoO}} :=$	$\begin{pmatrix} -235.343 \\ -234.402 \\ -233.625 \\ -233.428 \\ -232.970 \\ -232.709 \\ -232.656 \\ -232.827 \\ -233.353 \\ -234.348 \\ -243.217 \end{pmatrix}$
---------------------	--

$h_{\text{Co}_3\text{O}_4} :=$	$\begin{pmatrix} -909.774 \\ -908.999 \\ -907.802 \\ -907.337 \\ -905.043 \\ -902.293 \\ -899.139 \\ -895.639 \\ -892.206 \\ -889.197 \\ -881.838 \end{pmatrix}$
--------------------------------	--

$$D_{\text{O}} := 5.4 \cdot 10^{-8} \quad T_s := 1000 \quad C_{\text{As}} := 1$$

$$\beta(C) := \frac{D_{\text{O}} \cdot (-\Delta H_{\text{rxn}})_s}{C_{\text{As}} \cdot k(1000) \cdot T_s} \quad +$$

$$\beta(1000) = 2.222 \times 10^{-8}$$

## B.6 Solution of the Growth Model

### Diffusivity of Oxygen(cm<sup>2</sup>/s):

$$D(T) := 50 \cdot 10^0 \cdot \exp\left(\frac{-95000}{8.314 \cdot T}\right) \quad \text{as given in part 3.4.1.}$$

### Reaction Rate Constant(1/s):

$$k_s(T) := 1.98 \cdot 10^{39} \cdot \exp\left(\frac{-960000}{8.314 \cdot T}\right)$$

from: Wong, B., *Thermochemical Heat Storage for Concentrated Solar Power*, U.S. Department of Energy under DE-FG36-08GO18145, GENERAL ATOMICS PROJECT 30314, 2011.

### Molecules per unit volume of formed oxide layer (mol/cm<sup>3</sup>):

$$\rho_m := \frac{8}{(8.08 \cdot 10^{-10})^3 \cdot 6.02 \cdot 10^{23} \cdot 10^6} = 0.025$$

from:  
Wang, J., *Low Energy Electron Diffraction Studies of Transition Metal Oxide Surfaces and Films*, obtained from <http://nbn-resolving.de/urn/resolver.pl?urn=nbn%3Ade%3Aagbv%3A3-000007962>, 2005.

or from the density of cobalt oxide:

$$\frac{6110 \cdot 1000}{240 \cdot 10^6} = 0.025$$

### Surface Concentration (mol/cm<sup>3</sup>):

$$C_{O_s}(T) := \frac{5.885}{10^6} \cdot \exp\left(\frac{-37870}{8.314 \cdot T}\right) \quad \text{from the study:}$$

### Parameters

$$\alpha(T) := 2 \cdot C_{O_s}(T) \cdot \frac{D(T)}{\rho_m} \quad \beta(T) := k_s(T) \cdot \frac{C_{O_s}(T)}{\rho_m}$$

### Oxide Layer Thickness (cm):

$$\delta(T, t) := \frac{(2 \cdot D(T))}{(k_s(T))} \cdot \left( \sqrt{1 + \frac{2 \cdot C_{O_s}(T) \cdot k_s(T)}{D(T) \cdot \rho_m} \cdot t} - 1 \right)$$

$D(1000) = 5.451 \times 10^{-4}$   
 $k_s(1000) = 1.411 \times 10^{-11}$   
 $C_{O_s}(1000) = 6.188 \times 10^{-8}$

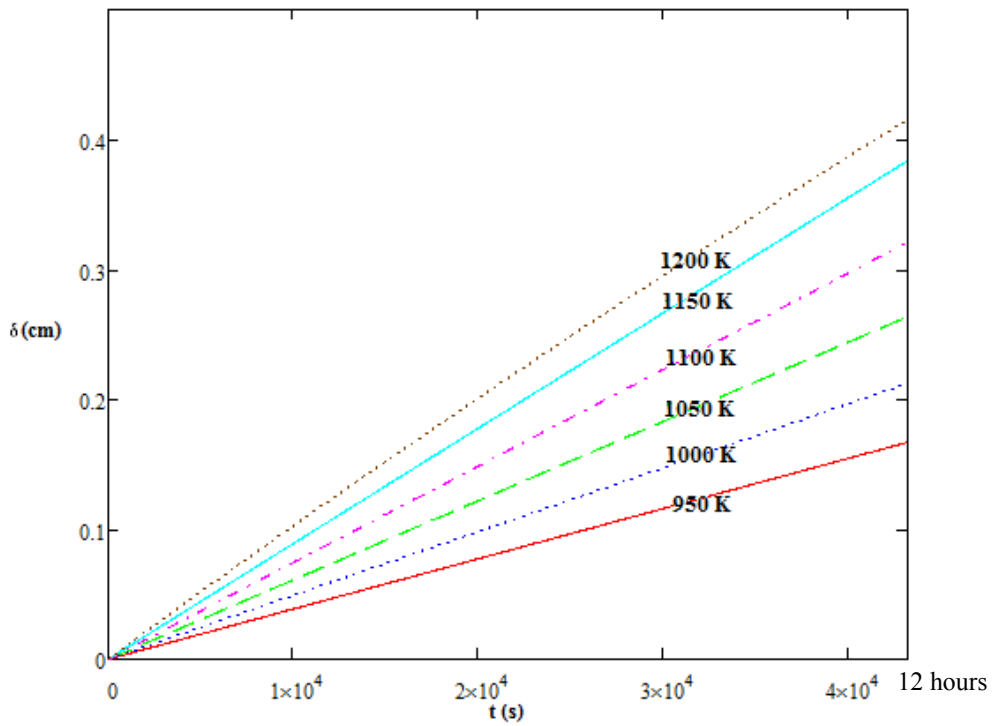
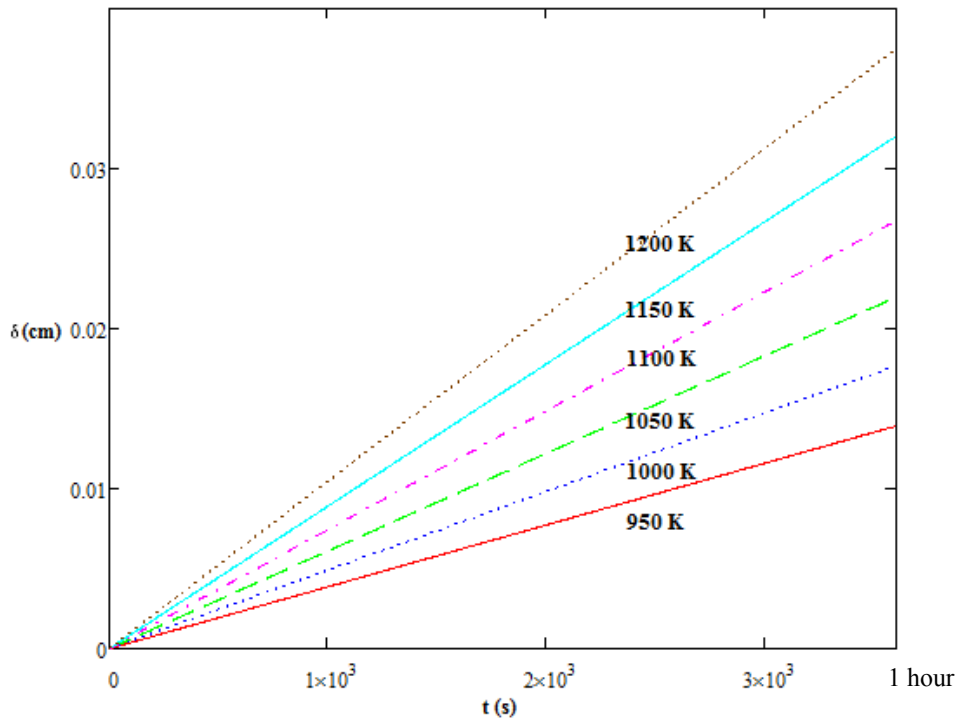


Figure B:9 Increase in oxide layer thickness in time

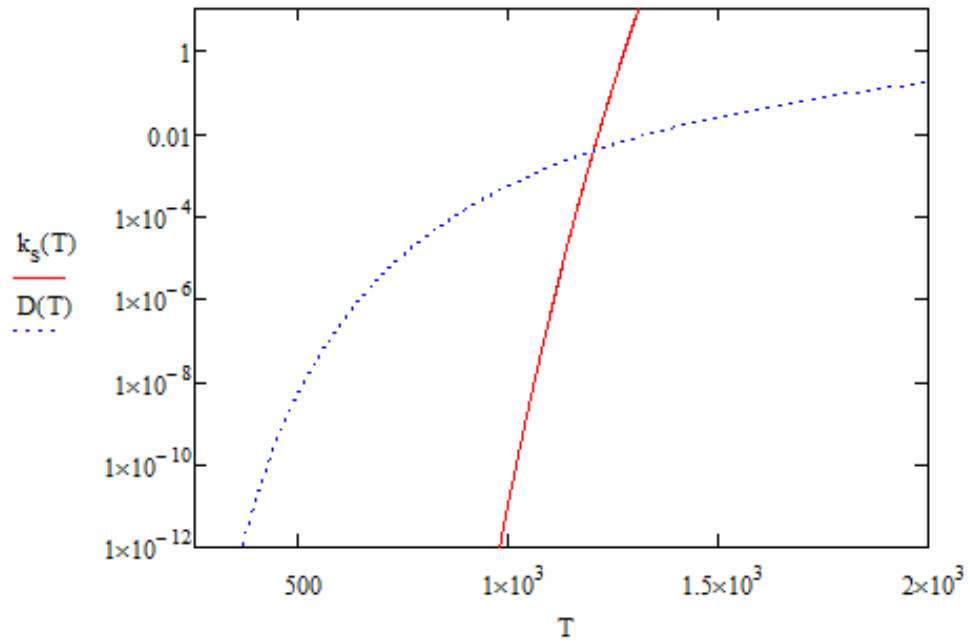


Figure B:10 Reaction constant (1/s) and Diffusivity of Oxygen ( $\text{cm}^2/\text{s}$ ) as a function of temperature (K)

Da number is also defined as follows, which shows that expected conversion is more than 90% for temperatures above 1000 K.

$$T := 1..2000 \quad a := (0.38 \cdot 6110)^{-1} = 4.307 \times 10^{-4} \text{ m}^2$$

$$\text{Da}(T) := \frac{k_s(T)}{D(T) \cdot a} \cdot 10000 \quad \text{Da}_{\text{number}}$$

$$\text{Da}(1030) = 12.445$$

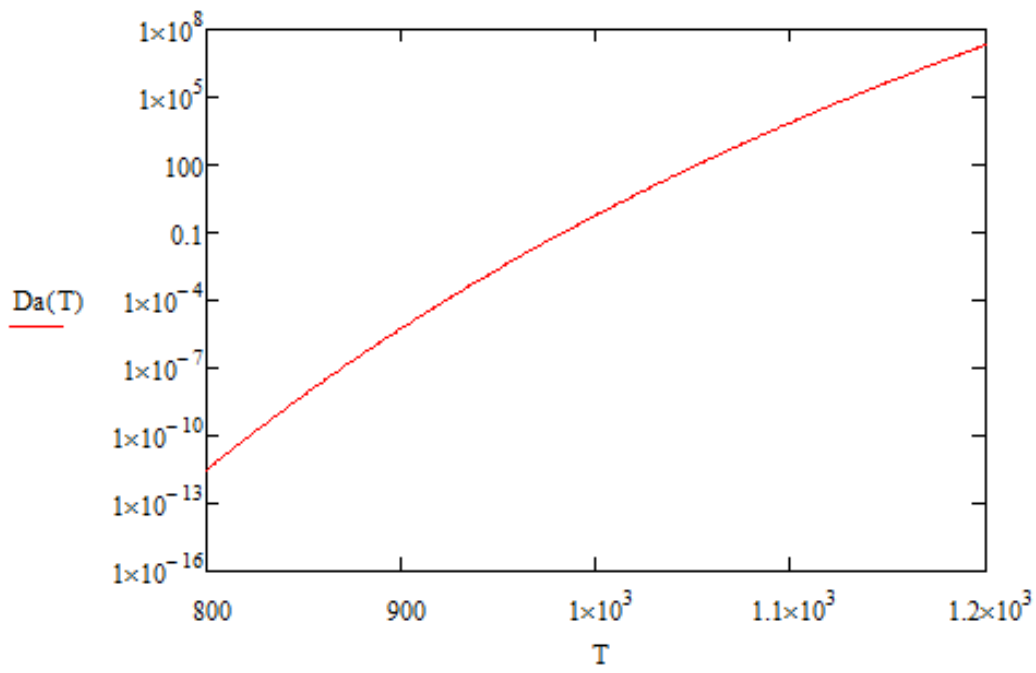


Figure B:11 Da number as a function of temperature (K)

## B.7 Simulation of Heat Transfer Problem in the Reactors Used for CO Production

### B.7.1 Steel Reactor

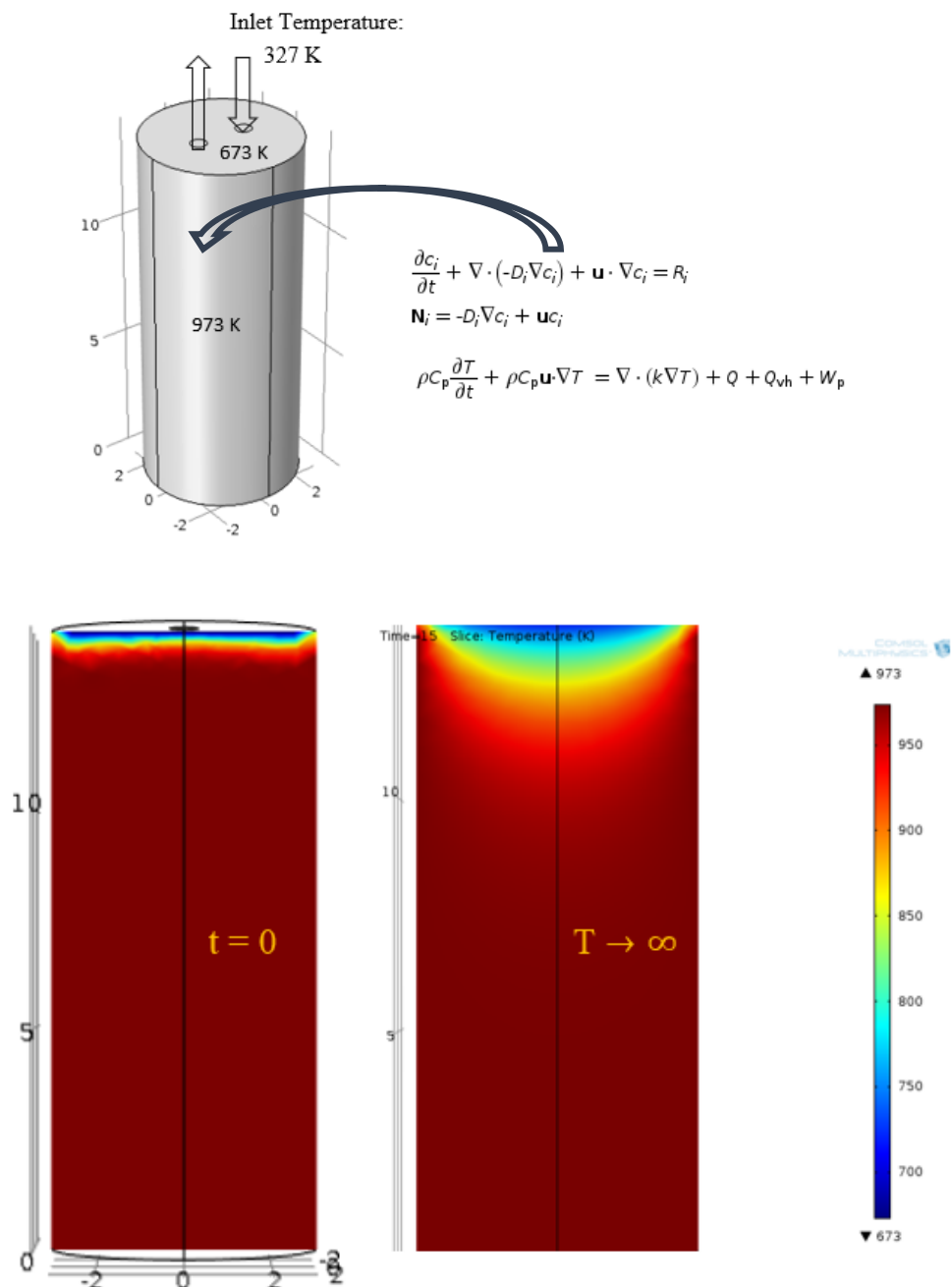


Figure B:12 Temperature profile for the steel reactor

## B.7.2 Quartz Reactor

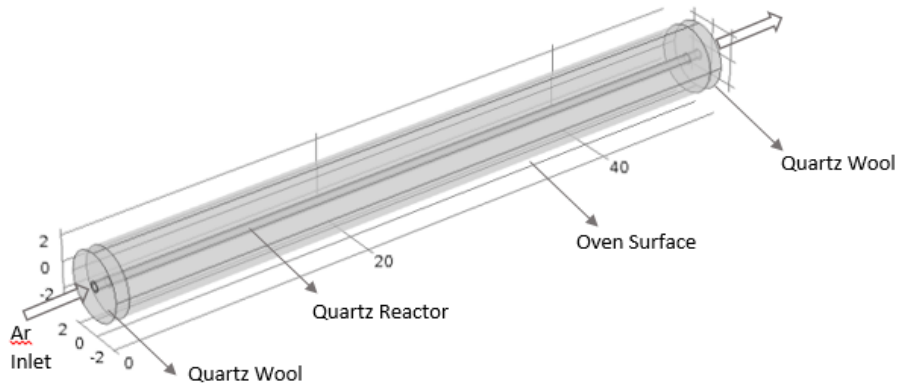


Figure B:13 Schematics of the quartz reactor

For the quartz reactor, reactor properties are given for quartz glass and domain between the oven and the reactor is defined as air. Heating of the oven was simulated based on surface temperature dependent on time as in the experiment. Quartz wools were added to both ends opened to the room temperature environment as well. Midpoint temperature was recorded in the model until system reaches steady state. Results are given below.

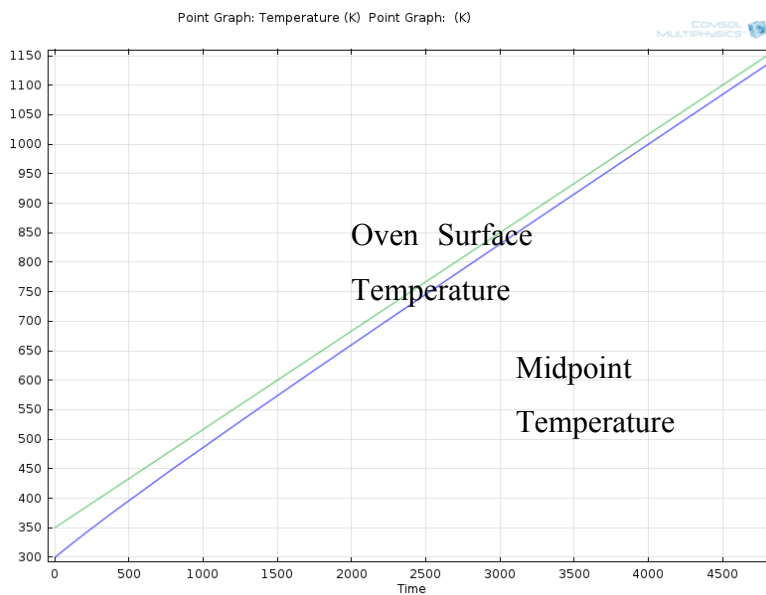


Figure B:14 Temperature of the midpoint in the quartz reactor as a function of time

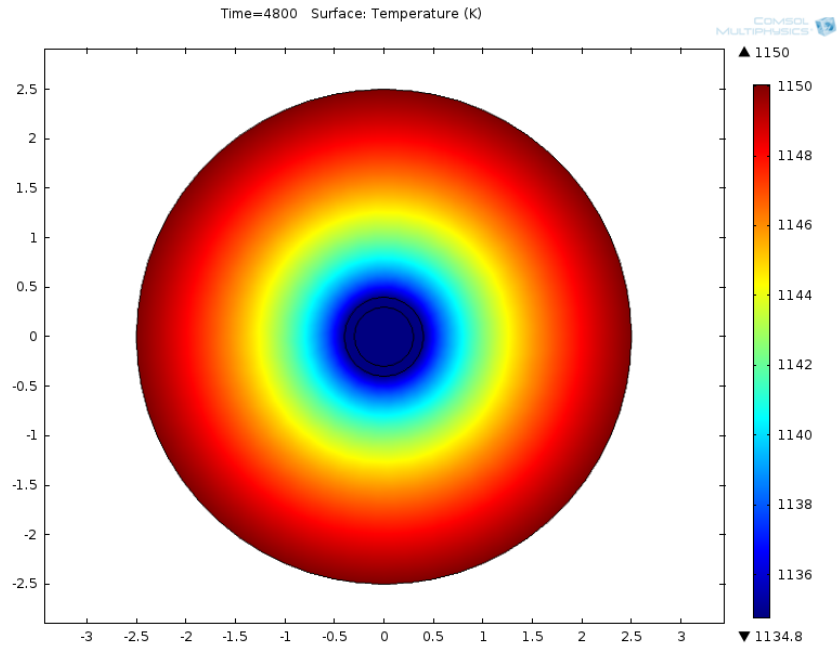


Figure B:15 Temperature profile of the midpoint cross section in the quartz reactor at steady state

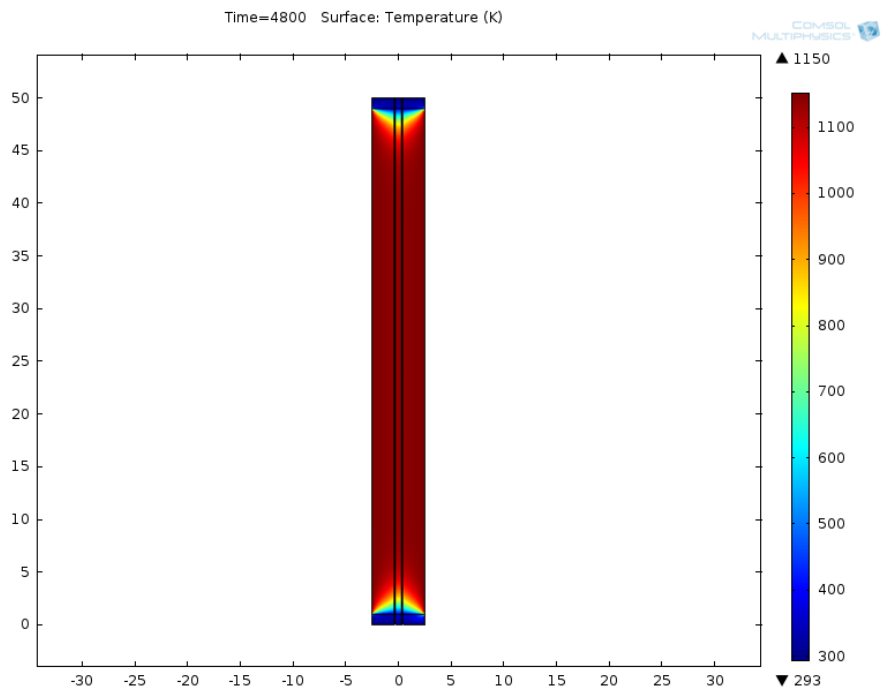


Figure B:16 Temperature profile of the axial cross section in the quartz reactor at steady state

## B.8 Physical Properties used in Reactor Modeling

$$MW_{\text{CoO}} = 74.933 \text{ g/mol [1]}$$

$$MW_{\text{Co}_3\text{O}_4} = 240.8 \text{ g/mol [1]}$$

$$\rho_{\text{CoO}} = 6440 \text{ kg/m}^3 \text{ [2]}$$

$$\rho_{\text{Co}_3\text{O}_4} = 6110 \text{ kg/m}^3 \text{ [2]}$$

$$k_c = 150.4892 - 0.1903T + 8.9428 \times 10^{-5} T^2 \text{ W/mK [2]}$$

$$Cp_{\text{CoO}} = (0.0102T + 45.789) / MW_{\text{Co}_3\text{O}_4} \text{ J/kgK [3]}$$

$$Cp_{\text{Co}_3\text{O}_4} = (0.1322T + 78.032) / MW_{\text{CoO}} \text{ J/kgK [3]}$$

$$\Delta H_{\text{Co}_3\text{O}_4 \rightarrow \text{CoO}} = (-5 \times 10^{-5} T^2 + 0.0758T + 178.72) / MW_{\text{Co}_3\text{O}_4} \text{ kJ/kg Co}_3\text{O}_4 \text{ reacted [3]}$$

[1] Felder, R.M. and Rousseau, R.W., *Elementary Principles of Chemical Processes*, 3<sup>rd</sup> Ed., John Wiley & Sons, Inc., New York, 2000.

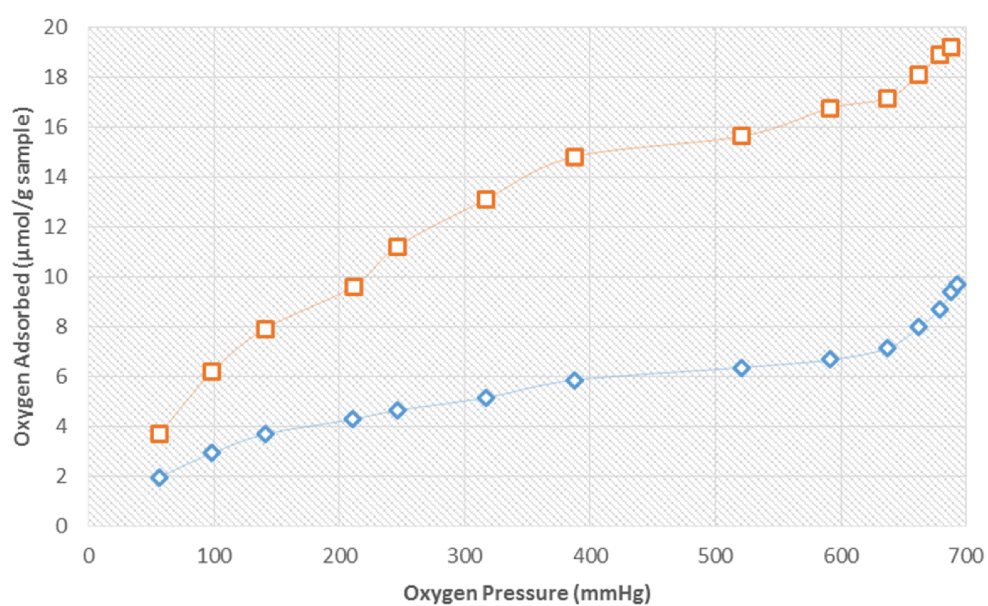
[2] Yaws, C.L., *Chemical Properties Handbook*, McGraw-Hill, New York, 1999.

[3] Barin, I., *Thermochemical properties of Pure Substances*, Weinheim, Basel, 1989.

## APPENDIX C

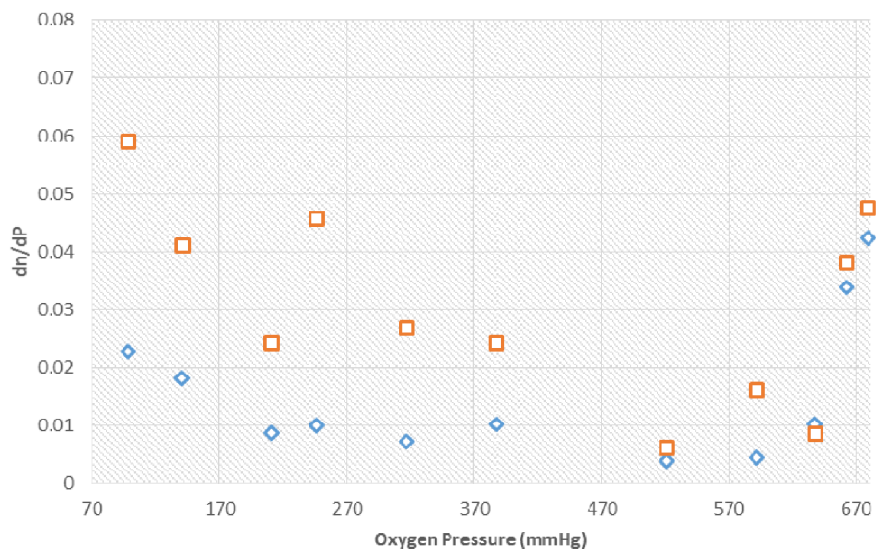
### EXPERIMENTAL DATA

#### C.1 Adsorption-Desorption of Oxygen on Cobalt Oxide

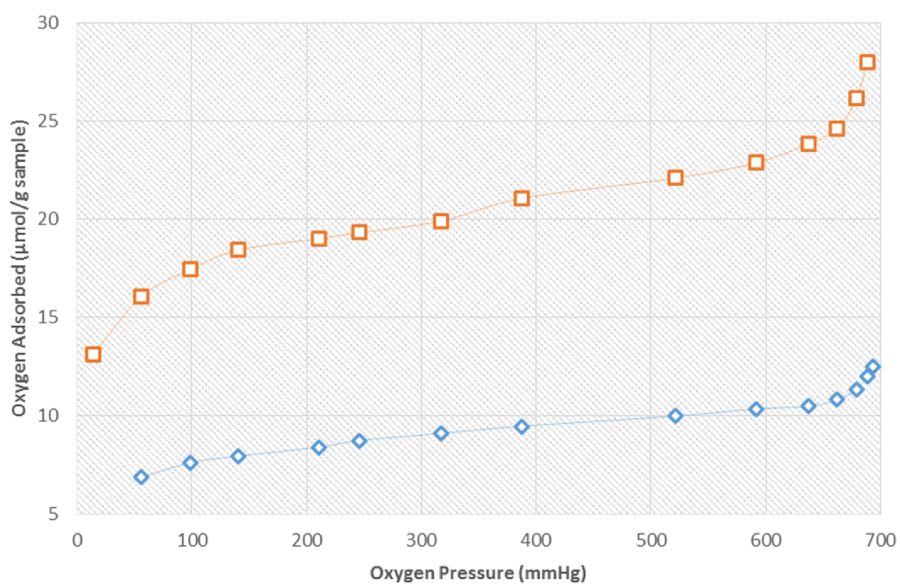


(a) 1<sup>st</sup> adsorption isotherms for CA-0913-1[◇] and CA-0913-1(2) [□]

Figure C:1 Comparison of oxygen adsorption isotherms at room temperature for sample CA-0913-1 and CA-0913-1(2)

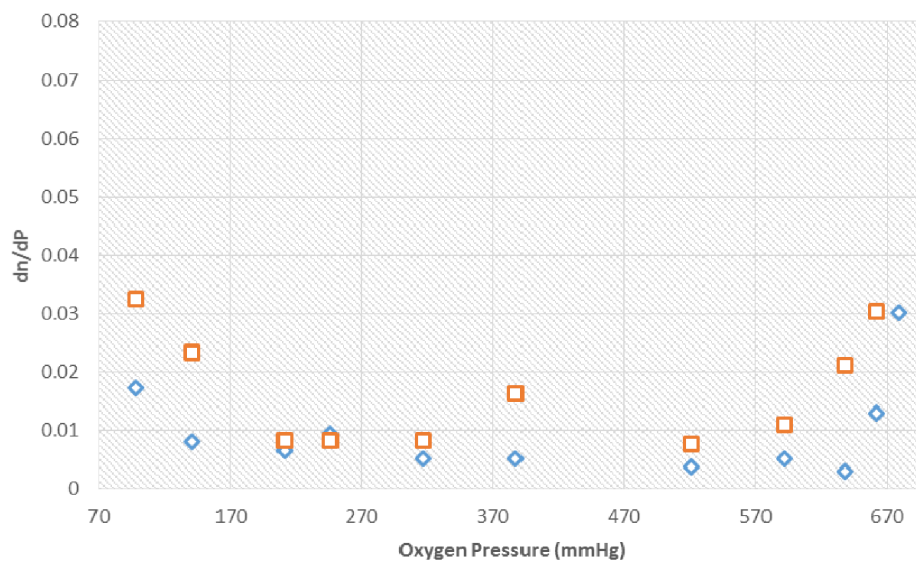


(b) Rate of change of adsorbed oxygen amount with increasing pressure for CA-0913-1[◇] and CA-0913-1(2) [□] – based on 1<sup>st</sup> adsorption isotherms

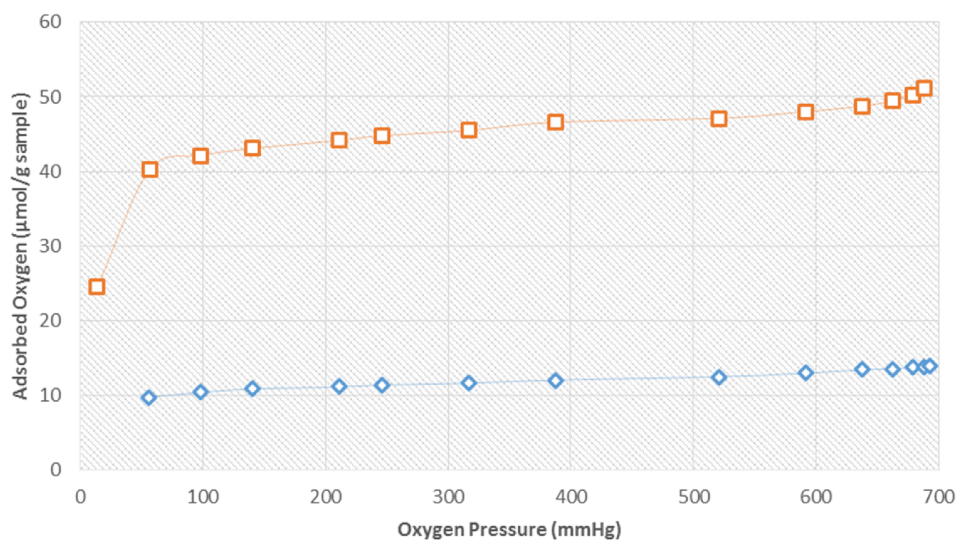


(c) 2<sup>nd</sup> adsorption isotherms for CA-0913-1[◇] and CA-0913-1(2) [□]

Figure C:1 Comparison of oxygen adsorption isotherms at room temperature for sample CA-0913-1 and CA-0913-1(2) (continued)

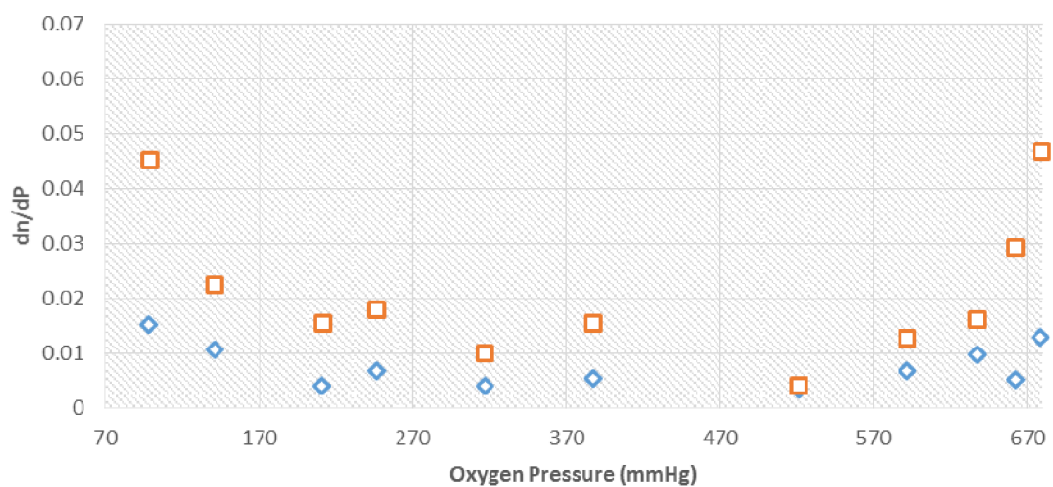


(d) Rate of change of adsorbed oxygen amount with increasing pressure for CA-0913-1[◇] and CA-0913-1(2) [□] – based on 2<sup>nd</sup> adsorption isotherms



(e) 3<sup>rd</sup> adsorption isotherms for CA-0913-1[◇] and CA-0913-1(2) [□]

Figure C:1 Comparison of oxygen adsorption isotherms at room temperature for sample CA-0913-1 and CA-0913-1(2) (continued)



(f) Rate of change of adsorbed oxygen amount with increasing pressure for CA-0913-1[◇] and CA-0913-1(2) [□] – based on 3<sup>rd</sup> adsorption isotherms

Figure C:1 Comparison of oxygen adsorption isotherms at room temperature for sample CA-0913-1 and CA-0913-1(2) (continued)

## C.2 Production of Hydrogen over Reduced Cobalt Oxide

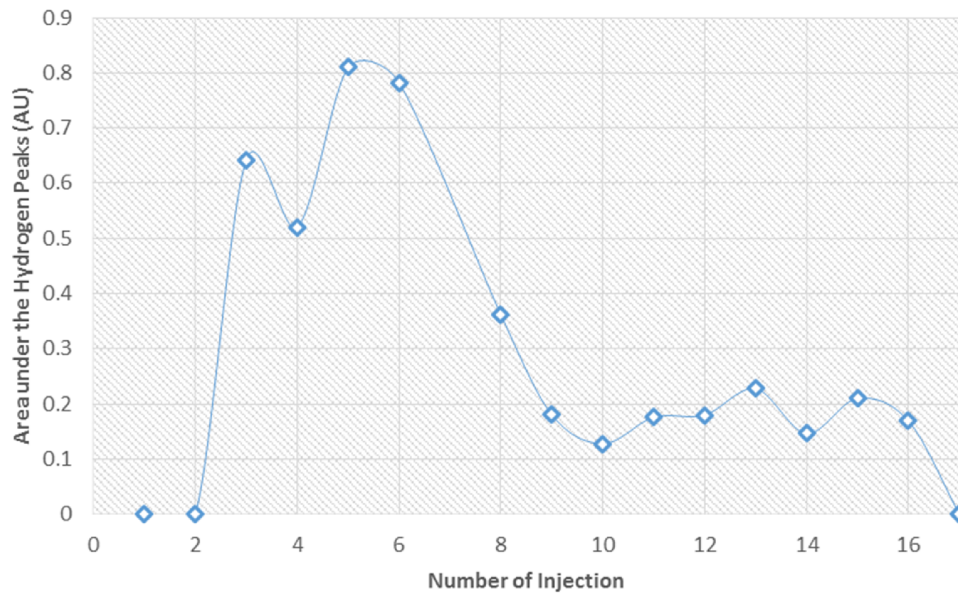


Figure C:2 Area for the produced hydrogen for each cycle with water splitting reaction

### C.3 Kinetic Analysis

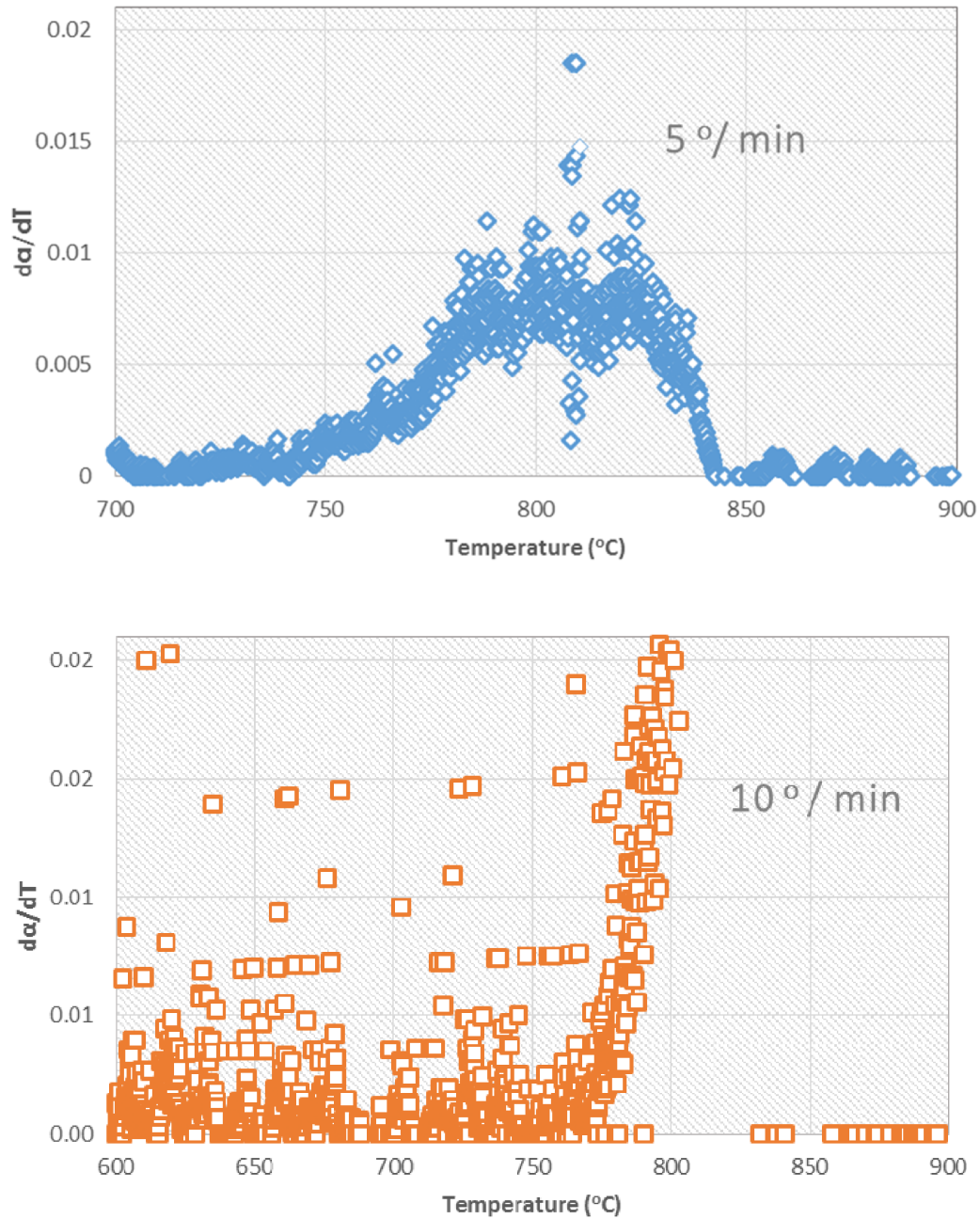


Figure C:3 DTA curves obtained at the heating rates of 5 °C, 10 °C and 15 °C for spinel cobalt oxide thermal decomposition

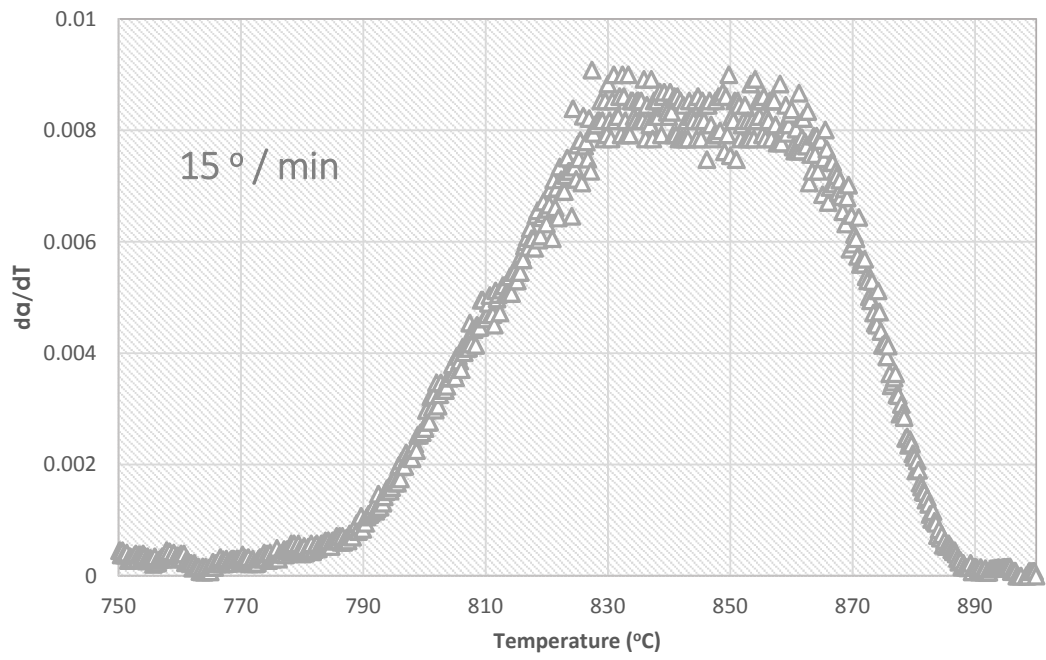


Figure C:3 DTA curves obtained at the heating rates of 5° C, 10° C and 15° C for spinel cobalt oxide thermal decomposition (continued)



## APPENDIX D

### DERIVATION OF MATHEMATICAL MODELS

#### D.1 Isothermal Gradientless Reactor

Conservation of mass has been defined from the Avrami [108,109] model as follows:

$$\frac{d\alpha}{dt} \left[ \frac{1}{s} \right] = k \left[ \frac{1}{s} \right] \cdot f(\alpha)$$
$$k \left[ \frac{1}{s} \right] \cdot f(\alpha) = A \left[ \frac{1}{s} \right] \exp\left(-\frac{E_a}{RT}\right) (1 - \alpha)^n$$

where A and n were found experimentally as given in part 5.3.

Initial condition was selected as;

$$\alpha(0) = 0$$

Implying that initially there is only  $\text{Co}_3\text{O}_4$ . To be able to solve the ODE, a reaction temperature is selected arbitrarily.

## D.2 Non-isothermal Gradientless Reactor

For non-isothermal model, equation for conservation of mass was combined with the conservation of energy for a batch reactor [97];

$$\frac{d\alpha}{dt} \left[ \frac{1}{s} \right] = k \left[ \frac{1}{s} \right] \cdot f(\alpha) = A \left[ \frac{1}{s} \right] \exp \left( -\frac{E_a}{RT} \right) (1 - \alpha)^n$$

$$\frac{dT}{dt} [K/s] = \frac{\dot{Q}[W] + \dot{W}_s[W] + (-\Delta H_{rxn})[J/mol](-r_A)[mol/m^3s]V[m^3]}{\sum_{i=1}^n m_i[kg]Cp_i [J/kgK]}$$

Each term in the equation is defined as follows;

$$\dot{Q} = 10^6 \frac{W}{m^2} \times \text{Surface Area}$$

$$\text{Surface Area} = \text{Volume}^{2/3}$$

$$\dot{W}_s = 0$$

$$\Delta H_{rxn} = (-5)10^{-5}T^2 + 0.0758T + 178.72 \quad \frac{kJ}{mol \text{ Co}_3\text{O}_4\text{reacted}}$$

$$Cp_{\text{Co}_3\text{O}_4} = (0.1322T + 78.032)/MW_{\text{Co}_3\text{O}_4} \text{ J/K/kg}$$

$$Cp_{\text{CoO}} = (0.0102T + 45.789)MW_{\text{CoO}} \text{ J/K/kg}$$

As the mass of cobalt oxide phases are changing with time, they were defined as a function of  $\alpha$ ;

$$\text{Initial Mass [kg]} = W_{\text{initial}} = V_0[m^3] \cdot 6440 \text{ kg/m}^3$$

$$MW_{\text{Co}_3\text{O}_4} = 240.8 \text{ g/mol}$$

$$MW_{\text{CoO}} = 74.933 \text{ g/mol}$$

$$Final\ Mass = W_{final}[kg] = W_{initial}[kg] \frac{\frac{3\ mol\ CoO}{1\ mol\ Co_3O_4} \times MW_{CoO} \left[ \frac{kg\ CoO}{kmol\ CoO} \right]}{MW_{Co_3O_4} \left[ \frac{kg\ Co_3O_4}{kmol\ Co_3O_4} \right]}$$

$$Mass_{Co_3O_4}[kg] = W = W_{initial}[kg] - \alpha(W_{initial} - W_{final})[kg]$$

$$Mass_{CoO}[kg] = \alpha(W_{initial} - W_{final})[kg] = W_{initial}[kg] - W[kg]$$

$$\sum_{i=1}^n m_i[kg]Cp_i \left[ \frac{J}{kgK} \right] = Cp_{Co_3O_4}W + Cp_{CoO}(W_{initial} - W)$$

Similarly, rate term was derived as follows;

$$\alpha = \frac{W_{initial} - W}{W_{initial} - W_{final}}$$

$$\frac{dW}{dt} \left[ \frac{kg}{s} \right] = - \left( \frac{d\alpha}{dt} \right) \left[ \frac{1}{s} \right] (W_{initial} - W_{final})[kg]$$

If above expression is divided by the a factor  $\beta$ ;

$\beta =$  how much weight is lost per mol  $Co_3O_4$  reacted

$$\beta = MW_{Co_3O_4} \times 1\ mol - 3 \times MW_{CoO} \times 1\ mol = 16 \frac{g}{mol\ Co_3O_4}$$

$$\frac{1}{\beta} \frac{dW}{dt} \left[ \frac{mol}{s} \right] = - \frac{1}{\beta} \left( \frac{d\alpha}{dt} \right) \left[ \frac{1}{s} \right] (W_{initial} - W_{final})[mol] = (-r_A)[mol/m^3s]V[m^3]$$

$$(-r_A) \left[ \frac{mol}{m^3s} \right] V[m^3] = A \exp \left( - \frac{E_a}{RT} \right) (1 - \alpha)^n (W_{initial} - W_{final}) / (16)$$

If all those expressions are substituted into the conservation of energy equation, following was obtained:

$$\frac{dT}{dt} = \frac{Q + (-\Delta H_{rxn}(T) \times A \exp\left(-\frac{E_a}{RT}\right) (1 - \alpha)^n (W_{initial} - W_{final}))}{Cp_{Co_3O_4}W + Cp_{CoO}(W_{initial} - W)} \quad (16)$$